UCLouvain

epl

École polytechnique de Louvain

Quantifying microstructural brain anomalies in patients with Alzheimer's disease via diffusion Magnetic Resonance Imaging

Author: **Alexandre Berger**
Supervisors: **Benoit Macq, Laurence Dricot**
Readers: **Bernard Hanseeuw, Frank Peeters, Gaëtan Rensonnet**
Academic year 2019–2020
GBIO2M : Master [120] in Biomedical Engineering

Abstract

The rising elderly population in our society increases the prevalence of Alzheimer's disease, an aging-associated disease, making this neurodegenerative disorder a primary concern in our society. Recently, there has been a growing interest in shifting the diagnostic criteria of Alzheimer's disease from a clinical definition based on symptoms towards a biological definition based on neuropathological hallmarks of the disease. This approach promoted the search for new biomarkers that would refine the diagnosis, improve the clinical management of the patients, enhance clinical trials and accelerate the research for drug development. Diffusion-weighted magnetic resonance imaging is a rapidly evolving, non-radiating and non-invasive technology that measures the diffusion of water molecules that are restricted by biological barriers within the brain. This Master's thesis aims at quantifying microstructural brain anomalies in patients with different clinical stages of Alzheimer's disease with microstructure imaging, a technique that consists in using mathematical models to infer microstructural features of brain tissues based on diffusion data. In this study, four models were used: Diffusion Tensor Imaging (DTI), Neurite Orientation Dispersion and Density Imaging (NODDI), DIstribution of 3D Anisotropic MicrOstructural eNvironments in Diffusion-compartment imaging (DIAMOND) and Microstructure Fingerprinting (MF). This study brings out the great potential for DIAMOND and MF, two recently developed models that have never been used to quantify brain anomalies in patients with Alzheimer's disease, to define new biomarkers of the pathology.

Acknowledgements

I wish to express my sincere appreciation to my supervisors Pr. Benoît Macq and Pr. Laurence Dricot for giving me the opportunity to discover the fascinating topic of diffusion magnetic resonance imaging.

I am deeply indebted to Pr. Laurence Dricot and PhD. Gaëtan Rensonnet for spending hours sharing their knowledge and guide me through the realization of this Master's thesis.

I would like to extend my sincere thanks to Pr. Bernard Hanseeuw for giving me the opportunity to work on Alzheimer's disease and for his very valuable comments on this work.

I greatly appreciate the collaborative work we undertook with Nicolas Delinte and Ysaline Leman during the realization of our respective Master's theses.

Finally, I would like to express my profound gratitude to all the people who encouraged me during my studies.

Contents

Abstract i

Acknowledgements ii

List of Figures v

List of Tables vi

Nomenclature vii

Introduction 1

1 Theoretical background 2
1.1 Nuclear Magnetic Resonance . . . 2
1.1.1 Basics of quantum mechanics . . . 2
1.1.2 Macroscopic magnetization . . . 3
1.1.3 Radiofrequency pulse . . . 5
1.1.4 Larmor equation . . . 6
1.1.5 Relaxation . . . 6
1.1.6 Bloch equations and Free Induction Decay . . . 8
1.1.7 Spin Echo sequence . . . 9
1.1.8 Magnetic Resonance Imaging . . . 9
1.2 Diffusion-Weighted Magnetic Resonance Imaging . . . 11

2 DW-MRI models of the brain microstructure 13
2.1 Superposition principle . . . 13
2.2 Phenomenological models . . . 14
2.2.1 DTI . . . 14
2.2.2 DIAMOND . . . 15
2.3 Microstructural models . . . 18
2.3.1 NODDI . . . 18
2.3.2 Microstructure Fingerprinting . . . 21

3 Alzheimer's disease 24
3.1 Overview of Alzheimer's disease . . . 24
3.1.1 Figures, symptoms, causes and pathophysiology . . . 24
3.1.2 Staging of the disease and diagnostic biomarkers . . . 26
3.2 Literature survey of DW-MRI in Alzheimer's disease . . . 29
3.2.1 DTI . . . 29
3.2.2 NODDI . . . 30
3.2.3 Regions of interest . . . 32

4 Analysis of structural brain changes in Alzheimer's disease 36
4.1 Methods . . . 36
4.1.1 Subjects . . . 36
4.1.2 Data acquisition . . . 36
4.1.3 Image processing . . . 36
4.1.4 Image analysis . . . 38

4.2 Macrostructural changes : volumetric brain analysis . . . 41
4.3 Microstructural changes : DTI . . . 42
4.3.1 Whole-brain white matter analysis : results . . . 42
4.3.2 Region-based analysis : results . . . 46
4.3.3 Discussion . . . 51
4.4 Microstructural changes : NODDI . . . 52
4.4.1 Whole-brain white matter analysis : results . . . 52
4.4.2 Region-based analysis : results . . . 55
4.4.3 Discussion . . . 59
4.5 Microstructural changes : DIAMOND . . . 60
4.5.1 Whole-brain white matter analysis : results . . . 60
4.5.2 Region-based analysis : results . . . 62
4.5.3 Discussion . . . 65
4.6 Microstructural changes : Microstructure Fingerprinting . . . 66
4.6.1 Whole-brain white matter analysis : results . . . 66
4.6.2 Region-based analysis : results . . . 70
4.6.3 Discussion . . . 74
4.7 Final discussion . . . 75
4.8 Limitations . . . 78

Conclusion and perspectives **79**

Appendices **80**

A Summary of the literature survey of DW-MRI in Alzheimer's disease **81**

B Visualization of the regions of interest in Alzheimer's disease **84**
B.1 White matter tracts of interest . . . 84
B.2 Cortical and subcortical regions of interest . . . 86

C Functions of the regions of interest in Alzheimer's disease **90**

D Results of the region-based analysis **92**
D.1 Box plots for regions mildly affected by AD . . . 92
D.1.1 DTI . . . 92
D.1.2 NODDI . . . 94
D.1.3 DIAMOND . . . 96
D.1.4 Microstructure Fingerprinting . . . 97
D.2 Box plots of cortical and subcortical regions of interest . . . 99
D.3 Comprehensive table of metrics . . . 104

Bibliography **109**

List of Figures

1.1 Magnetic moment of a rotating charged particle . . . 2
1.2 Precession of a hydrogen nucleus in a superimposed static magnetic field B_0 . . . 3
1.3 Movement of the macroscopic magnetization . . . 5
1.4 T_1-relaxation curve after a 90°-pulse . . . 7
1.5 T_1-relaxation curves for different types of tissues . . . 7
1.6 T_2-relaxation after a 90°-pulse . . . 8
1.7 Free Induction Decay and Spin Echo signals . . . 8
1.8 Spin Echo sequence . . . 9
1.9 Schematic representation of an MRI system . . . 9
1.10 Double-echo SE sequence . . . 11
1.11 PGSE sequence for DW-MRI . . . 12
1.12 Effect of diffusion gradients on spins . . . 12

2.1 Ellipsoid representation of the diffusion tensors . . . 14
2.2 Example of DTI maps . . . 15
2.3 DIAMOND model . . . 17
2.4 Compartments considered in NODDI . . . 18
2.5 Example of Watson distribution . . . 20
2.6 Schematic representation of the hexagonal packing of cylinders in MF . . . 22

3.1 Biological processes involved in Alzheimer's disease . . . 26
3.2 Braak staging of Alzheimer's disease . . . 27

4.1 Set of analyses conducted to quantify brain anomalies in patients with AD . . . 38
4.2 Whole brain white matter analysis: mask-based and skeleton-based analyses . . . 40
4.3 Tissue segmentation of the HC, MCI patient and patient with dementia . . . 41
4.4 Box plots of DTI metrics in the whole-brain white matter (mask) . . . 43
4.5 Box plots of DTI metrics in the whole-brain white matter (skeleton) . . . 44
4.6 Regions of the skeleton showing abnormal DTI metrics . . . 45
4.7 Box plot of the fractional anisotropy in ROI . . . 47
4.8 Box plot of the mean diffusivity in ROI . . . 48
4.9 Box plot of the axial diffusivity in ROI . . . 49
4.10 Box plot of the radial diffusivity in ROI . . . 50
4.11 Box plots of NODDI metrics in the whole-brain white matter (mask) . . . 52
4.12 Box plots of NODDI metrics in the whole-brain white matter (skeleton) . . . 53
4.13 Regions of the skeleton showing abnormal NODDI metrics . . . 54
4.14 Box plot of the Orientation Dispersion Index in ROI . . . 56
4.15 Box plot of the Neurite Density Index in ROI . . . 57
4.16 Box plot of the volume fraction of Gaussian isotropic diffusion in ROI . . . 58
4.17 Box plots of DIAMOND metrics in the whole-brain white matter (mask) . . . 60
4.18 Box plots of DIAMOND metrics in the whole-brain white matter (skeleton) . . . 61
4.19 Coronal view of DIAMOND maps centered on the corpus callosum . . . 61
4.20 Regions of the skeleton showing abnormal DIAMOND metrics . . . 62
4.21 Box plot of the fraction of the extra-axonal restricted compartment in ROI . . . 63
4.22 Box plot of the fraction of the fascicles in ROI . . . 64
4.23 Box plot of MF metrics in the whole-brain white matter (mask) . . . 67
4.24 Box plot of MF metrics in the whole-brain white matter (skeleton) . . . 68

4.25 Regions of the skeleton showing abnormal MF metrics 69
4.26 Box plot of the fraction of the extra-axonal restricted compartment in ROI 71
4.27 Box plot of the total fiber volume fraction in ROI 72
4.28 Box plot of the mean apparent axonal radius in ROI 73
4.29 Final discussion about the metrics of multi-compartment models 76
4.30 Comparison of the F_{aniso} metric (DIAMOND) and the FVF metric (MF) 77

B.1 Tractography of the corpus callosum 84
B.2 Tractography of the forceps major and forceps minor 84
B.3 Tractography of the corona radiata 85
B.4 Tractography of the thalamic radiation 85
B.5 Tractography of the fornix 85
B.6 Tractography of the uncinate fasciculus 86
B.7 Tractography of the cingulum 86
B.8 Visualization of the precuneous cortex 86
B.9 Visualization of the middle temporal gyrus 87
B.10 Visualization of the inferior temporal gyrus 87
B.11 Visualization of the hippocampus entorhinal cortex 87
B.12 Visualization of the occipital fusiform gyrus 87
B.13 Visualization of the frontal pole 88
B.14 Visualization of the superior frontal gyrus 88
B.15 Visualization of the parahippocampal gyrus 88
B.16 Visualization of the cingulate gyrus 88
B.17 Visualization of the hippocampus 89
B.18 Visualization of the amygdala 89

D.1 FA (DTI) evaluated in regions mildly affected by Alzheimer's disease 92
D.2 MD (DTI) evaluated in regions mildly affected by Alzheimer's disease 93
D.3 AxD (DTI) evaluated in regions mildly affected by Alzheimer's disease 93
D.4 RD (DTI) evaluated in regions mildly affected by Alzheimer's disease 94
D.5 ODI (NODDI) evaluated in regions mildly affected by Alzheimer's disease 94
D.6 NDI (NODDI) evaluated in regions mildly affected by Alzheimer's disease 95
D.7 f_{iso} (NODDI) evaluated in regions mildly affected by Alzheimer's disease 95
D.8 F_{iso} (DIAMOND) evaluated in regions mildly affected by Alzheimer's disease . . . 96
D.9 F_{aniso} (DIAMOND) evaluated in regions mildly affected by Alzheimer's disease . . 96
D.10 F_{iso} (MF) evaluated in regions mildly affected by Alzheimer's disease 97
D.11 FVF (MF) evaluated in regions mildly affected by Alzheimer's disease 97
D.12 mRad (MF) evaluated in regions mildly affected by Alzheimer's disease 98
D.13 Box plot of the mean diffusivity in cortical ROI 100
D.14 Box plot of the Orientation Dispersion Index in cortical ROI 101
D.15 Box plot of the Neurite Density Index in cortical ROI 102
D.16 Box plot of the volume fraction of Gaussian isotropic diffusion in cortical ROI . . . 103

List of Tables

4.1 Volumetric brain analysis report of the healthy control, the MCI patient and the patient with dementia. 41

A.1 Summary table of the literature survey of DW-MRI in Alzheimer's disease 83

C.1 Functions of the tracts and regions of interest undergoing microstructural changes in Alzheimer's disease 91

D.1 ROI-based analysis: comprehensive table of DTI, NODDI, DIAMOND and MF metrics 108

Nomenclature

List of Physical Constants

h	Plank Constant	$6.62607 \times 10^{-34}\,[J \cdot s]$
k	Boltzmann Constant	$1.38 \times 10^{-23}\,[J \cdot K^{-1}]$
γ	Gyromagnetic Ratio (for ^1H)	$2\pi \cdot 42.58\,[rad \cdot MHz \cdot T^{-1}]$

List of Symbols

n	Principal Quantum Number	$[-]$
l	Azimuthal Quantum Number	$[-]$
m_l	Magnetic Quantum Number	$[-]$
I	Spin Quantum Number	$[-]$
T	Tesla	$[kg \cdot A^{-1} \cdot s^{-2}]$
Hz	Hertz	$[s^{-1}]$
τ	Torque	$[N \cdot m]$
μ	Magnetic Moment	$[N \cdot m \cdot T^{-1}]$
B_0	External Magnetic Field Strength	$[T]$
f_0	Larmor Frequency of Precession	$[Hz]$
ω_0	Larmor Angular Frequency of Precession	$[rad \cdot s^{-1}]$
M_0	Macroscopic Magnetization	$[N \cdot T^{-1} \cdot m^{-2}]$
V	Volume	$[m^3]$
N_1	Population of Higher Energy Spins	$[-]$
N_2	Population of Lower Energy Spins	$[-]$
M_{xy}	Transverse Magnetization	$[T]$
M_z	Longitudinal Magnetization	$[T]$
α	Flip Angle	$[rad]$
P	Angular Momentum	$[kg \cdot m^2 \cdot s^{-1}]$
T_{RF}	Duration of the RF-pulse	$[s]$
ϕ	Phase Angle of the RF-pulse	$[rad]$
ρ	Spin Density	$[m^{-3}]$
T_1	Longitudinal Relaxation Time	$[s]$
T_2	Transverse Relaxation Time	$[s]$

ν	Viscosity	$[kg \cdot m^{-1} \cdot s^{-1}]$
r	Radius of a Spherical Molecule	$[m]$
T_2^*	Effective Transverse Relaxation Time	$[s]$
ω_{frame}	Frequency of Rotation of the Reference Frame	$[rad \cdot s^{-1}]$
ε	Electromotive Force	$[V]$
G_y	Phase Encoding Gradient	$[T \cdot m^{-1}]$
G_z	Slice Selection Gradient	$[T \cdot m^{-1}]$
G_x	Frequency Encoding Gradient	$[T \cdot m^{-1}]$
T_y	Duration of the Phase Encoding Gradient	$[s]$
f_c	Center Frequency	$[Hz]$
Λ	Diagonalized Diffusion Tensor	$[-]$
D	Diffusion Tensor	$[-]$
f_i	Volume Fraction of Compartment i	$[-]$
b_{PGSE}	b-value of a PGSE Sequence	$[-]$
Ω_i	Diffusion Compartment i	$[-]$
S_0	Reference Signal without Diffusion Gradients	$[-]$
A_{ic}	Normalized Signal from the Intra-cellular Compartment	$[-]$
A_{ec}	Normalized Signal from the Extra-cellular Compartment	$[-]$
A_{iso}	Normalized Signal from the CSF Compartment	$[-]$
M	Confluent Hypergeometric Function	$[-]$
κ	Concentration Parameter in Watson Distribution	$[-]$
F	Single-Fascicle Sub-Dictionary	$[-]$
Γ_p	Multivariate Gamma Function	$[-]$
$mv - \Gamma$	Matrix Variate Gamma Distribution	$[-]$
Σ_j	Scale Parameter of the j^{th} population in the mv-Γ distribution	$[-]$
κ_j	Shape Parameter of the j^{th} population in the mv-Γ distribution	$[-]$

List of Abbreviations

$A\beta$	Amyloid Beta
AD	Alzheimer's Disease
$APOE$	Apolipoprotein E
AUC	Area Under the ROC Curve
AxD	Axial Diffusivity
CSF	Cerebrospinal Fluid
DCI	Diffusion Compartment Imaging
$DIAMOND$	Distribution of 3D Anisotropic Microstructural Environments in DCI
DTI	Diffusion Tensor Imaging

$DW-MRI$	Diffusion-Weighted Magnetic Resonance Imaging
EAR	Extra-Axonal Restricted
FA	Fractional Anisotropy
FE	Frequency Encoding
FID	Free Induction Decay
$fMRI$	Functional Magnetic Resonance Imaging
FOV	Field Of View
FT	Fourier Transform
GM	Gray Matter
$HARDI$	High Angular Resolution Diffusion Imaging
HEI	Heterogeneity Index
IQR	Interquartile Range
MCI	Mild Cognitive Impairment
MD	Mean Diffusivity
MF	Microstructure Fingerprinting
$MMSE$	Mini Mental State Examination
MR	Magnetic Resonance
MRI	Magnetic Resonance Imaging
MTG	Middle Temporal Gyrus
NDI	Neurite Density Index
NFT	Neurofibrillary Tangles
$NIA-AA$	National Institute on Aging and Alzheimer's Association
$NODDI$	Neurite Orientation Dispersion and Density Imaging
ODI	Orientation Dispersion Index
PE	Phase Encoding
PET	Positron Emission Tomography
$PGSE$	Pulsed Gradient Spin Echo
PiB	Pittsburgh Compound B
RD	Radial Diffusivity
ROA	Region Of Avoidance
ROI	Region Of Interest
SE	Spin Echo
SLF	Superior Longitudinal Fasciculus
SS	Slice Selection
$TBSS$	Tract-Based Spatial Statistics
WM	White Matter

Introduction

The rising elderly population in our society increases the prevalence of aging-associated diseases such as Alzheimer's disease (AD). Knowing that more than 18 million individuals are expected to be affected by dementia (an advanced stage of AD where the patients experience memory losses and behavioral symptoms that interfere with their everyday activities) in Europe by 2050 [1], this neurodegenerative disease is a primary concern in today's society. Although no pharmacologic treatment is nowadays available to prevent the disease or stop its spread, the research is highly active to better understand the mechanisms involved. Recently, there has been a growing interest in shifting the diagnostic criteria of that mental disorder from a clinical definition based on symptoms towards a biological definition based on neuropathological hallmarks of the disease. This approach promoted the search for new biomarkers that would refine the diagnosis, improve the clinical management of the patients (e.g. with personalized treatments), enhance clinical trials and promote the research for drug development.

Diffusion-Weighted Magnetic Resonance Imaging (DW-MRI) is a non-invasive and non-radiating imaging technique used to assess microstructural features of tissues by measuring the diffusion of water molecules that are restricted by biological barriers within the brain. Broadly speaking, using mathematical models to link the diffusion magnetic resonance signal with microstructural properties of the tissues is known as "microstructure imaging". Since microstructural alterations appear years before the onset of symptoms, this "virtual histology" [2] may help to discover new biomarkers that reliably discriminate pathological cases from normal cases, are specific and sensitive to the earliest signs of the disease and give an insight about the underlying biological mechanisms involved.

The goal of this Master's thesis is to identify and characterize microstructural brain anomalies in patients with different clinical stages of AD: dementia and Mild Cognitive Impairment (stage of the disease where the cognitive decline of the patients does not interfere with everyday activities). In the first chapter, theoretical aspects of DW-MRI are addressed to give an insight into that imaging technology. In the second chapter, diffusion models used in this Master's thesis are presented: Diffusion Tensor Imaging (DTI), Neurite Orientation Dispersion and Density Imaging (NODDI), DIstribution of 3D Anisotropic MicrOstructural eNvironments in Diffusion-compartment imaging (DIAMOND) and Microstructure Fingerprinting (MF). Although DTI and NODDI are models that have been widely reported in the literature to quantify microstructural brain anomalies in patients with AD, DIAMOND and MF have never been used to that end. The third chapter aims at presenting biological processes known to be involved in AD, the different stages of the disease and the current diagnostic biomarkers. This chapter is also focusing on results of previous studies where diffusion models were used to characterize microstructural alterations in patients with dementia, MCI patients and healthy elderly. Lastly, the study of structural brain changes in the MCI patient and the patient with dementia can be found in chapter 4. The analyses were conducted on DW-MRI data acquired at St-Luc University Hospital. The chapter is organized as follows: a volumetric brain analysis to characterize macrostructural changes in the patients and analyses of microstructural changes inferred from the DW-MRI data with the four diffusion models presented previously. Then, the limitations of the study and the future perspectives are discussed.

Chapter 1

Theoretical background

1.1 Nuclear Magnetic Resonance

1.1.1 Basics of quantum mechanics

Magnetic properties of nuclei are the fundamental basis of nuclear magnetic resonance (NMR). According to quantum mechanics, a nucleus is described by different quantities: the principal quantum number (n), the azimuthal quantum number (l), the magnetic quantum number (m_l) and the spin quantum number (I) [3]. The spin is the intrinsic angular momentum of the nucleus and can be an integer or a half-integer depending on the mass number (number of protons and neutrons) and the atomic number (number of protons) of the atom. Molecules with an even mass number and an even atomic number (e.g. ^{12}C or ^{18}O) have a zero spin quantum number. Atoms with an odd mass number and an odd atomic number (e.g. ^{1}H, ^{13}C, ^{15}N) have a half-integer nuclear spin. Finally, atoms with an even mass number and an odd atomic number have an integer nuclear spin [4] (e.g. ^{14}N, ^{2}H, ^{10}B). Since a nucleus with a spin can be viewed as spinning around an axis and since the nucleus is a charged particle only composed of protons and neutrons, a rotating nucleus creates an electric current and a magnetic field characterized by a magnetic moment μ [4]. Nuclei can therefore be compared to magnets as illustrated in Fig.1.1.

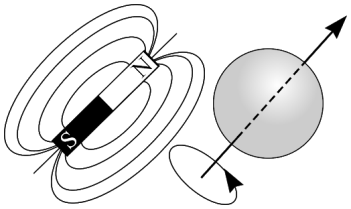


Figure 1.1: Magnetic moment of a rotating charged particle [5].

When no magnetic field is applied on the particle, the orientation of the magnetic moment is random due to the thermal motion of particles. However, when a magnetic field is applied on a particle with a non-zero quantum spin number, the orientation of the magnetic moment is discretized according to 2I+1 possible orientations (where I is the spin quantum number). As discussed later, since protons (^{1}H) show good magnetic properties and are abundant in the human body, Magnetic Resonance Imaging (MRI) mainly focus on imaging hydrogen atoms [6] and therefore on particles with a 1/2 spin quantum number. The magnetic moment of such particles under an external magnetic field ($\boldsymbol{B_0} = B_0\boldsymbol{e_z}$) can therefore take two possible orientations called parallel spin (or "spin up") and antiparallel spin (or "spin down") as illustrated in Fig.1.2.

When an external magnetic field is applied, the magnetic moment of the spinning particle is subjected to a torque defined by:

$$\overrightarrow{\tau} = \overrightarrow{\mu} \times \overrightarrow{B}, \tag{1.1}$$

where:

- $\overrightarrow{\tau}$ is a vector that represents the torque experienced by the magnetic dipole moment ;

- $\overrightarrow{\mu}$ is a vector that represents the magnetic moment of the nucleus ;
- $\overrightarrow{B}$ is the external magnetic field vector.

Therefore, a precession movement is observed around the direction of the external magnetic field with a frequency of precession defined by:

$$f_0 = \frac{\gamma}{2\pi} B_0, \tag{1.2}$$

where:

- f_0 is the frequency of precession expressed in Hz ;
- $\frac{\gamma}{2\pi}$ is the gyromagnetic ratio expressed in MHz/T. The gyromagnetic ratio of ^1H is 42.58 MHz/T [4] ;
- B_0 is the magnitude of the external magnetic field expressed in T.

The frequency of precession is also called "Larmor frequency". The movement of precession is represented in Fig.1.2.

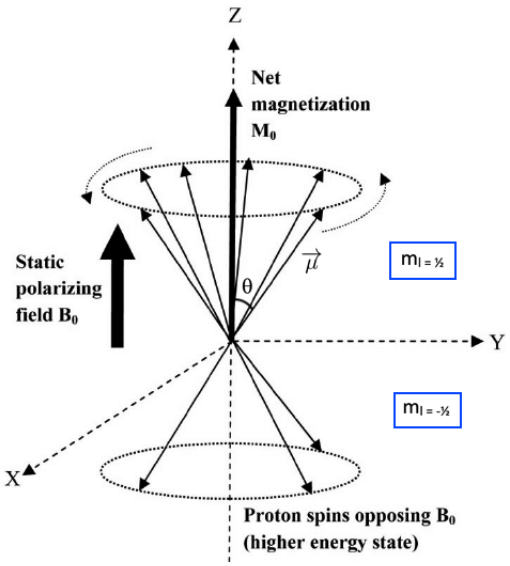


Figure 1.2: Precession of a hydrogen nucleus in a superimposed static magnetic field B_0. Adapted from [7].

1.1.2 Macroscopic magnetization

For all nuclei that are subjected to an external magnetic field $\mathbf{B_0}$, individual spins can be considered as a whole that determines the macroscopic magnetization, defined by [4]:

$$\overrightarrow{M} = \frac{1}{V} \sum_i \overrightarrow{\mu_i}, \tag{1.3}$$

where:

- $\overrightarrow{M}$ is the macroscopic magnetization ;
- V is the volume of the ensemble of spins ;
- $\overrightarrow{\mu_i}$ is the magnetic moment vector of an individual nucleus in V.

When no external magnetic field is applied, spins are randomly oriented and the macroscopic magnetization is non-existent. However, when an external magnetic field is applied on nuclei with

half-integer spin quantum numbers, two orientations are possible and a macroscopic magnetization exists. The energy of a magnetic dipole in a magnetic field $\mathbf{B_0}$ is defined by [6]:

$$E = -\overrightarrow{\mu} \cdot \overrightarrow{B_0} = -\mu \cdot \cos\theta \cdot B_0 = -\mu_z \cdot B_0, \tag{1.4}$$

where:

- θ is the angle between the magnetic dipole moment and the external magnetic field.

Since the magnetic moment of individual spins in the external induction field is [6]:

$$\mu_z = \gamma P_z, \tag{1.5}$$

where:

- P_z is the z-component of the angular momentum vector of the nucleus ;

and knowing that the angular momentum of the nucleus is discretized such that:

$$P_z = \frac{h}{2\pi} \cdot m_l, \tag{1.6}$$

one can obtain a quantum mechanical description of the energy of the magnetic moment with equations (1.4),(1.5) and (1.6) [6]:

$$E_{m_l} = -\gamma \frac{h}{2\pi} m_l B_0, \tag{1.7}$$

where:

- $m_l = 1/2$ (spin up) or -1/2 (spin down) for ^1H ;
- h is the Planck constant ($6.6 \cdot 10^{-34} Js$).

Therefore, the energy of the magnetic dipole is minimum when the magnetic moment is parallel to the external magnetic field and maximum when the magnetic moment is antiparallel to the external magnetic field. The difference in energy of the two states is defined by [4]:

$$\Delta E = E_{-\frac{1}{2}} - E_{\frac{1}{2}} = \gamma \frac{h}{2\pi} B_0 = h f_0. \tag{1.8}$$

The occupation ratio of the two energy levels is described by the Boltzmann distribution [4]:

$$\frac{N_1}{N_2} = e^{-\frac{\Delta E}{kT}}, \tag{1.9}$$

where:

- N_1 is the number of spins of higher energy state ;
- N_2 is the number of spins of lower energy state ;
- k is the Boltzmann constant ($1.38 \cdot 10^{-24} J/K$) ;
- T is the absolute temperature in K.

Since $\frac{N_1}{N_2} \in]0, 1[$, more spins are pointing upwards (lower energy state) than downwards (higher energy state). The equilibrium macroscopic magnetization is non-zero and is defined by [4]:

$$M_0 = \frac{(\frac{\gamma}{2\pi})^2 h^2 \rho B_0 I(I+1)}{3kT}, \tag{1.10}$$

where:

- ρ is the number of spins per unit volume, also called “spin density” ;
- I is the spin of the nuclei. I = 1/2 for ^1H.

1.1.3 Radiofrequency pulse

As observed in Eq.1.10, the macroscopic magnetization is proportional to the number of spins per unit volume and the gyromagnetic ratio. MRI is focusing on ^1H due to their significant presence in the human body, mostly composed of water. Moreover, ^1H have a high gyromagnetic ratio (42.58 Mhz/T) leading to a strong macroscopic magnetization.

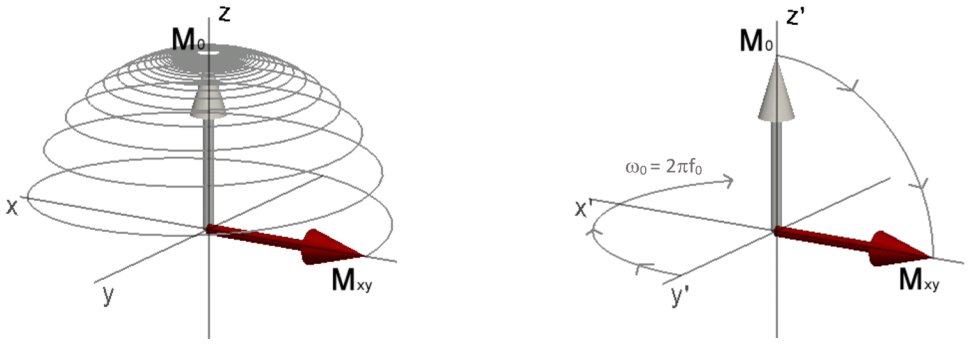
The macroscopic magnetization is oriented in the direction of the external magnetic field. In order to obtain a measurable signal, the magnetization has to be moved away from the direction of the external magnetic field. A time-varying radiofrequency field that oscillates at Larmor frequency is used for that purpose. This magnetic field called "RF-pulse" is linearly polarized since it is applied in a fixed direction [4]. The expression of the RF-pulse is described by [4]:

$$\mathbf{B_1}(\mathbf{t}) = 2B_1(t)cos(2\pi f_{RF}t + \phi)\mathbf{1}_{xy}), \tag{1.11}$$

where:

- f_{RF} is the frequency of the RF-pulse and is equal to f_0 (the Larmor frequency) to observe a condition of resonance ;
- $\mathbf{1}_{xy}$ is a unit vector in the (x,y)-plane.

The effect of the RF-pulse on the magnetization can be observed in the laboratory frame (a fixed frame) or a rotating frame (for more convenience) as represented in Fig.1.3. The advantage of considering a rotating frame is that spins precessing at Larmor frequency appear stationary in the frame.



(a) Laboratory frame **(b)** Rotating frame

Figure 1.3: Movement of the macroscopic magnetization when a RF-pulse oscillating at Larmor frequency is irradiating the spins. Adapted from [8].

When the RF-pulse is applied, the macroscopic magnetization is tilted away from the initial direction of the external magnetic field B_0. The angle between the z-direction and the magnetization is called the "flip-angle" and is defined by [4]:

$$\alpha = \gamma \int_{T_{RF}} B_1(t)dt, \tag{1.12}$$

where:

- T_{RF} is the duration of the RF-pulse.

If one considers a finite duration of the pulse and a constant amplitude B_1 (i.e. observed in a reference frame rotating at Larmor frequency), the flip angle is defined by [4]:

$$\alpha = \gamma B_1 T_{RF}. \tag{1.13}$$

In Fig.1.3, the pulse applied with specific parameters T_{RF} and B_1 is called a 90°-pulse since the macroscopic magnetization is tilted away with a 90°-angle. Since the magnetization is moved

away from the z-direction, a new component in the (x,y)-plane appears and the expression of the magnetization becomes [4]:

$$\mathbf{M} = M_z\mathbf{1_z} + M_{xy}\mathbf{1_{xy}}, \tag{1.14}$$

where:

- M_z is the longitudinal magnetization ;
- M_{xy} is the transverse magnetization.

1.1.4 Larmor equation

The movement of the magnetization when a time-varying magnetic field $B_1(t)$ and an external magnetic field B_0 are applied is described by Larmor equation [6]:

$$\frac{d\overrightarrow{M}}{dt} = -\gamma\left(\overrightarrow{B_1(t)} + \Delta\overrightarrow{B^{eff}}\right) \times \overrightarrow{M}, \tag{1.15}$$

where:

- $\Delta B^{eff} = B_0 - \frac{\omega_{frame}}{\gamma}$;
- ω_{frame} is the frequency of rotation of the reference frame around the z-axis.

When the frame is not rotating around the z-axis, the magnetization is observed in the laboratory frame. Therefore, the reference frame is stationary, the frequency of the frame is $\omega_{frame} = 0$ and the equation becomes:

$$\frac{d\overrightarrow{M}}{dt} = -\gamma\left(\overrightarrow{B_1}(t) + \overrightarrow{B_0}\right) \times \overrightarrow{M}. \tag{1.16}$$

When the movement of the magnetization is observed in a rotating frame that rotates around the z-axis at Larmor frequency $\omega_{frame} = \omega_0$, the equation becomes:

$$\frac{d\overrightarrow{M}}{dt} = -\gamma\overrightarrow{B_1}^1 \times \overrightarrow{M}. \tag{1.17}$$

1.1.5 Relaxation

After applying the RF-pulse, the system tends to go back to equilibrium. This is called "relaxation" and two phenomena appear. The first process is the longitudinal relaxation, also called "spin-lattice relaxation" or "T_1-relaxation" [4] (Fig.1.4). After applying the pulse, an energy-exchange arises between the spins of the system and the external environment by the means of collisions or electromagnetic interactions. During the relaxation, the net magnetization recovers to its original value M_0. One can mathematically describe the recovery of the magnetization through time after the RF-pulse being applied, by [6]:

$$M_z(t) = M_0(1 - e^{-\frac{t}{T_1}}) + M_z(0)e^{-\frac{t}{T_1}}, \tag{1.18}$$

where:

- M_0 is the equilibrium magnetization ;
- $M_z(0)$ is the longitudinal magnetization at time t = 0 after the excitation ;
- T_1 is a characteristic time that describes the time needed for M_z to recover 63% of the equilibrium magnetization.

1 Note that the RF field has a constant amplitude when observed in a reference frame rotating at the Larmor frequency.

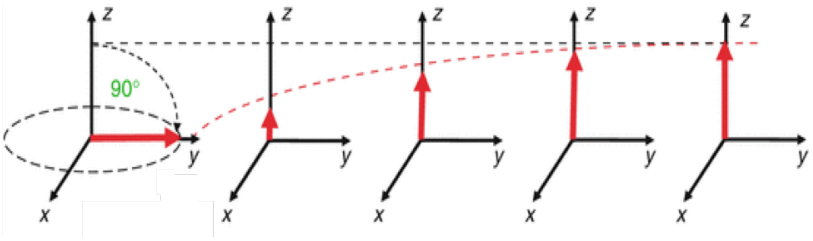


Figure 1.4: T_1-relaxation curve after a 90°-pulse [9].

Applying a magnetic field and a RF-pulse on different substances (i.e. different types of human tissues) leads to different relaxation times as depicted in Fig.1.5. This is mainly due to their different composition that directly influences the rotational correlation times[2] and therefore the relaxation rate. If one considers spherical molecules, the rotational correlation time is defined by [6]:

$$\tau_c = \frac{4\pi\nu r^3}{3kT}, \tag{1.19}$$

where:

- ν is the viscosity. A high viscosity means a high correlation time since molecules are less prone to movement ;
- r is the radius of the molecule ;
- k is the Boltzmann constant ;
- T is the temperature.

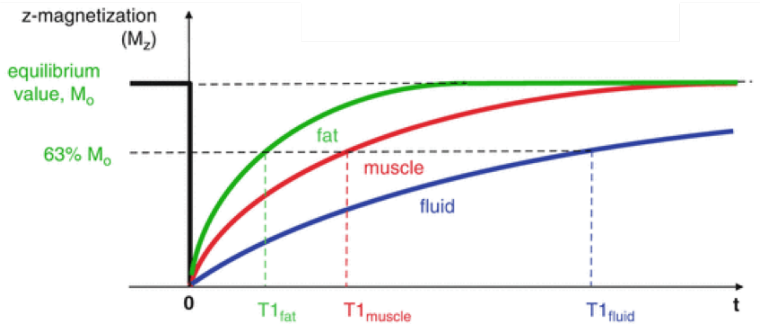


Figure 1.5: T_1-relaxation curves for different types of tissues [9].

The second phenomenon is the transverse relaxation, also called "spin-spin relaxation" or "T_2-relaxation" (Fig.1.6). An interaction between the spins leads to a loss of coherence between them. Different tissues also have different T_2-relaxation times. The recovery of the transverse magnetization through time after the RF-pulse is defined by [6]:

$$M_{xy}(t) = M_{xy}(0)e^{\frac{-t}{T_2}}, \tag{1.20}$$

where:

- $M_{xy}(0)$ is the transverse magnetization at time t = 0 after the excitation ;
- T_2 is a characteristic time that describes the time needed for M_{xy} to lose 63% of its initial value.

2 The rotational correlation time is defined as the time needed for a molecule to rotate one radian [6].

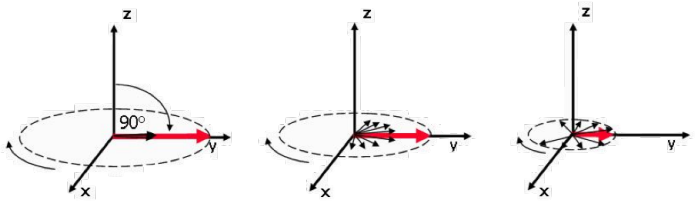


Figure 1.6: T_2-relaxation after a 90°-pulse [9].

In practice, the transverse magnetization decays faster than expressed by the mathematical expression taking T_2 into account. This is mainly due to inhomogeneities in the magnetic field rather than molecular interactions [6]. This relaxation time, denoted T_2^*, is called the "effective relaxation time" and is linked to T_2 by the expression [4]:

$$\frac{1}{T_2^*} = \frac{1}{T_2} + \gamma \Delta B_0, \tag{1.21}$$

where:

- ΔB_0 represents the inhomogeneities in the external magnetic field.

1.1.6 Bloch equations and Free Induction Decay

Considering that the evolution of the magnetization is observed in a reference frame rotating at Larmor frequency, knowing that $\overrightarrow{B_1}(t) = (B_x(t), B_y(t), B_z(t))$ and that $\overrightarrow{M}(t) = (M_x(t), M_y(t), M_z(t))$, Larmor equation (1.17) can be rewritten as the following system:

$$\begin{cases} \frac{dM_x}{dt} = \gamma \left(B_z(t)M_y(t) - B_y(t))M_z(t)\right) \\ \frac{dM_y}{dt} = \gamma \left(B_x(t)M_z(t) - B_z(t))M_x(t)\right) \\ \frac{dM_z}{dt} = \gamma \left(B_y(t)M_x(t) - B_x(t))M_y(t)\right) \end{cases} \tag{1.22}$$

This system can be adapted by taking the relaxation phenomena into account, leading to the Bloch system of equations defined by [6]:

$$\begin{cases} \frac{dM_x}{dt} = \gamma \left(B_z(t)M_y(t) - B_y(t))M_z(t)\right) - \frac{M_x(t)}{T_2} \\ \frac{dM_y}{dt} = \gamma \left(B_x(t)M_z(t) - B_z(t))M_x(t)\right) - \frac{M_y(t)}{T_2} \\ \frac{dM_z}{dt} = \gamma \left(B_y(t)M_x(t) - B_x(t))M_y(t)\right) - \frac{M_z(t) - M_0}{T_1} \end{cases} \tag{1.23}$$

By using a coil situated in the transverse plane, the evolution of the transverse magnetization creates a Free Induction Decay (FID) signal. According to Faraday's law of induction, a change in the magnetic flux in a closed circuit (the coil in the transverse plane) creates an electromotive force (ε) in the coil. This change in voltage induces a current that can be measured. The induced voltage is a dampened sinusoid with a constant frequency (the resonance frequency) as depicted in Fig.1.7A. Indeed, the intensity of the induced voltage decreases as the spins dephase. The envelope of the signal is decreasing exponentially according to the T_2^* constant.

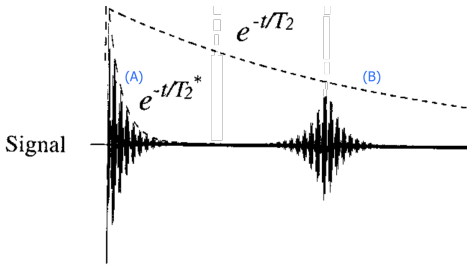


Figure 1.7: (A) Envelope of FID signal in a coil obtained with dephasing of the transverse magnetization. (B) Envelope of SE signal. Adapted from [4].

1.1.7 Spin Echo sequence

Since the amplitude of the signal rapidly decreases when the induced voltage has an envelope relying on T_2^*, the signal can not be measured. In some MRI systems, a transceiver coil is used to transmit the RF-pulse and detect the signal [4]. A small time is needed to change the status of the coil from "transmitter" to "receiver" and the loss of signal during that time is important [6]. A spin echo (SE) sequence can therefore be used to avoid that situation. A SE sequence consists in a 90°-pulse at time t=0 (Fig.1.8(1)) used to tilt the longitudinal magnetization into the transverse plane. The spins will then dephase and rotate at different frequencies due to the inhomogeneities in the magnetic field [4]. One can consider spin isochromates[3] such that the external isochromates rotate faster than the internal isochromate (denoted "1" in Fig.1.8(3)) that rotates at Larmor frequency. At time t=τ, a 180°-pulse is applied (Fig.1.8(4)), such that all the spins are mirrored with respect to the x-axis is the (x,y)-plane. Since the higher-order isochromates still rotate faster than the lower-order ones, all the spins will tend to rephase. A spin echo is therefore observed at time t=2τ, when all the spins are refocused (Fig.1.8(6)). The envelope of the signal measured relies on T_2 and not T_2^* unlike the FID signal (Fig.1.7B). A sequence of one 90°-pulse followed by multiple 180°-pulses, each separated by a period of 2τ, can create a signal composed of multiple SEs.

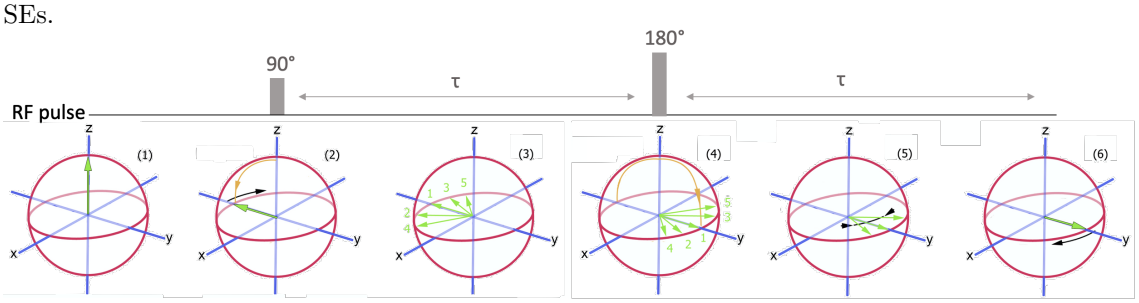


Figure 1.8: Spin Echo sequence with the 90°-pulse and 180°-pulse respectively at time t = τ and t = 2τ. (1) Spins are aligned with the external magnetic field B_0. (2) A 90°-pulse is applied to convert the longitudinal magnetization into transverse magnetization. (3) The spins isochromates rotate at different frequencies. (4) A 180°-pulse is applied to flip the isochromates. (5) Refocusing of the spins. (6) A spin echo is observed at time t = 2τ. Adapted from [10].

1.1.8 Magnetic Resonance Imaging

An MRI system consists in a magnet that generates the static magnetic field B_0, gradient coils to create spatially-varying magnetic fields, one ("transceiver") or two RF coils (one for the transmission and the other for the reception) and a processing system [4], as depicted in Fig.1.9. In clinical MRI, the field strength generated by the magnet lies around 1 to 7 Tesla (T) [6]. In research MRI for humans, "ultra-high fields" of 11.7 T [11] are being developed. In animal research, magnetic fields with a strength of 11 T are commonly used and ultra-high fields with a strength up to 17.6 T have been used [12].

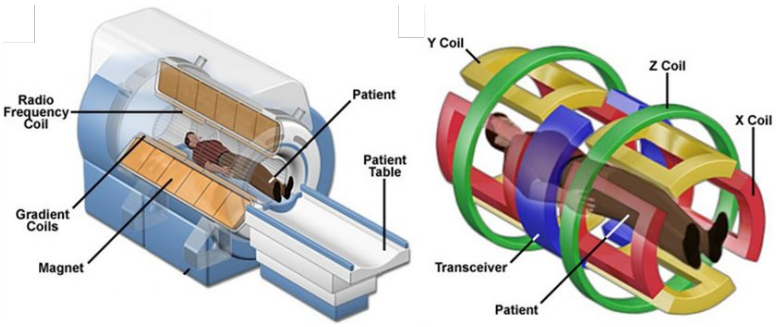


Figure 1.9: Schematic representation of an MRI system and gradient coils used for the spatial encoding in the three dimensions [13].

3 A spin isochromate is defined as a "group of spins in an infinitesimally small volume element in which the magnetic field can be considered to be homogeneous" [4].

In MRI, a specific region of the patient is imaged and not the entire volume. Therefore, magnetic field gradients are used to excite a specific slice of the patient and capture spatial information in the signal. Gradient fields are generated by gradient coils (Fig.1.9). For example, two coils are used to create a magnetic gradient along the z-direction. An electrical current passes through both of them but in opposite directions. According to the Biot and Savart's law, the strength of the magnetic field depends on the closeness to the coil. At the exact center of the two coils, the two magnetic fields generated are equal but opposite. The contribution of the magnetic field created by one of the coils is increased when one gets closer to it [6]. The magnetic field experienced when magnetic gradients are used can be written [4]:

$$\mathbf{B} = \mathbf{B_0} + (\mathbf{G} \cdot \mathbf{r})\mathbf{1_z} = \mathbf{B_0} + (G_x x + G_y y + G_z z)\mathbf{1_z}. \tag{1.24}$$

The gradient of a magnetic field oriented along the z-direction that varies spatially along x,y and/or z is therefore denoted [6]:

$$\overrightarrow{G} \equiv \frac{d\overrightarrow{B_z}}{d\overrightarrow{r}}. \tag{1.25}$$

The slice selection gradient (G_z) is a magnetic field that varies linearly along the z-direction, such that the Larmor frequency increases linearly with the z-position. The Larmor frequency experienced at the z-position is [4]:

$$f(z) = \frac{\gamma}{2\pi}\left(B_0 + G_z z\right). \tag{1.26}$$

Therefore, using a RF-pulse of bandwidth $\Delta f = \frac{\gamma}{2\pi} G_z \Delta z$ will excite a portion of spins within a slice of thickness Δz. For a specific bandwidth Δf, the stronger the gradient, the thinner the slice selected. The center frequency is defined by $f_c = f_0 + \frac{\gamma}{2\pi} G_z z_0$ [4]. In order to obtain an ideal rectangular slice profile, a RF-pulse with the following shape is needed [4]:

$$B_1(t) = A sinc(\pi \Delta f t) exp(-i 2\pi f_c t). \tag{1.27}$$

However, a sinc RF-pulse with an infinite duration cannot be obtained and therefore the profile of the slice will not be ideally rectangular. Since the slice-selective excitation introduces a phase shift that leads to signal loss, a refocusing gradient is used to recover the phase shift [4] Fig.1.10(B). The slice being selected, gradient fields in other directions are needed to encode spatial information. A phase encoding gradient is used along the y-direction (Fig.1.10(C)). During the time the phase encoding gradient (G_y) is turned on, the spins dephase proportionally to their y-position. When the gradient is turned off, the phase shift acquired by the spins remains and is defined by [4]:

$$\phi(y) = -\gamma G_y y T_y, \tag{1.28}$$

where:

- $\phi(y)$ is the phase acquired at the y-position after turning off the phase encoding gradient ;
- T_y is the duration of the phase encoding gradient.

Finally, a frequency encoding gradient (G_x) along the x-direction is applied to encode spatial information in the x-direction (Fig.1.10(D)). Since the spins are uniquely defined with a phase and a frequency when this sequence of magnetic gradient is used, spins can be localized [4]. The frequency encoding gradient has to be turned on during the recording of the signal [4]. In order to reconstruct an image, this experiment is repeated multiple times with different values of phase encoding gradients. Each repetition fills a line in a space, called the "k-space". The "k-space" is a grid of raw data containing frequency information that is directly obtained from the MR signal measured. An inverse 2D Fourier Transform (FT) is used to recover spatial information contained in the MR signal [4].

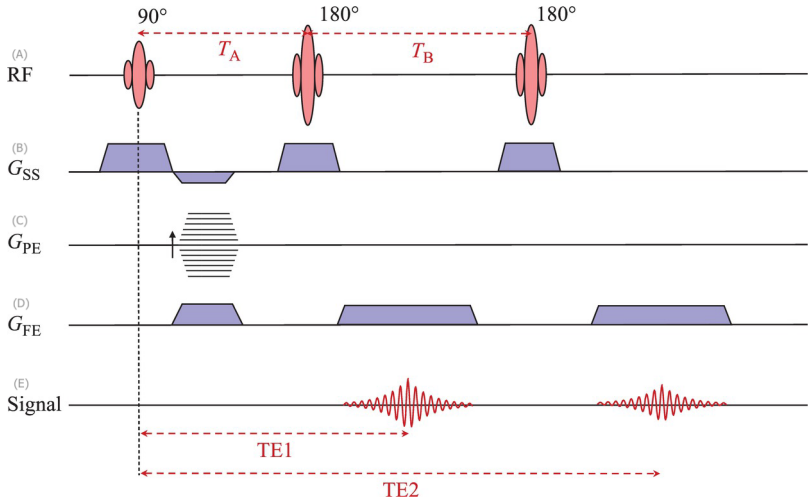


Figure 1.10: Double-echo SE sequence. (A) RF-pulses of a (multiple) SE sequence. (B) Slice selection gradient along the z-direction. (C) Phase encoding gradient along the y-direction, with a different intensity at each repetition. (D) Frequency encoding gradient along the x-direction. (E) MR signal obtained with the sequence that relies on T_2 [14].

1.2 Diffusion-Weighted Magnetic Resonance Imaging

Diffusion-Weighted Magnetic Resonance Imaging (DW-MRI) has revolutionized clinical neuroimaging [15]. This technology allows pathological tissues to be detected very early with a higher specificity than conventional MRI sequences [15]. Microstructure-imaging that emerged from DW-MRI is used to explore microscopic properties of tissues for a better understanding of pathologies. DW-MRI images capture the diffusion of water molecules within the brain [15].

Water molecules experience a random thermal movement called Brownian motion [15]. The diffusion of water molecules depends on the environment and the architecture of the brain tissues [15]. Water molecules in the gray matter (GM), white matter (WM) or cerebrospinal fluid (CSF) diffuse differently. With a specific DW-MRI sequence, an image with contrasts that show differences in the diffusion of water molecules in the brain structure can be obtained [15]. The Pulsed Gradient Spin Echo (PGSE) sequence is the most popular diffusion-weighted sequence used. This modified SE sequence is composed of two supplementary gradients. As represented in Fig.1.11, a diffusion gradient is observed after the first 90°-pulse and another diffusion gradient after the 180°-pulse of the classical SE sequence. For the sake of clarity, the slice selection gradient, the phase encoding gradients and the frequency encoding gradient are not represented in Fig.1.11 but are still used to obtain spatial information, as in the regular SE sequence. The first diffusion gradient is used to dephase the magnetization and the second gradient is used to rephase the magnetization. The PGSE sequence is characterized by a "b-value" defined by [15]:

$$b_{PGSE} = (\gamma G \delta)^2 \left(\Delta - \frac{\delta}{3} \right), \tag{1.29}$$

where:

- b_{PGSE} is the "b-value" that characterizes the PGSE sequence and is often expressed in $[s/mm^2]$. The b-value is sometimes expressed in $[ms/\mu m^2]$;
- G is the magnitude of the diffusion gradients ;
- δ is the duration of the diffusion gradients ;
- Δ is the time between the first diffusion gradient and the second diffusion gradient.

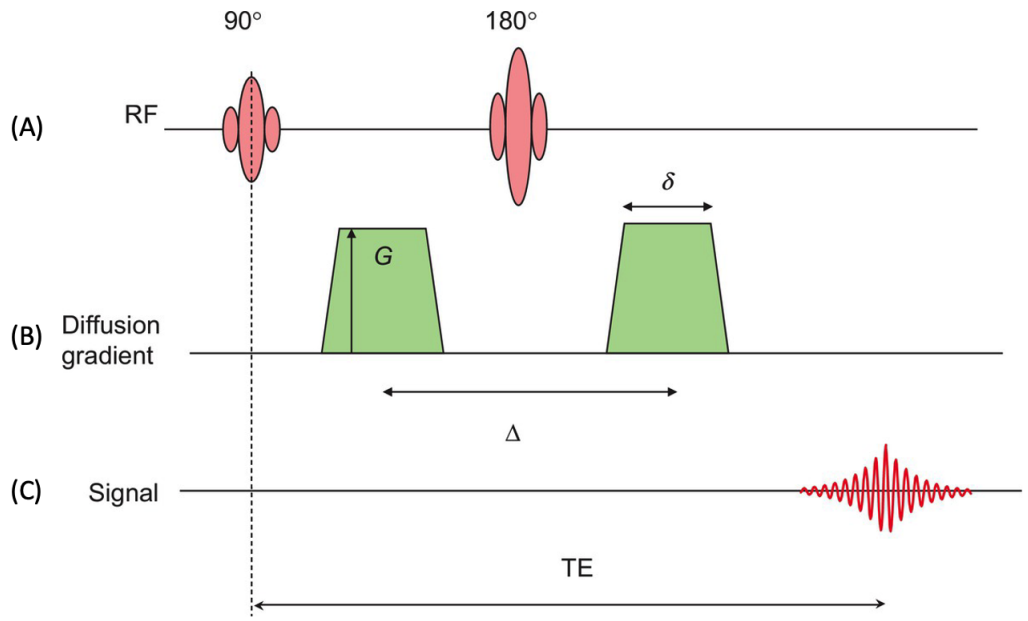


Figure 1.11: PGSE sequence for DW-MRI. (A) RF-pulse of a SE sequence. (B) Diffusion gradients used for dephasing and rephasing the magnetization. (C) MR signal obtained containing diffusion information [14].

In Fig.1.12(A), when the first diffusion gradient is applied, the spins are dephased proportionally to their position. When the second diffusion gradient is applied, since no diffusion occurred, the spins are rephased and the MR-signal measured is maximum. However, if diffusion occurs after the first diffusion gradient (Fig.1.12(B)) due to Brownian motion, the spins will not be totally rephased after the second diffusion gradient. Indeed, the magnetic field needed to rephase the spins is not adapted to their position anymore. Therefore, the MR-signal measured is weaker.

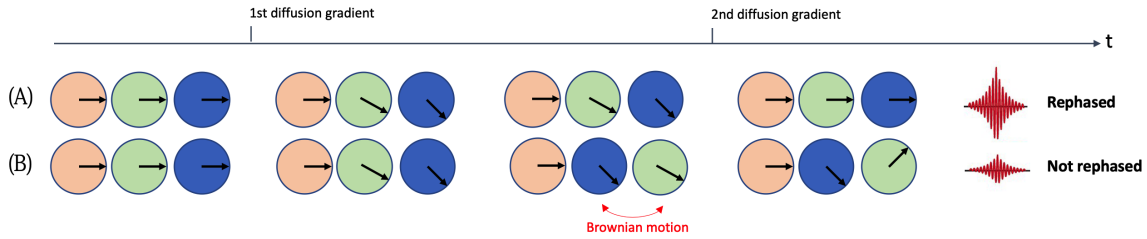


Figure 1.12: Effect of diffusion gradients on spins in the situation where (A) water molecules do not diffuse and (B) water molecules diffuse.

Although not addressed here, other diffusion-weighted sequences can be used, such as the double PGSE (dPGSE) sequence where two consecutive diffusion encodings are obtained, the Oscillating Gradient Spin Echo (OGSE) sequence where oscillating gradient pulses are used, etc.

Chapter 2

DW-MRI models of the brain microstructure

DW-MRI models intent to retrieve information about tissue microstructure embedded in the diffusion signal measured. Two categories of models exist: phenomenological models and microstructural models. Phenomenological models fit the measured signal with a mathematical expression to obtain information about the diffusion process of water molecules rather than actual microstructural features of the tissues. Microstructural models are multi-compartment models that use the superposition principle to infer microstructural features of the brain tissue.

2.1 Superposition principle

The superposition principle is the key concept of multi-compartment imaging. This principle claims that the signal measured can be decomposed as the "union of individual signals emerging from mutually disjoint and independent structures with perfectly reflecting boundaries" [16] (e.g. the extracellular space, the intracellular space and the CSF). The DW-MRI signal measured can therefore be decomposed as:

$$S(b_{PGSE};\Omega) = \sum_{i=1}^{K} f_i S(b_{PGSE};\Omega_i), \tag{2.1}$$

with:

$$\sum_{i=1}^{K} f_i = 1, \tag{2.2}$$

where:

- $S(b_{PGSE};\Omega)$ is the signal measured for a diffusion environment Ω with a PGSE sequence defined by "b_{PGSE}" ;
- Ω_i (i = 1,...,K) are mutually disjoint compartments with perfectly-reflecting boundaries. $\|\Omega_i\|$ is the volume of compartment i ;
- f_i is the volume fraction of the compartment i, defined by $f_i = \frac{\|\Omega_i\|}{\|\Omega\|}$.

In reality, cell membranes are not totally impermeable and the superposition principle is based on the hypothesis that the signal is obtained from mutually disjoint and independent structures. However, the time scale of a DW-MRI acquisition lies around 100 ms. One can therefore consider a tiny transfer of molecules during that time, making the assumption of independence presumably suitable. This is called the "slow transfer limit" [17].

2.2 Phenomenological models

2.2.1 DTI

The idea of Diffusion Tensor Imaging (DTI) is to analyze the three-dimensional diffusion of water molecules to obtain valuable information about the microstructure of brain tissues [15]. The diffusion of water molecules is strongly influenced by the neuroarchitecture. In the CSF, the diffusion of water molecules is globally the same in every direction (Fig.2.1(A)) and the signal obtained is the same no matter the orientation of the diffusion gradients [15]. However, the diffusion is highly anisotropic in axons (Fig.2.1(B)). When the diffusion gradients are applied in the direction of the axons, the diffusion of water molecules is important. When the diffusion gradients are applied perpendicularly to the direction of the axons, the diffusion of water molecules is more restricted. The diffusion of water molecules is described by a 3×3 tensor constructed by repeating the PGSE sequence with different orientations of diffusion gradients. The tensor describing the anisotropic diffusion of water molecules in 6 different directions is described by the symmetric and positive-definite tensor [6]:

$$D = \begin{pmatrix} D_{xx} & D_{xy} & D_{xz} \\ D_{yx} & D_{yy} & D_{yz} \\ D_{zx} & D_{zy} & D_{zz} \end{pmatrix}. \tag{2.3}$$

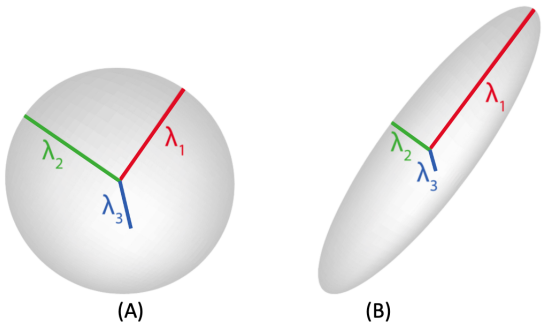


Figure 2.1: Ellipsoid representation of the diffusion tensors with (A) an isotropic diffusion (e.g. CSF) and (B) an anisotropic diffusion (i.e. axons). λ_1, λ_2 and λ_3 represent the eigenvalues of the diffusion tensor [18].

The attenuation of the signal obtained with a PGSE sequence characterized by a b-value "b_{PGSE}" is linked to the diffusion of water molecules by the Stejskal-Tanner equation. This equation is solved to reconstruct the diffusion tensor. When the diffusion is isotropic and in the absence of barrier, the diffusion is represented by a scalar and the Stejskal-Tanner equation is [19]:

$$E(b_{PGSE}, \mathbb{R}^3) = e^{-b_{PGSE}D}, \tag{2.4}$$

where:

- E is the attenuation of the signal measured when a PGSE sequence is used ;
- b_{PGSE} is the b-value of the PGSE sequence ;
- D is the diffusion coefficient of water molecules.

When the diffusion is anisotropic, the Stejskal-Tanner equation becomes [19]:

$$E(b_{PGSE}, \mathbb{R}^3) = e^{-b_{PGSE}\hat{\mathbf{g}}^{\mathbf{T}}\mathbf{D}\hat{\mathbf{g}}}, \tag{2.5}$$

where:

- **D** is a positive-definite diffusion tensor ;
- $\hat{\mathbf{g}}$ is the unit gradient direction.

Different image representations can be obtained after the reconstruction of the diffusion tensor. Diagonalization of the tensor leads to a matrix with the eigenvalues λ_1, λ_2 and λ_3 in the diagonal entries of the tensor and zeroes for the off-diagonal terms [6]:

$$\Lambda = \begin{pmatrix} \lambda_1 & 0 & 0 \\ 0 & \lambda_2 & 0 \\ 0 & 0 & \lambda_3 \end{pmatrix}, \tag{2.6}$$

where:

- Λ is the diagonalized diffusion tensor ;
- λ_1, λ_2 and λ_3 are the eigenvalues of the diffusion tensor. λ_1 is also called the axial diffusivity (AxD) and (λ_2 + λ_3) / 2 is the radial diffusivity (RD).

The eigenvalues are used to compute different metrics that characterize each voxel. Brain maps representing those metrics in every voxel can be constructed. A popular DTI metric is the Fractional Anisotropy (FA) (Fig.2.2(A)) defined by [18]:

$$FA = \sqrt{\frac{3}{2}} \frac{\sqrt{(\lambda_1 - MD)^2 + (\lambda_2 - MD)^2 + (\lambda_3 - MD)^2}}{\sqrt{\lambda_1^2 + \lambda_2^2 + \lambda_3^2}}, \tag{2.7}$$

where:

- MD is the Mean Diffusivity defined by (λ_1 + λ_2 + λ_3) / 3 (Fig.2.2(B)) ;
- FA is the Fractional Anisotropy. An isotropic diffusion has a FA of 0.

Other representations such as the "diffusion direction map" exist. The color assigned to the voxel represents the direction of the fibers and the brightness of the color depends on the anisotropy of the fibers (Fig.2.2(C)).

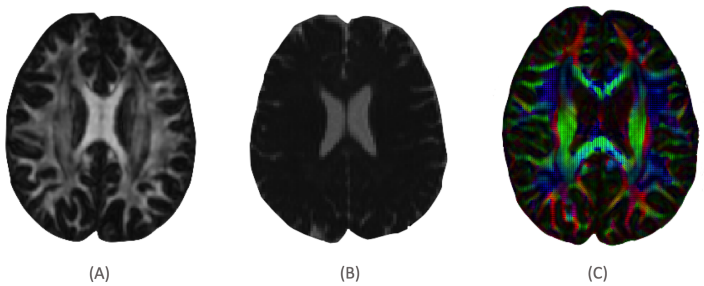


Figure 2.2: DTI maps: (A) FA map (B) MD map and (C) Diffusion direction map. *Representations obtained with FMRIB Software Library (FSL). Data from St-Luc University Hospital.*

Advantages and Limitations

DTI metrics are indirectly related to biological features, such as the myelination or the tissue organization [2, 20]. DTI is useful to describe tissue properties (e.g. eigenvalues of the diffusion tensor, MD or FA) in parallel fibers. In this model, a diffusion tensor characterizing the diffusion process is computed in each voxel [21]. This model would be correct if every voxel was composed of fascicles with a specific orientation, diameter and degree of myelination, such that every voxel defines a single type of fibers [21]. In reality, a complex organization of fibers is observed in every voxel and the model cannot capture complex configurations. For example, crossing fibers are modeled by a large diffusion tensor with DTI rather than two narrow tensors each one characterizing a fiber independently.

2.2.2 DIAMOND

DIAMOND stands for "DIstribution of 3D Anisotropic MicrOstructural eNvironments in Diffusion-compartment imaging". This model is a multi-compartment model that considers a large number

of "spin packets". A spin packet is defined as an ensemble of spins that experience the same magnetic field such that the displacement of the molecules in the packet is globally homogeneous and different from other spin packets [22]. This model needs an estimation of the number of tissue compartments in each voxel in order to estimate characteristics such as the compartment mean diffusivity (cMD), the compartment axial diffusivity (cAxD), the compartment radial diffusivity (cRD), the compartment fractional anisotropy (cFA) or the compartment heterogeneity index (cHEI) [23]. The MR-signal obtained from a voxel can be described as the integration of the signal arising from different compartments (e.g. multiple fascicles and the extra-cellular space). This model describes the three-dimensional nature of the diffusion of each spin packet by the mean of a diffusion tensor $\mathbf{D}$ that captures the restriction and hindrance of the diffusion [23].

The fraction of spin packets in the voxel characterized by a diffusion tensor $\mathbf{D}$ is described by a matrix-variate distribution $P(\mathbf{D})$. A homogeneous population described by a diffusion tensor $\mathbf{D^0}$ corresponds to a distribution $\mathrm{P}(\mathbf{D^0})$ that is equal to the delta function $\delta(\mathbf{D} - \mathbf{D^0})$ (Fig.2.3B). A sum of homogeneous populations is a multi-tensor model (MTM) and in the case where only one population is present, the DIAMOND model reduces to the DTI model. In Fig.2.3B, different homogeneous compartments are represented, each one defined by a delta function according to the tensor characterizing the environment. The diffusion-weighted signal is modeled by [23]:

$$S_k = S_0 \int_{\mathbf{D}\in Sym^+(3)} P(\mathbf{D}) \exp\left(-b_k \mathbf{g}_k^T \mathbf{D} \mathbf{g}_k\right) d\mathbf{D} \tag{2.8}$$

where:

- S_k is the diffusion-weighted signal.
- $Sym^+(3)$ is the set of 3×3 symmetric positive-definite matrices ;
- $\mathbf{D}$ is the diffusion tensor describing an anisotropic 3D Gaussian diffusion ;
- $\mathbf{g_k}$ is the orientation of the diffusion gradient ;
- $P(\mathbf{D})$ is the matrix-variate distribution describing the fraction of spins with a diffusion tensor $\mathbf{D}$;
- b_k is the b-value of the sequence.

DIAMOND describes the microstructural environments with a certain degree of heterogeneity such that each compartment is defined by a peak-shaped distribution (Fig.2.3C) rather than a delta function. A narrow distribution designates a homogeneous microstructure and a wide one indicates a highly heterogeneous population [23]. The matrix-variate Gamma (mv-Γ) distribution can therefore be used to describe the distribution of each population. The fraction of spin packets in the voxel characterized by a diffusion tensor $\mathbf{D}$ is described by [23]:

$$P(\mathbf{D}) = \sum_{j=1}^{N_p} f_j P_{\kappa_j, \Sigma_j}(\mathbf{D}) \tag{2.9}$$

where:

- N_p is the number of populations of spin packets considered ;
- $\mathbf{D}$ is a 3×3 symmetric positive-definite random matrix that follows a mv-Γ distribution ;
- f_j is the fraction of occupancy of the j^{th} population ;
- κ_j is the shape parameter of the j^{th} population ;
- Σ_j is the scale parameter of the j^{th} population.

Eq.(2.8) with Eq.(2.9) becomes:

$$S_k = S_0 \sum_{j=1}^{N_p} f_j \int_{\mathbf{D}\in Sym^+(3)} P_{\kappa_j, \Sigma_j}(\mathbf{D}) \exp\left(-b_k \mathbf{g}_k^T \mathbf{D} \mathbf{g}_k\right) d\mathbf{D} \tag{2.10}$$

where the mv-Γ distribution has a density defined by:

$$P_{\kappa,\Sigma}(\mathbf{D}) = \frac{|\mathbf{D}|^{\kappa-(p+1)/2}}{|\Sigma|^{\kappa}\,\Gamma_p(\kappa)} \exp\left(-Tr(\Sigma^{-1}\mathbf{D})\right) \tag{2.11}$$

where:

- $|\cdot|$ is the matrix determinant ;
- Γ_p is the multivariate Gamma function ;
- p is equal to 3 since $\mathbf{D}$ is a symmetric positive-definite matrix of dimension 3×3 ;

and the mv-Γ function is defined by [23]:

$$\Gamma_p(\kappa) = \pi^{p(p-1)/4} \prod_{j=1}^{p} \Gamma\left[\kappa - (j-1)/2\right], \tag{2.12}$$

where $\Gamma(z)$ is the Gamma function: $\Gamma(z) = \int_0^\infty t^{z-1}e^{-t}dt$.

An analytical expression of Eq.(2.8) is found [23]:

$$S_k = S_0 \sum_{j=1}^{N_p} f_j \exp\left(-\kappa_j \log\left(1 + \frac{b_k \mathbf{g}_k^T \mathbf{D}_j^0 \mathbf{g}_k}{\kappa_j}\right)\right) \tag{2.13}$$

$$= S_0 \sum_{j=1}^{N_p} f_j \mathcal{D}(\mathbf{D}_j^0, \kappa_j), \tag{2.14}$$

where:

- $\mathbf{D}_j^0$ is the expectation of the j^{th} mv-Γ distribution defined as $\Sigma_j \kappa_j$.

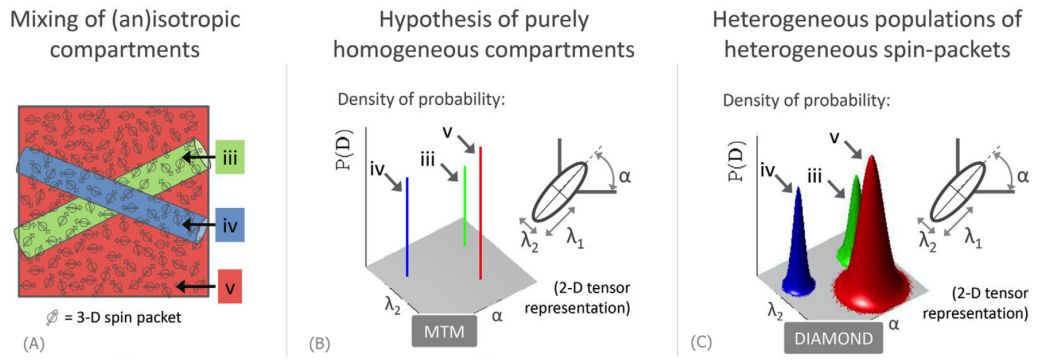


Figure 2.3: DIAMOND model. (A) Multi-compartment model with isotropic and anisotropic compartments. (B) With the hypothesis of homogeneous compartments, the model becomes a multi-tensor model (MTM). (C) Peaked-shaped distributions describing the multi-dimensional diffusivity with heterogeneities in each compartment [23].

This model can consider a compartment representing the restricted diffusion, where the diffusivity is computed from the data and can represent the isotropic diffusion of water molecules trapped in an isotropic environment (i.e. an isotropic diffusion with a diffusivity lower than the diffusivity of free water at 37°: $3 \cdot 10^{-3}$ $[mm^2/s]$). This isotropic trapped diffusion can be observed in glial cells [24]. The signal expression in a voxel where N_p populations with anisotropic diffusion and an isotropic compartment are considered can be written as:

$$S_k = S_0 \left(\sum_{j=1}^{N_p} f_j \mathcal{D}(\mathbf{D}_j^0, \kappa_j) + f_{iso} \exp\left(-b d_{iso}\right)\right), \tag{2.15}$$

where:

- d_{iso} is the diffusivity of the compartment representing the isotropic restricted diffusion and is estimated from the data ;
- f_{iso} is the fraction of occupancy of the compartment with isotropic restricted diffusion. All the fractions of occupancy sum to one.

Advantages and Limitations

This multi-compartment model considers multiple fascicles in the voxels and can therefore capture precise features of brain tissues by characterizing fascicles individually. This model characterizes the 3D-diffusivity of the fascicles with compartmentalized DTI metrics (cMD, cRD, cFA, cAxD) and the heterogeneity index (cHEI[1]) of the fibers. When multiple fascicles are estimated within a voxel, their respective fractions of occupancy are computed by the model. From those parameters, microstructural features can be deduced. The concentration parameter κ defines the heterogeneity of the compartment that depends on the heterogeneity of the fascicle orientation, the axonal diameter or the axonal density [23]. A small value indicates a high heterogeneity while a large value indicates a low heterogeneity. Microstructural changes can be captured with this model, such as an increase in the axonal diameter reflected by an increase in the compartment radial diffusivity. Moreover, considering a compartment representing the restricted diffusion can model the trapped diffusion of water molecules as observed in glial cells. The fraction of that compartment and the diffusivity are computed in every voxel. A limitation of the model could be the number of fascicles that is unknown: the maximum number of fascicles that can be estimated in every voxel is provided by the user. However, this may not be considered as a proper "limitation" since a maximum number of 3 fascicles is usually considered and is reasonable for the amount of data that can be acquired nowadays.

2.3 Microstructural models

2.3.1 NODDI

NODDI stands for "Neurite Orientation Dispersion and Density Imaging". This microstructural model was designed to estimate the complexity of dendrites and axons (i.e. neurite density and orientation dispersion) in vivo [25]. NODDI is a multi-compartments model organized in two levels. The first stage differentiates non-tissues (i.e. CSF) from tissues (i.e. GM and WM). This level is further divided into intra-neurite space and extra-neurite space (Fig.2.4). Therefore, this model takes three compartments into account:

- Intra-cellular compartment: space bounded by the cellular membrane of the axon or the dendrite ;
- Extra-cellular compartment: space around the cellular membrane ;
- CSF compartment: space occupied by the cerebrospinal fluid.

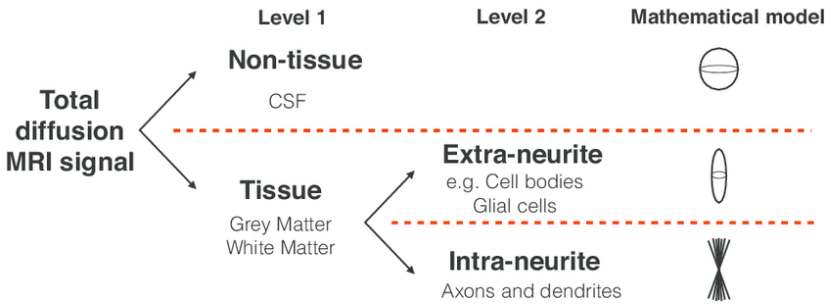


Figure 2.4: Compartments considered in NODDI. NODDI is a three-compartment model that models non-tissue and tissue diffusion (further divided into extra-neurite and intra-neurite diffusion). [26].

1 Compartment heterogeneity index is defined as $cHEI(\kappa) = (2/\pi)arctan(1/\kappa)$

The signal is described as a mathematical expression considering the signals emerging from the three compartments independently. The diffusion pattern is unique for each of those compartment [25]. The total normalized diffusion signal A can therefore be decomposed as:

$$A = (1 - f_{iso})(f_{ic}A_{ic} + (1 - f_{ic})A_{ec}) + f_{iso}A_{iso}, \tag{2.16}$$

where:

- A_{iso} is the normalized signal of the CSF compartment ;
- f_{iso} is the volume fraction of the CSF compartment ;
- A_{ec} is the normalized signal of the extra-cellular compartment ;
- f_{ec} is the volume fraction of the extra-cellular compartment ;
- A_{ic} is the normalized signal of the intra-cellular compartment ;
- f_{ic} is the volume fraction of the intra-cellular compartment (also known as "Neurite Density Index" or NDI).

Intra-cellular Model

The intra-cellular compartment models the axons by cylinders with zero-radii, referred as "sticks" (Fig.2.4). This model describes the diffusion of water as highly restricted perpendicularly to the axons but not in the direction of the axons [25]. If one considers a single stick with an orientation "**n**" and a gradient applied with an orientation "**g**", the attenuation of the signal in the stick is modeled by:

$$A_{ic_1} = e^{-b_\parallel d_{i,\parallel}} * e^{-b_\perp d_{i,\perp}}, \tag{2.17}$$

where:

- $d_{i,\parallel}$ is the axial diffusivity of the intra-neurite space ;
- $d_{i,\perp}$ is the radial diffusivity of the intra-neurite space, that is neglected in the intra-cellular model ($d_{i,\perp} = 0$).

Since the diffusion perpendicularly to the stick is considered as non-existent (the stick has a zero-radius), the expression of the attenuation becomes:

$$A_{ic_1} = e^{-b_\parallel d_{i,\parallel}} = e^{-|\hat{g}\cdot\hat{n}|(\gamma\delta G)^2(\Delta - \frac{\delta}{3})d_{i,\parallel}}. \tag{2.18}$$

By integration over all possible sticks orientations, the expression becomes [25]:

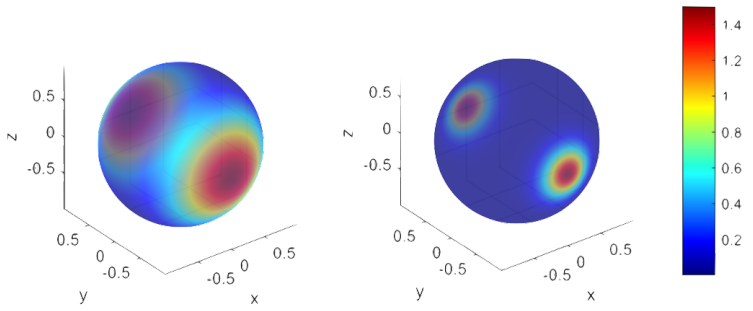
$$A_{ic} = \int_{\mathbb{S}^2} f(\mathbf{n}) s^{-bd_{i,\parallel}(\mathbf{g}\cdot\mathbf{n})^2} d\mathbf{n}, \tag{2.19}$$

with:

$$f(n) = M\left(\frac{1}{2}, \frac{3}{2}, \kappa\right)^{-1} e^{\kappa(\boldsymbol{\mu}\cdot\boldsymbol{n})^2}, \tag{2.20}$$

where:

- f(n) is the orientation distribution function modeled with a Watson distribution. The Watson distribution describes a spherical distribution of the sticks (Fig.2.5). $f(\mathbf{n})d\mathbf{n}$ gives the probability of finding sticks along orientation $\mathbf{n}$;
- M is the confluent hypergeometric function, also known as Kummer's function ;
- $\boldsymbol{\mu}$ is the principal orientation of Watson distribution ;
- κ is the concentration parameter, measuring the extent of orientation dispersion around $\boldsymbol{\mu}$.



(a) $\kappa = 1$. (b) $\kappa = 10$.

Figure 2.5: Example of Watson distribution on the unit sphere S^2 for different κ parameters ($\kappa = 1$ and $\kappa = 10$) [27].

Extra-cellular Model

This compartment is modeled by an anisotropic Gaussian distribution since the diffusion of water molecules is hindered by glial cells or cell bodies, but not restricted [25]:

$$A_{ec} = e^{-b\mathbf{g}^T(\int_{\mathbb{S}^2} f(\mathbf{n})D(\mathbf{n})d\mathbf{n})\mathbf{g}}, \tag{2.21}$$

where:

- $D(\mathbf{n})$ is a diffusion tensor with the principal direction of diffusion $\mathbf{n}$. By opposition to the intra-cellular model, the diffusion is described by a tensor since the diffusion perpendicularly to the axon is not neglected anymore. The tensor defines the axial diffusivity of the extra-neurite space ($d_{e,\parallel}$) and the radial diffusivity of the extra-neurite space ($d_{e,\perp}$). It is assumed that $d_{e,\parallel}$ is equal to the axial diffusivity of the intra-neurite space ($d_{i,\parallel}$).

CSF Model

An isotropic Gaussian diffusion (with isotropic diffusivity d_{iso}) is used to model this compartment:

$$A_{iso} = e^{-bd_{iso}}. \tag{2.22}$$

Parameters

The parameters in NODDI are: the intra-cellular volume fraction (f_{ic}), the isotropic volume fraction (f_{iso}), the intra-neurite diffusivity ($d_{i,\parallel}$), the axial diffusivity of the extra-neurite space ($d_{e,\parallel}$), the radial diffusivity of the extra-neurite space ($d_{e,\perp}$), the isotropic diffusivity (d_{iso}), the concentration parameter of Watson distribution (κ) and the principal orientation of Watson distribution $\boldsymbol{\mu}$. However, in order to avoid poor estimations of the parameters, some values are fixed *a priori* [28]. The number of parameters to be estimated is consequently reduced. It is therefore assumed that:

- $d_{iso} = 3 \cdot 10^{-3}$ $[mm^2s^{-1}]$;
- $d_{e,\parallel} = d_{i,\parallel} = 1.7 \cdot 10^{-3}$ $[mm^2s^{-1}]$ (for adults). The diffusivity is fixed to $2 \cdot 10^{-3}$ $[mm^2s^{-1}]$ for newborns [28]. Those values were fixed based on typical *in vivo* values ;
- $d_{e,\perp} = d_{e,\parallel}(1 - f_{ic})$. The perpendicular diffusivity of the extra-neurite space is linked to the parallel diffusivity of the extra-neurite space by the tortuosity model.

Based on those assumptions, the remaining parameters that are computed by the model are: f_{ic}, f_{iso}, κ and $\boldsymbol{\mu}$. Once the model is fitted with the data, the Orientation Dispersion Index (ODI) is computed as [25]:

$$OD = \frac{2}{\pi} arctan(1/\kappa). \tag{2.23}$$

Advantages and Limitations

This microstructural model allows to capture key features of neurites morphology: the neurite density (with the Neurite Density Index, NDI, that measures the volume fraction of the neurites) and the neurites orientation (with the Orientation Dispersion Index, ODI). Those features are determined in a clinically feasible acquisition time [25] for the whole brain. A large ODI is supposed to reflect a structure composed of highly dispersed neurites (e.g. GM) and a small index reflects aligned axons (e.g. white matter) [29]. Therefore, an ODI of "0" describes parallel fibers and an ODI of "1" defines randomly oriented fibers. However, assumptions are made with NODDI. While different microstructural properties have been observed in the brain, this model considers a single type of fibers [23]. This model neglects the radial diffusivity in the axons and considers only a single fascicle compartment in the voxel. An ensemble of crossing fascicles are therefore represented by an increased dispersion without being characterized individually [23]. Different assumptions are made by the model (e.g. fixed values for the diffusivities in the compartments, based on *in vivo* typical values). As described in [28], "this approach seems to defeat the purpose of biophysical modeling". Indeed, this approach leads to a loss of information about the tissue microstructure and biased values may be computed for the remaining parameters that are estimated by the model [30]. Moreover, fixing the axial diffusivity is a "problematic assumption" [30] since a biological variability in this value is expected in different regions in the extra-axonal space and the intra-axonal space and could be used as a biomarker of pathological conditions [30]. Finally, linking the radial diffusivity to the axial diffusivity in the extra-axonal space with the tortuosity model prevents an independent analysis of the quantities whereas changes in those parameters may reflect different biological processes [30].

2.3.2 Microstructure Fingerprinting

This multi-compartment model based on Monte Carlo simulations of the diffusion of the water molecules is used to estimate microstructural features of the brain tissues. This microstructural model is based on the superposition principle of crossing fascicles[2]. If one considers a voxel of WM composed of K fascicles and a partial volume of CSF, the DW-signal obtained at the echo time can be decomposed with the superposition approximation for crossing fascicles as [19]:

$$\begin{aligned} S &= M_0 \cdot \left[\sum_{k=1}^{K} \nu_k A_{fasc}(\mathbf{\Omega}_k, \mathbf{T}_k, \mathbf{u}_k; \mathbf{g}) + \nu_{csf} A_{csf}(D_{csf}, \mathbf{T}_{csf}; \mathbf{g}) \right] \\ &= \sum_{k=1}^{K} w_k A_k + w_{csf} A_{csf} \end{aligned} \tag{2.24}$$

where:

- M_0 is the net initial transverse magnetization of the voxel after the initial 90°-RF pulse ;
- $A_{fasc}(\mathbf{\Omega}_k, \mathbf{T}_k, \mathbf{u}_k; \mathbf{g})$ is the modeled normalized DW-MRI signal that would arise from an environment composed of a fascicle with an orientation u_k, microstructural parameters Ω_k and parameters T_k, characterizing the NMR relaxation of the tissues (such as T_1, T_2 and proton density) ;
- D_{csf} is the diffusivity in the CSF ;
- ν_k is the fraction of the physical volume of the voxel occupied by the k-th fascicle, defined as: $\nu_k = \frac{w_k}{\sum_{k=1}^{K} w_k}$;
- w_k is the weight of the k-th fascicle in the NMR-apparent signal reflecting the contribution of the fascicle that can be defined as $w_k := M_0 \nu_k$.

The framework of the inverse problem that defines the optimal combination of fascicles to explain the diffusion signal in every voxel can be described as follows:

2 The superposition principle of crossing fibers in the "assumption that the total diffusion-weighted MRI signal is the sum of the signals arising from each fascicle independently, even when the fascicles intermingle in a voxel" [31]

First, a discrete sampling of the Ω-space of single-fascicle microstructural parameters justified by tissue biology is performed to obtain structural parameters of interest: $\mathbf{\Omega_1}, ..., \mathbf{\Omega_N}$. This model represents fascicles with a hexagonal packing of impermeable cylinders representing the axons [32], as depicted in Fig.2.6A. The fascicles are characterized by an apparent axonal radius (r) and a spacing between the axons (s).

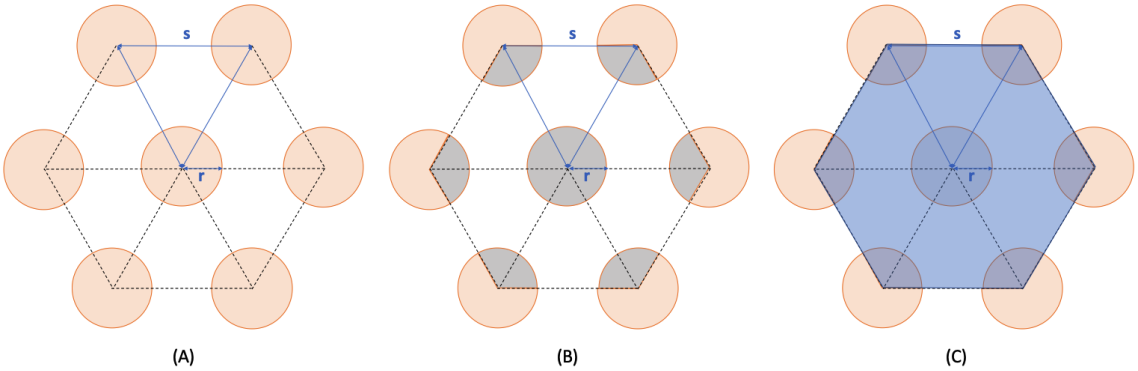


Figure 2.6: (A) Schematic representation of the hexagonal packing of cylinders representing the axons within a single fascicle, characterized by an apparent axonal radius (r) and a spacing between the axons (s), (B) the gray-shaded area is the "$A_{axons \subset hexagon}$" area in Eq.2.25 and (C) the blue-shaded area is the "$A_{hexagon}$" area in the equation.

For more convenience, a fascicle can be described by its intra-axonal volume fraction (or "fiber volume fraction"), defined as the ratio of the area of axons within the hexagon (gray-shaded area in Fig.2.6B), with the area of the hexagon (blue-shaded area in Fig.2.6C):

$$fvf_{fasc} = \frac{A_{axons \subset hexagon}}{A_{hexagon}} = \frac{2\pi}{\sqrt{3}} \left(\frac{r}{s}\right)^2 . \tag{2.25}$$

Based on the structural parameters chosen, a dictionary is built and contains the DW-MRI fingerprints of N selected microstructural configurations for a single fascicle along a fixed direction u_0 obtained with Monte Carlo simulations of the random diffusion of water molecules [19]:

$$\mathbf{F}^0 = \left[A_1^0, ..., A_N^0\right] , \ \mathbf{F}^0 \in \mathbb{R}^{M \times N}, \tag{2.26}$$

where:

$$A_j^0 = \left[A_{fasc}\left(\mathbf{\Omega_j}, \mathbf{T_0}, \mathbf{u_0}; \mathbf{g}_i\right)\right]_{i=1}^{M} . \tag{2.27}$$

The steps detailed so far are the "pre-computing steps" that consisted in building the dictionary composed of DW-MRI signals (or "fingerprints") obtained with Monte Carlo simulations of the random walk of water molecules in environments defined by a hexagonal packing of cylinders with different microstructural parameters.

The next steps are computed at runtime and consist in finding the optimal microstructure parameters that describe the diffusion signal acquired. Once a dictionary composed of Monte Carlo DW-MRI fingerprints is pre-computed, an estimation of the number of fascicles (K) and their orientations $\mathbf{u}_1, ..., \mathbf{u}_k$ are evaluated by means of an external routine [32]. Based on $\mathbf{F}^0$, a routine computes the single-fascicle dictionaries $\mathbf{F}^1, ..., \mathbf{F}^K$ along the K orientations defined in the previous step.

Finally, the optimization problem is solved under sparsity constraints. The sparsity constraints ensure that only one fascicle (with specific microstructural properties) is chosen out of all possible fascicles for a specific orientation. Solving the sparse optimization problem involves finding the optimal combination of fascicles in every voxel (where the number and orientation of the fascicles in the voxel were determined in a previous step with an external routine) such that a minimum difference between the simulated signal and the actual DW-MRI signal [19] is obtained. The fascicles selected when solving the problem define the optimal microstructural properties, leading

to the most accurate interpretation of the diffusion signal. Solving the sparse optimization problem can be mathematically defined as [32]:

$$(\hat{j_1}, ..., \hat{j_K}) = \underset{1 \leqslant j_1, ..., j_K \leqslant N}{\operatorname{argmin}} \min_{\mathbf{w} \geqslant 0} \left\| \mathbf{y} - \left[\mathbf{A}^1_{j_1} \mid ... \mid \mathbf{A}^K_{j_K} \mid \mathbf{A}_{csf} \right] \cdot \begin{bmatrix} w_1 \\ ... \\ w_K \\ w_{csf} \end{bmatrix} \right\|_2^2, \tag{2.28}$$

where:

- $\mathbf{y}$ is the measured signal ;
- $\hat{j_k}$ is the optimal fingerprint in $\mathbf{F^k}$ defining the optimal microstructural parameter $\hat{\mathbf{\Omega}}_\mathbf{k}$.

Advantages and Limitations

This model based on Monte Carlo simulations is powerful since the simulation of the random walk of water molecules is known to provide "near groundtruth for DW-MRI signals" [19]. From *in vivo* data, an "apparent" axonal radius index (a single radius value is considered to describe the intra-axonal signal [32]) and an axonal density index are estimated for each fascicle in every voxel. In this model, a dictionary is pre-computed and a convex optimization problem is solved in order to determine microstructural features of brain tissues. The only assumption made to use the superposition principle of crossing fibers was that no exchange of water occurred between the fascicles during the acquisition time [19]. The sparsity constraints used for solving the convex optimization problem prevent multiple fingerprints from being selected to describe the DW-MRI signal arising from a fascicle in a voxel. As described in [32], "this could be a limitation for fascicles consisting of several well-delimited sub-regions exhibiting distinct microstructural properties". Another limitation of this model is the computational cost for the creation of the dictionary that can be highly increased when the size of the dictionary is increased to obtain a finer resolution of microstructural parameters [19]. However, it is mentioned that Monte Carlo simulations "provide exact signals for any tissue geometry" [32]. Moreover, a study conducted on a rat model of spinal cord injury showed that parameters obtained with Monte Carlo simulations are "generally more specific and interpretable" [32] than metrics obtained with forward signal models such as NODDI and DIAMOND, with results that are consistent with histology [32].

Chapter 3

Alzheimer's disease

3.1 Overview of Alzheimer's disease

3.1.1 Figures, symptoms, causes and pathophysiology

Alzheimer's disease (AD) is a neurodegenerative disease that damages and destructs brain cells progressively with symptoms that are proportional to the brain damage. The rising elderly population leads to an increase of the prevalence of AD, making the disease a primary concern in today's society. According to the 2019 Alzheimer Europe Report [1]:

- 1.69% is the percentage of Belgian population affected by dementia[1] in 2019 ;
- 10.67% is the percentage of men aged 80-84 affected by dementia in Europe in 2019 ;
- 13.05% is the percentage of women of age 80-84 affected by dementia in Europe in 2019 ;
- 9 780 678 is the number of individuals affected by dementia in Europe in 2019 ;
- 18 846 286 is the expected number of individuals affected by dementia in Europe in 2050.

Microstructural changes in the brain may occur 20 years before the appearance of symptoms [33]. Although nerve cells involved in cognitive functions are damaged in AD (leading to memory loss, difficulty in thinking and learning), other parts of the brain may also be affected, leading to difficulty in walking and swallowing, depression, personality changes, loss of interest, etc. [33]. AD is progressive and irreversible [33]. The causes of the disease are still unknown but some risk factors are: aging, nutrition, traumatic brain injuries, education, social engagement, other diseases (e.g. cardiovascular diseases) or genetics [33].

The strongest genetic factor for the late-onset AD (i.e. the age of onset is 65 years or older [34]) is the $\varepsilon 4$ allele of the apolipoprotein E gene ($APOE - \varepsilon 4$). The apolipoprotein E is a protein that maintains cholesterol homeostasis in the brain. This protein is essential for axonal growth, synaptic formation and remodeling [35]. The APOE gene is a sequence of nucleotides in the DNA that is involved in the production of the apolipoprotein E. The APOE gene exists under different forms ($\varepsilon 2$, $\varepsilon 3$ and $\varepsilon 4$) and each individual has two copies of the gene. Proteins created under the instruction of different APOE genes have different structures and functions. More specifically, the $APOE - \varepsilon 4$ genetic variant presents a pathological shape and constitutes a risk factor with an increased lifetime risk of developing AD [35] for patients presenting a copy of the allele (e.g. $\varepsilon 2/\varepsilon 4$). The risk is even higher in the case of $APOE - \varepsilon 4$ homozygotes patients who carry two copies of the allele (e.g. $\varepsilon 4/\varepsilon 4$) [35]. Early-onset AD (i.e. the disease affects people before the age of 65) represents 5% to 6% cases of AD [36]. Early-onset AD is usually associated with a mutation of the amyloid precursor protein[2] (under the instruction of the APP gene), presenilin 1[3] (under

1 A clinical stage of AD, where patients experience memory and behavioral symptoms that alter their autonomy in their daily life activities.

2 A protein that generates the $A\beta$ residues when broken down (the breakdown of proteins is called "proteolysis" [37]).

3 Presenilin 1 is involved in proteolysis of other proteins [38].

the instruction of the PSEN1 gene) or presenilin 2[4] (under the instruction of the PSEN2 gene) [36]. A mutation of those proteins leads to an accumulation of the amyloid precursor protein or an aberrant cleavage of the protein [36]. Finally, the presence of $APOE - \varepsilon 4$ is also known to be a strong genetic factor of early-onset AD [36].

Biologically, an accumulation of neurotoxic amyloid beta ($A\beta$) peptide plaques (called "senile plaques") is observed in AD outside of the neurons (in the GM and in the extra-axonal space of the white matter that lies immediately beneath the GM [40]) and an accumulation of an abnormal form of tau proteins (also called "tau tangles") inside the neurons (Fig.3.1). $A\beta$ plaques interfere with synaptic communication between neurons, leading to cell death. The deposition pattern of amyloid plaques is linked to the progression of the disease, with an accumulation in neocortical areas first, to subsequently accumulate in subcortical areas [41]. In healthy brains, microglia prevents the development of AD by removing Aβ from the extracellular space [42]. The microglia is a type of glial cells that is involved in tissue homeostasis maintenance, injury response and pathogen defense [42] by means of phagocytosis. It was hypothesized in previous studies that microglia compacted Aβ aggregates to prevent them to further develop when they are not able to keep up with the phagocytosis of $A\beta$.

As described in [43], "whether microglia reaction is beneficial, detrimental or both to AD progression is still unclear and the subject of intense debate". Although studies hypothesized that microglia reacted to neuronal dysfunctions (e.g. $A\beta$ plaques and tau aggregates) [43] and therefore had a secondary implication in the progression of the disease, a study [44] proved that those glial cells may have a primary role in AD. Indeed, genes known to be risk factors of the disease were found to be "preferentially or exclusively expressed in glial cells" [43].

Moreover, a study conducted on a mouse model of aggressive amyloid pathology (5xFAD mice) with an extensive plaque formation that received a treatment (with PLX3397) resulting in the elimination of 80% of microglia showed that eliminating microglia "prevents the synaptic and neuronal loss without affecting plaque loads" [45]. This observation indicates that microglia are directly involved in neuronal losses in AD. An activation disturbance of microglia is observed in AD and the function of the immune cells becomes inadequate to prevent the "onset and progression of the disease" [42]. The disequilibrium in the activation of microglia observed in AD creates a chronic neuroinflammatory environment with the secretion of neurotoxic cytokines that injure the neurons, destruct synapses excessively and facilitate the progression of the tau pathology [42].

Another study aimed at identifying the role of microglia in the initial deposition of Aβ plaques in AD was conducted on the same mouse model of aggressive amyloid pathology (5xFAD mice) that received a sustained treatment with PLX5622 to eliminate microglia before and during the pathology development [46]. No plaque formation was observed in the absence of microglia in the mouse model of AD [46]. This proves that microglia are involved in the initial deposition of Aβ plaques. It was therefore hypothesized that microglia may "(1) secrete factors that facilitate Aβ fibrillization[5], (2) physically form plaque cores from extracellular Aβ via compaction or (3) ingest, aggregate and modify extracellular Aβ internally, which is eventually released to seed plaques" [46]. Those findings indicate that, with a better understanding of the mechanisms involved in the disease, microglia may be an attractive target to stop or limit the progression of AD [43].

An accumulation of an abnormal form of tau proteins is also observed inside the neurons in AD. In healthy brains, microtubules[6] transport nutrients and molecules inside the neurons. Tau proteins are bound to the microtubules and keep them straight and functional. In AD, the hyperphosphorylated tau proteins are not able to bind to microtubules but rather aggregate into structures called neurofibrillary tangles (NFTs), as depicted in Fig.3.1. This pathological process is called tauopathy. The microtubules are weakened and not able to sustain the transport of nutrients into the neurons. The cell death leads to atrophy of brain structures.

4 Presilin 2 is involved with enzymes in the breakdown of the amyloid precursor protein [39].

5 Fibrillization is the formation of amyloid fibrils, an abnormal fibrous proteins deposit.

6 A microtubule is a protein-based polymer that is part of the cytoskeleton of a cell, a network that plays a vital role in many cell processes such as nutrients transportation, cell division, cells shape maintenance, etc. [47]

Although no pharmacologic treatment is nowadays available to stop the destruction of neurons [33], the scientific community is highly active in the field of AD to better understand its mechanisms. Since microstructural changes occur in early stages of the disease, the development of new therapies could help to intervene early in the progression of the disease [33] as soon as biomarkers[7] are measured. This encourages the search of biomarkers that could detect the earliest changes occurring in AD.

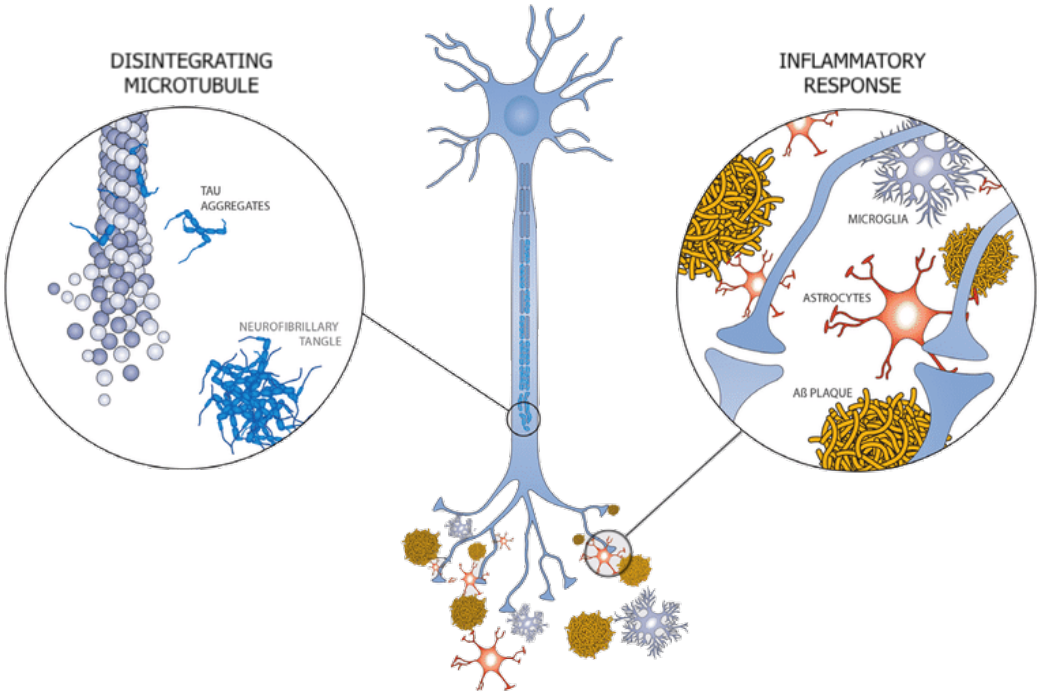


Figure 3.1: Biological processes involved in AD: Accumulation of $A\beta$ plaques and tau aggregates forming neurofibrillary tangles and leading to the disintegration of microtubules. An inflammatory response is triggered, activating microglia that eliminate cells debris and neurotoxic proteins. In AD, the activation disturbance of microglia leads to a chronic neuroinflammatory state. Adapted from [49].

3.1.2 Staging of the disease and diagnostic biomarkers

AD can be decomposed into three distinct clinical stages [33]:

- Preclinical AD where no symptoms are observed. Some biomarkers in the CSF or the blood can indicate the earliest signs of AD. As mentioned in [50], autopsy studies observed early stages of Aβ and tau pathologies during the preclinical stage of AD.
- Mild Cognitive Impairment (MCI) where the cognitive decline of the patients does not interfere with their everyday activities. Structural changes occur in the brain of the patients ($A\beta$ plaques and tau tangles). Half of cases of MCI are due to AD.
- Dementia where the patients experience memory losses and behavioral symptoms that interfere with everyday activities. The degree of the symptoms is correlated to the extent of the damaged territory.

The National Institute on Aging and Alzheimer's Association (NIA-AA)[8] shifted their diagnostic criteria from a "clinical definition" towards a "biological definition" based on biomarkers of the pathology and therefore considering the disease as a continuum [48]. According to the NIA-AA,

7 "A biomarker is defined as a quantifiable characteristic of biological or pathogenic processes or pharmacologic responses to a therapeutic intervention" [48].

8 The National Institute on Aging (NIA) is an Institute of the National Institutes of Health (NIH), the agency of medical research that is part of the U.S. Department of Health and Human Services (https://nia.nih.gov). The Alzheimer's association (AA) is a "voluntary health organization in Alzheimer's care, support and research". Based in Chicago IL, this association is committed to accelerating research across the globe (https://alz.org).

biomarkers of AD can be classified into three categories with the ATN Biomarker Classification[9]: (A) $A\beta$ deposition, (T) hyperphosphorylated tau aggregates and (N) neuronal injury [48].

A staging of the disease based on biomarkers can enhance the diagnostic accuracy [48] with a biological-based explanation to characterize the stages of the disease. For example, the Braak neurofibrillary tangle staging of AD defines stages of the disease based on the distribution pattern of NFTs. This pattern is very specific to the progression of the disease [51]. Moreover, assessing the tau pathology is important since cognitive decline and neuronal injury are more closely associated with the presence of NFTs than amyloid plaques [50]. Before the accumulation of NFTs, pretangle material (an abnormal tau deposition prior to fibril formation) is observed in the locus coeruleus, the upper raphe nuclei and the magnocellular nuclei [52] and characterizes stages a-c [51] (Fig.3.2). Braak NFT stages I-II are defined by an accumulation of NFTs mainly in the transentorhinal and entorhinal regions. Braak NFT stages III-IV are defined by an accumulation of NFTs in neocortical areas of higher-order such as the hippocampus, the amygdala, the basal temporal cortex, the insular cortex and the basal frontal cortex [52]. Braak NFT stages V-VI are characterized by a widespread accumulation of NFTs in the neocortex [51]. Braak stages a-VI are represented in Fig.3.2.

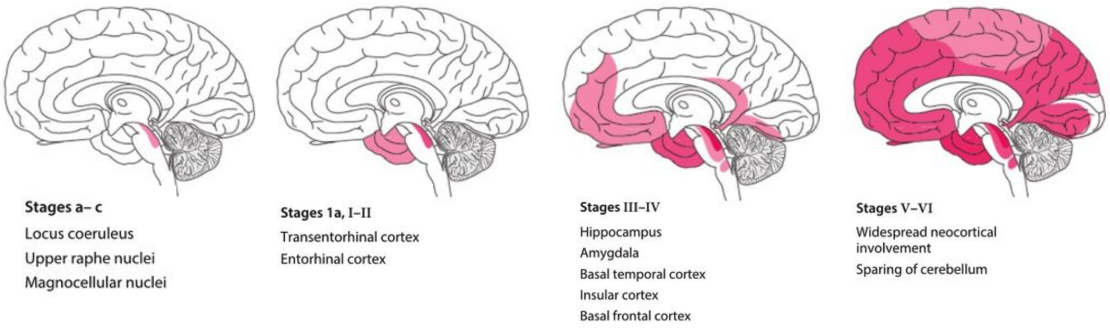


Figure 3.2: Braak staging of AD based on the progression of hyperphosphorylated tau aggregates: an accumulation of pretangle material is observed in stages a-c and an accumulation of NFTs in stages I-IV [52].

As described in [48], no biomarker alone can accurately diagnose AD but a combination of biomarkers is used to improve the accuracy of the diagnosis. The research is highly active to find new biomarkers of the disease that would refine the diagnosis, improve the clinical management of the patients, enhance clinical trials and promote the research for drug development. In this section, various diagnostic biomarkers of AD are presented.

CSF analysis

Lumbar puncture is a procedure performed to collect a sample of CSF to analyze the level of proteins that are known to be involved in pathological processes in AD. This procedure has minimal side effects [48] and determines the level of peptide amyloid and tau proteins in the CSF [48]. The "AD signature" in the CSF is defined by a decreased concentration ($\sim -50\%$) of $A\beta 42$ (42 amino-acid-long peptides) being correlated to the accumulation of $A\beta$ plaques in the brain [53] and an increased concentration ($\sim +200\%$) of phosphorylated tau proteins (p-tau) [48] being correlated with the presence of neocortical NFTs [53]. Although the analysis of those biomarkers is sensitive and specific to differentiate AD patients from healthy controls ($A\beta 42$: sensitivity = 80%, specificity = 82% and p-tau: sensitivity = 80%, specificity = 83%), this technique is not as efficient to differentiate AD dementia from other dementias ($A\beta 42$: sensitivity = 73%, specificity = 67% and p-tau: sensitivity = 79%, specificity = 80%) [48].

9 The "ATN Biomarker Classification" was developed by the NIA-AA in 2018 [48]

Molecular imaging

A variety of Positron Emission Tomography (PET) radiotracers were developed to target $A\beta$ plaques. Since the development of Pittsburgh Compound B (PiB), a radiopharmaceutical compound with a short half-life (^{11}C, $T_{1/2}$ = 20 minutes) [48], making its use difficult in clinical practice, new compounds (bound to ^{18}F, $T_{1/2}$ = 109.75 minutes) were developed such as: the florbetapir (sensitivity = 90%, specificity = 81%), the florbetaben (sensitivity = 89%, specificity = 89%) or the flutemetamol (sensitivity = 95%, specificity = 87%) [54]. The sensitivity and specificity were determined in studies comparing patients with AD dementia and healthy controls. However, an elevated level of $A\beta$ is also observed in healthy elderly and in patients with non-AD dementias (e.g. Lewy body dementia) [55]. Finally, there is a growing interest in using radioligands to assess the tau pathology rather than the presence of amyloid loads since the tau pathology is more closely associated with cognitive decline and neuronal injury than the presence of amyloid plaques [50].

Radiotracers used in PET with tau-specific ligands provide a characterization of the accumulation of pathological tau-proteins at early stages of AD [56]. Although different carrier molecules are used to target the abnormal form of tau-protein, the radionuclide used is fluorine-18 (^{18}F), a positron-emitting radioligand. Since the first PET tracer [^{18}F]FDDNP, a compound with a lack of *in vivo* specificity for tau tangles (i.e. this molecule also binds to Aβ plaques), a set of new tracers entered the field such as [^{18}F]MK-6240, [^{18}F]RO-948, [^{18}F]PI-2620, [^{18}F]GTP1, [^{18}F]PM-PBB3, [^{18}F]JNJ64349311 and [^{18}F]AV-1451 [56].

A study [57] proved that binding patterns of the radiopharmaceutical [^{18}F]MK-6240 (a recently discovered PET tracer [58]) corresponds to the Braak staging of NFTs (including Braak I-II) in Aβ-positive individuals with cognitive decline. This proves the sensitivity of the tracer to early NFTs deposition [57]. It was shown that this tracer leads to minimal off-target binding in the human brain [57]. [^{18}F]MK-6240 "strongly binds to neurofibrillary tangles in AD but does not seem to bind to a significant extent to tau aggregates in non-Alzheimer tauopathies" [58] (e.g. Pick's disease, progressive supranuclear palsy or chronic traumatic encephalopathy) or to Aβ plaques. Therefore, this tracer has a strong affinity with the uniquely structured tau tangles observed in AD [58]. Autoradiography experiments on postmortem brain tissues of AD individuals showed a strong binding of [^{18}F]MK-6240 in the hippocampal formation and frontal, temporal, parietal and occipital cortices containing NFTs [58]. No binding was observed in AD individuals and controls in the cerebellum (a region used as reference since no tau tangle is observed in this area in AD[10]), in the WM, in the basal ganglia nor in tau tangle-free cortical regions [58]. The [^{18}F]MK-6240 tracer shows off-target binding to venous sinuses[11] and cells containing neuromelanin (but to a lower extent than [^{18}F]AV-1451), "including pigmented neurons in the substantia nigra (regardless of the presence or absence of nigral tau pathology), leptomeningeal melanocytes, metastatic melanoma and retinal pigment epithelium, with some weaker off-target binding to brain hemorrhages as well" [58]. Those off-binding sites have to be taken into account when interpreting imaging results [58].

Microglia having a "double-edged sword"[42] function in AD, new radioligands targeting those glial cells are being developed to better understand the mechanisms that trigger the neuroinflammation. Although not yet considered as a biomarker for the diagnosis of the disease [61], the neuroinflammation may be crucial in the development of AD and microglia may therefore be an interesting target to limit the progression of the disease [43]. The PET tracers that have been used in studies to target microgliosis are [^{11}C]-PK11195 and [^{11}C]-PBR28 [61].

Magnetic Resonance Imaging

Structural MRI is used to observe atrophies in AD patients [48]. However, this technique is more likely to detect changes in late stages of the disease [48]. Diffusion MRI is a rapidly evolving technology that already demonstrated its ability to detect early microstructural alterations in AD (e.g. loss of myelin, loss of axons, etc.) [35, 20, 62, 63, 29, 64]. The development of new microstructure

10 Nowadays, this hypothesis is being questioned in the scientific community since studies have proved that the cerebellum may be affected by AD [58, 59]. However, this region may be one of the last regions to be affected by the disease.

11 The venous sinuses are venous channels within the dura mater that drain the venous blood from the cranial cavity to the heart [60].

models could help to better characterize microscopic properties of brain tissues. This technology being non-radiating and non-destructive [2], the research is highly active to find new biomarkers of the disease. Although more research is needed to fully understand how microglia may influence diffusion MRI signals in AD, studies showed encouraging evidence that multi-compartment diffusion MRI models could detect changes in microglial density [24, 65].

3.2 Literature survey of DW-MRI in Alzheimer's disease

In this section, results of previous studies that used diffusion models (DTI and NODDI) to characterize microstructural alterations in AD are presented. Tracts and (sub)cortical regions of interest that were highlighted in the literature are presented in the next section. A summary of the results mentioned in this section can be found in Appendix A.

3.2.1 DTI

- Three tracts of interest that best discriminated the preclinical AD group (38 subjects) and the MCI group (22 subjects) were highlighted in [20]: the parahippocampal cingulum (with an increased radial diffusivity), the posterior thalamic radiations (with a decreased fractional anisotropy) and the forceps major (with an increased mean diffusivity). In the study, the diffusion metrics were correlated with cognitive performances of MCI patients. A lower FA indicated a loss of organization and an increased mean diffusivity (MD) or radial diffusivity (RD) showed a breakdown of neurobiological barriers [20] and a decrease in myelination [63].

- A longitudinal study [63] revealed a decreased FA and increased MD within a one-year period, for the AD group (34 subjects) and the healthy controls (33 subjects), with exclusive changes in the hippocampal cingulum region for the AD group. Although less extensive than in the AD group, changes in diffusion metrics in healthy controls were due to the aging process. The fact that WM deteriorates during aging (cortical disconnection and myelin-breakdown), "has a mediating role in cognitive decline associated with advancing age" [66]. Compared to the healthy controls, the AD group showed a lower FA and higher MD in the hippocampal cingulum, the corpus callosum, the internal and external capsules, the corona radiata, the posterior thalamic radiation, the superior and inferior longitudinal fasciculi, the fronto-occipital fasciculus, the cingulate gyri, the fornix, the uncinate fasciculi and the tapetum [63].

- In [66], a decrease in FA and an increase in AxD, MD and RD were measured in the AD group (79 subjects) in the occipital, temporal, parietal and frontal WM as well as the corpus callosum and the fornix compared to MCI patients (55 subjects) and patients with preclinical AD (30 subjects).

- A study [64] involving pathologically-staged AD patients (46 subjects) without other dementia-related pathology who had antemortem MRI and autopsy showed an increased MD and decreased FA in the medial temporal limbic connections and the medial parietal WM. Those changes in diffusion metrics, more specifically in the ventral limbic connections (e.g. ventral cingulum tract, the crus of the fornix and the entorhinal WM), were strongly correlated to high Braak neurofibrillary tangle staging of AD. Finally, abnormal DTI values were associated to the clinical severity of the disease of patients for whom their disease had been confirmed with an autopsy [64].

- A study [41] conducted on 256 cognitively healthy older individuals showed that a lower hippocampal volume (hypothesized to follow neuronal damage, partially due to early tau pathology in the medial temporal lobe) was associated with abnormal DTI values such as an increased MD, an increased AxD and an increased RD in the hippocampal cingulum. Abnormal DTI values in the hippocampal cingulum bundle were associated to a higher tau accumulation in downstream-connected regions (i.e. the posterior cingulate cortex), suggesting that the tau pathology propagated via axonal connectivity rather than spatial proximity. Memory decline of amyloid-positive patients with a high tau binding in the posterior cingulate cortex was predicted by DTI values in the hippocampal cingulum bundle [41].

- A large-scale study [35] involving cognitively normal middle-aged $APOE-\varepsilon 4$ carriers (256 non-carriers and 275 carriers), i.e. individuals presenting a copy of the strongest genetic factor for late-onset AD, analyzed diffusivity properties in WM. The RD was highly increased in the WM in those individuals, essentially in superior longitudinal fasciculi. The AxD was also increased but less severely. This observation indicated a "disruption of the myelin sheath rather than pure axonal damage" [35]. Those changes in diffusion metrics appeared early and prior to axonal loss. Damage to myelin sheaths, more pronounced in individuals carrying two copies of $APOE-\varepsilon 4$, lead to a decreased axonal transmission speed and an increased metabolic consumption to sustain transmission [35]. The metabolism being impacted, the capacity of microglia to remove amyloid deposition could be compromised [35], leading to an accumulation of amyloid substance.

- A study [62] reconstructed a continuous fornix bundle of AD patients (23 subjects) and healthy elderly (23 subjects) to evaluate the diffusion characteristics of the tract. A lower FA, a higher RD and a higher MD were observed in the fornix of AD patients but the AxD was not increased compared to healthy controls. Moreover, no volumetric change in the fornix was observed, showing that diffusion metrics were more sensitive to fornix degeneration in AD. Abnormal DTI values were mainly observed in the body and the crus of the fornix [62].

- It was is shown in [67] that a lower FA in the fornix and an elevated $A\beta$ burden lead to an acceleration of cognitive decline in episodic memory over time. The study was conducted on clinically normal adults (253 subjects) who underwent diffusion MRI and Pittsburgh Compound B (PiB) PET, a technique using a radiotracer targeting the $A\beta$ burden. Moreover, microstructural changes in WM tracts directly connected to the hippocampus may interact "with elevated Aβ burden to hasten cognitive decline in clinically normal older individuals" [67]. Changes in DTI metrics observed in the fornix were associated with the progression from normal to MCI and from MCI to AD dementia [67]. With those findings, the study suggested that the evaluation of the microstructure of the fornix could help in the prediction of memory difficulties in patients with a high Aβ burden and could explain the accelerating memory decline in early AD [67].

- Studies mentioned in [68] observed changes in MD in AD patients and MCI patients. A study [69] conducted on MCI patients (18 MCI subjects and 18 healthy controls) mentioned that the increased MD in the hippocampus was the "strongest independent predictor of episodic memory decline". An increased MD in the hippocampus, the amygdala, the medial temporal GM and the frontal GM of AD patients (13 subjects) compared to healthy controls (13 subjects) was observed in [70]. Another study [71] observed an increased MD in the precuneous cortex, the posterior cingulate cortex and the frontal cortices of MCI patients (20 subjects) compared to healthy controls (20 subjects).

3.2.2 NODDI

- NODDI values were strongly correlated to histological measurements of the level of hyperphosphorylated tau protein in GM in a mouse model of human tauopathy (rTg4510) [29]. In the mouse model of human tauopathy, the dispersion of dendrites was reduced (lower ODI), the neurite density was increased (higher NDI) and the fraction of isotropic diffusion was increased (higher f_{iso}). The presence of tau burden in the TG animals lead to the atrophy of cortical layers, the loss of neurite structures and a reduction in the dendritic complexity. As described in [29], "[...] the tissue becomes less dispersed, leading to lower ODI and the reduced volume of cortex with higher density is reflected by higher NDI in the TG group. As the cortical structure atrophies, the space becomes occupied by CSF. The higher CSF contamination increases the free diffusion compartment reflected by a higher isotropic volume fraction". In the WM, a decrease in NDI and a decrease in ODI were observed in the hippocampal fiber tracts (i.e. the limbic system) in the mouse model of human tauopathy, indicating respectively a loss of neurite projections and a reduced dispersal of neuron projections [29].

- A study [72] showed that NDI and ODI indices were significantly decreased in the WM of MCI patients (14 subjects) and AD patients (14 subjects) compared to healthy controls (14

subjects). The volume fraction of isotropic diffusion (f_{iso}) was notably increased in MCI patients and the AD group compared to the healthy controls [72]. NDI values were essentially reduced in the splenium of the corpus callosum and the bilateral superior longitudinal fasciculi. $A\beta$ deposition lead to neurons and axons destruction in WM, resulting in a decreased NDI. f_{iso} was increased in the AD and MCI groups (with a larger increase in the AD group than in the MCI group), mainly in the brain stem and in the bilateral medial temporal lobes. According to [29], the increase in f_{iso} indicated a cell shrinkage and a decreased tissue volume fraction, pointing out the degree of atrophy. Although other studies observed an increased ODI in WM tracts of AD patients, a study [72] observed a decrease in ODI. Indeed, ODI was notably lower in the AD group and the MCI group compared to healthy controls in the WM of the frontal and occipital lobes [72]. The histological explanation of the decreased ODI was that a "reduced orientation dispersion reflects loss of secondary crossing fibers to leave more aligned neurons in the primary tracts, perhaps mediated by selective axonal degeneration" [73].

- For the diagnosis of AD, it was shown in [72] that the area under the ROC curve (this area evaluates the diagnostic performance of parameters) for the NDI values of the splenium of the corpus callosum was larger than the area for the FA. Moreover, the area under the ROC curve for f_{iso} values in the right cerebral peduncle was also larger than the one for the FA. Those observations showed that NODDI indices were more sensitive to WM microstructural changes than DTI metrics. This proved that NODDI may be a better tool than DTI for the diagnosis of AD, since it reflected more accurately the clinical status of the patient [72].

- A study [74] evaluated GM microstructure alterations in young onset AD (38 subjects) compared to healthy controls (22 subjects). Patients with young onset AD are individuals being less than 65 years old with symptom onset. The NODDI model was used to compute NDI and ODI values in five regions known to be associated with early atrophy in AD (i.e. entorhinal cortex, inferior temporal gyrus, middle temporal gyrus, fusiform gyrus and precuneous) and another region relatively spared in AD (i.e. precentral gyrus). ODI estimates neurite dispersion, "which in the context of GM may reflect the degree of complexity of dendritic trees" [74] and NDI values estimate the neurite density. NDI values were decreased in all regions while ODI values were decreased in the inferior and middle temporal gyri, fusiform gyrus and precuneous cortex in young onset AD patients compared to healthy controls. While no macroscopic change in the cortical thickness was observed in the precentral gyrus (a structure relatively spared in AD), NDI values in that region were decreased. This could raise the "possibility that such decreases in NDI may precede macroscopically detectable differences in cortical structure and may be a more sensitive marker of AD pathology" [74]. An association between cortical NDI values and the results of the Mini Mental State Examination (MMSE), a test for evaluating cognitive functions and memory performance of patients was also found.

- A study [75] assessing age-dependent differences in brain tissue microstructure with NODDI, hypothesized that the aging process was associated with decreased ODI and NDI in GM. Those findings indicated a loss in neurite arborization [75]. This study was conducted on 116 healthy participants of age between 45.4 to 72. It was suggested that ODI may increase with age in WM due to a greater dispersion of axons. NDI may decrease with age in WM, indicating a reduced packing density [75]. Finally, the volume fraction of Gaussian isotropic diffusion may increase in WM with age, reflecting a cell shrinkage [75].

- A tract-specific study [20] assessing WM alterations in early-stage AD observed a decreased NDI and an increased ODI in patients with preclinical AD (38 subjects) and MCI (22 subjects) compared to healthy controls (40 subjects). Those alterations suggested a "more advanced axonal degeneration and loosened axonal bundles" [20]. Such changes in the NODDI parameters were mainly observed in the left parahippocampal cingulum, the forceps major and the left posterior thalamic radiation.

- A TBSS-analysis in a study [76] evaluated NODDI parameters in young-onset AD patients (45 subjects), i.e. patients younger than 65 years with symptom onset [34] compared to healthy controls (23 subjects). This study also evaluated NODDI metrics in individuals with different genotypes (with or without APOE $\epsilon 4$). This study was conducted on 22 APOE $\epsilon 4+$ individuals and 17 APOE $\epsilon 4-$ individuals. This specific variant of APOE is known to be

associated with higher risk of disease manifestations for young-onset AD [76] and late-onset AD [35]. A decreased NDI and decreased ODI were observed in young-onset AD patients compared to healthy controls, suggesting alterations in the spatial organization of axons. An increased volume fraction of isotropic water was also observed around the corpus callosum and the fornix in young-onset AD patients compared to healthy controls.

The diffusion MRI models provide brain tissue characterization by means of interpretations (e.g. an increased fraction of isotropic water molecules indicating a cell shrinkage). As described above, some indices are a matter of debate since opposite trends and different interpretations were mentioned in previous studies (e.g. the ODI metric of the NODDI model : although some studies observed an increased ODI in the WM of AD patients and was interpreted as a greater dispersion of axons [75], other studies observed a decreased ODI in the WM of AD patients, interpreted as a "loss of secondary crossing fibers to leave more aligned neurons in the primary tracts, perhaps mediated by selective axonal degeneration" [73]). Tractography images of the WM tracts highlighted in previous studies and atlas based representations of the GM regions of interest can be found in Appendix B. The structures of interest in AD are:

- WM tracts: the fornix, the corpus callosum, the cingulum, the posterior thalamic radiation, the superior longitudinal fasciculus, the superior corona radiata, the forceps minor, the forceps major and the uncinate fasciculus.
- Cortical and subcortical structures: the hippocampus entorhinal cortex, the inferior temporal cortex, the middle temporal cortex, the fusiform cortex, the precuneous cortex, the frontal pole, the superior frontal gyrus, the parahippocampal gyrus, the posterior cingulate cortex, the hippocampus and the amygdala.

3.2.3 Regions of interest

As mentioned in previous studies, WM tracts and cortical regions undergo microstructural changes in AD. Those regions revealed changes in DTI values and/or NODDI values in AD patients, MCI patients and healthy elderly. It is therefore useful to report the functions of each region of interest to understand how (micro)structural changes may be associated with AD symptoms. The functions of the tracts and regions of interest (ROI) are summarized in Appendix C.

White Matter Tracts

The **corpus callosum** is a large fiber bundle composed of 200 million fibers of different diameters [77], that connects the two hemispheres and allows transmission of interhemispheric information [78]. A tractography of the corpus callosum is represented in Fig.B.1 of Appendix B. As described in [78], "changes of the corpus callosum associated with brain disorders may reflect changes in the functional integrity of inter-hemispheric association fibers". The corpus callosum can be decomposed into different parts from the anterior part to the posterior part as: the rostrum, the genu, the rostral body, the mid-body, the isthmus and the splenium [78]. The rostrum and the genu connect the hemispheres with fibers from inferior frontal and anterior parietal regions. The mid-body of the corpus callosum allows connections with fibers from the mid-temporal region. The splenium connects parieto-occipital regions between the two hemispheres [78]. The corpus callosum allows two types of connections between the hemispheres: homotopic connections (connections of identical regions in the two hemispheres) and heterotopic connections (connections of different regions in the two hemispheres) [77]. The size of the corpus callosum decreases during the aging process, resulting in memory decline [79]. A variety of tests performed in [79] suggested that the body of the corpus callosum may mostly be involved in verbal coding in memory while the splenium of the corpus callosum may be responsible for non-verbal coding in memory [79]. **Tapeta** of the corpus callosum are the WM tracts from the splenium that are not projecting to the occipital lobe but rather extend to the temporal region. The left tapetum and the right tapetum can be observed in Fig.B.1.

The **forceps major** are the fibers that connect the occipital lobes by passing through the splenium of the corpus callosum. The **forceps minor** are fibers that pass through the genu of the corpus callosum and connect the two frontal lobes. A damaged forceps minor is known to be implicated

in cognitive dysfunction [80]. This tract connects regions that are involved in the control of attention [80]. A tractography of the forceps major and the forceps minor is represented in Fig.B.2 of Appendix B.

The **corona radiata** transmits information between the cerebral cortex (involved in motor function) and the brain stem (involved in sensations) [81]. This fiber bundle is important for sending messages from the cerebral cortex to the body, to control the motor function and to transmit sensory input from the body to the cerebral cortex [81]. A tractography of the corona radiata is represented in Fig.B.3 of Appendix B.

The **posterior thalamic radiations** are thalamo-occipital fibers that connect the thalamus (caudal part) with the occipital and parietal lobes. This fiber bundle is a relay for sensory information [82]. The thalamic radiations (the anterior thalamic radiation and the posterior thalamic radiation) are represented in Fig.B.4 of Appendix B.

The **external capsule** is an ensemble of WM tracts known as association fibers [83]. Those fibers project from the cortex to the striatum of the basal ganglia (composed of caudate nucleus, putamen and ventral striatum). As described in [83], "the striatum is associated with inhibiting or regulating responses from the cortex, as well as learning and behavior". The **internal capsule** separates the caudate nucleus and the putamen/ventral striatum [84].

The **superior longitudinal fasciculus** (SLF) is a WM bundle that connects temporo-parietal language regions to ipsilateral frontal areas [85]. It was proved in [85] that deterioration of the SLF was associated with impaired verbal fluency. The SLF is crucial for word production [86]. Damage to this bundle can therefore lead to impaired phonological processing and phonological retrieval [86]. This bundle is also important for the working memory (or "short-term memory"), a system holding information briefly before further processing [87]. The working memory "has a significant influence in cognitive efficiency, learning and academic performance" [87] and different studies observed an impairment of the working memory in AD patients [88].

The **fornix** is a C-shaped WM bundle that extends from the hypothalamus (involved in the emotional behavior, energy maintenance, memorizing, etc. [89]) to the mammillary bodies (involved in the episodic memory, the memory one uses to remember events of one's life). Pathology involving the fornix is expected to lead to memory deficits [90]. It is suggested in [90] that "the left fornix primarily carries verbal memory information, while the right carries visuospatial memory information". It is also mentioned that "the medial fornix carries fibers from the caudal hippocampus, which processes exteroceptive signals[12] and integrates object recognition within a spatial context (i.e. scene learning). The lateral aspect of the fornix is presumed to carry projections from the more rostral hippocampus, which processes interoceptive signals[13] for emotional and motivational learning and memory" [90]. A tractography of the fornix is represented in Fig.B.5 of Appendix B.

The **uncinate fasciculus** is a WM bundle that connects the anterior temporal lobe with the lateral orbitofrontal cortex and the anterior prefrontal cortex. As described in [92], the function of this bundle is not well established yet, but "empirical evidence indicates a role for language as well as episodic memory and social emotional processing" [92]. A study [93] hypothesized that microstructural alterations of the uncinate fasciculus may lead to episodic memory and emotional processing impairments. A tractography of the uncinate fasciculi is represented in Fig.B.6 of Appendix B.

The **cingulum** is a WM bundle that, from the entorhinal cortex (in the medial temporal lobe), passes through the cingulate cortex [94]. The cingulum bundle is involved in the cognitive control and executive functions [94]. DTI metrics of the cingulum bundle are correlated with scores assessing the working memory, the attention, the executive functions and the language [94]. Different parts of the cingulum bundle are known to be associated with different functions. A pathology

12 Exteroception is "the perception of environmental stimuli originating outside of the body (e.g. visual, acoustic, or tactile stimuli)" [91]

13 Interoception is "the perception of the body's internal state through the processing of signals arising from within the body, e.g. blood pressure, heart beats, etc."[91]

involving the anterior cingulum is associated with emotional disorders (e.g. anxiety, depression, hostility, affective disorders), lack of motivation (apathy) and executive functions impairment (e.g. attention disorder). The parahippocampal cingulum is mainly associated with the episodic memory and the spatial processing. Damages to the parahippocampal cingulum can therefore lead to amnesia and topographic disorientation [94]. A tractography of the cingulum is represented in Fig.B.7 of Appendix B.

Cortical and Subcortical Regions

The **precuneous cortex** is situated in the postero-medial part of the parietal lobe [95]. Results of functional magnetic resonance imaging (fMRI) studies and PET studies aimed at exploring the functional neuroanatomy of cognitive functions divided the precuneous functions into four categories: the visuo-spatial imagery, the episodic memory retrieval, the self-processing and the consciousness [95]. A significant activation of the precuneous during visuo-spatial imagery tasks was observed for coordination of motor behavior, attentive tracking of moving targets, attention orientation, attention shift between objects, motor imagery, music perception and mental navigation (mental simulation of memorized routes) [95]. The precuneous cortex was also highly activated during episodic memory retrieval tasks such as auditory sentence recognition, verbal episodic memory retrieval, musical episodic memory retrieval and autobiographical event recollection [95]. Finally, an activation was also observed during self-processing tasks such as intentional self-processing (judgments on self-descriptive versus non-self-descriptive personality traits), emotional state attribution and social cognition [95]. A ROI for the precuneous is represented in Fig.B.8 of Appendix B.

A study [96] divided the **middle temporal gyrus** (MTG) to assess its functions: the anterior subregion, the middle subregion, the posterior subregion and the sulcus subregion. The middle part of the MTG is important for the semantic memory (or the "general knowledge") [96]. The posterior part of the MTG is involved in semantic processing of visually presented words and affective prosody (i.e. the expression of emotions during a talk) [96]. The anterior part is involved in acoustic-phonetic and semantic processing [96]. The sulcus part might be important for speech intelligibility [96]. The **inferior temporal gyrus** is involved in object recognition, face perception and number recognition [97] and is known to be part of the ventral stream of the visual system (a stream processing high-level visual information, aimed at analyzing the object itself rather than its position in space, the latter being handled by the dorsal stream of the visual system) [77]. ROIs for the middle temporal gyrus and the inferior temporal gyrus are respectively represented in Fig.B.9 and Fig.B.10 of Appendix B.

The **hippocampus entorhinal cortex** is located in the medial temporal lobe. Functional MRI studies proved that the entorhinal cortex was highly activated during memory tasks [98]. The entorhinal cortex is a relay between the hippocampus and neocortical regions. As described in [99], "although the entorhinal-hippocampal interaction is undoubtedly essential for initial memory acquisition, the entorhinal cortex contributes to memory retrieval". Moreover, memory consolidation involves strengthening of connections between the entorhinal cortex and the medial prefrontal cingulate cortex [99]. A ROI for the hippocampus entorhinal cortex is represented in Fig.B.11 of Appendix B.

The **occipital fusiform gyrus** is located in the temporal and occipital lobes. The occipital fusiform gyrus is known to be involved in higher visual information processing (e.g. object identification, face recognition and word recognition) [100]. However, the functions of the occipital fusiform gyrus are not yet totally established [100]. A ROI for the fusiform gyrus is represented n Fig.B.12 of Appendix B.

The prefrontal cortex is known to be involved in higher-order cognition and plays a role in memory and perception [101]. More specifically, the **frontal pole cortex** (or "Broadmann's area 10") is involved in social and emotional behaviour, mnemonic functions and anticipation and processing of outcomes [101]. The **superior frontal gyrus** is involved in working memory [102] and attention [103]. ROIs for the frontal pole cortex and the superior frontal gyrus are represented in Fig.B.13 and Fig.B.14 of Appendix B.

The **parahippocampal gyrus** is a cortical region close to the hippocampus. This region is known to be involved in episodic memory and visuospatial processing (e.g. scene perception, spatial representation and navigation) [104]. This cortical region also plays a role in emotional processing [104]. A ROI for the parahippocampal gyrus is represented in Fig.B.15 of Appendix B.

The **posterior cingulate cortex** is the caudal part of the cingulate gyrus. This region plays an important role in the retrieval of autobiographical memories [105]. The posterior cingulate cortex is also involved in the regulation of the focus of attention [105]. A ROI for the cingulate cortex is represented in Fig.B.16 of Appendix B.

The **hippocampus** is a structure in the temporal lobe [106]. The hippocampus is connected to the entorhinal cortex [106]. This structure is involved in memory, learning, spatial navigation and emotional behavior. It was proved that damages to the hippocampus may cause retrograde amnesia as well as anterograde amnesia [106]. The **amygdala** is a structure in the temporal lobe. The amygdala is involved in the regulation of emotions, recognition of facial expressions, recognition of emotions, perception of gaze direction, modulation of attention and memory [107]. ROIs for the hippocampus and the amygdala are represented in Fig.B.17 and Fig.B.18 of Appendix B.

Chapter 4

Analysis of structural brain changes in Alzheimer's disease

4.1 Methods

4.1.1 Subjects

Structural brain changes of three individuals were studied in this section: a 41-year-old healthy control without amyloid deposition, a 69-year-old MCI patient with amyloid deposition and a 70-year-old amyloid-positive patient with dementia. The amyloid status of each patient was determined by a lumbar puncture, a diagnostic tool that measures the concentrations of amyloid peptides and hyperphosphorylated tau proteins in the CSF.

4.1.2 Data acquisition

Anatomical and diffusion MRI images were acquired at St-Luc University Hospital on a 3T GE (Chicago, IL) SIGNA^{TM} Premier scanner, equipped with a 48-channel head coil. The anatomical images were obtained with gradient recalled echo MRI sequence with the following properties: repetition time (TR) = 2187.84 ms and echo time (TE) = 2.96 ms. The slice thickness was 1 mm and the voxel size was 1 x 1 x 1 mm^3. Diffusion MRI images were acquired with a PGSE sequence with the following properties: TR = 4842 ms and TE = 77.4 ms. A multi-shell diffusion scheme was used with the following acquisition protocol: a baseline with a b-value of 0 $[s \cdot mm^{-2}]$, a b-value of 1000 $[s \cdot mm^{-2}]$ (64 directions), a b-value of 2000 $[s \cdot mm^{-2}]$ (32 directions, with a b-value of 0 after 16 and 32 directions), a b-value of 3000 $[s \cdot mm^{-2}]$ (32 directions, with a b-value of 0 after 16 and 32 directions) and a b-value of 5000 $[s \cdot mm^{-2}]$ (32 directions, with a b-value of 0 after 16 directions). The gradient intensities were 30.8, 43.55, 53.34 and 68.86 $[mT/m]$ for the shells with b-values of respectively 1000, 2000, 3000 and 5000 $[s \cdot mm^{-2}]$. The FOV was 220 x 220 mm^2, the in-plane matrix size was 256 x 256 and the data contained 68 axial slices with 2-mm thickness (no inter-slice gap), leading to a voxel size of 0.8594 x 0.8594 x 2 mm^3. A multi-slice excitation scheme was used during the acquisition with a hyperband slice factor of 3 to reduce the acquisition time. The duration of the diffusion gradients pulses (δ) was 23.824 ms and their onset separation (Δ) was 35.66 ms.

4.1.3 Image processing

Image format and corrections

Some of the images were obtained in the Digital Imaging and Communications in Medicine (DICOM) format and were therefore converted into the Neuroimaging Informatics Technology Initivative (NIFTI) format with the MRIcroGL software[1]. The gradient design tools of the scanner enabled the calculation of the induced currents [108]. The eddy currents were controlled and the geometric distortions due to the eddy currents were minimized by the system [108]. Therefore, no further processing was done to remove them. The motion correction was achieved with FMRIB

1 https://nitrc.org/projects/mricrogl

Software Library[2] (FSL), a software for MRI data analysis written in C++ by the FMRIB Analysis group from Oxford University. The motion correction was realized with the "eddy_correct" command that registered all the volumes acquired with the first b_0 image. The "fdt_rotate_bvecs" FSL command was used to rotate the original gradient orientations according to the transformation matrices computed during the motion correction step.

DTI maps

DTI (Diffusion Tensor Imaging) maps were obtained with FSL. First, the brain was extracted from the raw diffusion data with the Brain Extraction Tool (BET) and a binary mask of the brain was saved for the computation of DTI maps. The DTIFIT Reconstruct Diffusion Tensors plug-in was then used to compute DTI maps based on the new rotated "bvec" file and the motion corrected diffusion data. The maps computed were: the fractional anisotropy map, the mean diffusivity map, the axial diffusivity map (L1) and the radial diffusivity map (a combination of two output maps computed as (L2+L3)/2).

NODDI maps

NODDI (Neurite Oritentation and Dispersion Density Imaging) maps were obtained with the Quantitative Imaging Toolkit[3] (QIT), a software package implemented with a combination of Java and Python. The maps were obtained with the VolumeNoddiFit module that required the diffusion data, the gradient directions, a binary mask of the brain and the b-values. For the computation of the maps, this model considered an isotropic compartment with a diffusivity of $3 \cdot 10^{-3}$ $[mm^2 s^{-1}]$ and a compartment for the extra-neurite space with an axial diffusivity of $1.7 \cdot 10^{-3}$ $[mm^2 s^{-1}]$.

DIAMOND maps

DIAMOND (DIstribution of 3D Anisotropic MicrOstructural eNvironments in Diffusion-compartment imaging) maps were created with the research code implemented by B. Scherrer [4]. First, brain masks were created and used for computation time savings. The maximum number of fascicles per voxel was set to 2. The AICU automatic model selection was used to determine the number of fascicles in each voxel. A compartment representing the restricted isotropic diffusion was considered. The diffusivity of that compartment is computed from the data and is not necessarily the diffusivity of free water molecules at 37° ($3 \cdot 10^{-3}$ $[mm^2 s^{-1}]$).

Microstructure Fingerprinting maps

This model estimates brain tissue properties based on a dictionary of Monte Carlo MRI simulations. The maps were created with the research code implemented by G. Rensonnet, who also pre-computed the dictionary of Monte Carlo DW-MRI fingerprints. In this model, fascicles are represented by a hexagonal packing of straight and impermeable cylinders (representing the axons) with a cylinder radius ('r', interpreted as the apparent axonal radius index [32]) and a cylinder packing density ('f', interpreted as the axonal density index [32]). A 2-fascicle model was considered and dictionaries composed of 931 atoms (N = 931) were created with Monte Carlo simulations and represent DW-MRI fingerprints for N different microstructural configurations. The number of possible microstructural configurations is defined by the number of candidate radii × the number of candidate packing density indices defined when discretizing the Ω-space (i.e. the space of microstructural parameters) justified by tissue biology [32]. One considered 24 possible values of apparent axonal radius and 40 values of axonal density. Out of 960 possible microstructural configurations (24x40), 29 unrealistic configurations were discarded due to the lack of space allowed between the axons, yielding to 931 possible microstructural configurations. A compartment representing the restricted isotropic diffusion (a "ball"-like compartment) was considered and a dictionary composed of the fingerprints for 10 different microstructural properties (M = 10, representing 10 possible values for the diffusivity of the compartment) were computed with Monte Carlo

2 https://fsl.fmrib.ox.ac.uk
3 http://cabeen.io/qitwiki
4 Benoit Scherrer, Computational Radiology Laboratory (CRL), Boston Children's Hospital, 2018.

MRI simulations. For computation time savings, that compartment was considered and included when solving of the sparse optimization problem only when 0 or 1 fascicle was estimated in the voxel. This compartment was therefore not included when 2 fascicles were estimated in the voxel. Indeed, considering a 2-fascicle model with a compartment for the restricted isotropic diffusion requires solving $N^2 \cdot M$ or 8667610 sub-problems with 3 variables.

4.1.4 Image analysis

A multi-scale study, composed of four different types of analyses, was conducted to evaluate changes that occurred in the MCI patient and the patient with dementia compared to the healthy control. Each analysis has advantages and limitations, making them complementary. The principles (methods, advantages and limitations) of each analysis is described in this section. The set of analyses performed in this study is represented in Fig.4.1.

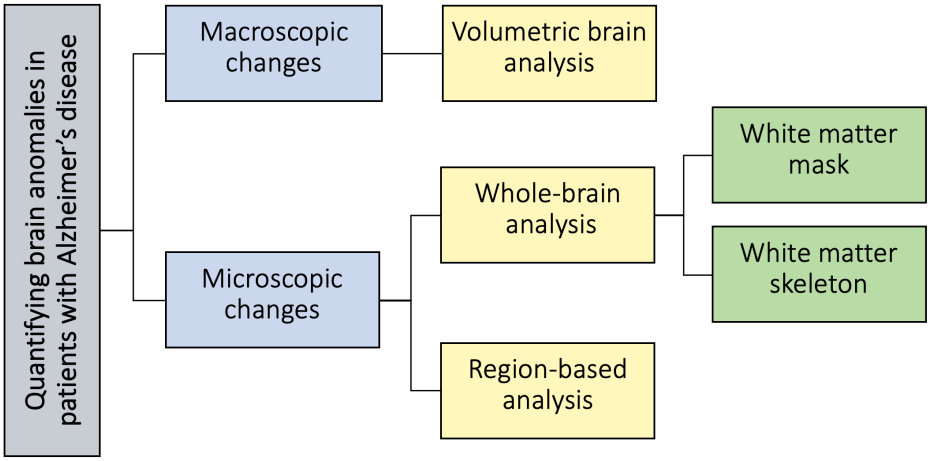


Figure 4.1: Set of analyses conducted to quantify brain anomalies in patients with AD.

Macrostructural changes : volumetric brain analysis

A volumetric brain analysis gives an overview of the macroscopic changes that occurred in different types of tissues in the AD group compared to the healthy control. A volumetric analysis report was obtained with the "volBrain" tool [109], an MRI brain volumetry system that performs segmentation and computes the volume of different structures and types of tissues based on T1-weighted images.

Microsutructural changes : whole-brain white matter analysis

This analysis aims at finding microstructural changes that occurred in the WM of the MCI patient and the patient with dementia. In order to avoid wrong interpretations of the metrics in the WM, two different analyses were performed in the whole-brain WM for each patient: an analysis based on a patient specific WM mask and an analysis based on an alignment-invariant WM skeleton (as represented in Fig.4.2). Each analysis has advantages and limitations that are discussed here.

(a) *Analysis based on a patient specific white matter mask* - In this analysis, box plots of the models' metrics in the WM of each patient are represented. A WM mask was created based on anatomical images of the patients with FSL. First, the brain was extracted from the anatomical images with the BET tool. The FAST segmentation tool was then used to segment the T1-weighted brain images and create a patient specific WM mask. The diffusion maps investigated were then registered with the anatomical images of the brain using the FLIRT linear registration tool. The values of the metrics in the WM were extracted by computing the intersection of the binary mask with the diffusion maps after registration.

Advantages - This analysis gives an overview of changes that occurred in the whole-brain WM in each patient based on a patient specific mask.

Limitations - This analysis does not highlight specific regions of the WM where abnormal values are observed in the AD patients compared to the healthy control. Indeed, a comparison between the subjects is complicated since each mask is patient specific. By considering the entire WM, models' metrics are also evaluated in voxels with highly variable and crossing fascicles. It is known that models such as DTI and NODDI were not designed for characterizing the diffusion in voxels with crossing fascicles. The metrics estimated may be biased and not interpretable due to the crossing fibers in the voxels. For example, crossing fibers will be modeled by a large diffusion tensor with DTI, that does not reflect the "real" diffusion in each fiber. Therefore, another analysis that characterizes metrics in regions where those models performs fairly well is needed. Finally, this analysis based on patient specific WM masks uses a registration step to align the diffusion maps with the anatomical images and may suffer from registration errors.

(b) *Analysis based on an alignment-invariant white matter skeleton* - This analysis aims at highlighting differences along a WM skeleton mainly[5] composed of voxels with coherently aligned axons. This skeletonized WM prevents inter-subject variability since the skeleton is alignment-invariant and therefore not sensitive to registration errors. The skeletonized WM tract was created according to the steps used in the Tract-Based Spatial Statistics (TBSS) method [110]. This analysis was performed with FSL. The TBSS method can be decomposed into different steps. First, a nonlinear registration into a standard space (MNI152) was performed on the subjects' FA maps. Second, a mean FA map is created as the average of the subjects' registered FA maps. The mean FA map is generated to create a tract skeleton (the "mean FA skeleton") that is common to all subjects. A skeletonized step is then performed and searches for the center of the fiber bundles (i.e. considered as the voxels with the largest FA) on the mean FA map to obtain the mean FA skeleton. A 0.3-threshold was then applied to the skeleton in order to remove the voxels with a non-reliable correspondence between the subjects. Therefore, the noise due to misalignment of subjects' maps and the noise in the mean FA map due to the small number of subjects were removed [111]. The WM skeleton obtained can be observed in Fig.4.2B. In the next step, the registered FA images of the subjects are projected onto the mean FA skeleton. This is done by searching perpendicularly (with a constraint of distance) to the FA skeleton, for each voxel of the skeleton, the maximum FA value and assign that value to the voxel of the skeleton. This enables a voxelwise comparison of the subjects without needing a perfect registration of the maps. Indeed, only voxels in the WM that have been "successfully aligned across subjects" [111] will be analyzed. Once the WM skeleton was created, box plots of the metrics along the skeleton were represented for each subject. Due to the small number of subjects, the last step of the TBSS analysis that consisted in carrying voxelwise statistics was not performed. Instead, when a non-negligible difference in the mean metric was observed between the healthy control and the patients (in the box plots), the regions that showed an abnormal metric (e.g. decreased FA, etc.) along the skeleton were highlighted. Although this first TBSS analysis for the FA maps is needed to create the skeleton, this analysis can be extended to other map metrics (e.g. MD, ODI, etc.). The projection vectors were computed during the TBSS analysis of the FA maps and are used to project values of other metrics onto the mean FA skeleton. Therefore, a TBSS analysis of FA is compulsory before conducting non-FA TBSS analyses. The FSL "tbss_non_FA" command performs all the steps needed (i.e. registration and projection) to create the skeletonized map of non-FA metrics for each patient.

Advantages - In this analysis, alignment problems that may have occurred during the registration step are alleviated by opposition to the previous analysis. This is done by projecting the diffusion metrics onto an alignment-invariant tract representation, after a registration step. Therefore, TBSS "aims to improve the sensitivity, objectivity and interpretability of analysis of multi-subject diffusion imaging studies" [110]. By applying a threshold on the skeleton, voxels in coherently aligned axons are kept. Therefore, in most voxels that belong to the skeleton, the hypothesis of single-fascicle models (e.g. DTI and NODDI) are met. Once the skeleton maps are created, a voxelwise comparison of the patients can be performed since only voxels with good correspondences across subjects were kept. This voxelwise comparison highlights regions of the skeleton that show

5 Although some voxels with crossing fibers belong to the WM skeleton (e.g. in the corona radiata, where the intersection of the corpus callosum, the corticospinal tract and the superior longitudinal fasciculus occurs), most of the skeleton is composed of coherently aligned axons that show a good correspondence between the subjects.

abnormal metrics. Moreover, this analysis does not need pre-defined tracts of interest where the metrics have to be evaluated since those metrics are evaluated along the whole-brain skeletonized WM.

Limitations - Although this was an advantage for one-fascicle models, diffusion metrics are only analyzed in highly aligned fascicles, while multi-fascicles models can investigate metrics in voxels with crossing fascicles with accuracy.

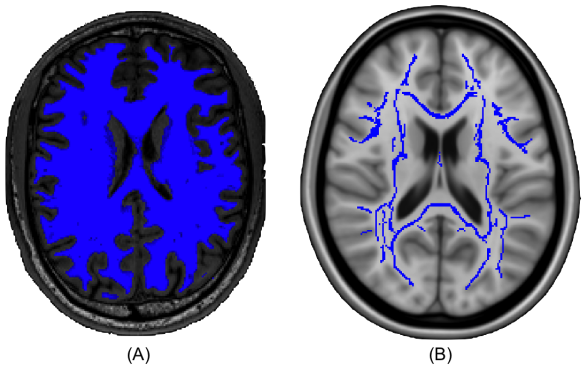


Figure 4.2: Whole brain white matter analysis conducted with (A) a patient specific white matter mask (the mask of the healthy control was represented here) created by segmentation of the anatomical images and (B) an alignment-invariant white matter skeleton, common to all subjects, created with the TBSS method (the skeleton was superimposed onto the standard MNI152).

Microsutructural changes : region-based analysis

A ROI-based analysis was conducted to better characterize microstructural differences between the healthy control, the MCI patient and the patient with dementia. By opposition to the previous analyses that evaluated the differences in models' metrics in the whole-brain WM, this ROI-based analysis was performed to represent box plots of the metrics in regions known to be affected by AD. Indeed, the metrics of the models were evaluated in various WM regions known to be affected by AD and that were mentioned in previous studies. The WM tracts of interest were discussed in section 3.2.3 and can be visualized in Appendix B. The WM tracts considered are: the fornix, the corpus callosum (genu, body and splenium), the cingulum (the cingulate gyrus part and the parahippocampal part), the posterior thalamic radiation, the superior longitudinal fasciculus, the superior corona radiata, the forceps minor and the uncinate fasciculus. In the region-based analysis, the model maps were registered with the FSL standard MNI "MNI152_T1_2mm_brain", defining a standard space for a better inter-subjects comparison. The registration was performed with FLIRT Linear Registration tool using an affine 12-parameter model. A mask for each ROI was extracted from FSL's available Atlases in a NIFTI format. The Atlases used to localize ROI of the WM were the JHU White-Matter Tractography Atlas and the Juelich Histological Atlas. Changes highlighted in the ROI-based analysis are then compared to the changes observed in the skeleton-based analysis to determine whether changes are also observed in the same regions along the skeletonized WM. When regions were highlighted in both analyses, possible function impairments were discussed. Although the primary purpose of this region-based analysis was to evaluate microstructural changes in ROI of the WM, a supplementary analysis was performed and evaluated the metrics in GM (cortical and subcortical) ROI. This analysis can be found in Appendix D.2.

Advantages - This analysis represents box plots for each ROI. This enables a thorough comparison of how metrics are changed in different ROI.

Limitations - A comprehensive survey is needed to determine the tracts of interest on which the analysis will be performed. This pre-specification of ROI is a limitation since the entire brain is not investigated. Moreover, misregistrations may lead to biased metrics evaluated in ROI. Finally, the ROI may include voxels with crossing-fascicles, where one-fascicle models are not performing optimally.

4.2 Macrostructural changes : volumetric brain analysis

Results This section aims at analyzing macrostructural changes in AD. The volumetric analysis report for the healthy control, the MCI patient and the patient with dementia is represented in Table 4.1. This volumetric brain analysis revealed important changes in the AD group compared to the healthy control. Macroscopic changes can be observed in segmented brain images as depicted in Fig.4.3. An increased CSF volume was observed in both AD patients (especially pronounced in the patient with dementia). A reduction of WM and GM volumes was also observed in the MCI patient and the patient with dementia compared to the healthy control with a decrease more pronounced in the patient with dementia.

Patient	Tissue type	Volume [cm^3]	Volume [%]
Healthy control (age: 41)	White matter	601.62	40.78
	Grey matter	710.07	48.13
	Cerebrospinal fluid	163.73	11.1
	Intracranial cavity	1475.41	100
MCI patient (age: 69)	White matter	404.13	30.84
	Grey matter	624.26	47.64
	Cerebrospinal fluid	282.12	21.53
	Intracranial cavity	1310.5	100
Patient with dementia (age: 70)	White matter	374.71	26.88
	Grey matter	619.16	44.42
	Cerebrospinal fluid	400.07	28.7
	Intracranial cavity	1393.94	100

Table 4.1: Volumetric brain analysis report of the healthy control, the MCI patient and the patient with dementia.

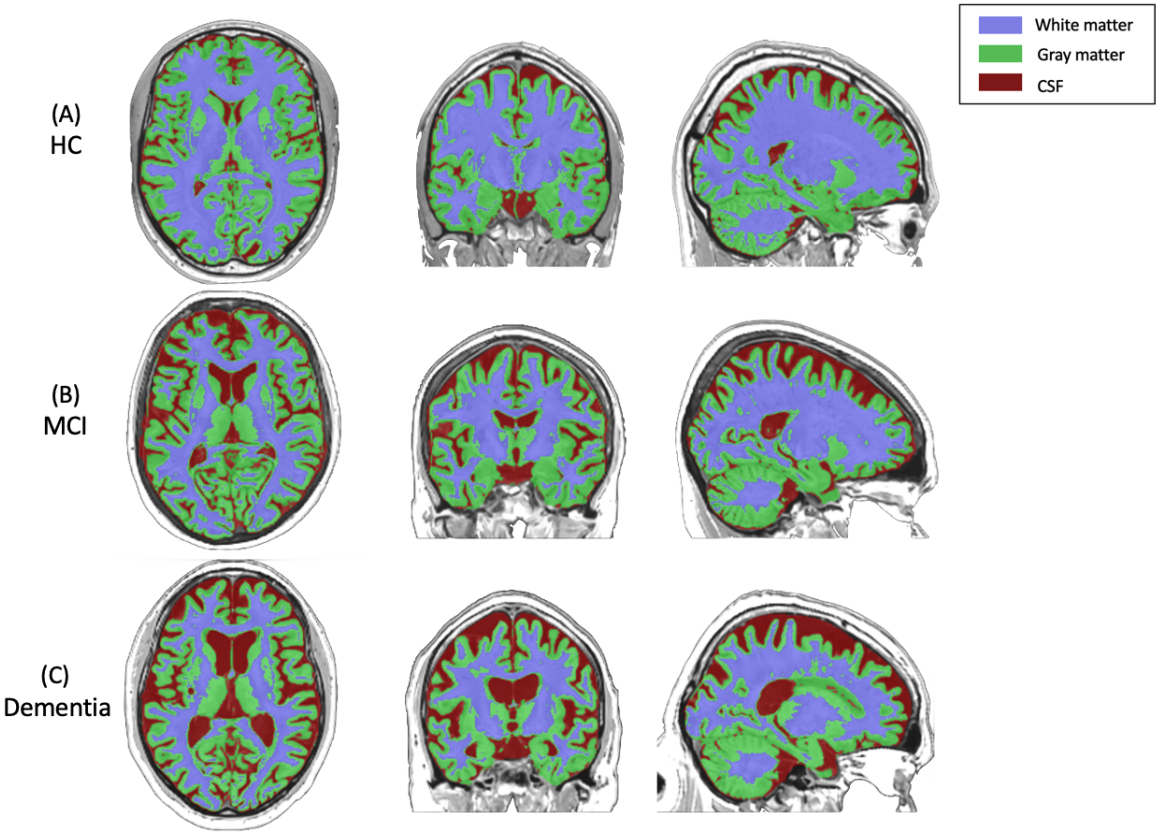


Figure 4.3: Tissue segmentation of (A) the healthy control, (B) MCI patient and (C) patient with dementia obtained with volBrain. The red color indicates the CSF, the green color indicates the GM and the purple color indicates the WM.

Discussion Macroscopic changes were observed in the MCI patient and the patient with dementia, with changes constantly larger in the patient with dementia. Those macroscopic changes therefore reflected the stage of the disease. The age of the MCI patient (69 years) and the patient with dementia (70 years) were close. Therefore, microstructural differences observed between those two patients were mainly due to the different clinical stages of the disease. Although the macroscopic changes observed in the AD patients are mainly due to the disease, the difference of age between the healthy control (41 years) and the AD patients (69 and 70 years) may have influenced the extent of the macrostructural differences observed.

4.3 Microstructural changes : DTI

The DTI metrics analyzed in this section are: the Fractional Anisotropy (FA), the Mean Diffusivity (MD, expressed in mm^2/s), the Axial Diffusivity (AxD, expressed in mm^2/s) and the Radial Diffusivity (RD, expressed in mm^2/s). More detailed information about DTI metrics can be found in section 2.2.1 *(Chapter 2 - Microstructural models - DTI).*

4.3.1 Whole-brain white matter analysis : results

Analysis based on a patient specific white matter mask

DTI metrics were evaluated in the WM of each patient, based on WM masks created by segmentation of T1-weighted images. Box plots of DTI metrics in the WM of each patient are represented in Fig.4.4 where the mean value of the metric in the WM was annotated. One can observe a decreased mean FA, increased mean MD, increased mean AxD and increased mean RD in the MCI patient and the patient with dementia compared to the healthy control. Changes in DTI metrics were constantly more pronounced in the patient with dementia than in the MCI patient.

Analysis based on an alignment-invariant white matter skeleton

The results of the skeleton-based analysis are represented in Fig.4.5, where the mean value of the metric in the entire skeleton was annotated. Although no decreased FA was observed in the MCI patient compared to the healthy control, a decreased FA was observed in the patient with dementia. Both AD patients showed an increased MD and AxD. A small increased RD was observed in the patient with dementia but was negligible in the MCI patient. The regions of the skeleton showing a decreased FA (in the patient with dementia), an increased MD (in both AD patients), an increased AxD (in both AD patients) and an increased RD (in the patient with dementia) are represented in Fig.4.6.

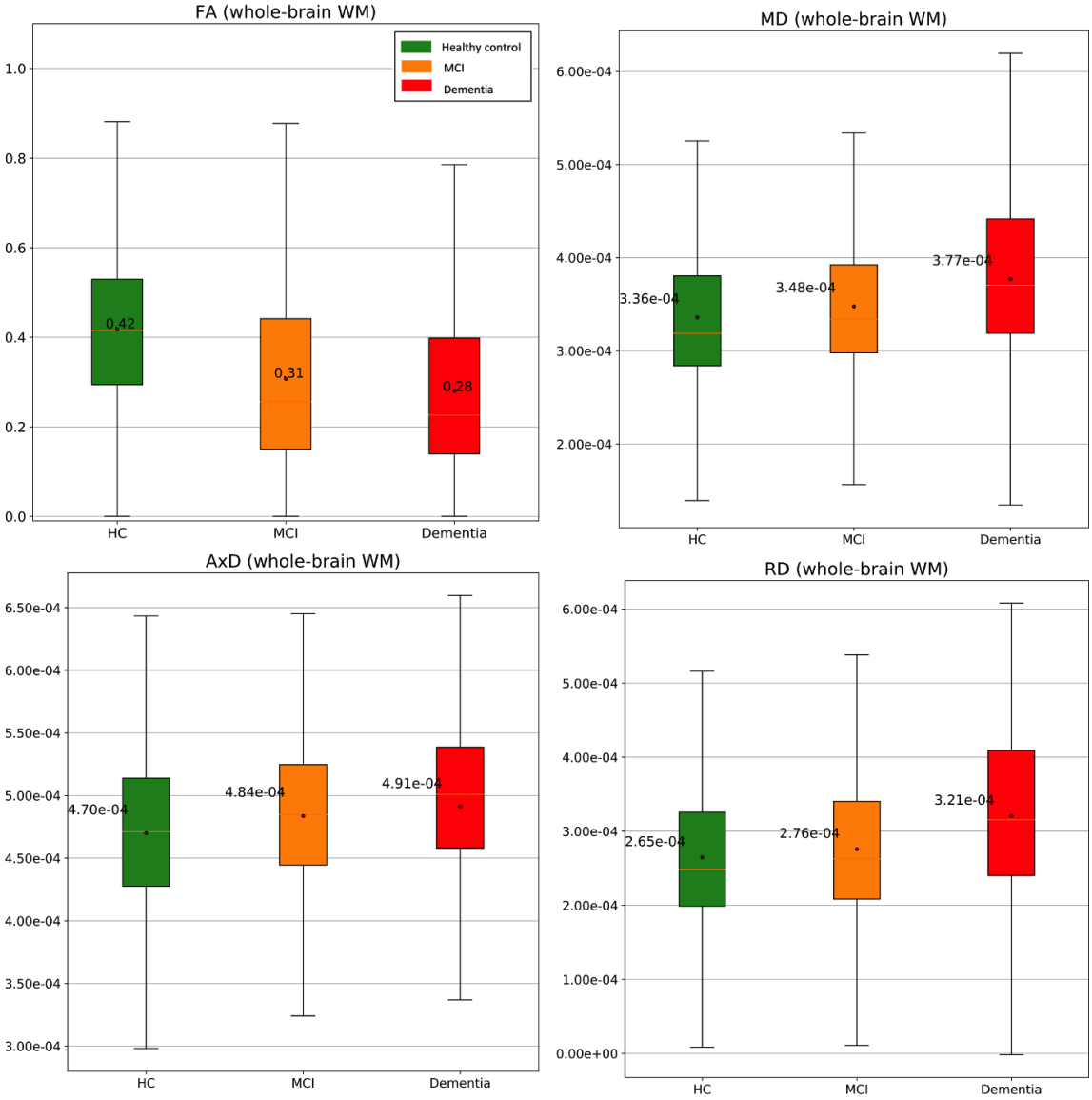


Figure 4.4: Box plots of DTI metrics (FA, MD, AxD and RD) in the white matter (a patient specific white matter mask was created by segmentation of anatomical images) of the healthy control (HC), the MCI patient and the patient with dementia. Diffusivities are expressed in mm^2/s. The horizontal orange line represents the median of the distribution and the black marker represents the mean metric.

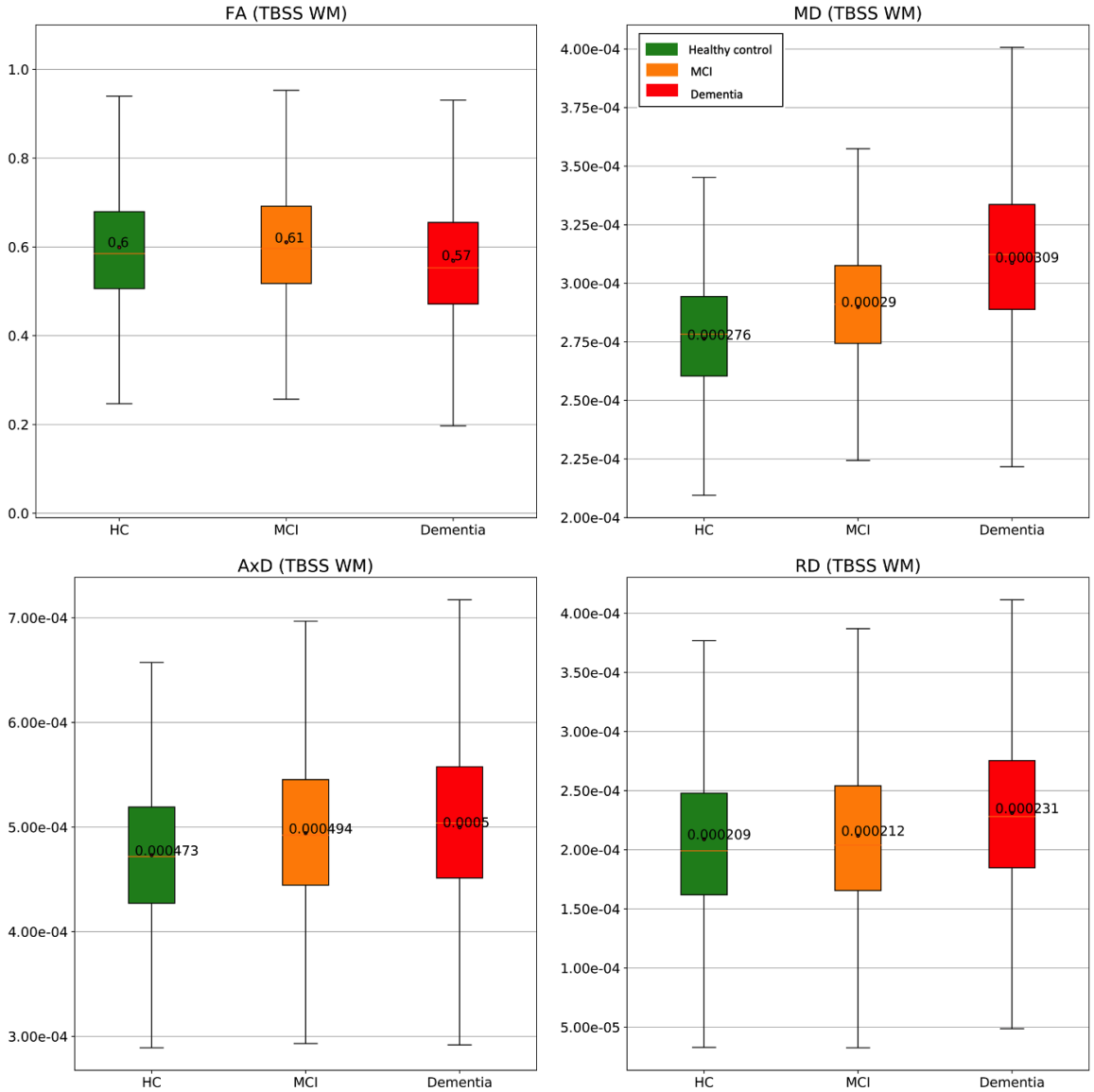


Figure 4.5: Box plots of DTI metrics (FA, MD, AxD and RD) in the white matter (on an alignment-invariant skeleton) of the healthy control (HC), the MCI patient and the patient with dementia. The horizontal orange line represents the median of the distribution and the black marker represents the mean metric.

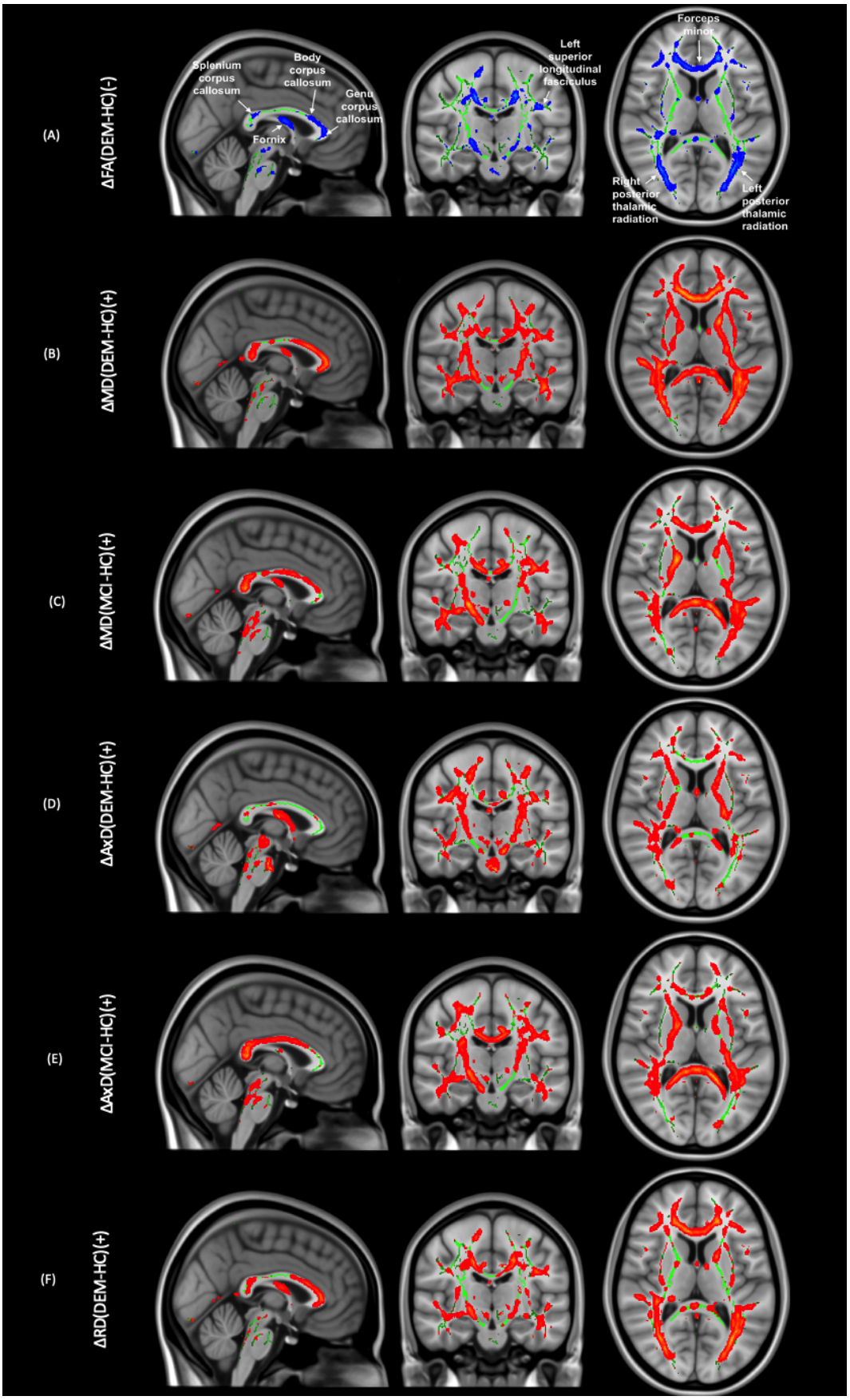


Figure 4.6: Regions of the skeleton showing (A) a decreased FA in the patient with dementia (DEM) compared to the healthy control (HC), (B) an increased MD in the patient with dementia, (C) an increased MD in the MCI patient, (D) an increased AxD in the patient with dementia, (E) an increased AxD in the MCI patient and (F) an increased RD in the patient with dementia.

4.3.2 Region-based analysis : results

The results of this ROI-based analysis evaluating the FA, MD, AxD and RD in regions known to be affected by AD are respectively represented in Fig.4.7, 4.8, 4.9 and 4.10. The results of the DTI metrics in regions mildly affected by AD can be found in Appendix D.

Some tracts were showing an abnormal diffusion metric while the other diffusion metrics were not affected. A decreased mean FA was observed in AD patients compared to the healthy control in the fornix, the corpus callosum (genu, body and splenium), the right posterior thalamic radiation, the left superior longitudinal fasciculus, the left superior corona radiata, the forceps minor and the right uncinate fasciculus. In the cerebellar peduncles (regions that are mildly affected by AD), no decreased FA was observed (Appendix D.1.1). In fact, an opposite trend was observed, proving that patients in the AD group did not show "abnormal" FA values (i.e. lowered values) in that region.

An increased mean MD in the AD patients compared to the healthy control was observed in the corpus callosum (genu, body and splenium), the right cingulum (parahippocampal part), the left and right posterior thalamic radiations, the left superior longitudinal fasciculus, the left and right corona radiata and the left and right uncinate fasciculi.

An increased mean RD in the AD patients compared to the healthy control was found in the fornix, the corpus callosum (genu and splenium), the right cingulum (parahippocampal part), the right posterior thalamic radiation, the left superior longitudinal fasciculus, the left and right superior corona radiata and the left and right uncinate fasciculi. In the region relatively spared by the disease (i.e. the cerebellar peduncles), no difference in RD was observed. An opposite trend (i.e. a decreased RD) was even observed in the inferior cerebellar peduncle of the AD group.

Finally, an increased mean AxD was observed in the AD group in the corpus callosum (body and splenium), the right cingulum (cingulate gyrus part and parahippocampal part), the left cingulum (cingulate gyrus part), the left and right posterior thalamic radiations, the left and right superior longitudinal fasciculi and the right superior corona radiata. Although a small increased AxD was observed in the cerebellar peduncle of the MCI patient, no increase was observed in the cerebellar peduncles of the patient with dementia.

The regions highlighted in this ROI-based analysis showing a decreased FA, increased MD, increased RD and/or increased AxD also showed changes in those metrics in the skeleton-based analysis in the MCI patient and/or the patient with dementia. However, by opposition to the ROI-based analysis, a decreased FA in the splenium of the corpus callosum, a decreased FA in the left and right cingulum (cingulate gyrus part), an increased MD in the right cingulum (the parahippocampal part) and an increased RD in the right uncinate fasciculus were observed in the patient with dementia in the skeleton-based analysis.

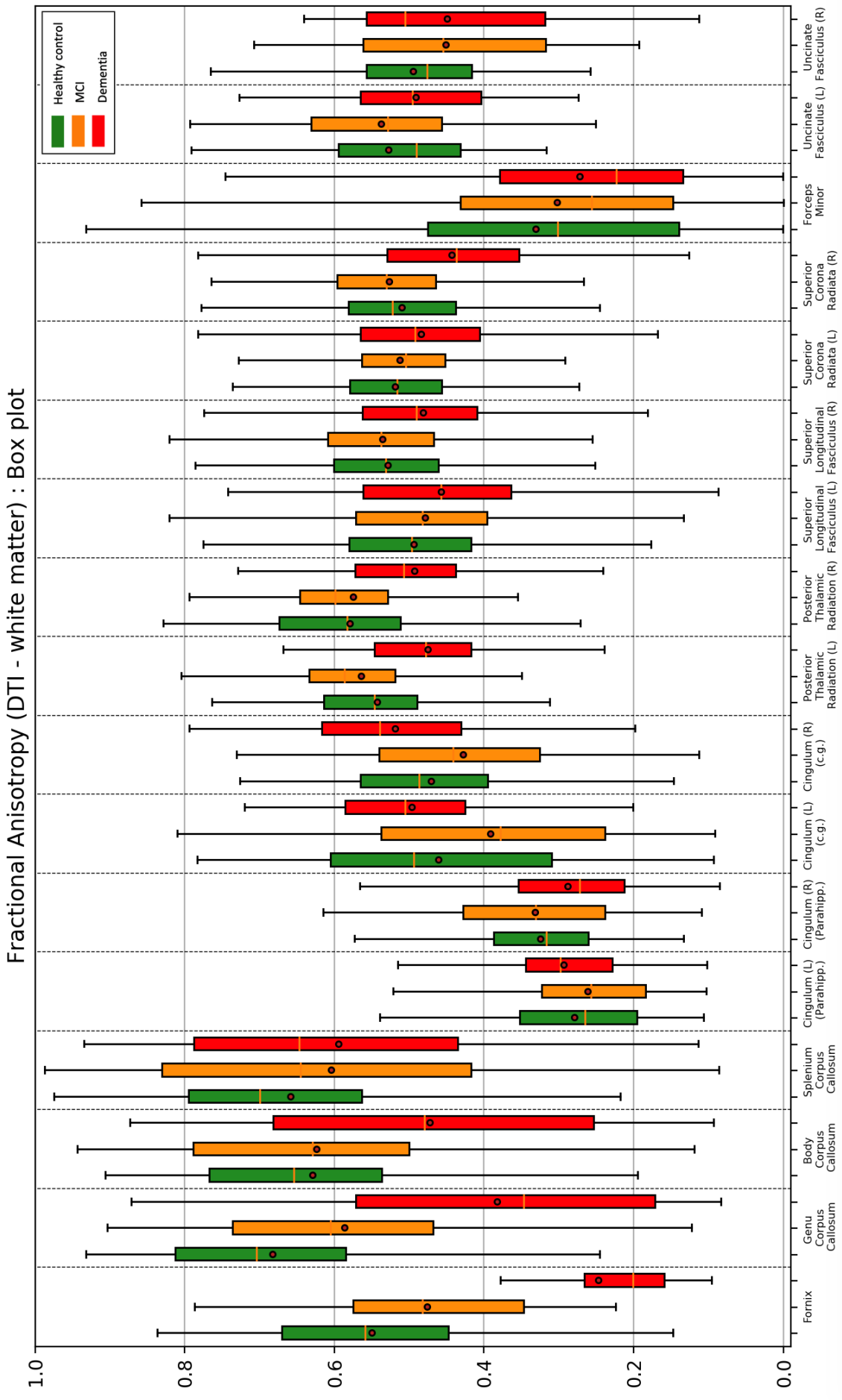


Figure 4.7: Box plot of the fractional anisotropy in regions of interest for the healthy control (green), the MCI patient (orange) and the patient with dementia (red). The horizontal orange line represents the median of the distribution and the black marker represents the mean FA in the tract of interest. From left to right, the tracts of interest are: fornix, genu of corpus callosum, body of corpus callosum, splenium of corpus callosum, left cingulum (parahippocampal part), right cingulum (parahippocampal part), left cingulum (cingulate gyrus part), right cingulum (cingulate gyrus part), left posterior thalamic radiation, right posterior thalamic radiation, left superior longitudinal fasciculus, right superior longitudinal fasciculus, left superior corona radiata, right superior corona radiata, forceps minor, left uncinate fasciculus, right uncinate fasciculus.

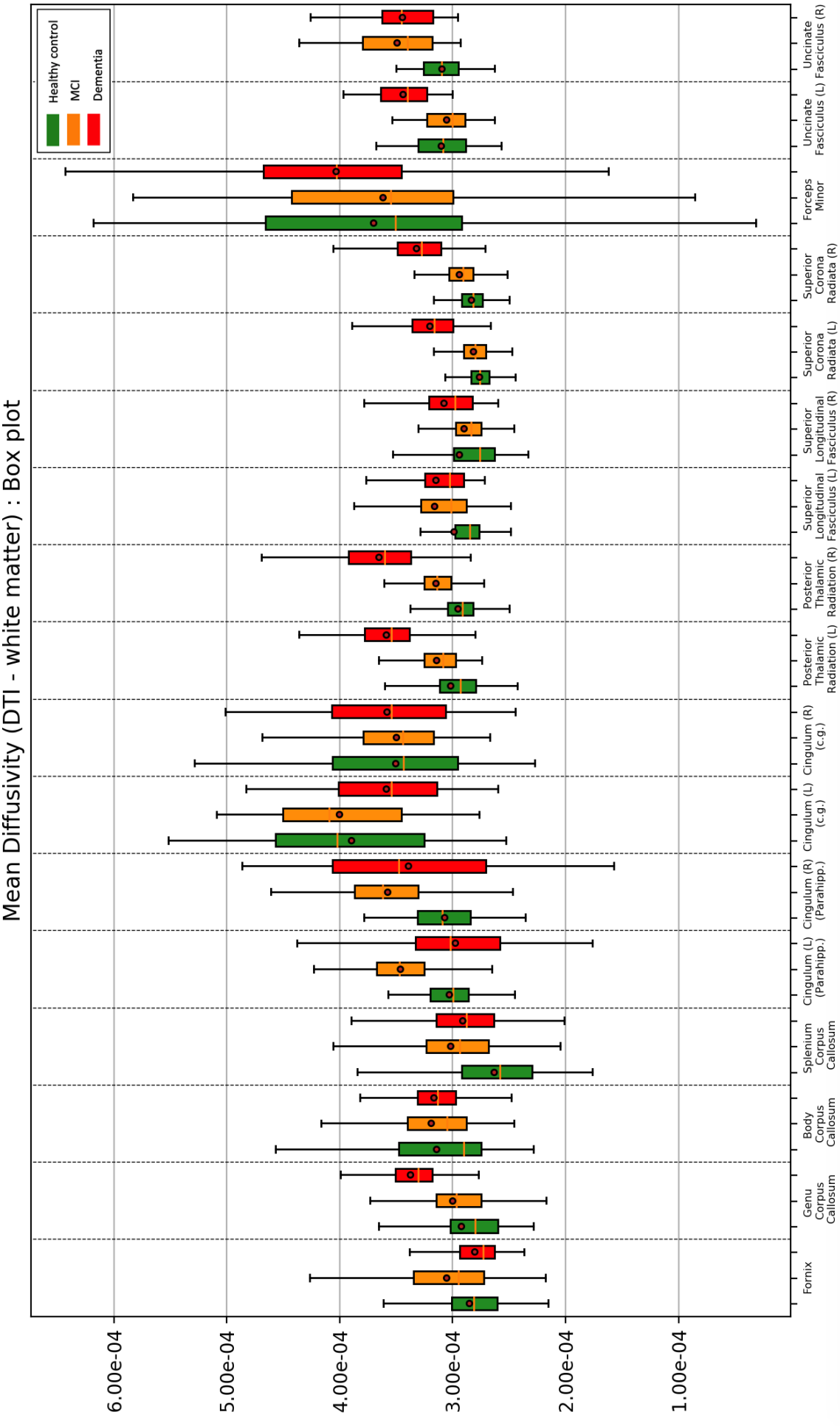


Figure 4.8: Box plot of the mean diffusivity in regions of interest for the healthy control (green), the MCI patient (orange) and the patient with dementia (red). The horizontal orange line represents the median of the distribution and the black marker represents the mean MD in the tract of interest. From left to right, the tracts of interest are: fornix, genu of corpus callosum, body of corpus callosum, splenium of corpus callosum, left cingulum (parahippocampal part), right cingulum (parahippocampal part), left cingulum (cingulate gyrus part), right cingulum (cingulate gyrus part), left posterior thalamic radiation, right posterior thalamic radiation, left superior longitudinal fasciculus, right superior longitudinal fasciculus, left superior corona radiata, right superior corona radiata, forceps minor, left uncinate fasciculus, right uncinate fasciculus.

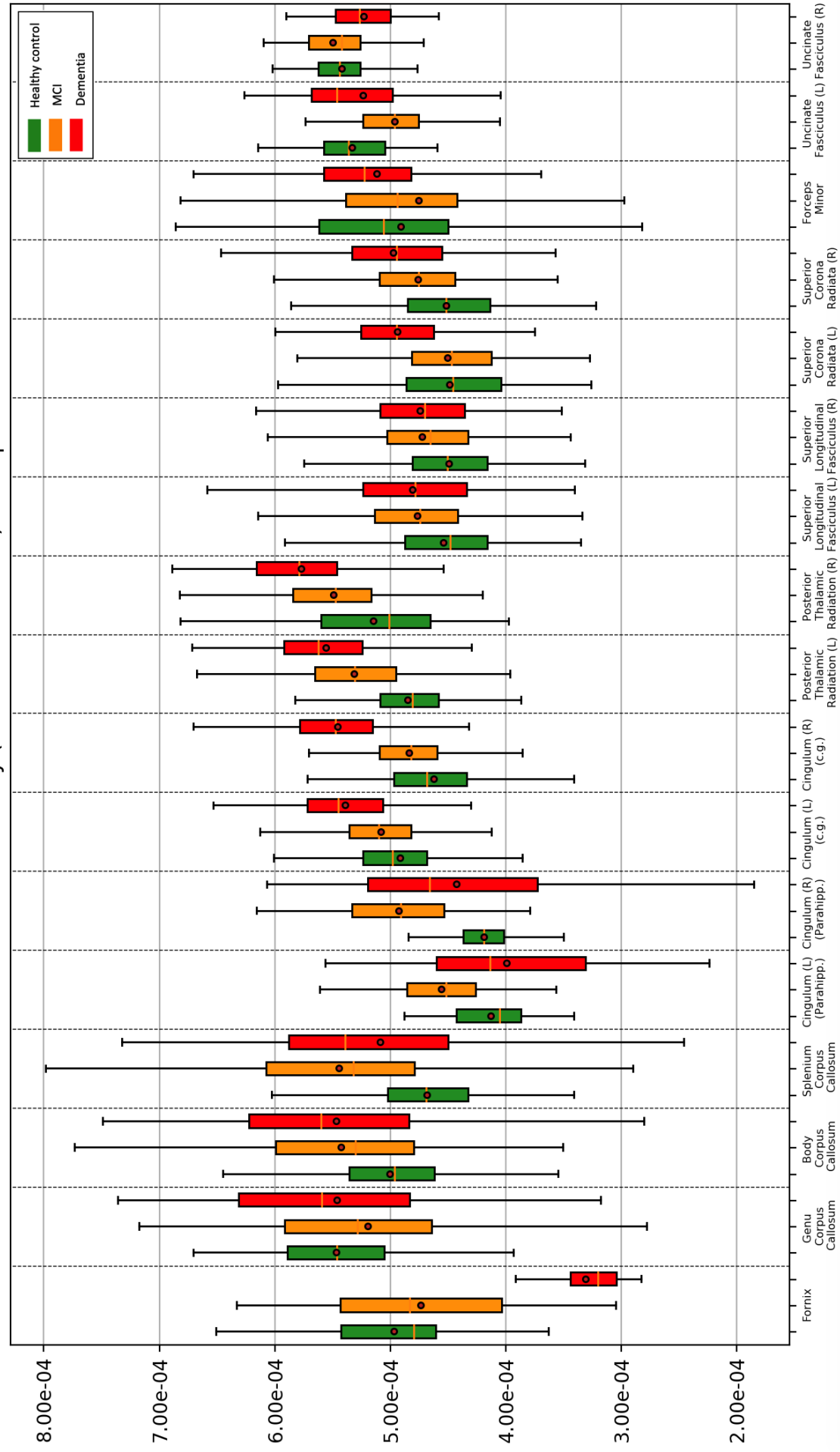


Figure 4.9: Box plot of the axial diffusivity in tracts of interest for the healthy control (pink), the MCI patient (blue) and the patient with dementia (beige). The horizontal orange line represents the median of the distribution and the black marker represents the mean AxD in the tract of interest. From left to right, the tracts of interest are: fornix, genu of corpus callosum, body of corpus callosum, splenium of corpus callosum, left cingulum (parahippocampal part), right cingulum (parahippocampal part), left cingulum (cingulate gyrus part), right cingulum (cingulate gyrus part), left posterior thalamic radiation, right posterior thalamic radiation, left superior longitudinal fasciculus, right superior longitudinal fasciculus, left superior corona radiata, right superior corona radiata, forceps minor, left uncinate fasciculus, right uncinate fasciculus.

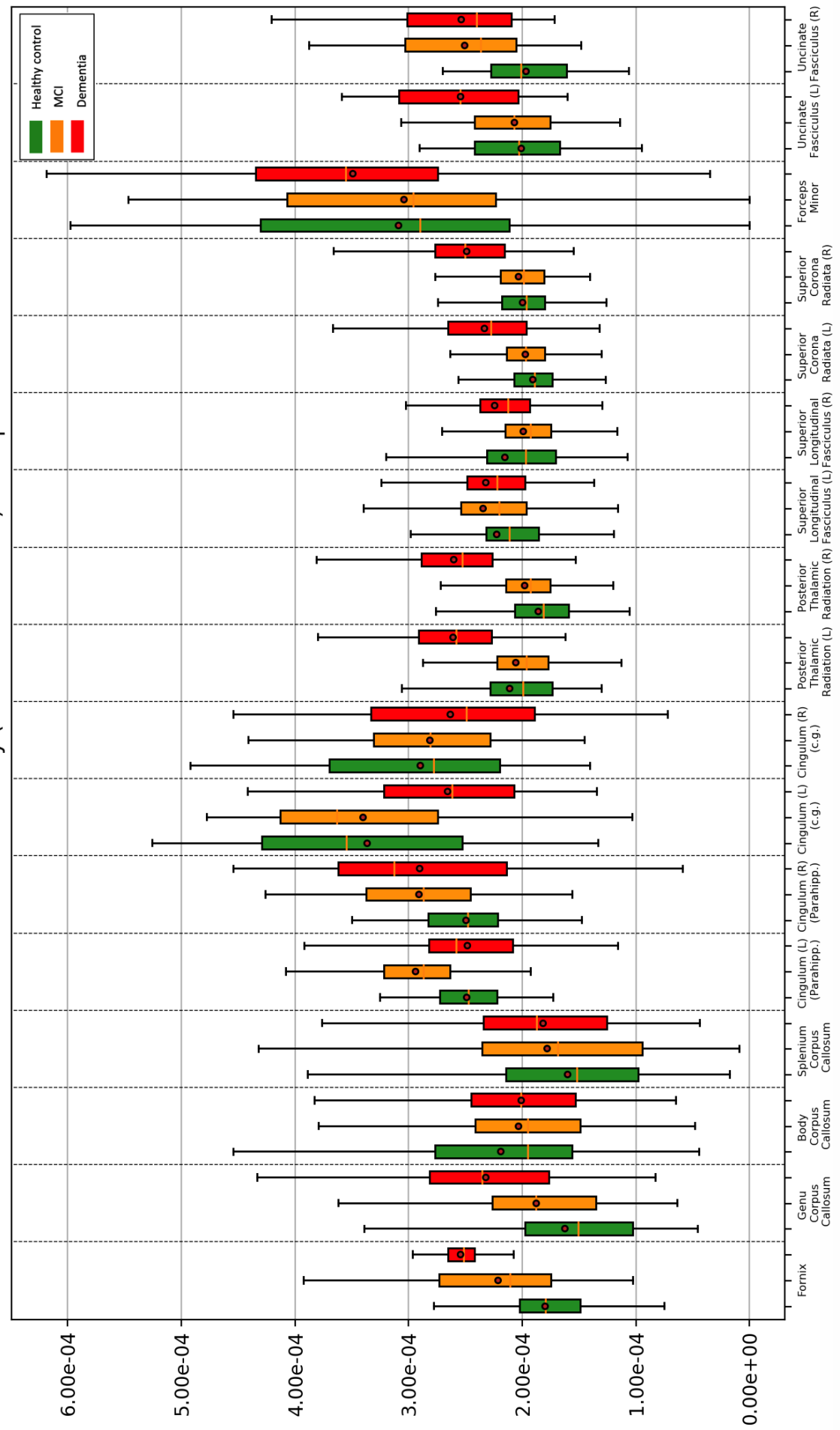


Figure 4.10: Box plot of the radial diffusivity in regions of interest for the healthy control (green), the MCI patient (orange) and the patient with dementia (red). The horizontal orange line represents the median of the distribution and the black marker represents the mean RD in the tract of interest. From left to right, the tracts of interest are: fornix, genu of corpus callosum, body of corpus callosum, splenium of corpus callosum, left cingulum (parahippocampal part), right cingulum (parahippocampal part), left cingulum (cingulate gyrus part), right cingulum (cingulate gyrus part), left posterior thalamic radiation, right posterior thalamic radiation, left superior longitudinal fasciculus, right superior longitudinal fasciculus, left superior corona radiata, right superior corona radiata, forceps minor, left uncinate fasciculus, right uncinate fasciculus.

4.3.3 Discussion

As expected, the whole-brain WM analysis that used a patient specific mask to extract values of diffusion metrics in the WM revealed a decreased FA, increased MD, increased AxD and increased RD in the AD patients compared to the healthy control. While DTI is suitable to characterize tissue properties of parallel fibers with a specific orientation, a defined diameter and a fixed degree of myelination [21], the tissue organization in every voxel is much more complex in most of the tracts. Therefore, the DTI metrics assigned in every voxel is an approximation of the structural parameters resulting from a complex tissue organization. In order to limit misinterpretations due to this limitation of the model, an analysis that evaluated the diffusion metrics along a WM skeleton was conducted. The skeleton was mainly composed of voxels with coherently aligned axons (to limit the influence of the voxels with crossing fibers). Except for the FA that was not decreased in the MCI patient in the skeleton-based analysis, the same trend of altered diffusion metrics was observed in the two analyses. The decreased FA in the MCI patient observed in the mask-based analysis has to be carefully considered and questioned since no decrease in FA was observed in the MCI patient when considering the entire WM skeleton mainly composed of one-fascicle voxels. The region-based analysis also confirmed the changes in diffusion metrics in regions known to be affected by AD, where changes were also observed in the skeleton-based analysis. As mentioned in [112], a decreased mean FA with an increased mean MD and an increased RD indicate axonal and myelin losses due to a chronic WM degeneration [112]. Changes in DTI metrics can be individually interpreted as: a decreased FA indicating a loss of tissue organization [20] ; an increased MD indicating a breakdown of neurobiological barriers (i.e. cell membrane deterioration) [20] ; a higher RD indicating a degradation of myelin sheaths [62] and a higher AxD that may reflect "a reduction in crossing fibers that results in a higher principal axis of diffusion because fibers running in other directions are no longer present" [62].

A summary of the functions of each tract can be found in Appendix C. The regions that showed abnormal DTI metrics in this ROI-based analysis and in the skeleton-based analysis are involved in a variety of cognitive functions. According to the results of the two analyses, a loss of tissue organization occurred in the patient with dementia in regions involved in the verbal and non-verbal coding in memory [79], the control of attention [80], the working memory [92] and the episodic memory [88]. A breakdown of neurobiological barriers occurred in the MCI patient and the patient with dementia (with a trend more pronounced in the patient with dementia), in WM bundles involved in many cognitive functions including: verbal and non-verbal coding in memory [79], transmission of sensory inputs [81], episodic memory, language [92], social processing [93], phonological processing and phonological retrieval [85]. A degradation of myelin sheaths occurred in regions involved in verbal fluency, word production [85] and working memory [88] in the MCI patient and the patient with dementia. Finally, a reduction in crossing fibers occurred in structures involved in the verbal and non-verbal coding in memory [79], attention, emotional behaviors [94] and working memory [85] in both patients. The patient with dementia showed larger differences in diffusion metrics with the healthy control than to the MCI patient with the healthy control in most of the regions showing abnormal metrics. Therefore, one can expect those functions to be more altered in the patient with dementia than in the MCI patient.

A recent study [113] suggested a "general reconsideration of the current interpretation of decreased diffusion anisotropy [...] as a marker of neuronal injury". This study conducted on murine brains depleted from microglia (treated with PLX5622) with "no known secondary effect on neurons or other neuroglial cell lines" [113] revealed significant changes in intracellular diffusion measures of the axonal integrity compared to control animals. The FA was significantly reduced in various regions of murine brain depleted from microglia, independently of biophysical alterations. Emerging evidence suggested the implication of microglia in chronic neurodegenerative disorders such as AD, involving a complex and highly dynamic microglial-mediated neuroinflammation [43, 44, 45, 46, 113, 61]. Since microglial density was proved to influence intracellular measures of diffusion anisotropy, the interpretation of DTI metrics may have to be carefully considered when assessing microstructural alterations in AD.

4.4 Microstructural changes : NODDI

The NODDI metrics that were analyzed are: the Orientation Dispersion Index (ODI), the Neurite Density Index (NDI) and the volume fraction of Gaussian isotropic diffusion (f_{iso}). More detailed information about NODDI metrics can be found in section 2.3.1 *(Chapter 2 - Microstructural models - NODDI)*.

4.4.1 Whole-brain white matter analysis : results

Analysis based on a patient specific white matter mask

Box plots of NODDI metrics evaluated in the WM of the subjects are represented in Fig.4.11. One can observe an increased ODI, decreased NDI and increased f_{iso} in the patient with dementia and the MCI patient compared to the healthy control. The changes in NODDI metrics were larger in the patient with dementia than in the MCI patient.

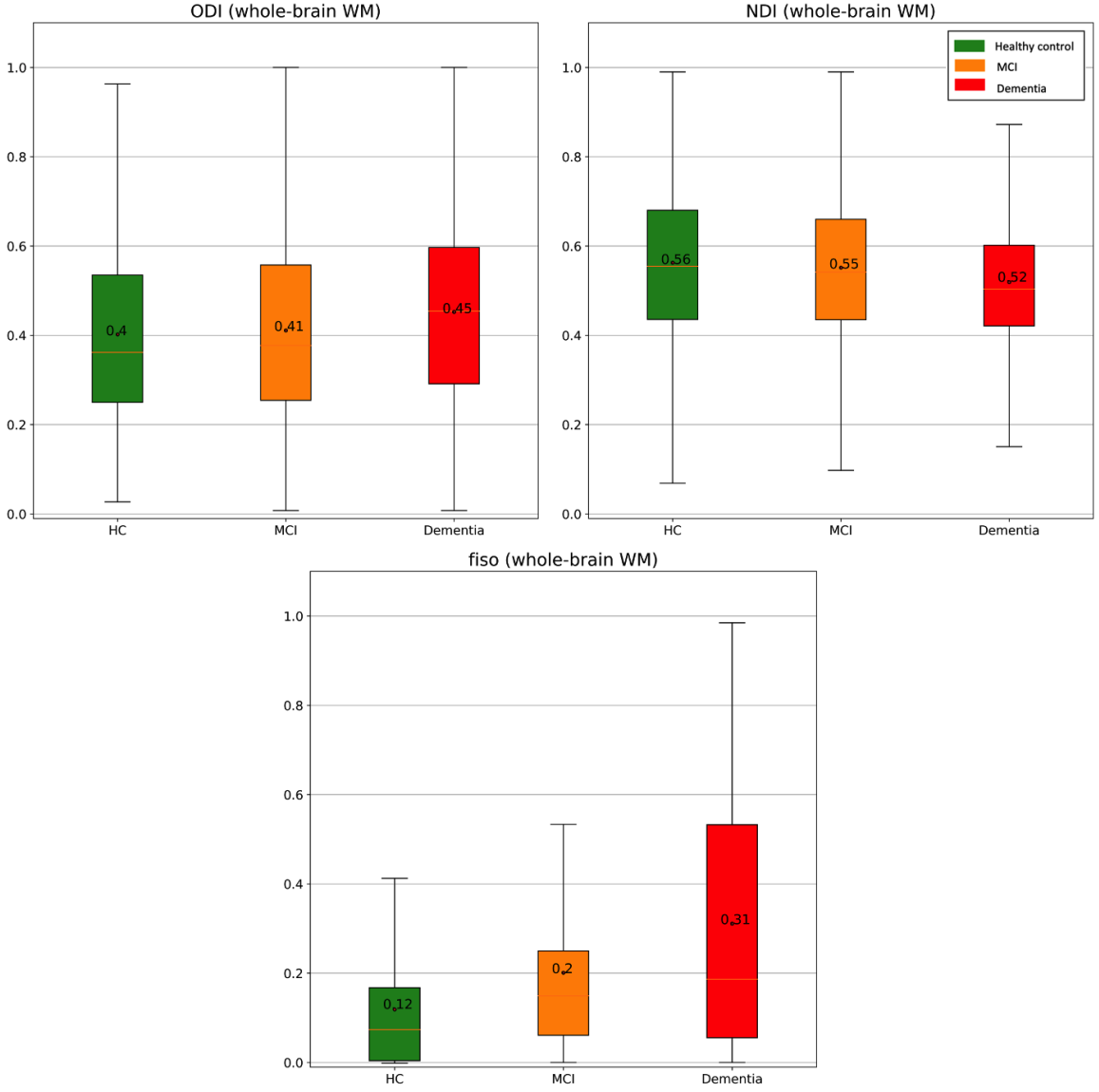


Figure 4.11: Box plots of NODDI metrics (ODI, NDI and f_{iso}) in the white matter (a patient specific white matter mask was created by segmentation of anatomical images) of the healthy control (HC), the MCI patient and the patient with dementia. The horizontal orange line represents the median of the distribution and the black marker represents the mean metric.

Analysis based on an alignment-invariant white matter skeleton

The results of the whole-brain WM analysis with the skeleton are represented in Fig.4.12. No difference in ODI values was observed in the skeleton between the healthy control and the AD patients. Both AD patients showed a decreased NDI and an increased f_{iso} compared to the healthy control. A similar increase in f_{iso} was observed in the MCI patient and the patient with dementia but the decrease in NDI was more pronounced in the patient with dementia than in the MCI patient. The regions of the skeleton showing a decreased NDI and an increased f_{iso} in the patient with dementia and the MCI patient are represented in Fig.4.13.

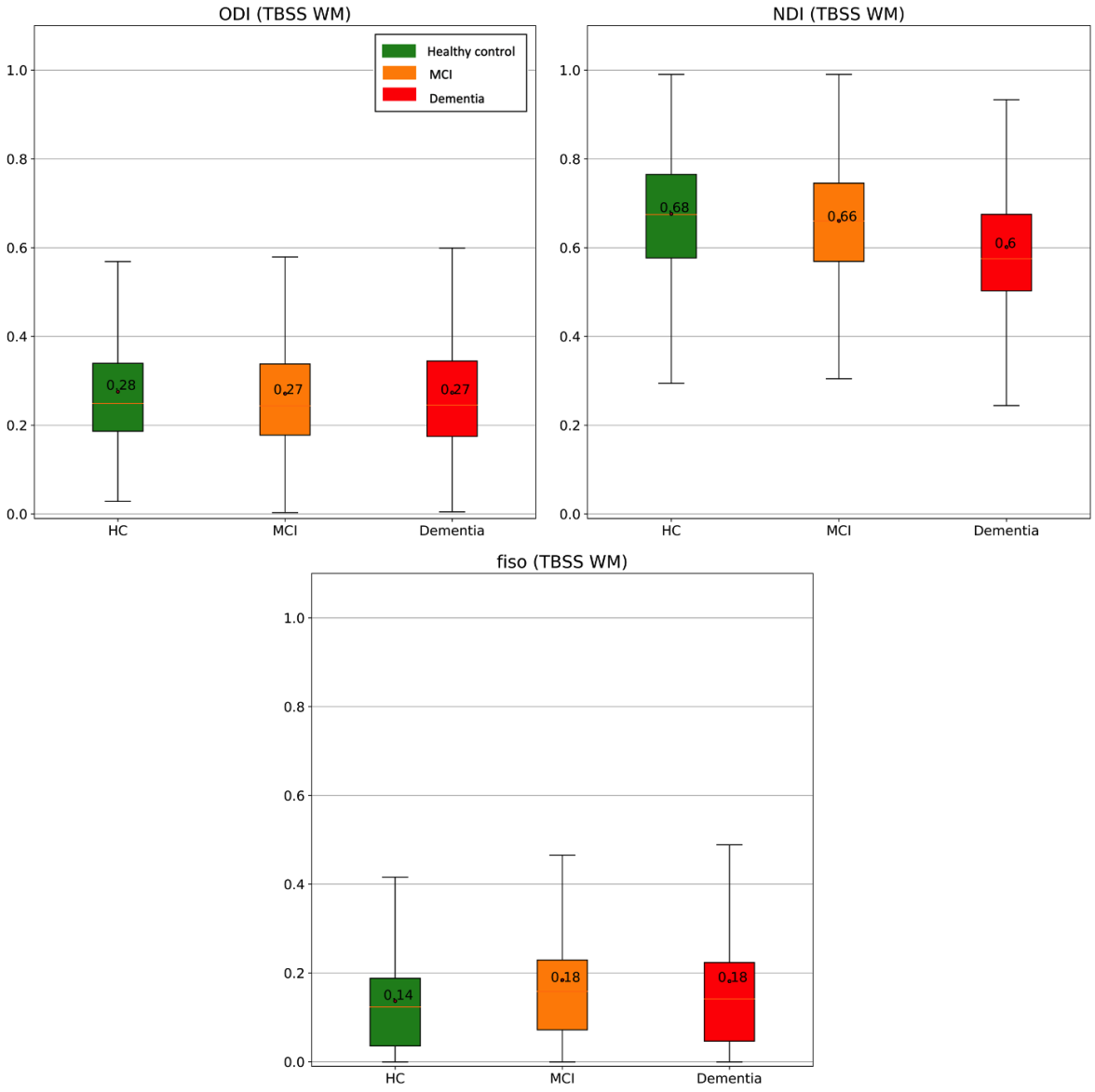


Figure 4.12: Box plots of NODDI metrics (ODI, NDI and f_{iso}) in the white matter (on an alignment-invariant skeleton) of the healthy control (HC), the MCI patient and the patient with dementia. The horizontal orange line represents the median of the distribution and the black marker represents the mean metric.

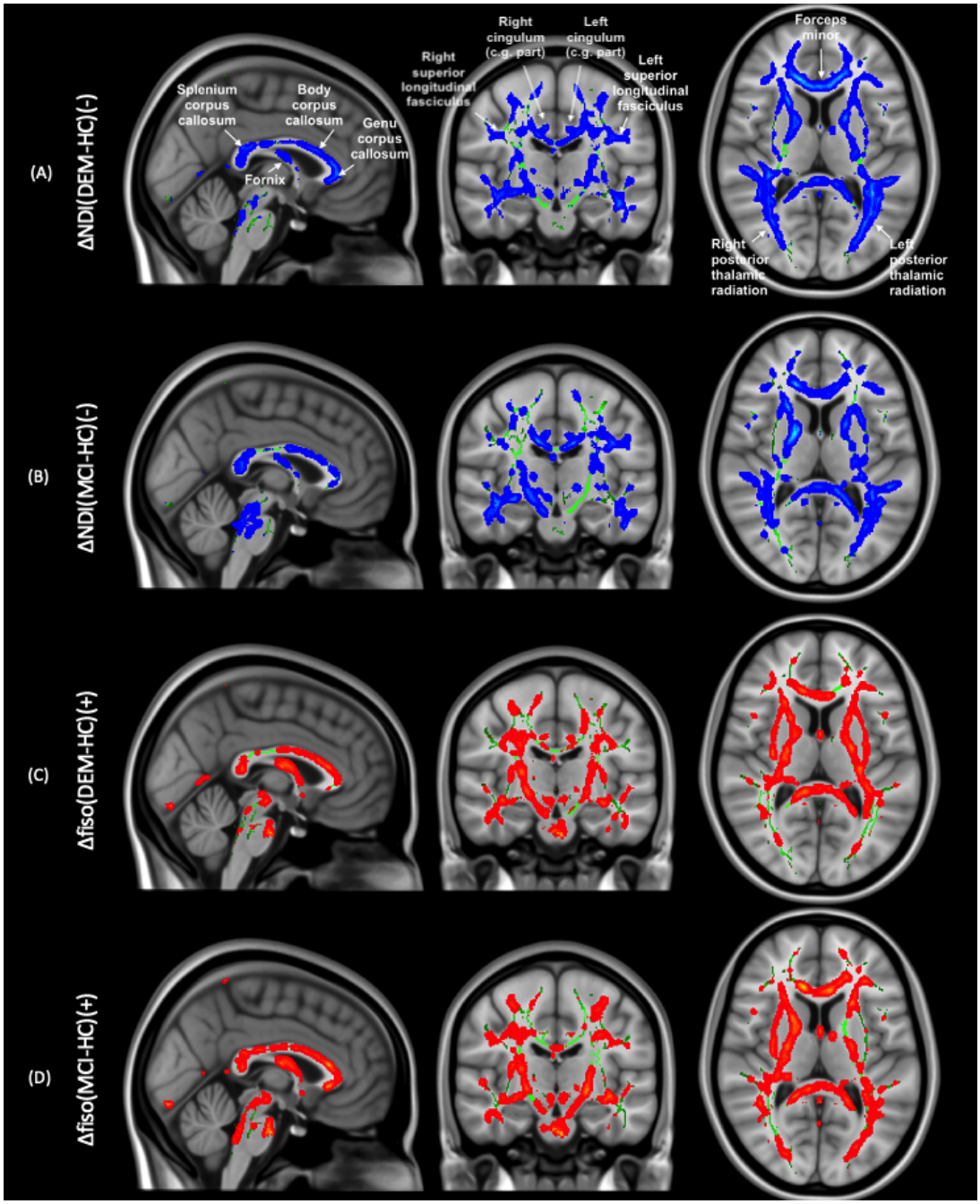


Figure 4.13: Regions of the skeleton showing (A) a decreased NDI in the patient with dementia (DEM) compared to the healthy control (HC), (B) a decreased NDI in the MCI patient, (C) an increased f_{iso} in the patient with dementia and (D) an increased f_{iso} in the MCI patient.

4.4.2 Region-based analysis : results

The results of the ROI-based analysis for the NODDI metrics are represented in Fig.4.14, Fig.4.15 and Fig.4.16. No large differences in ODI values were observed between the subjects (except in the fornix of the patient with dementia). The substantial increase in ODI observed in the fornix of the patients with dementia may be due to registration errors. Indeed, this structure being close to the CSF, a small misalignment of the structure with the mask from the atlas would lead to a biased mean metric evaluated in that region. A small increase in ODI was observed in the genu of the corpus callosum, the left cingulum (parahippocampal part), the right cingulum (parahippocampal part), the left uncinate fasciculus and the right uncinate fasciculus. Although not important, a small decrease in ODI was observed in the body of the corpus callosum, the left and right posterior thalamic radiations and the left superior longitudinal fasciculus in the AD group compared to the healthy control. Therefore, differences in ODI values between the subjects were very small and not consistent (i.e. a small increase in some ROI and small decrease in other regions in the AD group). Although no difference was expected in the cerebellum, a decreased ODI was observed in the cerebellar peduncles (Appendix D.1.2), a region known to be mildly affected by AD.

The ROI-based analysis revealed a decreased NDI in all the tracts of interest except in the left and right cingulum and the superior corona radiata. The decrease in NDI was constantly more pronounced in the patient with dementia than in the MCI patient. No difference in NDI was observed in the cerebellar peduncles that are mildly affected by the disease.

This ROI-based analysis suggested an increased f_{iso} in all the tracts of interest in the patient with dementia and in the MCI patient compared to the healthy control. The increased f_{iso} was constantly more pronounced in the patient with dementia. Although a small increased f_{iso} was observed in the inferior cerebellar peduncle, the other structures (the middle cerebellar peduncle and the superior cerebellar peduncle) of the region mildly affected by AD did not show differences in f_{iso} values between the AD patients and the healthy control.

This ROI-based analysis revealed changes in regions that also showed differences in NDI and f_{iso} values in the skeleton-based analysis in the MCI patient and in the patient with dementia. However, by opposition to this ROI-based analysis, the left and right cingulum (the parahippocampal parts and the cingulate gyrus parts) also showed a decreased NDI in the AD patients in the skeleton-based analysis.

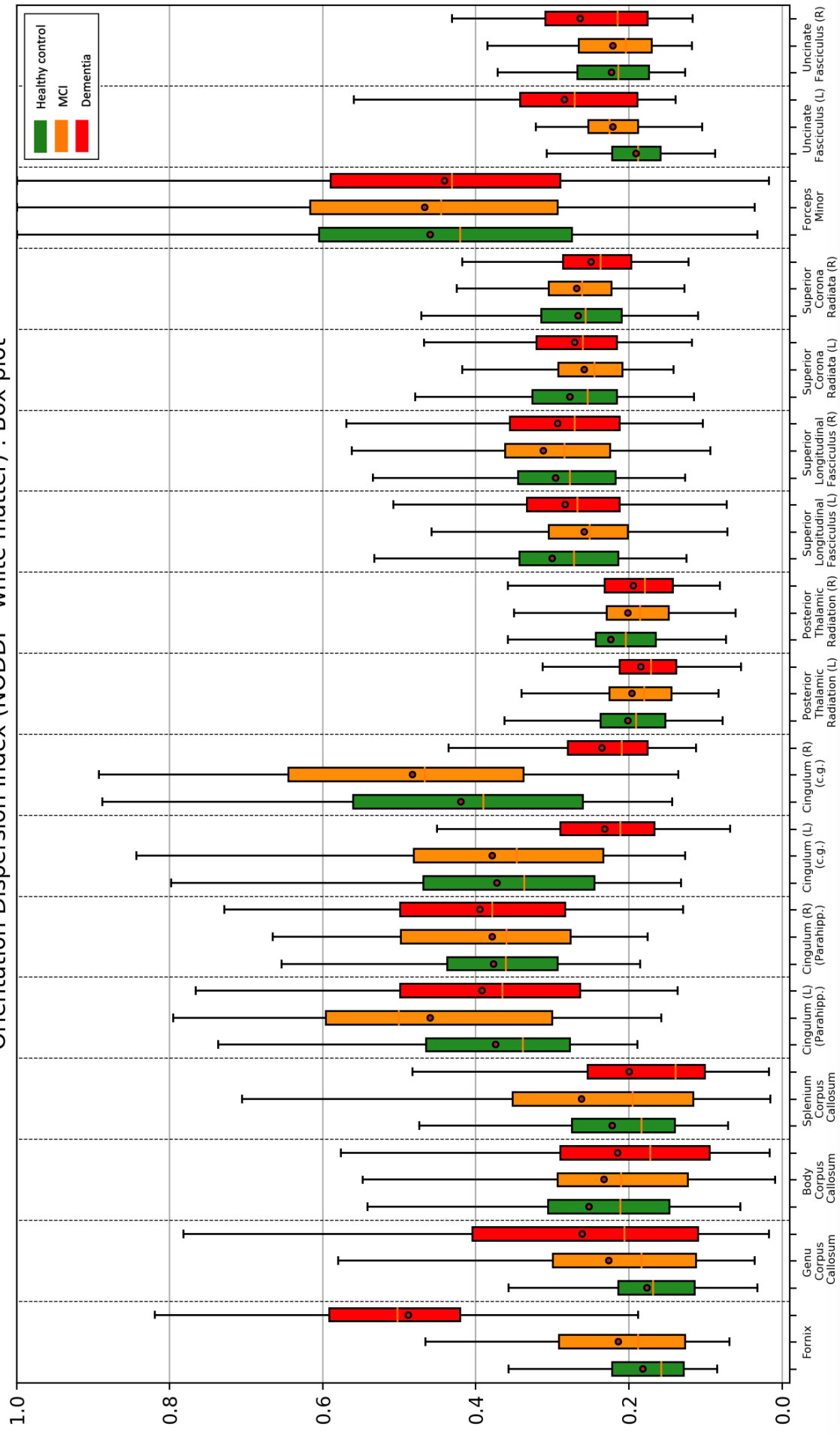


Figure 4.14: Box plot of the Orientation Dispersion Index in regions of interest for the healthy control (green), the MCI patient (orange) and the patient with dementia (red). The horizontal orange line represents the median of the distribution and the black marker represents the mean ODI in the tract of interest. From left to right, the tracts of interest are: fornix, genu of corpus callosum, body of corpus callosum, splenium of corpus callosum, left cingulum (parahippocampal part), right cingulum (parahippocampal part), left cingulum (cingulate gyrus part), right cingulum (cingulate gyrus part), left posterior thalamic radiation, right posterior thalamic radiation, left superior longitudinal fasciculus, right superior longitudinal fasciculus, left superior corona radiata, right superior corona radiata, forceps minor, left uncinate fasciculus, right uncinate fasciculus.

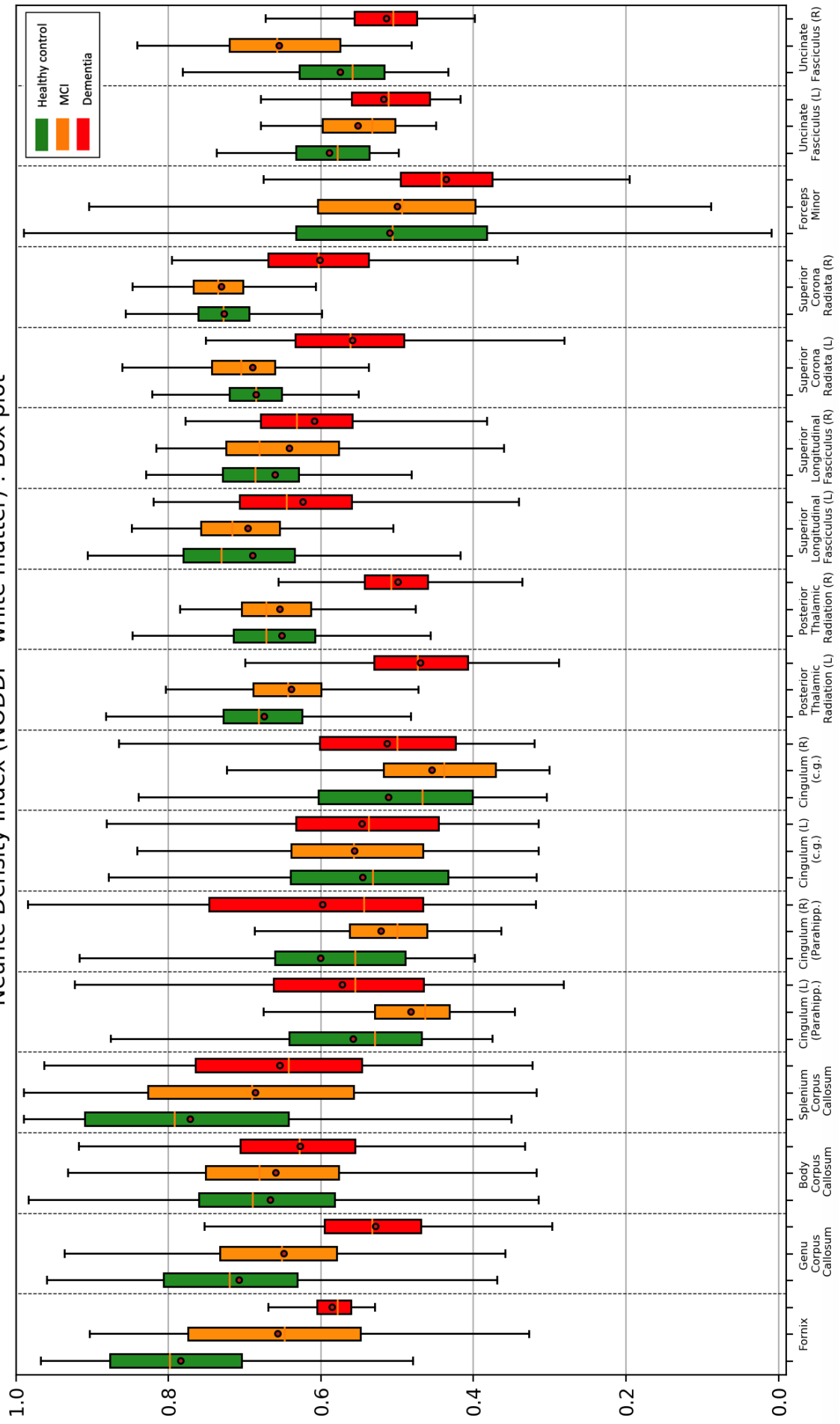


Figure 4.15: Box plot of the Neurite Density Index in regions of interest for the healthy control (green), the MCI patient (orange) and the patient with dementia (red). The horizontal orange line represents the median of the distribution and the black marker represents the mean NDI in the tract of interest. From left to right, the tracts of interest are: fornix, genu of corpus callosum, body of corpus callosum, splenium of corpus callosum, left cingulum (parahippocampal part), right cingulum (parahippocampal part), left cingulum (cingulate gyrus part), right cingulum (cingulate gyrus part), left posterior thalamic radiation, right posterior thalamic radiation, left superior longitudinal fasciculus, right superior longitudinal fasciculus, left superior corona radiata, right superior corona radiata, forceps minor, left uncinate fasciculus, right uncinate fasciculus.

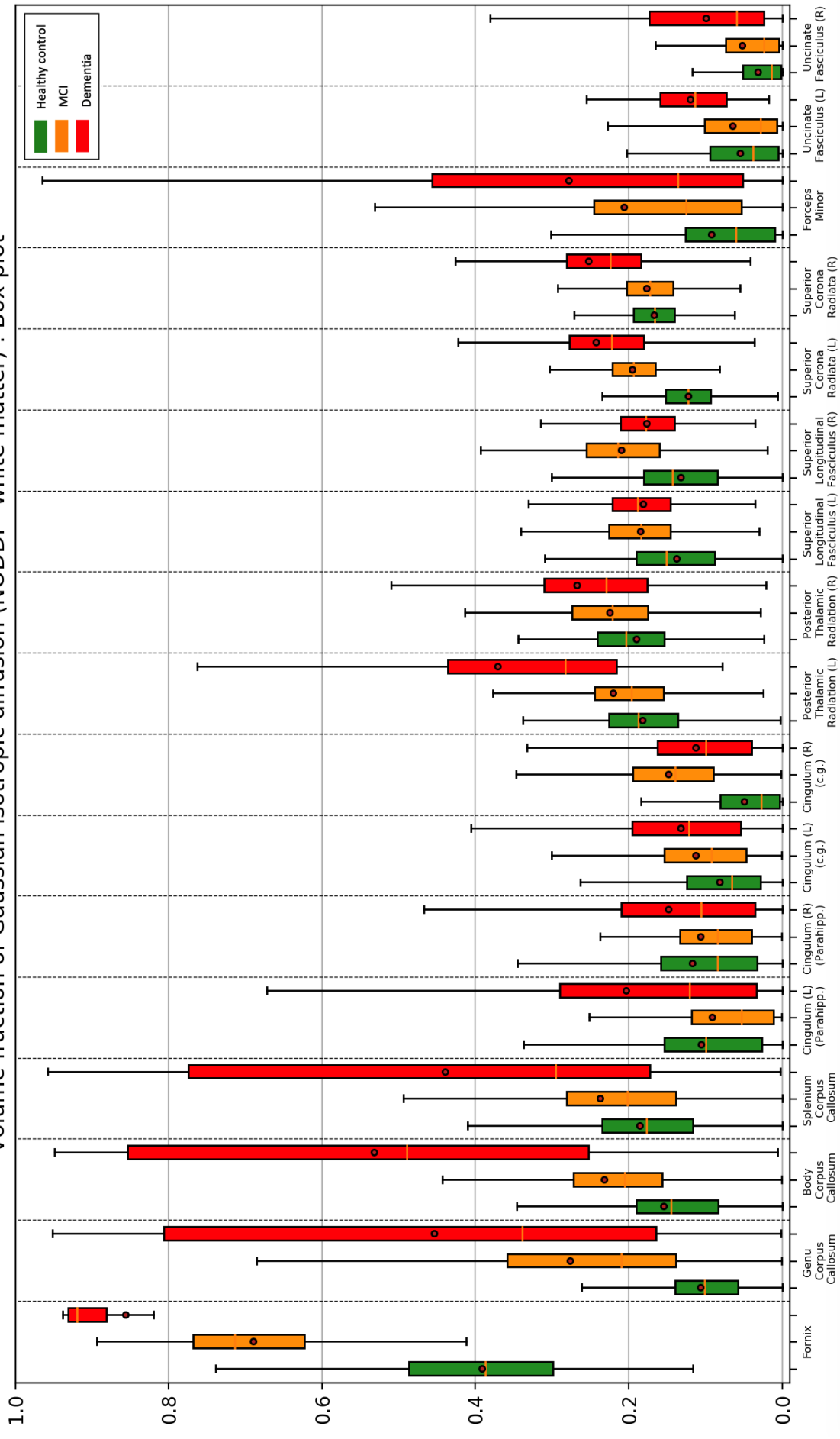


Figure 4.16: Box plot of the volume fraction of Gaussian isotropic diffusion (f_{iso}) in regions of interest for the healthy control (green), the MCI patient (orange) and the patient with dementia (red). The horizontal orange line represents the median of the distribution and the black marker represents the mean f_{iso} in the tract of interest. From left to right, the tracts of interest are: fornix, genu of corpus callosum, body of corpus callosum, splenium of corpus callosum, left cingulum (parahippocampal part), right cingulum (parahippocampal part), left cingulum (cingulate gyrus part), right cingulum (cingulate gyrus part), left posterior thalamic radiation, right posterior thalamic radiation, left superior longitudinal fasciculus, right superior longitudinal fasciculus, left superior corona radiata, right superior corona radiata, forceps minor, left uncinate fasciculus, right uncinate fasciculus.

4.4.3 Discussion

NODDI (Neurite Orientation and Dispersion Density Imaging) is a multi-compartment model that captures changes of neurite morphology *in vivo* [25]. This model evaluates the neurite density index (NDI), the neurite orientation index (ODI) and the volume fraction of Gaussian isotropic diffusion (f_{iso}) for the whole brain in a clinically feasible acquisition time [25].

The whole-brain WM analysis with the mask and the skeleton both revealed a decreased NDI and increased f_{iso} in the patient with dementia and the MCI patient compared to the healthy control. Although an increased ODI was observed in the analysis with the WM mask, the skeleton of the coherently aligned axons mainly composed of single-fascicle voxels did not reveal differences in ODI values between the AD patients and the healthy control. Since NODDI was not designed to capture microstructural features in voxels with crossing fascicles, the increased ODI observed with the WM mask has to be carefully considered. Therefore, considering the results for ODI from the skeleton-based analysis was more sound.

The ROI-based analysis revealed a decreased NDI and increased f_{iso}, confirming the findings of the whole-brain WM analyses. A decreased NDI indicates cholinergic neurons and axons reduction due to Aβ deposition [72]. The tracts that showed a decreased NDI in the ROI-based analysis and the skeleton-based analysis are involved in non-verbal coding in memory [79], attention, language [94], verbal fluency, word production, phonological processing and retrieval [87], relaying sensory information [82], working memory, episodic memory and social processing [92]. The ROI-based analysis and the skeleton-based analysis also revealed an increased f_{iso} in all the tracts of interest known to be affected by AD. An increase in f_{iso} represents cell shrinkage and a decreased tissue volume fraction [72]. The tracts showing an increased f_{iso} in both analyses are involved in a variety functions such as: verbal and non-verbal coding in memory [79], control of attention, verbal fluency, word production [86], episodic memory [95], social processing [92], semantic memory [96], etc. Most of the ROI showed a larger decrease in NDI and increase in f_{iso} in the patient with dementia than in the MCI patient, suggesting that those functions are expected to be more altered in the patient with dementia. A summary of the functions of each tract of interest can be found in Appendix C.

While the ODI metric in the WM was initially conceptualized to characterize the orientation complexity of neurites and therefore to give an insight on the diffusion of water molecules in the extra-neurite space without taking into account the influence of glial cells [65], a study [65] suggested a potential ability of the metric to sense neuroinflammation. The study was conducted on murine brains depleted from microglia that were compared to control animals. A positive correlation was observed between the microglial density and ODI values interpreted as a "greater hindered diffusion arising from the extra-neurite space" [65].

Although the analyses conducted did not reveal reliable differences in ODI values between the healthy control and the AD patients, a study comparing ODI values in a mouse model of human AD with and without microglia depletion may be useful to characterize how pathological components of the neuroinflammation in AD affect NODDI metrics. However, a greater level of understanding of the mechanisms involving microglia in AD are needed to better interpret quantitative metrics of multi-compartment models.

This model considers a single type of WM fibers while a wide range of microstructural features have been observed in the brain [23]. The radial diffusivity in the axons is neglected by the model. It was also reported that NODDI may not be suitable to characterize the microstructure in severe pathological conditions "where white matter microstructures are highly distorted" [20]. NODDI metrics assigned in every voxel characterize the overall population of fascicles localized in the voxel without characterizing each fascicle individually [23]. Multi-compartment models considering a complex organization of tissues with more realistic tissue properties could lead to a more accurate biological explanation of the diffusion signal observed.

4.5 Microstructural changes : DIAMOND

The DIAMOND metrics analyzed in this section are: the fraction of a compartment representing the restricted isotropic diffusion (F_{iso}, where the diffusivity of the compartment is estimated from the data) and the fraction of compartments with anisotropic diffusion ($F_{aniso} = F_{aniso1} + F_{aniso2}$, where F_{aniso1} and F_{aniso2} are respectively the fraction of the first and second population of spin packets characterized by an anisotropic diffusion. More detailed information about DIAMOND metrics can be found in section 2.2.2 *(Chapter 2 - Microstructural models - DIAMOND)*.

4.5.1 Whole-brain white matter analysis : results

Analysis based on a patient specific white matter mask

The results of the whole-brain WM analysis that evaluated DIAMOND metrics in patient specific WM masks are represented in Fig.4.17. Considerable differences in DIAMOND metrics were observed between the healthy control and the AD patients. Indeed, a large increase in F_{iso} and a large decrease in F_{aniso} were observed in the patient with dementia and the MCI patient. Changes observed were constantly larger in the patient with dementia than in the MCI patient.

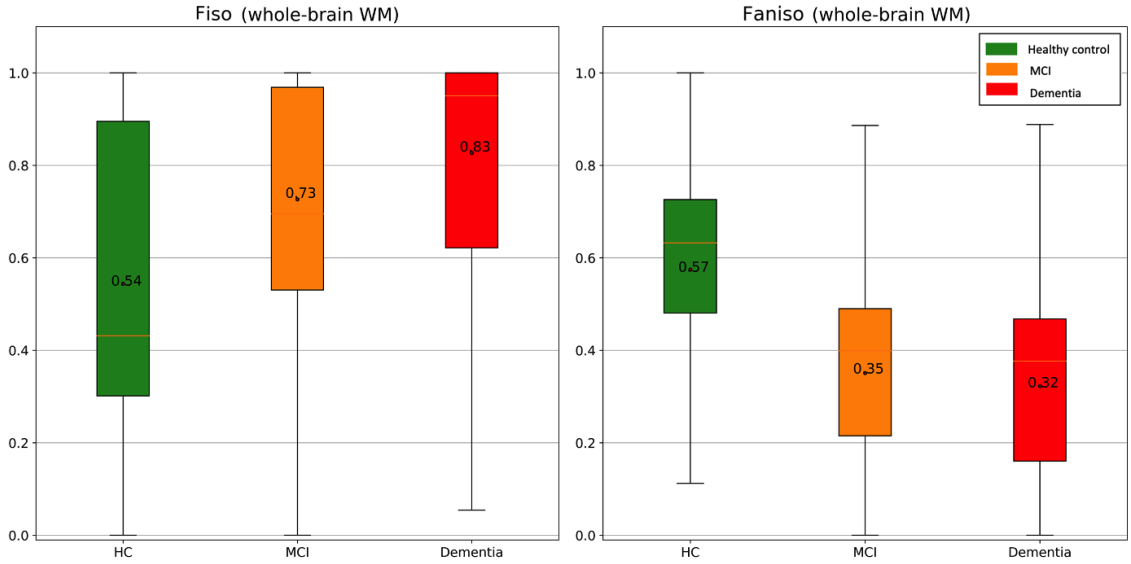


Figure 4.17: Box plots of DIAMOND metrics (F_{iso} and F_{aniso}) in the white matter (a patient specific white matter mask was created by segmentation of anatomical images) of the healthy control (HC), the MCI patient and the patient with dementia. The horizontal orange line represents the median of the distribution and the black marker represents the mean metric.

Analysis based on an alignment-invariant white matter skeleton

Box plots of DIAMOND metrics evaluated in the WM skeleton are represented in Fig.4.18. An important increase in F_{iso} and decrease in F_{aniso} were observed in the MCI patient and the patient with dementia in the coherently aligned axons of the WM. As expected, changes in DIAMOND metrics were larger in the patient with dementia than in the MCI patient. The regions of the skeleton showing an increased F_{iso} and a decreased F_{aniso} in the AD patients are represented in Fig.4.20.

For a better visualization of voxelwise differences in DIAMOND metrics between the healthy control and the AD patients, coronal views of DIAMOND maps centered on the corpus callosum[6] were depicted in Fig.4.19. Diffusion tensors characterizing each fiber individually were superimposed onto the DIAMOND maps. As expected, the model estimated a single fascicle in the corpus callosum and crossing fibers in the corona radiata (at the intersection of the corpus callosum and the corticospinal tract). Since a brighter color represents a higher metric value, one can observe an increase in F_{iso} and a decrease in F_{aniso} in the corpus callosum of the AD patients compared to the healthy control.

6 This structure is easily localized, known to be affected by AD and allows an easy comparison of the subjects.

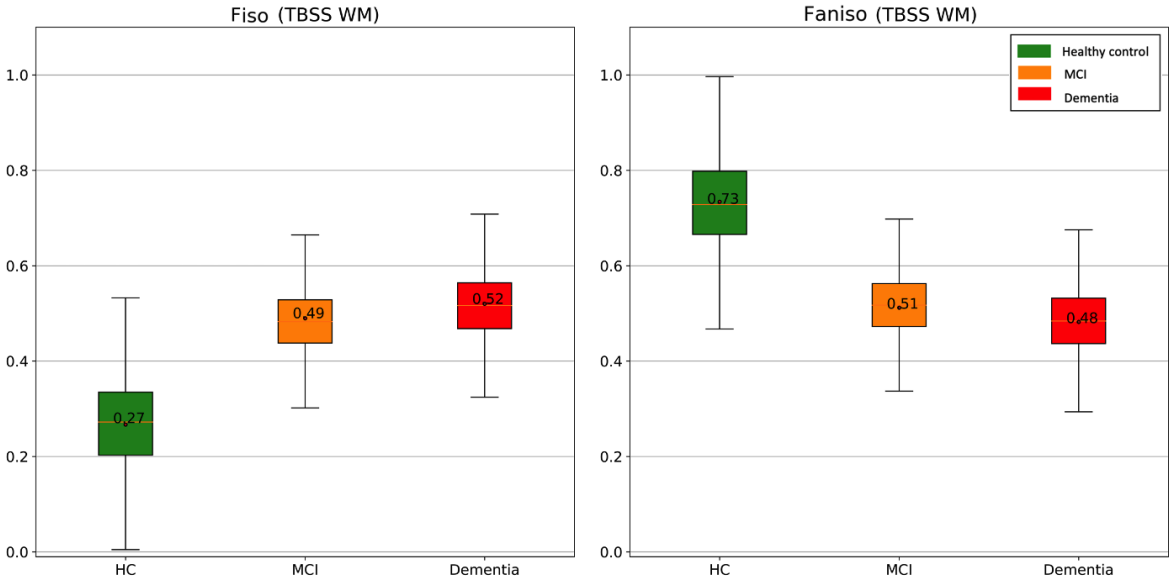


Figure 4.18: Box plots of DIAMOND metrics (F_{iso} and F_{aniso}) in the white matter (on an alignment-invariant skeleton) of the healthy control (HC), the MCI patient and the patient with dementia. The horizontal orange line represents the median of the distribution and the black marker represents the mean metric.

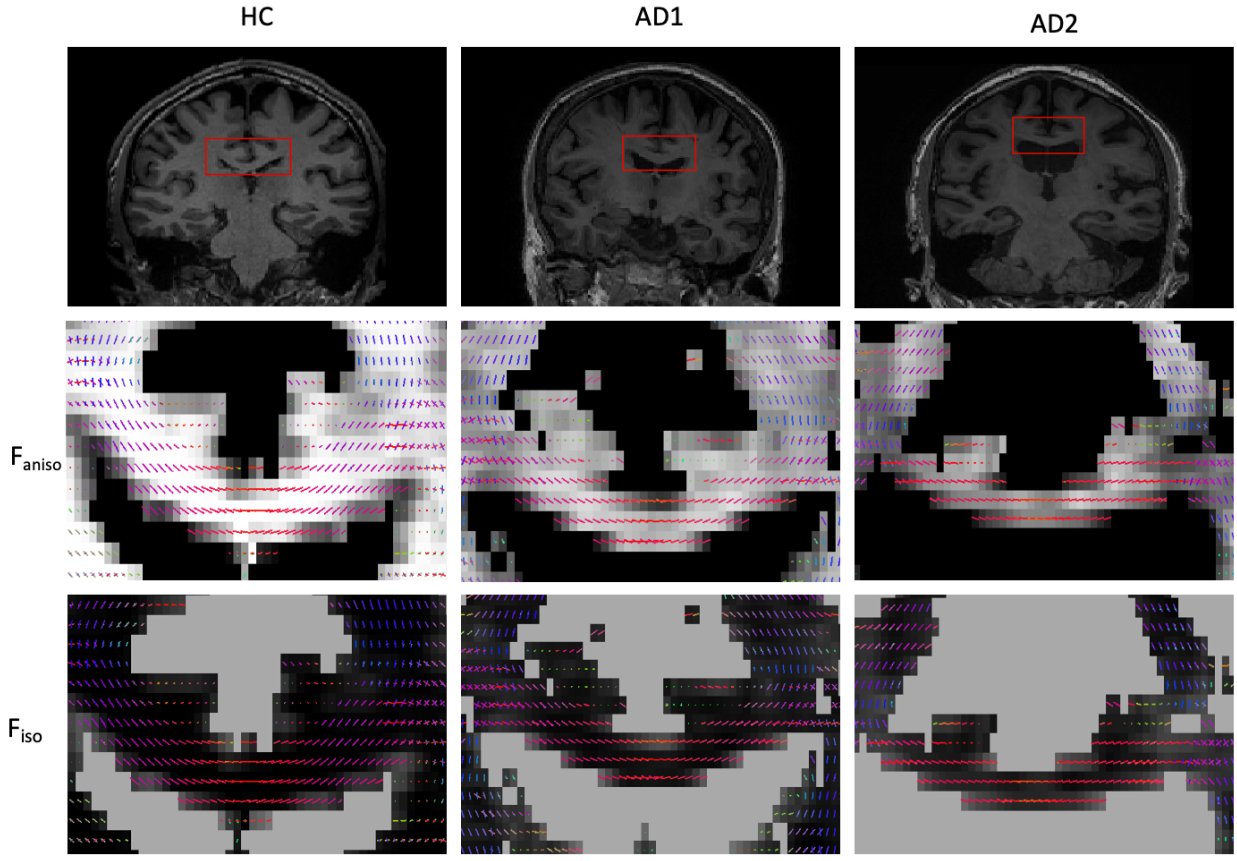


Figure 4.19: Coronal view of DIAMOND maps (F_{iso} and F_{aniso}) centered on the corpus callosum of the healthy control, the MCI patient and the patient with dementia. The tensors characterizing each fascicle were superimposed onto the maps. A higher value for the metric is depicted by a brighter voxel color. Those maps were created with MisterI software *(http://benoitscherrer.com/MisterI)*.

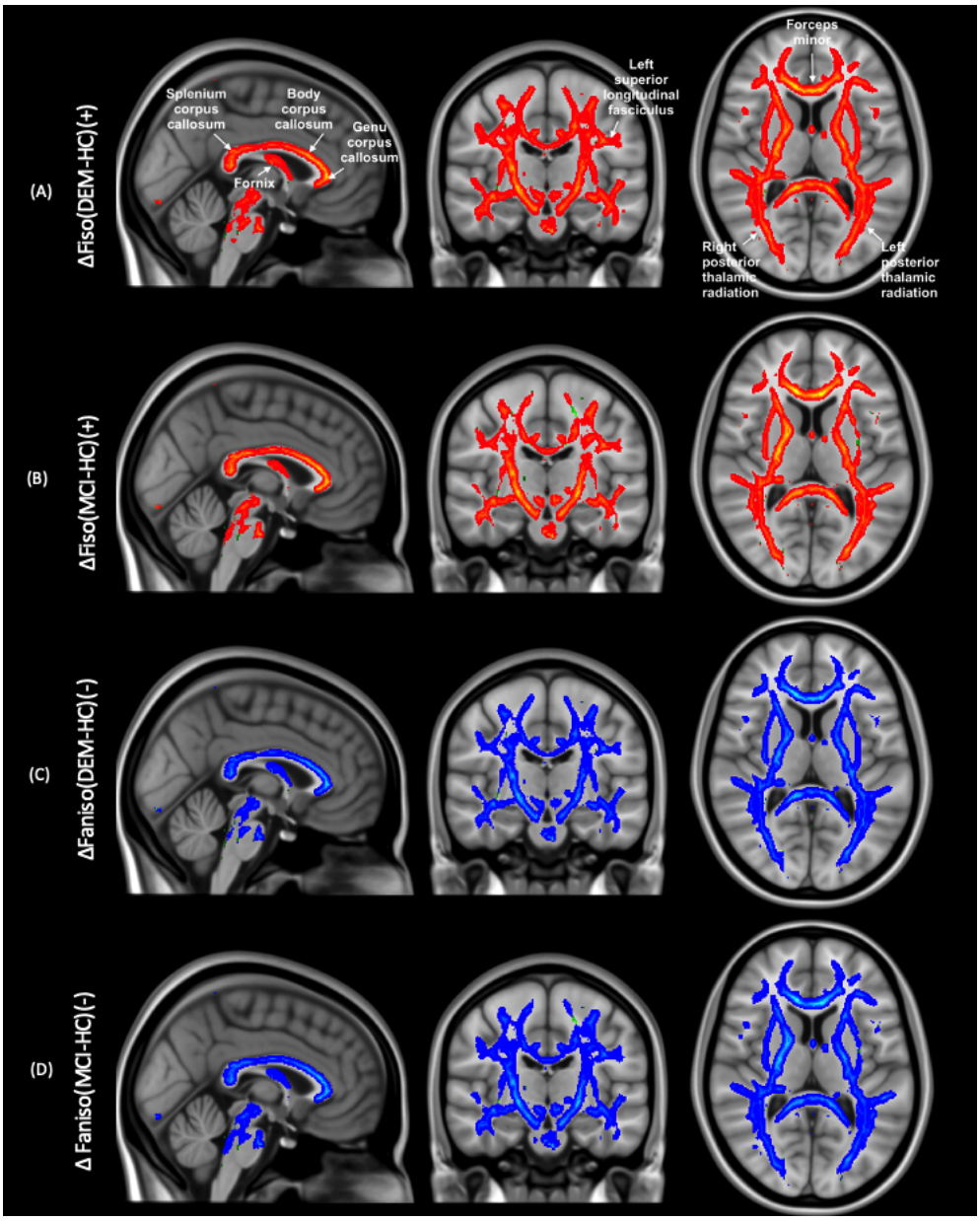


Figure 4.20: Regions of the skeleton showing (A) an increased F_{iso} in the patient with dementia (DEM) compared to the healthy control (HC), (B) an increased F_{iso} in the MCI patient, (C) a decreased F_{aniso} in the patient with dementia and (D) a decreased F_{aniso} in the MCI patient.

4.5.2 Region-based analysis : results

The results of this ROI-based analysis in structures known to be affected by AD are represented in Fig.4.21 and Fig.4.22. The DIAMOND metrics were also evaluated in regions mildly affected by AD (Appendix D.1.3) to better characterize the alterations of the tracts. An increased F_{iso} and a decreased F_{aniso} were observed in all the ROI in the MCI patient and the patient with dementia compared to the healthy control. As expected, the alterations were more pronounced in the patient with dementia than in the MCI patient in most tracts of interest. Although smaller than differences observed in ROI between the healthy control and the AD patients, a decreased F_{aniso} and increased F_{iso} were observed in the middle and right cerebellar peduncles in the AD group. All the regions highlighted in this ROI-based analysis showed an increased F_{iso} and decreased F_{aniso} in the patient with dementia and the MCI patient in the skeleton-based analysis.

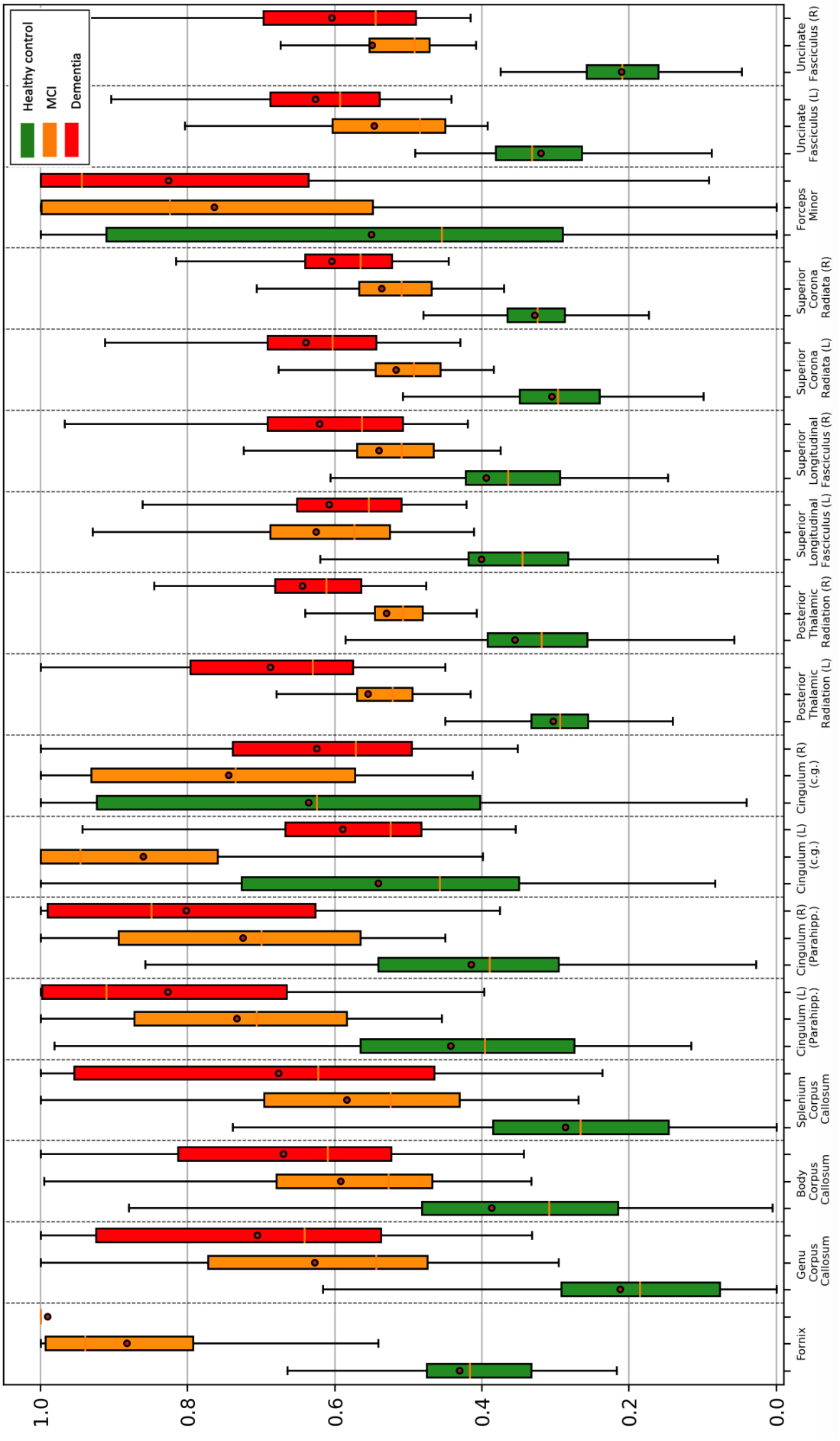


Figure 4.21: Box plot of the fraction of the compartment representing the restricted isotropic diffusion (F_{iso}) in regions of interest for the healthy control (green), the MCI patient (orange) and the patient with dementia (red). The horizontal orange line represents the median of the distribution and the black marker represents the mean F_{iso} in the region of interest. From left to right, the regions of interest are: the left hippocampus entorhinal cortex, the right hippocampus entorhinal cortex, the anterior division of the inferior temporal cortex, the posterior division of the inferior temporal cortex, the temporooccipital part of the inferior temporal cortex, the posterior division of the middle temporal cortex, the temporooccipital part of the middle temporal cortex, the fusiform cortex, the precuneous cortex, the frontal pole, the superior frontal gyrus, the parahippocampal gyrus (anterior division), the parahippocampal gyrus (posterior division), the posterior cingulate cortex, the left hippocampus, the right hippocampus, the left amygdala and the right amygdala.

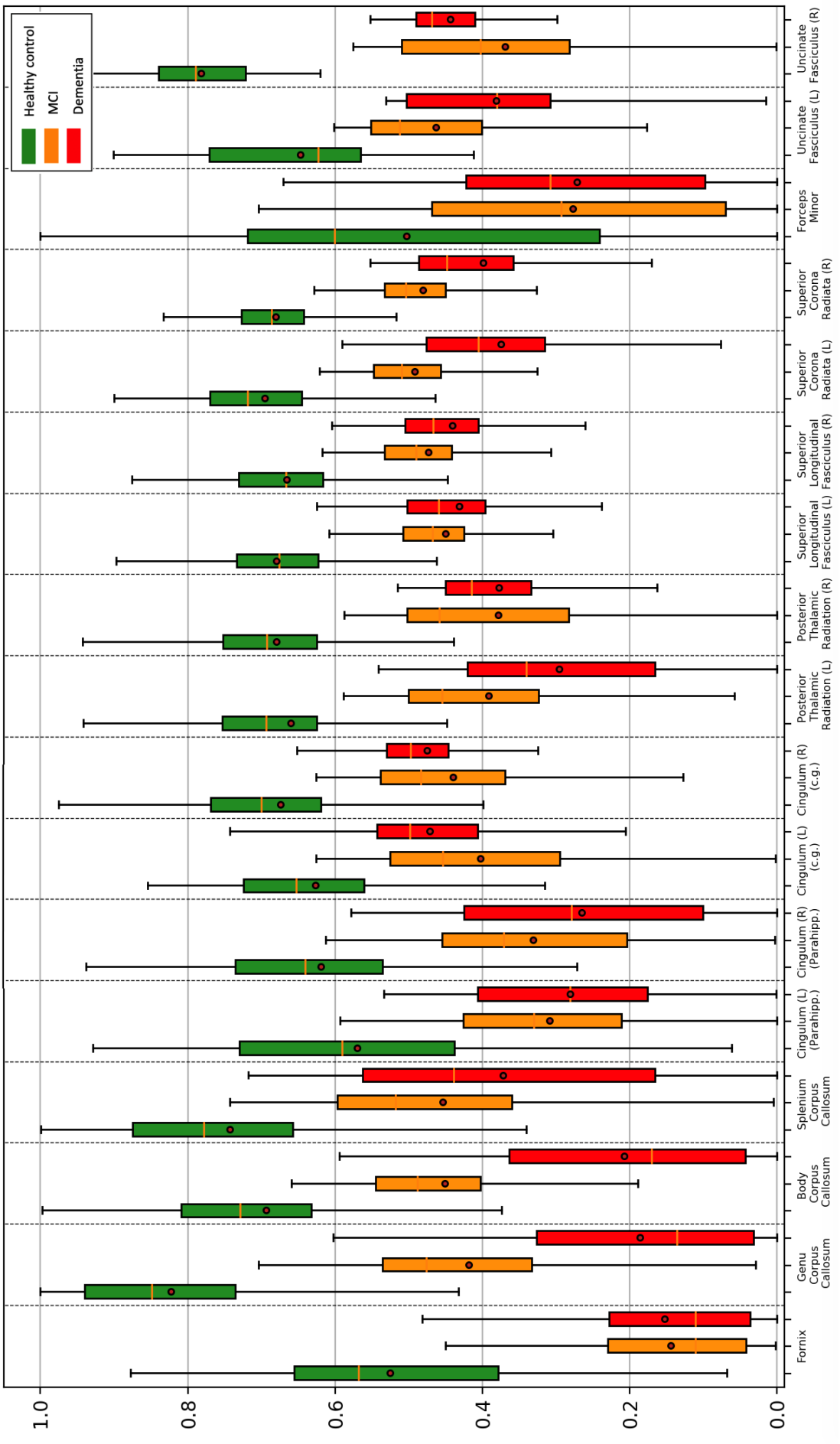


Figure 4.22: Box plot of the fraction of the anisotropic compartments (F_{aniso}) in regions of interest for the healthy control (green), the MCI patient (orange) and the patient with dementia (red). The horizontal orange line represents the median of the distribution and the black marker represents the mean F_{aniso} in the region of interest. From left to right, the regions of interest are: the left hippocampus entorhinal cortex, the right hippocampus entorhinal cortex, the anterior division of the inferior temporal cortex, the posterior division of the inferior temporal cortex, the temporooccipital part of the inferior temporal cortex, the posterior division of the middle temporal cortex, the temporooccipital part of the middle temporal cortex, the fusiform cortex, the precuneous cortex, the frontal pole, the superior frontal gyrus, the parahippocampal gyrus (anterior division), the parahippocampal gyrus (posterior division), the posterior cingulate cortex, the left hippocampus, the right hippocampus, the left amygdala and the right amygdala.

4.5.3 Discussion

DIAMOND (DIstribution of 3D Anisotropic MicrOstructural eNvironments in Diffusion-compartment imaging) is a phenomenological multi-compartment model that considers the signal in every voxel as arising from a finite number of microstructural environments in slow exchange. Therefore, this model considers multiple fascicles in the voxels and a compartment for the restricted isotropic diffusion of water molecules. A wide range of metrics are obtained with this model and can be analyzed, such as: compartmentalized DTI metrics characterizing each fiber in the voxel individually (e.g. "cFA"), the heterogeneity index of the fibers, the fraction of compartments with anisotropic diffusion, the fraction of the compartment representing the restricted isotropic diffusion or the diffusivity of that compartment. The diffusivity is computed from the data and can be different from the diffusivity of free water molecules at 37° ($3{\cdot}10^{-3}$ $[mm^2/s]$). In this study, the fraction of compartments with anisotropic diffusion (F_{aniso}) and the fraction of the compartment representing the restricted isotropic diffusion (F_{iso}) were examined in the WM of the patient with dementia and the MCI patient.

The two analyses performed on the whole-brain WM revealed considerable differences in DIAMOND metrics between the AD patients and the healthy control. A large increase in F_{iso} and a large decrease in F_{aniso} were observed in the patient with dementia and in the MCI patient. Those findings can be interpreted as a decreased fraction of fascicles in the voxels (represented by compartments characterized by an anisotropic diffusion), that was more pronounced in the patient with dementia than in the MCI patient.

The ROI-based analysis confirmed the findings of the whole-brain WM analyses: all the tracts of interest showed an increased F_{iso} and a decreased F_{aniso}. Changes in DIAMOND metrics were observed in structures involved in a variety of functions, including: the control of attention [80], word production, object recognition within a spatial context, working memory [85, 86, 87, 88], episodic memory, social processing [92], attention [94], etc. As expected, changes in those metrics were more pronounced in the patient with dementia in most ROI, suggesting that the functions in that patient are more altered than in the MCI patient. The functions of each ROI can be found in Appendix C.

Differences in DIAMOND metrics between the healthy control and the AD patients were larger than differences in DTI and NODDI metrics. Although more studies evaluating DIAMOND metrics in AD patients are needed to confirm those findings, those results suggested the substantial discriminatory capability of DIAMOND to differentiate altered tissues in AD from healthy tissues, even at an early clinical stage of the disease, suggesting the great potential for the metrics of the model to be used as biomarkers of neuronal damages in AD.

By considering multiple compartments in the voxels, DIAMOND enables to capture precise features of each compartment. Crossing fascicles in the voxels are therefore characterized individually and the diffusivity of the compartment representing the restricted diffusion is estimated from the data without making assumptions. This leads to a more realistic and biological interpretation than models considering only one fascicle in the voxel or a fixed representation of fascicles throughout the brain [23] (e.g. DTI and NODDI). While the exact number of fascicles in every voxel is not known, this model relies on an argument provided by the user that represents the maximum number of fascicles that can be estimated in the voxels before estimating the most probable configuration. However, this may not be considered as a limitation since a maximum number of 3 fascicles is usually considered in the voxels and is reasonable for the amount of data that can be acquired nowadays. Although more realistic, this model is more complex and the analysis becomes more intricate as more compartments are considered.

4.6 Microstructural changes : Microstructure Fingerprinting

Microstructure Fingerprinting (MF) is a model that represents the fascicles as a hexagonal packing of cylinders representing the axons. Each fascicle is characterized by a fiber volume fraction (e.g. fvf_1, for the first fascicle estimated in the voxel) and a fraction of occupancy of the voxel by the fascicle (e.g. f_1, for the first fascicle estimated in the voxel). Therefore, the "FVF" metric analyzed is the "total fiber volume fraction" and represents the total fraction of water inside the axons in the voxel. The FVF in every voxel when a two-fascicle model is considered is defined as: $FVF = f_1 * fvf_1 + f_2 * fvf_2$. In this section, the mean apparent axonal radius was evaluated and is defined as: $mRad = (rad_1 + rad_2)/2$ (with rad_1 and rad_2 being respectively the apparent axonal radius of the first and the second fascicle estimated in the voxel). For computation time savings, a compartment representing the restricted isotropic diffusion was only considered when 0 or 1 fascicle was estimated in the voxels. The fraction of that compartment (F_{iso}) was also analyzed in this section. More detailed information about the metrics of the model obtained with Monte Carlo simulations of DW-MRI signals can be found in section 2.3.2 *(Chapter 2 - Microstructural models - Microstructure Fingerprinting).*

4.6.1 Whole-brain white matter analysis : results

Analysis based on a patient specific white matter mask

The results of the whole-brain analysis based on patients-specific WM masks are represented in Fig.4.23. One can observe an increased F_{iso} in the AD patients, with a trend more pronounced in the patient with dementia. A wide range of F_{iso} values were observed in the whole-brain WM. Indeed, there was an important dispersion of F_{iso} values in the voxels of the WM in all the subjects, as shown by the large interquartile ranges[7] of the box plots. Half of the voxels in the WM were presenting a F_{iso} higher than 0.67 in the MCI patient and higher than 0.81 in the patient with dementia (as indicated by the median), with 25% of voxels having a F_{iso} of 1 in the AD patients. A decreased FVF was observed in both AD patients, with a larger decrease in the patient with dementia. Moreover, a decreased mRad was observed in the AD patients, with a decrease more pronounced in the patient with dementia.

Analysis based on an alignment-invariant white matter skeleton

The results of the whole-brain analysis that evaluated the metrics in strongly aligned axons are represented in Fig.4.24. An increase in F_{iso} (that was small compared to the mask-based analysis) was observed in the AD patients and was similar in the patient with dementia and the MCI patient. Moreover, the dispersion of F_{iso} values in the WM of the subjects was small (i.e. a smaller interquartile range) compared to the mask-based analysis. A decreased FVF was observed in both AD patients, with a decrease more pronounced in the patient with dementia. Finally, a decreased mRad was observed in the AD patients with a similar decrease in the patient with dementia and the MCI patient. Regions showing an increased F_{iso} and decreased FVF in the AD patients along the WM skeleton are represented in Fig.4.25.

7 The interquartile range (IQR) is a measure of the dispersion of the data in a box plot. The IQR represents the distribution of the middle-50% observations. This is the length of the "box" without considering the whiskers (upper and lower quartiles).

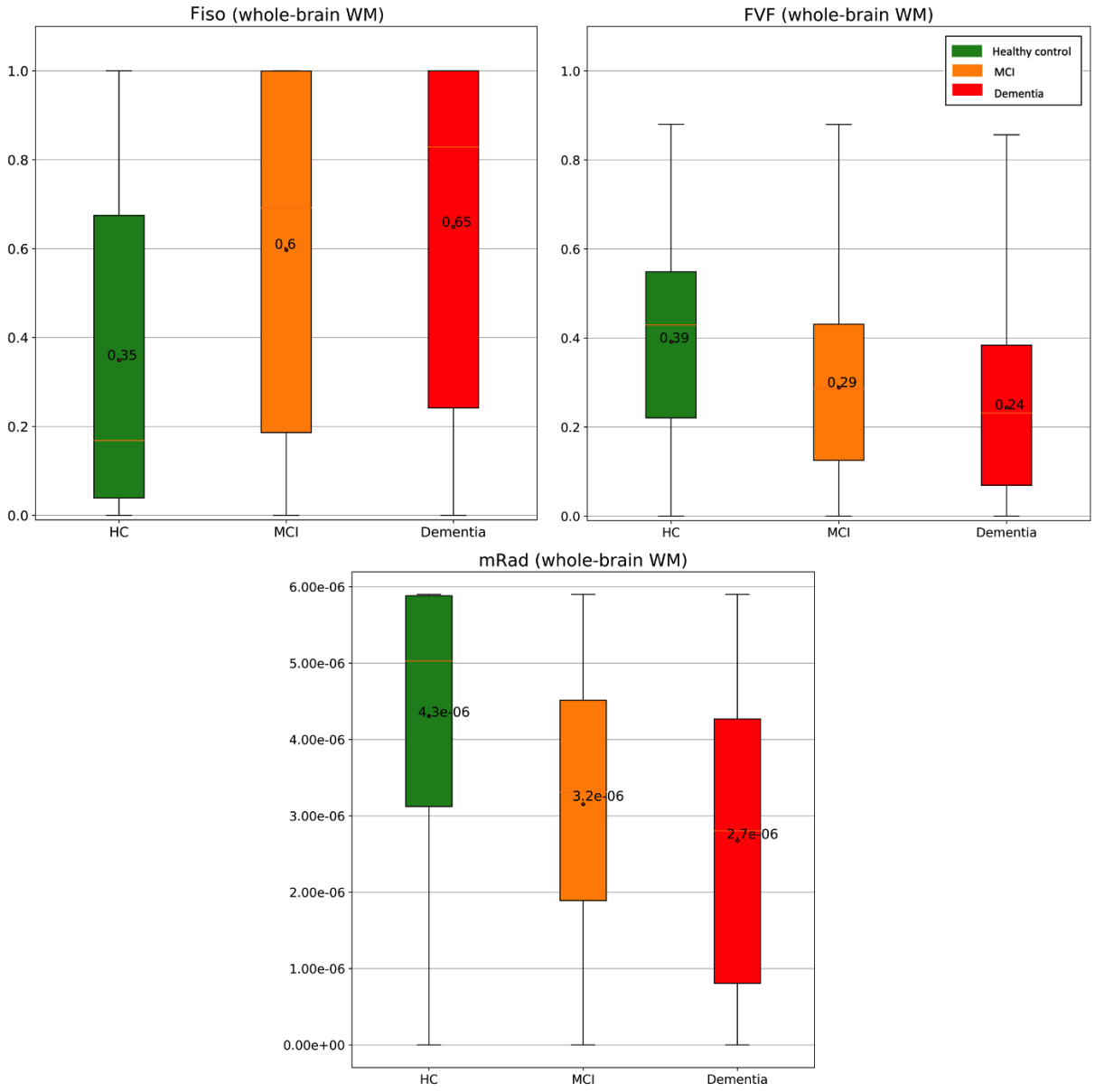


Figure 4.23: Box plot of MF metrics (F_{iso}, FVF and mRad) in the white matter (a patient specific white matter mask was created by segmentation of anatomical images) of the healthy control (HC), the MCI patient and the patient with dementia. The horizontal orange line represents the median of the distribution and the black marker represents the mean metric.

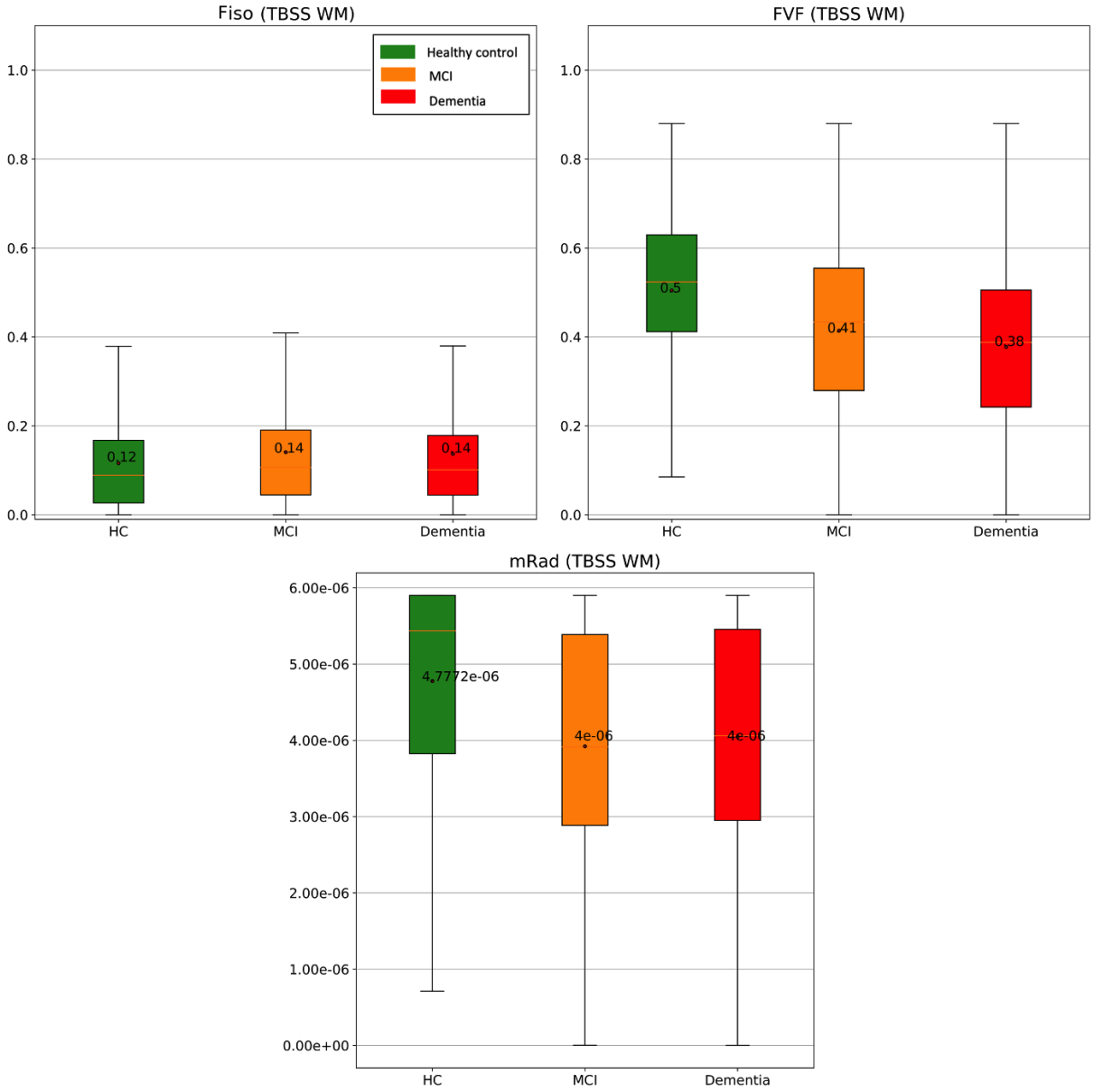


Figure 4.24: Box plot of MF metrics (F_{iso}, FVF and mRad) in the white matter (on an alignment-invariant skeleton) of the healthy control (HC), the MCI patient and the patient with dementia. The horizontal orange line represents the median of the distribution and the black marker represents the mean metric.

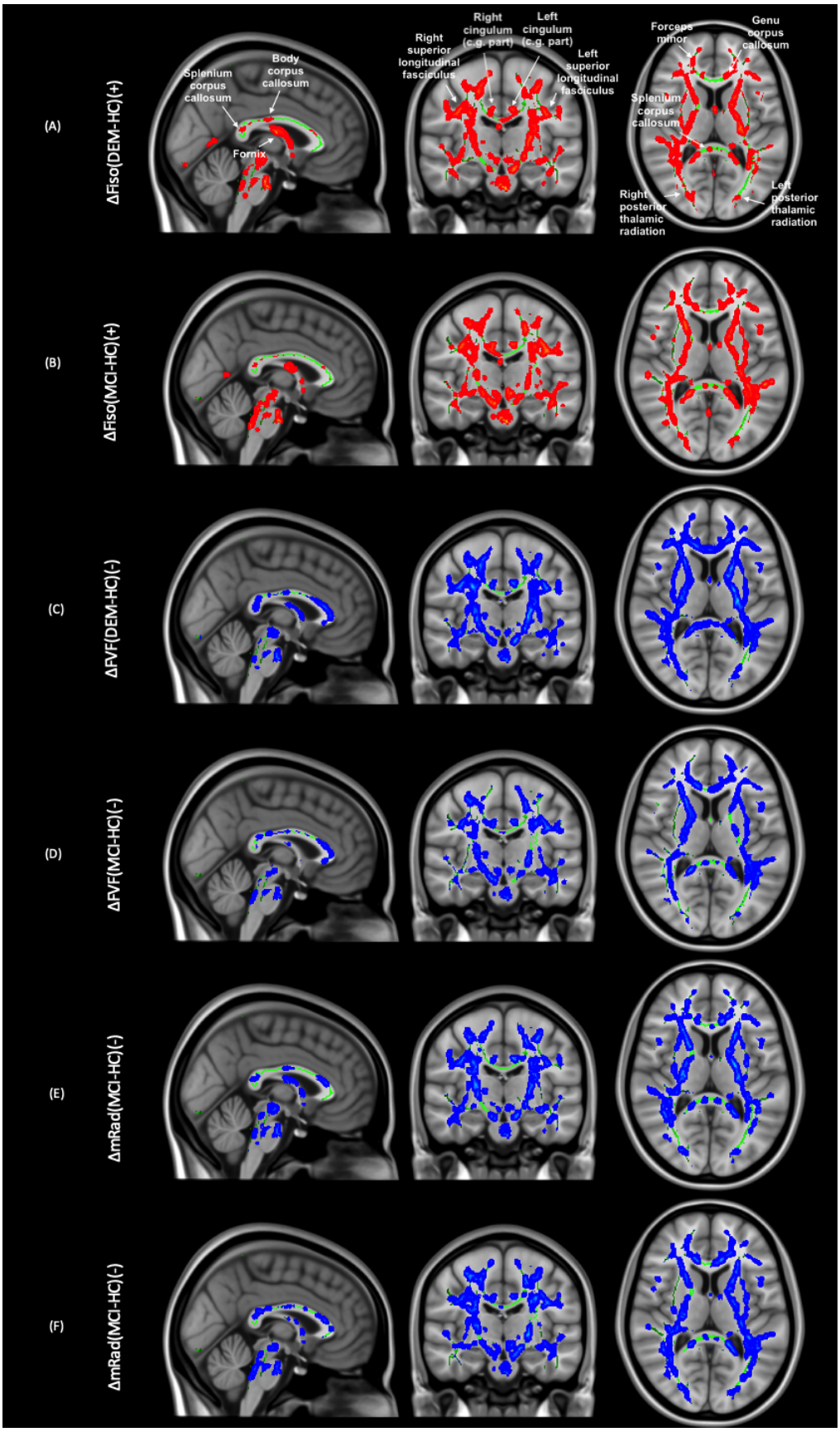


Figure 4.25: Regions of the skeleton showing (A) an increased F_{iso} in the patient with dementia (DEM) compared to the healthy control (HC), (B) an increased F_{iso} in the MCI patient, (C) a decreased FVF in the patient with dementia, (D) a decreased FVF in the MCI patient, (E) a decreased mRad in the patient with dementia and (F) a decreased mRad in the MCI patient.

4.6.2 Region-based analysis : results

The results of the ROI-based analysis, evaluating the MF metrics in regions known to be affected by AD are represented in Fig.4.26, Fig.4.27 and Fig.4.28. Box plots of the metrics evaluated in regions mildly affected by AD can be found in Appendix D.1.4.

An increased F_{iso} was observed in all the ROI in the AD patients except in the cingulum (the cingulate gyrus part). The increase in F_{iso} was more pronounced in the patient with dementia than in the MCI patient in most of the ROI, except in the left cingulum (the parahippocampal part), the left superior longitudinal fasciculus and the right posterior thalamic radiation. Although a small increased F_{iso} was observed in the middle cerebellar peduncle, the other regions known to be mildly affected by AD did not show differences in that metric between the healthy control and the AD patients.

A decreased FVF was observed in all the ROI, except in the right cingulum (the parahippocampal part) of the MCI patient, the left and right cingulum (cingulate gyrus parts) of the patient with dementia and the right uncinate fasciculus of the MCI patient. In most of the ROI, the decrease in FVF was more pronounced in the patient with dementia than in the MCI patient. Although no difference in FVF was observed in most of the regions mildly affected by AD, a small decreased FVF was observed in the middle cerebellar peduncle and the left superior cerebellar peduncle.

Finally, a decreased mRad was observed in all the ROI. The mRad was smaller in the patient with dementia than in the MCI patient in all the ROI, except in the right posterior thalamic radiation, the left superior longitudinal fasciculus, the forceps minor and the uncinate fasciculi. Although no difference in mRad was expected in the regions mildly affected by AD, a decreased mRad was observed in the cerebellar peduncles.

All the tracts highlighted in this ROI-based analysis also showed abnormal MF metrics in the skeleton-based analysis. However, by opposition to this ROI-based analysis, the skeleton-based analysis revealed an increased F_{iso} in the left and right cingulum (cingulate gyrus parts) in both AD patients.

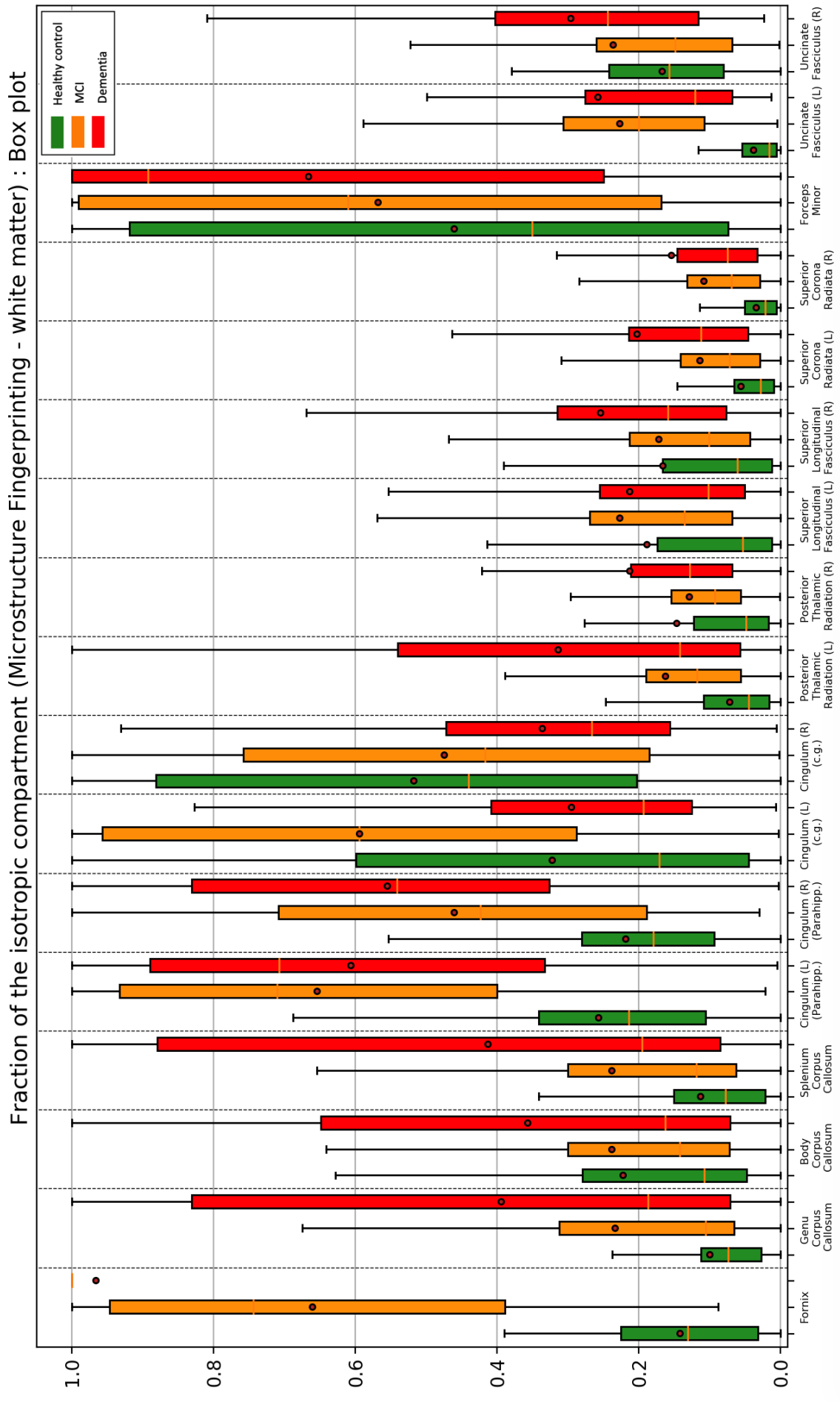


Figure 4.26: Box plot of the fraction of the compartment representing the isotropic diffusion (F_{iso}) in regions of interest for the healthy control (green), the MCI patient (orange) and the patient with dementia (red). The horizontal orange line represents the median of the distribution and the black marker represents the mean F_{iso} in the region of interest. From left to right, the regions of interest are: the left hippocampus entorhinal cortex, the right hippocampus entorhinal cortex, the anterior division of the inferior temporal cortex, the posterior division of the inferior temporal cortex, the temporooccipital part of the inferior temporal cortex, the posterior division of the middle temporal cortex, the temporooccipital part of the middle temporal cortex, the fusiform cortex, the precuneous cortex, the frontal pole, the superior frontal gyrus, the parahippocampal gyrus (anterior division), the parahippocampal gyrus (posterior division), the posterior cingulate cortex, the left hippocampus, the right hippocampus, the left amygdala and the right amygdala.

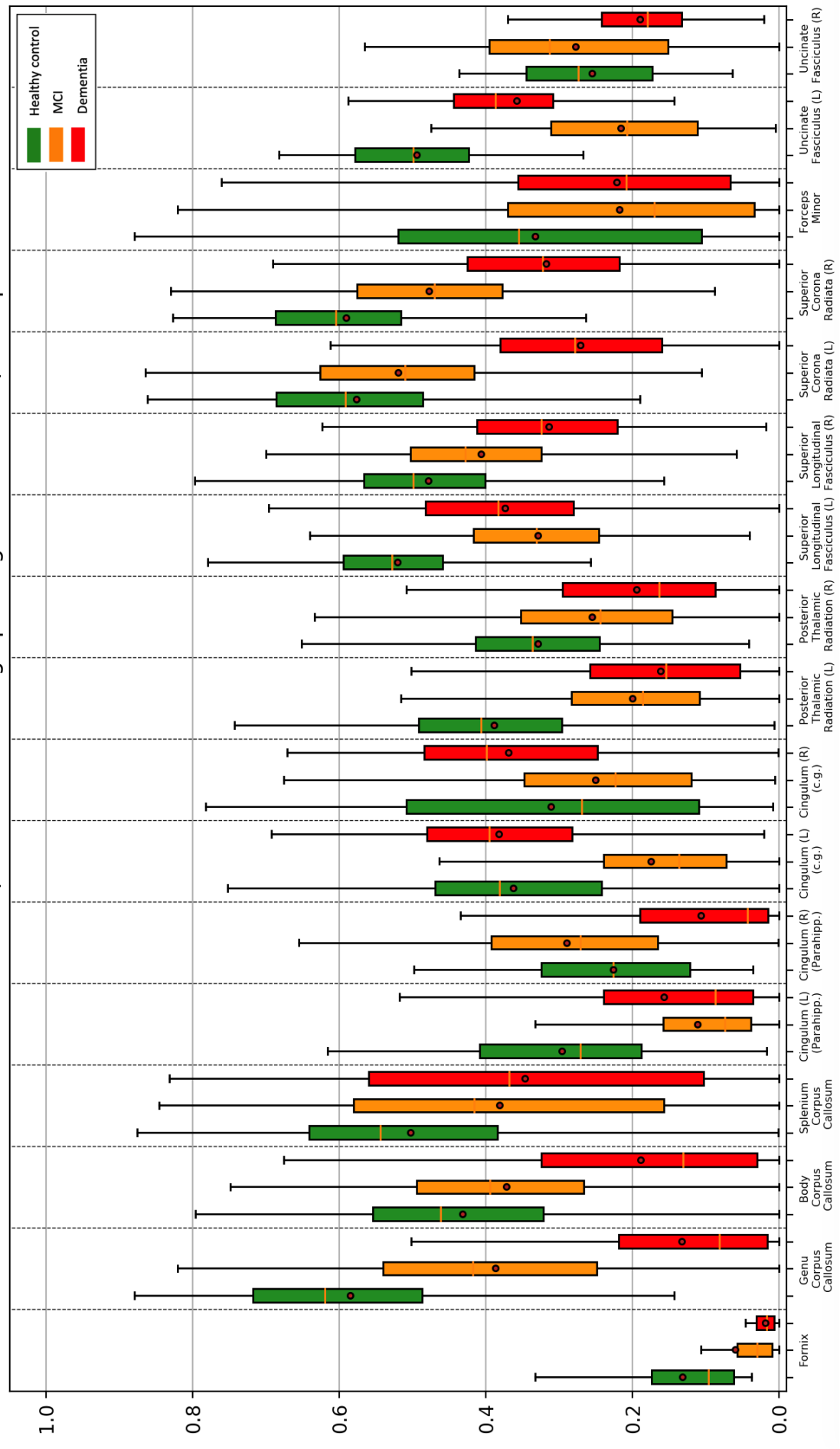


Figure 4.27: Box plot of the total fiber volume fraction (FVF) in regions of interest for the healthy control (green), the MCI patient (orange) and the patient with dementia (red). The horizontal orange line represents the median of the distribution and the black marker represents the mean FVF in the region of interest. From left to right, the regions of interest are: the left hippocampus entorhinal cortex, the right hippocampus entorhinal cortex, the anterior division of the inferior temporal cortex, the posterior division of the inferior temporal cortex, the temporooccipital part of the inferior temporal cortex, the posterior division of the middle temporal cortex, the temporooccipital part of the middle temporal cortex, the fusiform cortex, the precuneous cortex, the frontal pole, the superior frontal gyrus, the parahippocampal gyrus (anterior division), the parahippocampal gyrus (posterior division), the posterior cingulate cortex, the left hippocampus, the right hippocampus, the left amygdala and the right amygdala.

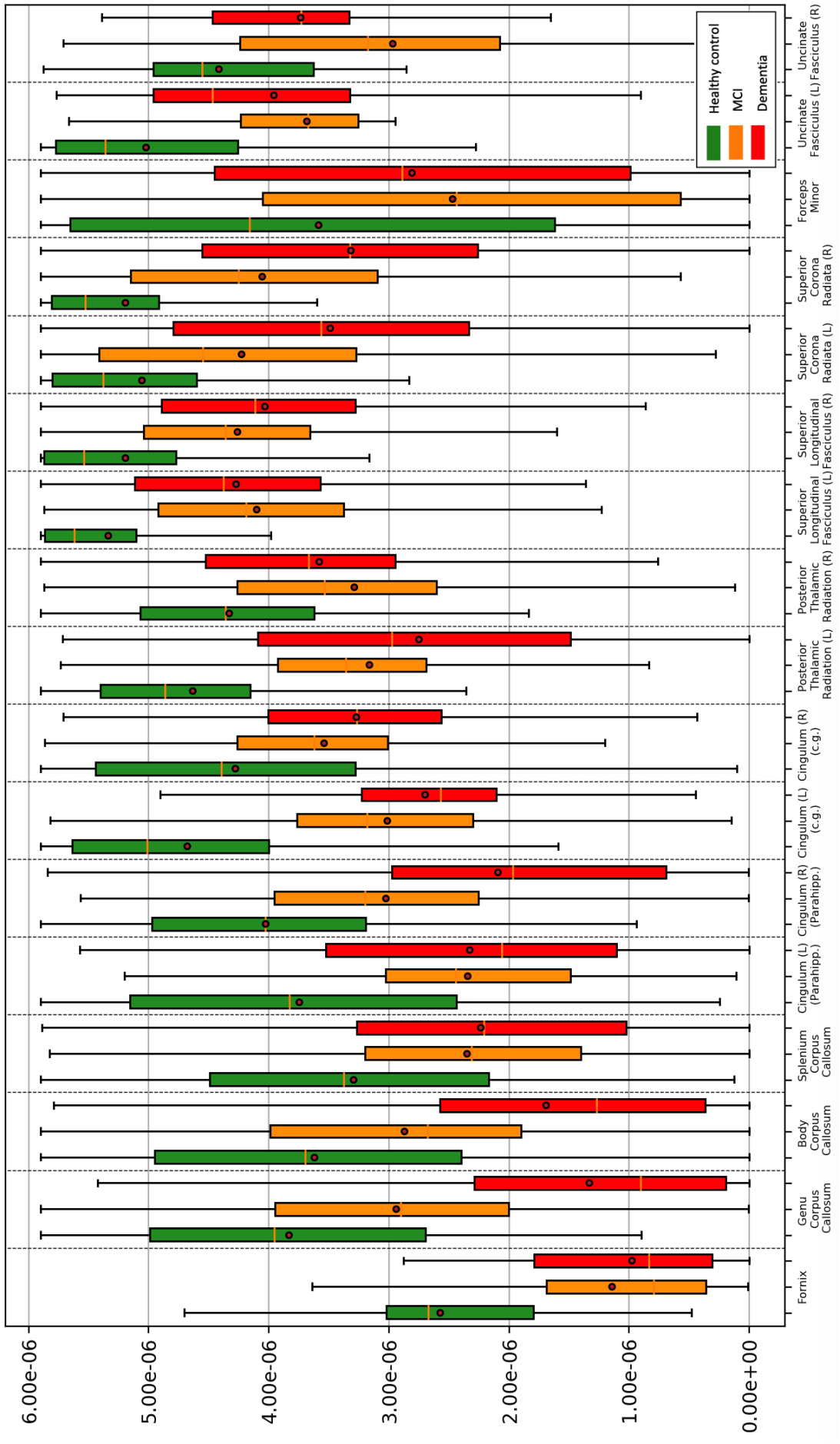


Figure 4.28: Box plot of the mean apparent axonal radius (mRad) in regions of interest for the healthy control (green), the MCI patient (orange) and the patient with dementia (red). The horizontal orange line represents the median of the distribution and the black marker represents the mean mRad in the region of interest. From left to right, the regions of interest are: the left hippocampus entorhinal cortex, the right hippocampus entorhinal cortex, the anterior division of the inferior temporal cortex, the posterior division of the inferior temporal cortex, the temporooccipital part of the inferior temporal cortex, the posterior division of the middle temporal cortex, the temporooccipital part of the middle temporal cortex, the fusiform cortex, the precuneous cortex, the frontal pole, the superior frontal gyrus, the parahippocampal gyrus (anterior division), the parahippocampal gyrus (posterior division), the posterior cingulate cortex, the left hippocampus, the right hippocampus, the left amygdala and the right amygdala.

4.6.3 Discussion

MF is a model that uses Monte Carlo simulations of the random walk of water molecules in different microstructural environments to link the DW-MRI signal to microstructural features of brain tissues by solving an optimization problem. The optimal microstructural parameters in a voxel are chosen by minimizing the difference between the actual signal measured in the voxel and the simulated signal that would arise from an environment characterized by those microstructural features (i.e. axons with specific apparent axonal radius and spacing between them). This model is based on the superposition principle of crossing fibers and assumes that no exchange of water between the fascicles occurs during the acquisition time. The MF metrics analyzed in this study were: the fraction of the compartment representing the restricted isotropic diffusion (F_{iso}), the total fiber volume fraction (FVF) and the mean apparent axonal radius of the fibers (mRad).

The whole-brain WM analyses revealed an increased F_{iso}, decreased FVF and decreased mRad. Those findings reflect the atrophy of neurons in AD patients as indicated by the decreased axonal radii and decreased volume of water inside the axons. In the mask-based analysis, a severe increase in F_{iso} was observed in the WM of AD patients while no large differences between the healthy control and the AD patients were observed in the skeleton-based analysis. This observation has two possible justifications.

(1) An increased F_{iso} occurred mainly in regions with the most variable tracts across the subjects (i.e. not in the highly aligned axons represented by the skeleton). Therefore, the voxels showing an increased F_{iso} may be situated directly beneath the GM, where the metrics are not evaluated in the skeleton-based analysis and where $A\beta$ deposits have been observed in a study conducted on autopsy specimens of pathologically verified AD patients [114].

(2) In the mask-based analysis, errors during the registration of MF maps with the anatomical images would lead to a biased F_{iso}. Indeed, if misregistrations with the WM mask occurred and that F_{iso} was evaluated in GM voxels (where $F_{iso} = 1$), higher values of the metric will be considered in the box plot.

Those results support the assumption that the mask-based analysis and the skeleton-based analysis are complementary. The ROI-based analysis confirmed the results of the whole-brain WM analyses and observed an increased F_{iso}, a decreased FVF and decreased mRad in the AD patients in most of the ROI. Those ROI are involved in a variety of cognitive functions including: the control of attention [80], working memory [88], episodic memory [92], social processing [92], verbal coding and non-verbal coding in memory [79], etc.

The sparsity constraints considered when solving the optimization problem ensure that, for a specific orientation, only one fascicle configuration is chosen out of all possibilities in the fascicle dictionary. This constitutes a limitation of the model since it prevents the selection of multiple configurations for fascicles presenting "delimited sub-regions with distinct microstructural properties" [32]. Moreover, generating the dictionary in the pre-computing step is computationally intensive. During runtime, the time complexity increases when more fascicles are considered in the voxels. The computation time is also increased for larger dictionaries that enable more possibilities of microstructural configurations to be evaluated. However, using larger dictionaries for the sparse optimization problem leads to a finer resolution [32].

This model is powerful and has many advantages. The model computes microstructural parameters such as the mRad and the FVF that are biologically interpretable without the need of *a posteriori* interpretation as for phenomenological models. The microstructural features computed lead to "more accurate, consistent and interpretable results than popular closed-form microstructural models" [32]. Monte Carlo simulations of DW-MRI signals are known to provide the exact signal for any tissue geometry [32]. Finally, since substantial differences in microstructural parameters were observed between the AD patients and the healthy control, those results suggested that MF could reliably discriminate AD cases from normal cases, even at an early clinical stage of the disease. Those results show the great potential for MF metrics to be used as biomarkers of neuronal injury in AD due to their specificity and interpretability.

4.7 Final discussion

NODDI, DIAMOND and MF are multi-compartment models that changed the way of quantifying microstructural brain anomalies from an analysis focusing on metrics that characterize an entire voxel towards an analysis that characterizes each compartment in every voxel individually. By opposition to NODDI, DIAMOND and MF consider multiple fascicle compartments, each one being characterized individually.

Neuronal injury is an important neuropathological hallmark of AD that was highlighted in the AD patients with those multi-compartment models. Some metrics showed substantial differences between the healthy control and the AD patients. However, practicalities have to be considered. Therefore, three metrics (one for each multi-compartment model) that showed the largest differences between the healthy control and the AD patients were further discussed in this section. This study revealed a decreased fraction of the intra-cellular volume fraction (decreased NDI in NODDI), a decreased fraction of the voxels occupied by compartments with an anisotropic diffusion, e.g. fascicles (decreased F_{aniso} in DIAMOND) and a decreased total fiber volume fraction (decreased FVF in MF). Box plots of previous results illustrating this discussion and a summary table are represented in Fig.4.29.

(1) It was suggested that NODDI assumptions were "problematic" [25] (e.g. axons with zero-radii and one type of fascicles throughout the brain) and "defeated the purpose of biophysical modeling" [25] since fixing *a priori* values (e.g. fixed isotropic diffusivity, fixed axial diffusivity in the extra-neurite space, fixed intra-neurite diffusivity and the radial diffusivity of the extra-neurite space is linked to the axial diffusivity of the space by the tortuosity model)[8] cannot reflect the "underlying biological reality" [25]. This approach may lead to biased estimation of the parameters.

(2) Moreover, DIAMOND and MF metrics showed larger differences between the AD patients and the healthy control (with a larger difference observed in DIAMOND metrics) than NODDI metrics, suggesting that DIAMOND and MF may be more reliable than NODDI to discriminate pathological tissues in AD from healthy tissues (Fig.4.29).

(3) Finally, the FVF metric computed by MF (a microstructural model) is biologically more interpretable than the F_{aniso} metric evaluated by DIAMOND (a phenomenological model). The difference between the two metrics is illustrated in Fig.4.30. For the sake of clarity, a one-fascicle voxel was chosen to illustrate the difference between those two metrics, but the interpretation is also valid for two-fascicle voxels. The F_{aniso} metric (DIAMOND) in that voxel was 0.83 while MF computed the FVF (i.e. total fiber volume fraction) representing the fraction of water inside the axons with a computation based on tissue geometry (e.g. axonal radius, axonal density and fraction of occupancy of the voxel by the fascicles). FVF was computed as the sum of individual fiber volume fractions (in this example, there is only one fascicle in the voxel), weighted by the fraction of occupancy of the voxel by the fascicles (estimated to 0.81 by the model in the one-fascicle voxel chosen). The fiber volume fraction of a fascicle is computed based on the apparent axonal radius ($r = 5.9 \cdot 10^{-6}$ [m]) and the spacing between the axons in the fascicle ($s = 1.55 \cdot 10^{-5}$ [m]) estimated by the model. Therefore, while DIAMOND gives information about the fraction of the voxel occupied by anisotropic compartments (e.g. fascicles), this model does not give an insight into the arrangement of axons in the fascicles.

The use of different types of analyses were needed to characterize more precisely the alterations due to AD and avoid wrong interpretations of the metrics. For example, while misregistration errors may occur in the mask-based analysis of the whole brain WM, the skeleton-based analysis is not sensitive to misregistrations but only evaluates metrics in highly aligned axons of the WM. Moreover, while one-fascicle models are known to perform well in voxels with a single fascicle (voxels that constitute most of the WM skeleton), their interpretation remains limited in voxels with crossing fascicles (i.e. tracts with high inter-subject variability that are not considered in the skeleton-based analysis). Those arguments show the importance of the complementarity of the analyses that were chosen to be conducted in this Master's thesis.

8 More information about the assumptions in NODDI can be found in section 2.3.1.

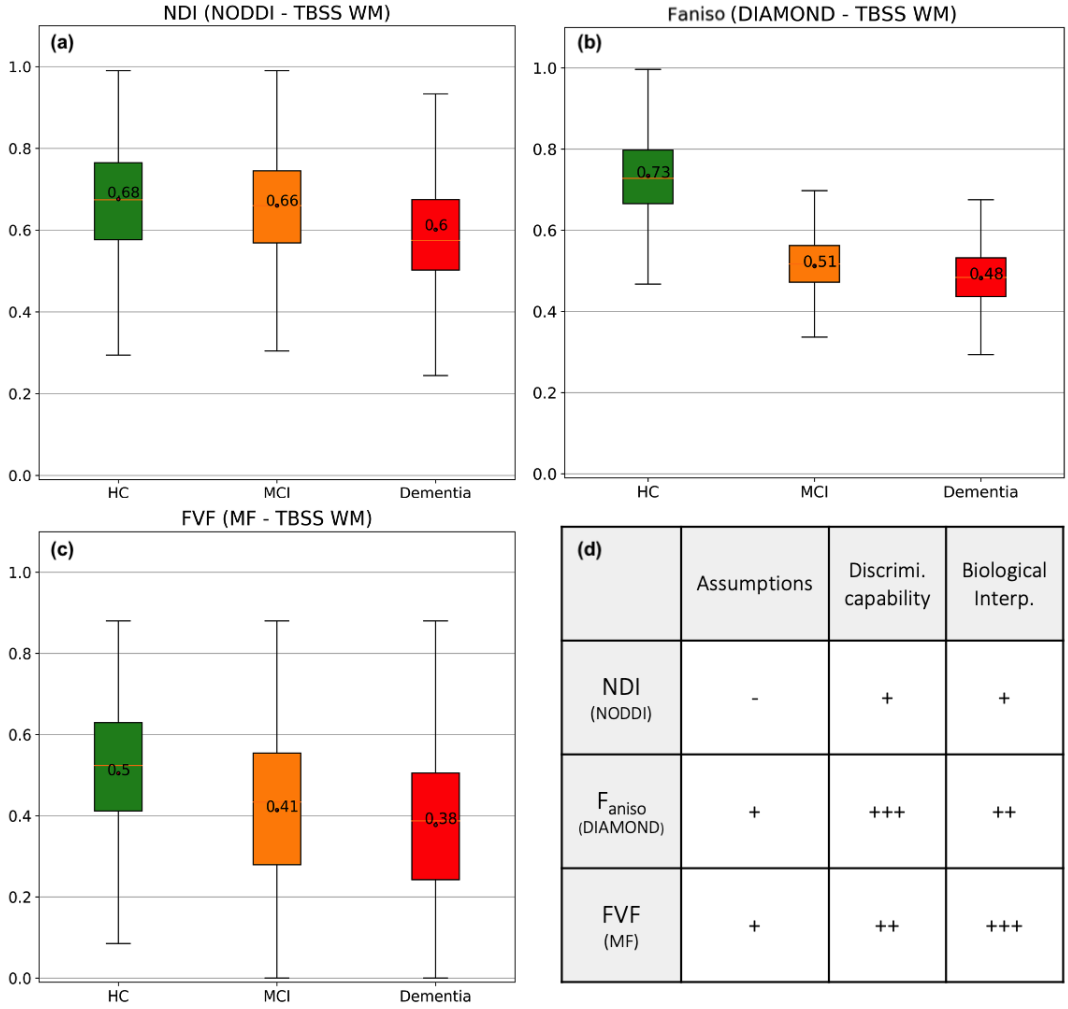


Figure 4.29: Final discussion about the metrics of multi-compartment models showing the largest differences between the healthy control and the AD patients. Those metrics reflected the neuronal injury in the AD patients: **(a)** a decreased intra-cellular volume fraction in NODDI (decreased NDI), **(b)** a decreased fraction of occupancy of the voxels by anisotropic compartments in DIAMOND (decreased F_{aniso}) and **(c)** a decreased total fiber volume fraction in MF (decreased FVF). Although previously reported, those results were included in this final discussion for a better visualization of the statements. The results presented were obtained with the analysis based on the alignment-invariant white matter skeleton. **(d)** A summary table that compares the models' metrics was included to illustrate the final discussion. ▶ The "**assumption**" category represents the hypotheses assumed by the model (-: strong assumptions are considered before fitting the model, e.g. one-fascicle compartment in the voxel, *a priori* fixed values, axons with zero-radii ; +: no such strong assumptions, e.g. various compartments representing the fascicles in the voxel, no *a priori* fixed values and no assumption about the type of fascicle in the voxels). ▶ The "**discriminatory capability**" category represents the magnitude of differences in the metrics between the AD patients and the healthy control (+++: largest differences observed ; ++: second largest differences observed ; +: smallest differences observed). Differences were even larger for MF when the metric was evaluated with a mask of the whole-brain white matter, that evaluated the metrics in voxels with crossing and highly variable fibers, where multi-fascicle models perform well. However, to fairly compare the models, the results along the skeleton were presented, where the hypothesis of NODDI (that considers one compartment for the fascicles) was met. ▶ The **biological interpretation** of the metrics is the last category evaluated (+++: this metric is easily interpreted and reflects the tissue biology with a computation based on tissue geometry, i.e. axonal radius and the fiber density ; ++: this metric represents the fraction of occupancy of the voxels by compartments with an anisotropic diffusion (e.g. fascicles) without giving an insight about the arrangement of the axons in the fascicles ; +: this model gives an estimation of the neurite density, but the interpretation suffers from the hypotheses assumed by the model, e.g. a single type of fiber considered throughout the entire brain and a single compartment characterizing the fascicles in every voxel).

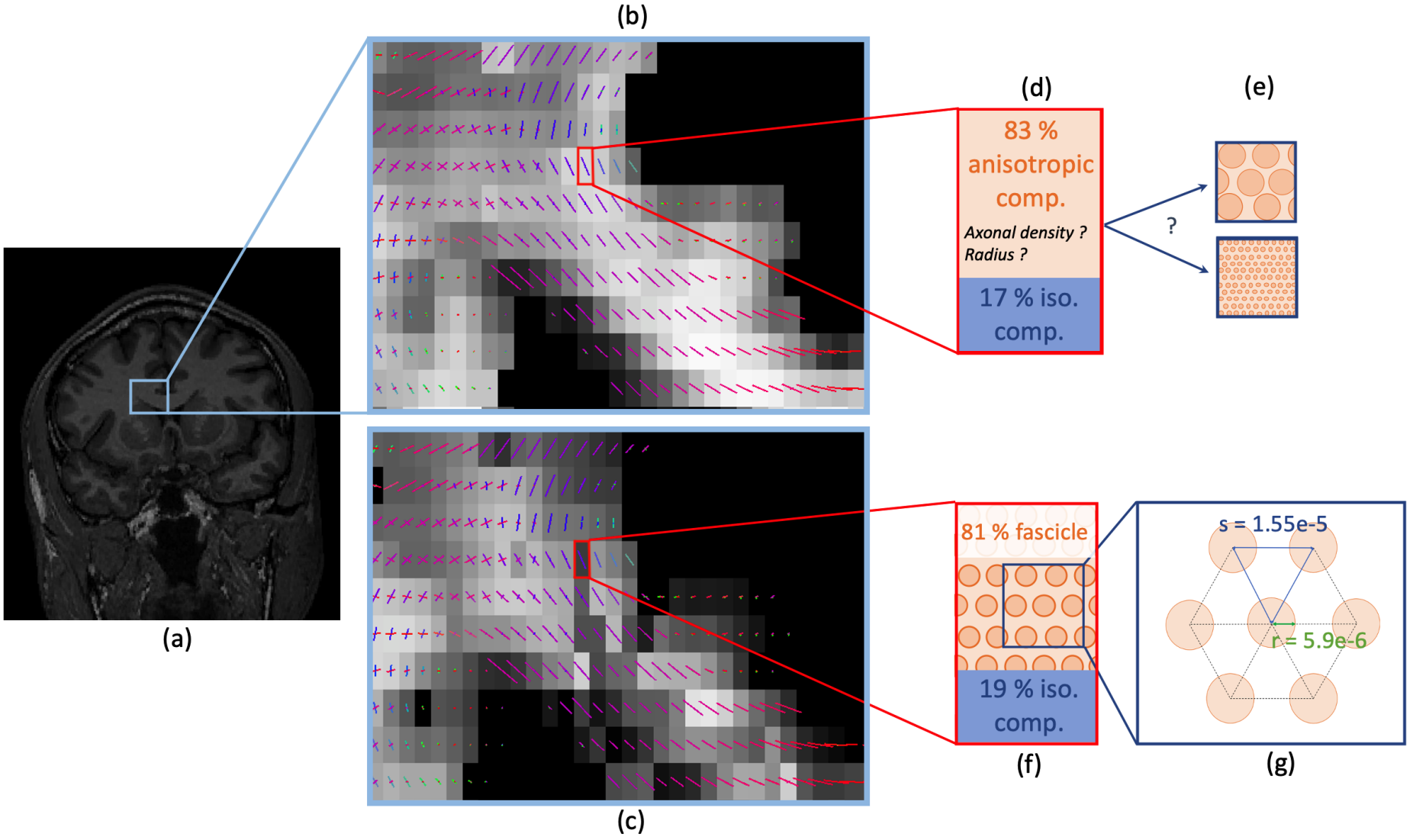


Figure 4.30: Comparison of the F_{aniso} metric (DIAMOND) and the FVF metric (MF). **(a)** T1-weighted image of the healthy control. A one-fascicle voxel was chosen randomly and highlighted in the **(b)** F_{aniso} (fraction of anisotropic compartments) map (DIAMOND) and the **(c)** FVF (total fiber volume fraction) map (MF). **(d)** The value of the voxel in the F_{aniso} map was 0.83 and represents the physical fraction of the voxel occupied by the anisotropic compartment (and 0.17 is the fraction of the isotropic compartment estimated in the voxel), **(e)** without knowing how the axons are arranged. **(f)** The value of FVF in the voxel was 0.42, the fraction of the fascicle (f_1) was 0.81 and the fiber volume fraction (fvf_1) of the fascicle was 0.52. The FVF being the sum of the fiber volume fraction of each fascicle, weighted by their respective physical fraction in the voxel, the total fiber volume fraction (FVF) is computed as: $FVF = f_1 \cdot fvf_1 + f_2 \cdot fvf_2 = 0.81 \cdot 0.52 + 0 = 0.81 \cdot \frac{2\pi}{\sqrt{3}} \left(\frac{r}{s}\right)^2 = 0.42$, **(g)** where 'r' is the apparent axonal radius (estimation: $5.9 \cdot 10^{-6}$ [m]) and 's' is the spacing between the axons in the fascicle (estimation: $1.55 \cdot 10^{-5}$ [m]) that are estimated by the model that considers a hexagonal packing of axons in the fascicle.

4.8 Limitations

A study conducted with a larger number of subjects could carry out voxelwise statistics across subjects on the skeletonized WM as proposed by the TBSS approach [110] in order to highlight voxels that show significant differences between the healthy control and the AD patients. Therefore, only portions of the skeletonized WM showing significant differences (p-value $< \alpha$, with α usually equal to 0.05) in diffusion metrics could be further investigated.

Although mentioned in the analysis of macroscopic changes, the age of the patients were not considered during the analyses of microstructural changes. Microstructural changes occur during the aging process (e.g. cortical disconnection, WM deterioration including myelin breakdown [66], etc.), leading to altered diffusion metrics. The age of the MCI patient (69 years) and the patient with dementia (70 years) are close, meaning that metric differences between those patients are mainly due to the clinical stage of their respective disease rather than their difference of age. However, the healthy control was younger (41 years). Therefore, differences in diffusion metrics between the AD patients (MCI patient and the patient with dementia) and the healthy control may be influenced by their difference of age. With a larger sample size, those age-related changes in AD could be partially ruled out by considering the age of the patients as a covariate for the voxelwise statistics (when comparing patients of different age groups). However, comparing patients in the same age group (healthy and AD patients) could help to characterize more precisely alterations driven by the disease. Moreover, various pathological conditions are common in the elderly such as WM hyperintensities (or "leukoaraiosis") resulting from small vessels diseases (e.g. hypoxia, ischemia) [115]. Those pathological appearances of the WM, frequently seen in older patients [115], should be inspected before analyzing the diffusion maps.

In the ROI-based analysis, a small misalignment of the patient maps with the standard MNI during the registration step could lead to a biased estimation of the diffusion metric in a ROI, especially in structures close to the CSF (e.g. the fornix). In order to alleviate misregistration problems, a tractography-based analysis could be conducted. However, investigating each tract of interest with this approach is laborious and becomes cumbersome when more subjects are included in the study. Indeed, this method requires a manual inspection, is hardly automated and prevents the whole-brain to be inspected [110].

Finally, neuropsychological scores assessing the cognitive functions of the patients would have enhanced the validity of the findings of this study, when possible function impairments were discussed for regions showing abnormal metrics.

Conclusion and perspectives

Four DW-MRI models (DTI, NODDI, DIAMOND and MF) were used in this Master's thesis to quantify microstructural brain anomalies in patients with different clinical stages of AD: a patient with dementia and an MCI patient. The advantages and limitations of each model were discussed. While DTI and NODDI are models that have been widely used in the literature to quantify brain anomalies in patients with AD, DIAMOND and MF are recently developed models that have never been used to that end.

In this study, different analyses of the brain microstructure were conducted: (1) a whole-brain WM analysis and (2) a region-based analysis. The whole-brain analysis was further divided into: (1a) a mask-based analysis, where the metrics of the models were evaluated along the WM of the subjects with patient specific WM masks created from anatomical images and (1b) a skeleton-based analysis that evaluated the metrics of the models along a WM skeleton mainly composed of voxels with coherently aligned axons and that prevents inter-subject variability. The complementarity of those analyses gave a detailed characterization of the brain tissue and reduced the risk of wrong interpretations that may result from the strong assumptions of the models or registration errors.

Based on the interpretation of the metrics, several pathological alterations in the patients with AD were highlighted. Microstructural changes were observed in WM regions involved in a variety of cognitive functions that are known to be altered in AD and that were discussed in this study. It was suggested that DIAMOND and MF had a greater discriminatory capability than DTI and NODDI, since larger differences in their respective metrics were observed between the healthy control and the patients with AD. Moreover, DIAMOND and MF are multi-compartment models that consider multiple fascicles of different types in the voxels and do not make assumptions about the parameters of the model. Lastly, MF estimates metrics that are biologically more interpretable than the metrics of phenomenological models or microstructural models that make strong assumptions to reduce the complexity of the problem. The results of this study brought out the great potential for DIAMOND and MF metrics to be used as biomarkers of neuronal injury in AD.

With the increasing evidence about the ability of multi-compartment models to capture the presence of reactive microglia and the key role of microglia in the neuroinflammation observed in AD, further research could investigate how metrics of multi-compartment models are changed in the presence of reactive microglia in AD. Those models can specifically model a compartment with restricted isotropic diffusion that can reflect the diffusion of water molecules trapped in reactive microglia. The influence of the presence of reactive microglia on the metrics of the models could be evaluated by comparing the metrics in a mouse model of human AD with and without microglia depletion, when an isotropic restricted compartment is considered. Further studies could also evaluate the metrics in regions where an accumulation of neurofibrillary tangles is observed with Positron Emission Tomography, a technique that enables *in vivo* characterization of the tau pathology. Assessing the presence of neurofibrillary tangles is crucial since their presence is more closely associated with cognitive deficits in AD, than the presence of $A\beta$ plaques, another key pathological component of the disease. If a signature of the presence of reactive microglia and neurofibrillary tangles in AD was found in the metrics of multi-compartment models, those models could help to better monitor the propagation of the disease and understand the neuroinflammatory response involving reactive microglia with a non-radiating, non-invasive, high-resolution and available technology. Finally, further research could also evaluate how different parameters of the diffusion-encoding sequences used for the acquisition of the diffusion data may improve the sensitivity to alterations when those models are used to quantify microstructural brain anomalies in patients with AD.

Appendices

Appendix A

Summary of the literature survey of DW-MRI in Alzheimer's disease

Study	Title	Results
	DTI and Extensions	
Q. Wen et al., 2019	*"White matter alterations in early-stage Alzheimer's disease: A tract-specific study"*	- Increased RD in the parahippocampal cingulum. - Decreased FA in posterior thalamic radiations. - Increased MD in forceps major. - Diffusion metrics correlated to cognitive performance of MCI individuals.
C.D. Mayo et al., 2016	*"Longitudinal changes in microstructural white matter metrics in Alzheimer's disease."*	- Decreased FA in one year for AD individuals and healthy controls. - Increased MD in one year for AD individuals and healthy controls. - Changes in AD are mainly observed in the hippocampal cingulum, the corpus callosum, the internal and external capsule, the corona radiata, the posterior thalamic radiation, the superior and inferior longitudinal fasciculus, the fronto-occipital fasciculus, the cingulate gyri, the fornix, the uncinate fasciculus and the tapetum. - Microstructural changes (FA and MD) due to the aging process.
N.T. Doan et al., 2017	*"Dissociable diffusion MRI patterns of white matter microstructure and connectivity in Alzheimer's disease spectrum"*	- Decreased FA in AD group in occipital, temporal, parietal and frontal WM, in the corpus callosum and in the fornix. - Increased axial diffusivity, MD and RD in AD group in occipital, temporal, parietal and frontal WM, in the corpus callosum and in the fornix.
H.L. Jacobs et al., 2018	*"Structural tract alterations predict downstream tau accumulation in amyloid-positive older individuals."*	- Lower hippocampal volume is associated with increased MD, increased axial diffusivity and increased RD in the hippocampal cingulum WM bundle. - Abnormal DTI values in the hippocampal cingulum bundle are associated to a higher tau accumulation in the posterior cingulate cortex. - Tau pathology propagates via connectivity. - DTI values of amyloid-positive patients predict their memory decline.

Study	Title	Results
	DTI and Extensions (continued)	
K. Kantarci et al., 2017	*"White-matter integrity on DTI and the pathologic staging of Alzheimer's disease."*	- Increased MD and decreased FA in the medial temporal limbic connections and the medial parietal WM. - Diffusivity values in the ventral cingulum tract, the crus of the fornix and the entorhinal WM were highly correlated to Braak NFT tangle staging.
R.D. Perea et al., 2018	*"Microstructural white matter alterations in preclinical Alzheimer's disease detected using free water elimination diffusion tensor imaging"*	- Decreased FA, increased RD and increased MD in the body and crus of the fornix of AD patients. - Axial diffusivity not increased. - No volumetric changes in the fornix. - Diffusion metrics more sensitive to fornix degeneration than volumetric changes in AD. - Lower Generalized FA (obtained with GQI model). - GFA more sensitive to degradation in myelin sheath when no volumetric change is observed.
G. Operto et al., 2018	*"White matter microstructure is altered in cognitively normal middle-aged APOE-4 homozygotes."*	- Increased RD (+++) and axial diffusivity (+) in WM of APOE-ε4 carriers, mainly in the superior longitudinal fascicule.
J.S. Rabin et al., 2019	*"Synergism between fornix microstructure and beta amyloid accelerates memory decline in clinically normal older adults"*	- Acceleration of cognitive decline in episodic memory with a lower FA in the fornix and an elevated Aβ burden. - Microstructural changes in WM tracts directly connected to hippocampus in interaction with Aβ burden, hasten cognitive decline. - Fornix degradation is linked to the progression of normal to MCI and MCI to AD dementia.
P.S. Weston et al., 2015	*"Diffusion imaging changes in gray matter in Alzheimer's disease: a potential marker of early neurodegeneration."*	- Increased MD in the hippocampus, the amygdala, the medial temporal GM and the frontal GM. - Increased MD in the hippocampi, the parahippocampal gyri, the amygdala, posterior congulate cortex and precuneous cortex. -Increased MD in precuneous cortex, posterior cingulate cortex and the frontal cortices.

Study	Title	Results
	NODDI	
X. Fu et al., 2019	*"Microstructural White Matter Alterations in Mild Cognitive Impairment and Alzheimer's Disease: Study Based on Neurite Orientation Dispersion and Density Imaging (NODDI)"*	- NDI values are strongly correlated to Aβ deposition and tau proteins. - Decreased NDI and ODI in WM in MCI and AD compared to healthy controls. - Increased fraction of isotropic water in MCI and AD compared to healthy controls, mainly in the bilateral medial temporal lobes. - NDI mainly reduced in the splenium of the corpus callosum and the bilateral superior longitudinal fasciculus. - ODI mainly reduced in WM of the frontal and occipital lobes. - AUC for the NDI values of the splenium >than AUC for FA. - AUC for the fraction of isotropic water of the right cerebral peduncle >than AUC for FA.
N. Colgan et al., 2015	*"Application of neurite orientation dispersion and density imaging (NODDI) to a tau pathology model of Alzheimer's disease"*	- NODDI values are correlated to histological measurements of the tau pathology in GM in a mouse model of human tauopathy. - Decreased in NDI and ODI in the hippocampal finer tracts (i.e. limbic system) of a mouse model of human tauopathy. - Decreased ODI in the cortex (GM) and increased in NDI and fraction of isotropic water.
T.D. Parker et al., 2018	*"Cortical microstructure in young onset Alzheimer's disease using neurite orientation dispersion and density imaging"*	- Decreased NDI (in young onset AD) in regions associated with early atrophy in AD (i.e. entorhinal cortex, inferior temporal gyrus, middle temporal gyrus, fusiform gyrus and precuneus) - Decreased NDI in a relatively spared region in AD (precentral gyrus) while no macroscopic change was observed. - NODDI values more sensitive marker to AD pathology. - Decreased ODI in inferior temporal gyri, middle temporal gyri, fusiform gyrus and precuneus in young onset AD.
J. Zhang, 2019	*"Applications of NODDI for imaging in vivo white matter pathology in neurodegenerative diseases"*	- Decreased NDI and decreased ODI observed in young-onset AD patients compared to healthy controls. - Increased f_{iso} was observed around the corpus callosum and fornix in young-onset AD patients compared to healthy controls.
Q. Wen et al., 2019	*"White matter alterations in early-stage Alzheimer's disease: A tract-specific study"*	- Increased in f_{iso}, increase in ODI and decrease in NDI in MCI patients and AD patients.
A.P. Merluzzi et al., 2016	*"Age-Dependent Differences in Brain Tissue Microstructure Assessed with Neurite Orientation Dispersion and Density Imaging"*	- Age would be associated with a decrease in NDI and ODI parameters in GM related to losses in neurite arborization. - It was hypothesized that the ODI in WM would increase with age due to a greater dispersion of axons. However, they observed a decrease in ODI. - NDI in WM could decrease with age due to a reduced packing density - f_{iso} is increased with age, reflecting cell shrinkage.

Table A.1: Summary table of the literature survey of DW-MRI in Alzheimer's disease

Appendix B

Visualization of the regions of interest in Alzheimer's disease

B.1 White matter tracts of interest

A High Angular Resolution Diffusion Imaging (HARDI) scheme was used. The data was acquired at St Luc University Hospital on a 3T GE (Chicago, IL) SIGNA^{TM} Premier scanner, equipped with 48-channel head coil. Diffusion images were acquired at a fixed b-value with more directions than the minimum number required in DTI. A total of 128 diffusion sampling directions were acquired. The b-value was 1000 s/mm^2. The tractography images were generated with DSI Studio.

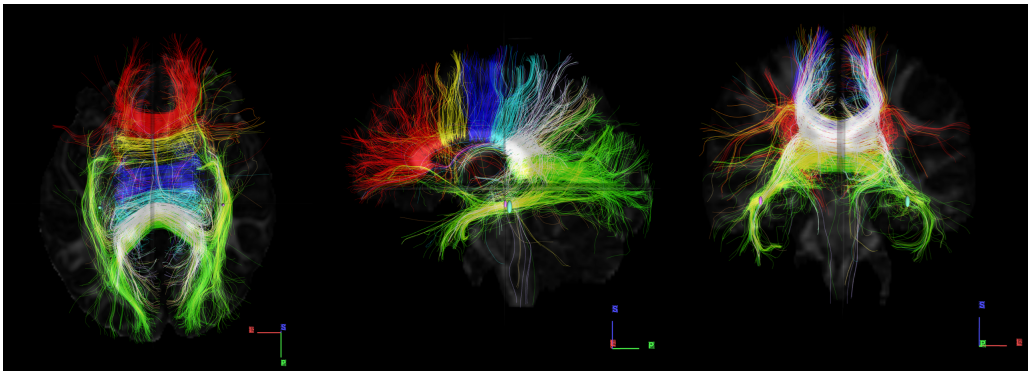


Figure B.1: Axial view (left), sagittal view (middle) and coronal view (right) of the corpus callosum with the genu (red), the anterior body (yellow), the central body (dark blue), the posterior body (light blue), the isthmus (white) and the splenium (green). The green fibers extending to the temporal lobe are the tapetum of the corpus callosum. Two Regions of Interest (ROIs) were drawn based on the DSI Atlases and tracts passing through those regions were represented.

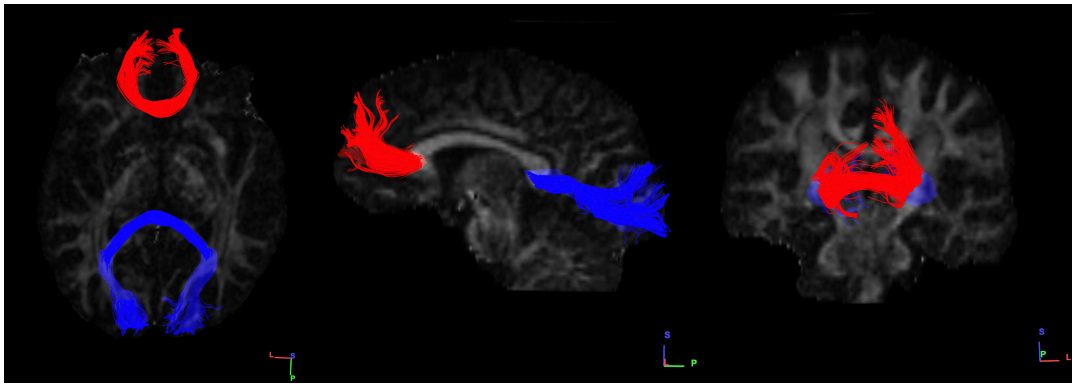


Figure B.2: Axial view (left), sagittal view (middle) and coronal view (right) of the forceps major (blue) and forceps minor (red).

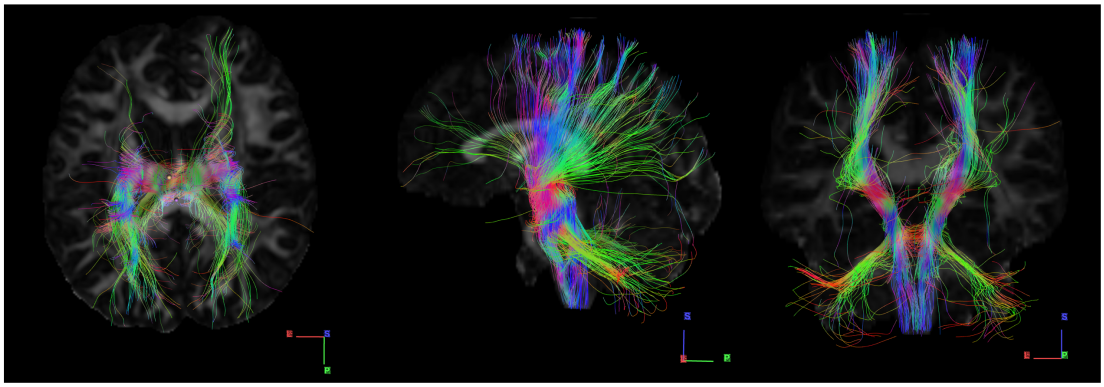


Figure B.3: Axial view (left), sagittal view (middle) and coronal view (right) of the corona radiata with the colors representing the directions of the fibers.

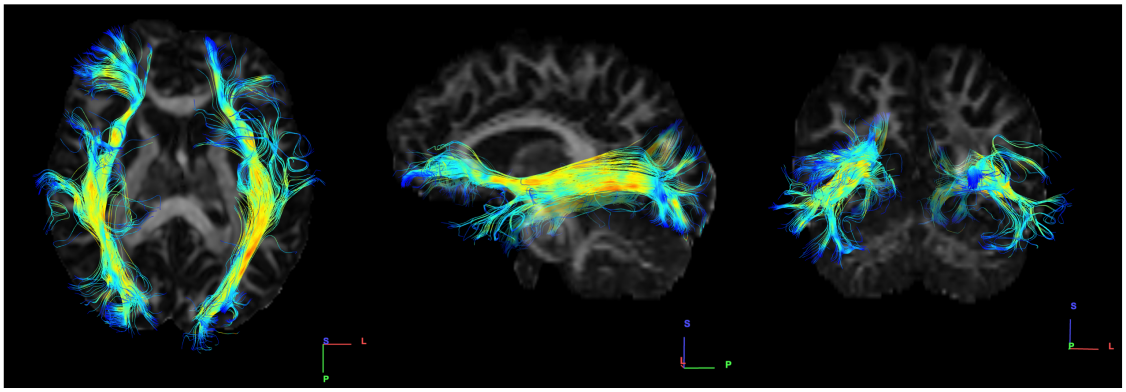


Figure B.4: Axial view (left), sagittal view (middle) and coronal view (right) of the thalamic radiation (anterior thalamic radiation in the rostral part of the brain and posterior thalamic radiation in the caudal part of the brain) with the colors representing the local index of FA.

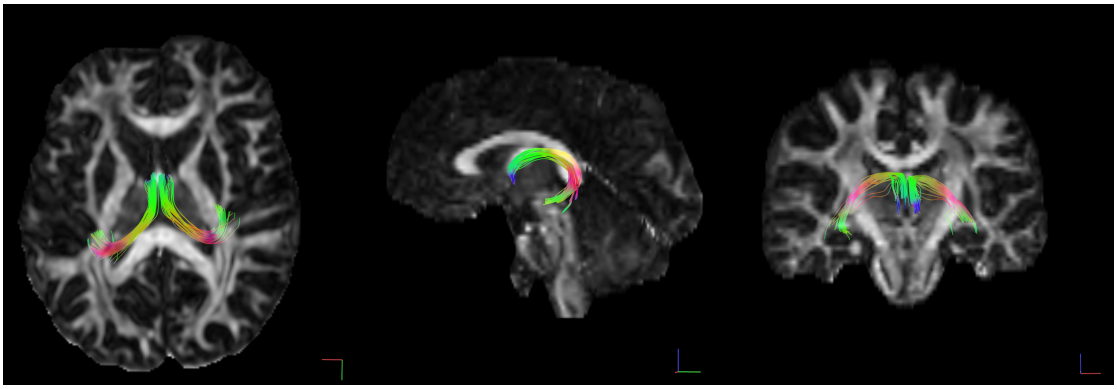


Figure B.5: Axial view (left), sagittal view (middle) and coronal view (right) of the fornix with the colors representing the directions of the fibers.

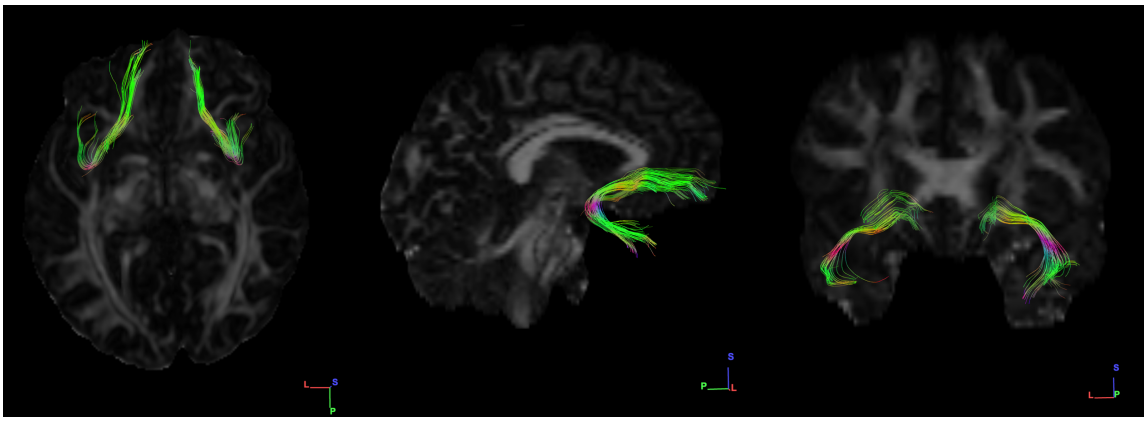


Figure B.6: Axial view (left), sagittal view (middle) and coronal view (right) of the uncinate fasciculus with the colors representing the directions of the fibers.

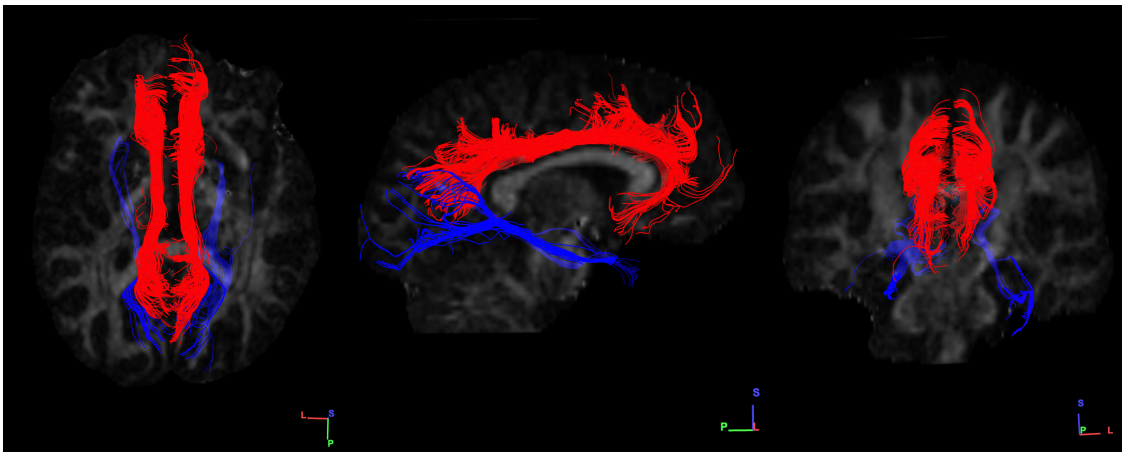


Figure B.7: Axial view (left), sagittal view (middle) and coronal view (right) of the cingulum with the red and blue colors respectively for the cingulate gyrus part and the parahippocampal part of the cingulum.

B.2 Cortical and subcortical regions of interest

All the images of the regions of interest were obtained with FSLeyes. The regions were highlighted with the available FSL Atlases (Harvard-Oxford Cortical Structural Atlas or Harvard-Oxford Subcortical Structural Atlas) and were superimposed onto the MNI152_T1_0.5mm FSL standard. The number of voxels in all three dimensions is (x,y,z) = (181,217,181)

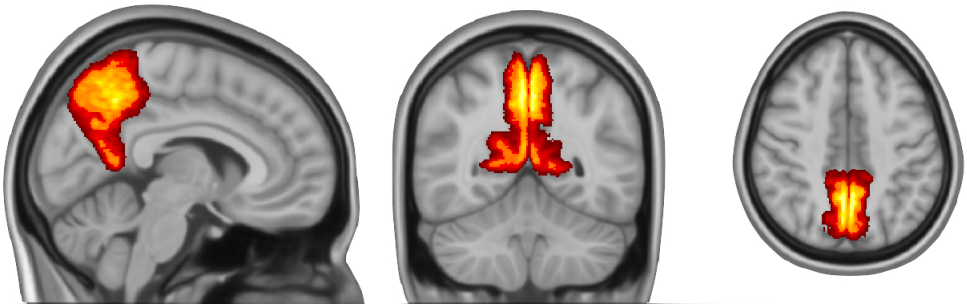


Figure B.8: Sagittal view (left), coronal view (middle) and axial view (right) of the precuneous cortex from the Harvard-Oxford Cortical Structural Atlas. Voxel location: (X,Y,Z) = (84,71,116).

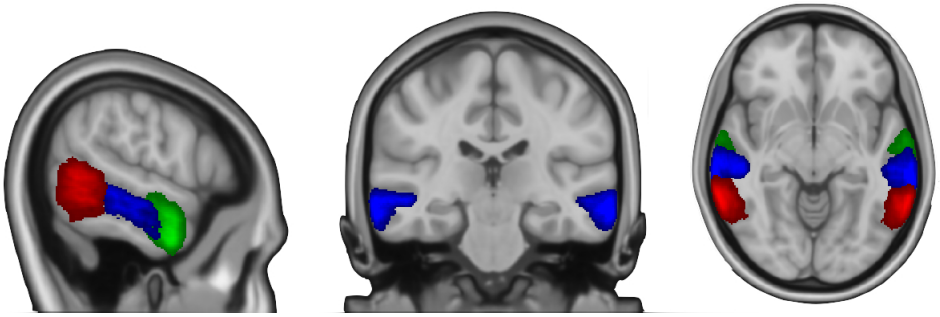


Figure B.9: Sagittal view (left), coronal view (middle) and axial view (right) of the middle temporal gyrus from the Harvard-Oxford Cortical Structural Atlas (green = anterior division, blue = posterior division, red = temporooccipital part). Voxel location: (X,Y,Z) = (147,101,65).

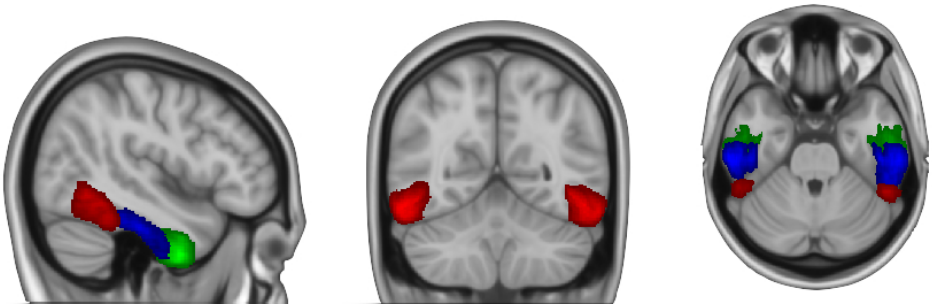


Figure B.10: Sagittal view (left), coronal view (middle) and axial view (right) of the inferior temporal gyrus from the Harvard-Oxford Cortical Structural Atlas (green = anterior division, blue = posterior division, red = temporooccipital part). Voxel location: (X,Y,Z) = (44,69,44).

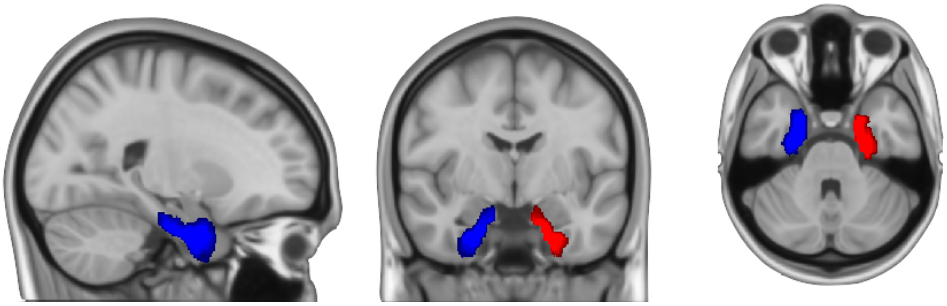


Figure B.11: Sagittal view (left), coronal view (middle) and axial view (right) of the hippocampus entorhinal cortex from the Harvard-Oxford Cortical Structural Atlas (blue = right, red = left). Voxel location: (X,Y,Z) = (67,120,40).

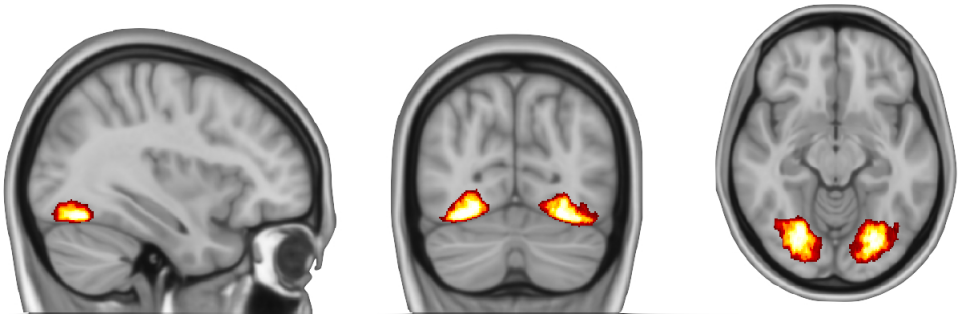


Figure B.12: Sagittal view (left), coronal view (middle) and axial view (right) of the occipital fusiform gyrus from the Harvard-Oxford Cortical Structural Atlas. Voxel location: (X,Y,Z) = (55,55,60).

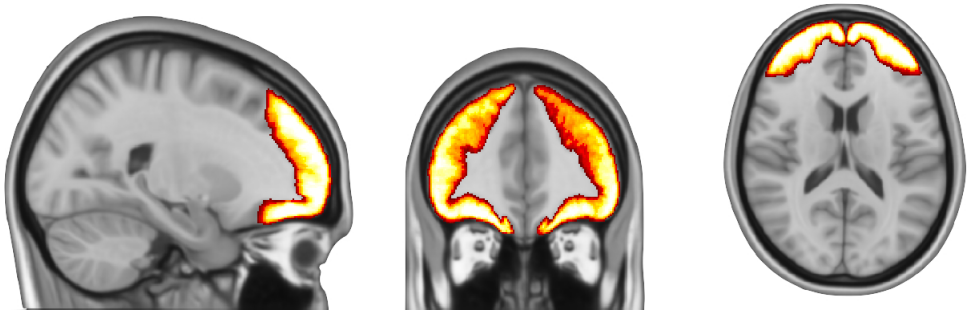


Figure B.13: Sagittal view (left), coronal view (middle) and axial view (right) of the frontal pole from the Harvard-Oxford Cortical Structural Atlas. Voxel location: (X,Y,Z) = (67,168,88).

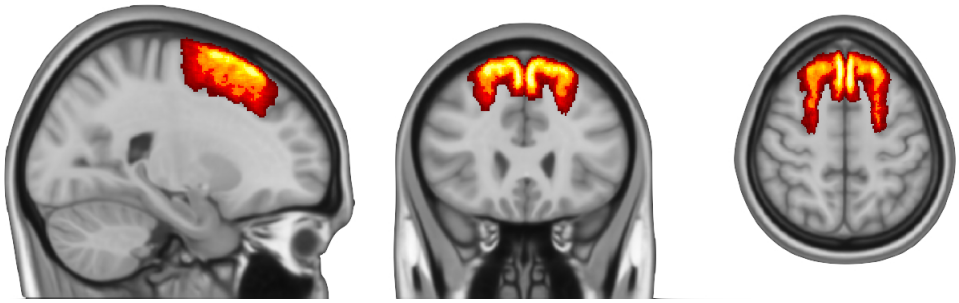


Figure B.14: Sagittal view (left), coronal view (middle) and axial view (right) of the superior frontal gyrus from the Harvard-Oxford Cortical Structural Atlas. Voxel location: (X,Y,Z) = (67,151,125).

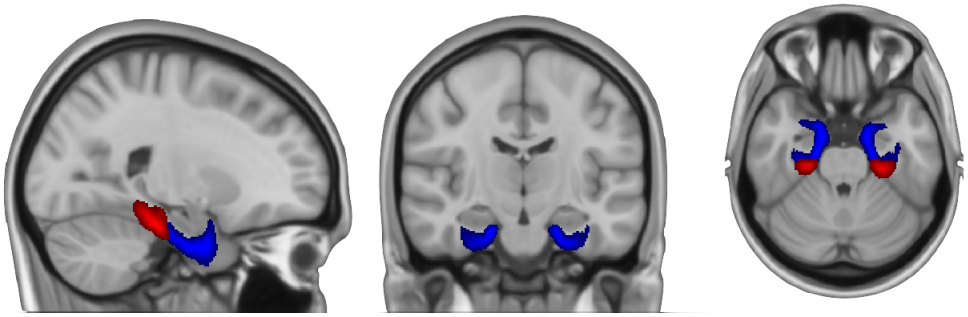


Figure B.15: Sagittal view (left), coronal view (middle) and axial view (right) of the parahippocampal gyrus from the Harvard-Oxford Cortical Structural Atlas (blue = anterior division, red = posterior division). Voxel location: (X,Y,Z) = (67,110,46).

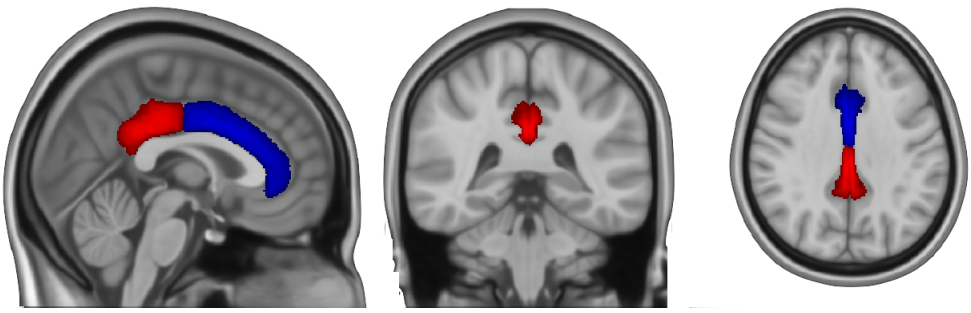


Figure B.16: Sagittal view (left), coronal view (middle) and axial view (right) of the cingulate gyrus from the Harvard-Oxford Cortical Structural Atlas (blue = anterior division, red = posterior division). Voxel location: (X,Y,Z) = (91,144,103).

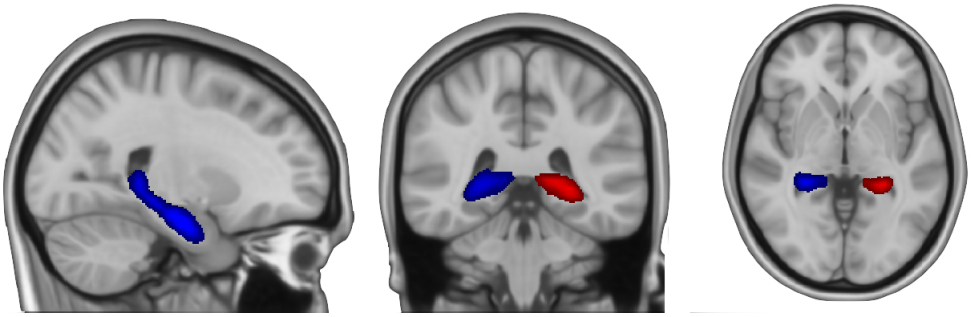


Figure B.17: Sagittal view (left), coronal view (middle) and axial view (right) of the hippocampi from the Harvard-Oxford Subcortical Structural Atlas (blue = right hippocampus, red = left hippocampus). Voxel location: (X,Y,Z) = (67,120,55).

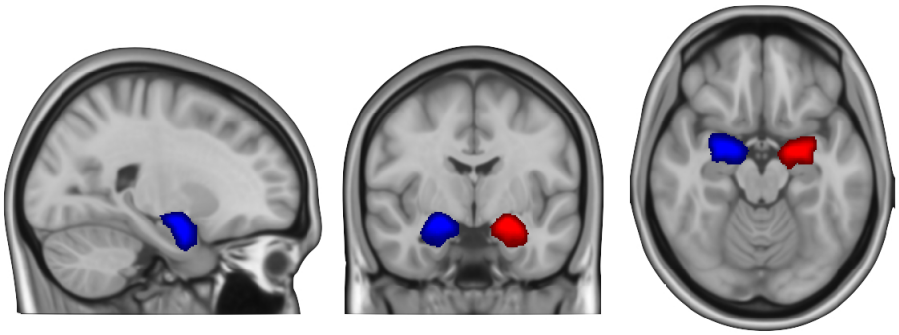


Figure B.18: Sagittal view (left), coronal view (middle) and axial view (right) of the amygdalae from the Harvard-Oxford Subcortical Structural Atlas (blue = right amygdala, red = left amygdala). Voxel location: (X,Y,Z) = (67,110,60).

Appendix C

Functions of the regions of interest in Alzheimer's disease

Structure	**Function**
White Matter	
Corpus callosum	- Transmission of interhemispheric information - Involved in verbal coding in memory (body) - Involved in non-verbal coding in memory (splenium)
Forceps minor	- Implicated in cognitive functions - Connects regions involved in the control of attention
Corona radiata	- Transmission of information between the cerebral cortex and the brain stem - Control of the motor function and transmission of sensory inputs
Posterior thalamic radiation	- Relay for sensory information
Superior longitudinal fasciculus	- Involved in verbal fluency and word production - Important for phonological processing and phonological retrieval - Involved in working memory
Fornix	- Carries verbal and visuospatial memory information - Processes exteroceptive signals - Involved in object recognition within a spatial context - Processes interoceptive signals for emotional and motivational learning and memory
Uncinate fasciculus	- Role for language, episodic memory and social processing
Cingulum	- Involved in cognitive control and executive functions: memory, attention, language (cingulate gyrus part) - Involved in emotional behaviours (cingulate gyrus part) - Involved in episodic memory and spatial processing (parahipp.)
Gray Matter	
Precuneous cortex	- Involved in visuospatial imagery, episodic memory retrieval, self-processing and consciousness, coordination of motor behaviour, tracking of moving targets, attention shift and orientation, music perception and mental navigation
Middle temporal gyrus	- Involved in semantic memory (mid.) - Involved in semantic processing of presented words (post.) - Involved in affective prosody (post.) - Involved in acoustic-phonetic and semantic processing (ant.) - Important for speech intelligibility (sulcus)
Fusiform gyrus	- Higher visual information processing, face recognition and word recognition

Structure	Function
Gray Matter (continued)	
Frontal pole	- Involved in social and emotional behaviour - Involved in mnemonic functions - Plays a role in anticipation and processing of outcomes
Superior frontal gyrus	- Involved in working memory - Involved in attention
Parahippocampal gyrus	- Involved in episodic memory - Involved in visuospatial processing (scene perception, spatial representation and navigation) - Play a role in emotional processing
Posterior cingulate gyrus	- Important for the retrieval of autobiographical memories - Involved in the regulation of the focus of attention
Hippocampus	- Involved in memory, learning, spatial navigation and emotional behaviour
Amygdala	- Involved in the regulation of emotions - Involved in recognition of facial expressions and emotions - Involved in the perception of gaze direction - Involved in the modulation of attention and memory

Table C.1: Functions of the tracts and regions of interest undergoing microstructural changes in Alzheimer's disease [79, 81, 82, 87, 86, 90, 92, 94, 95, 96, 99, 100, 101, 104, 105, 106, 107]

Appendix D

Results of the region-based analysis

D.1 Box plots for regions mildly affected by AD

D.1.1 DTI

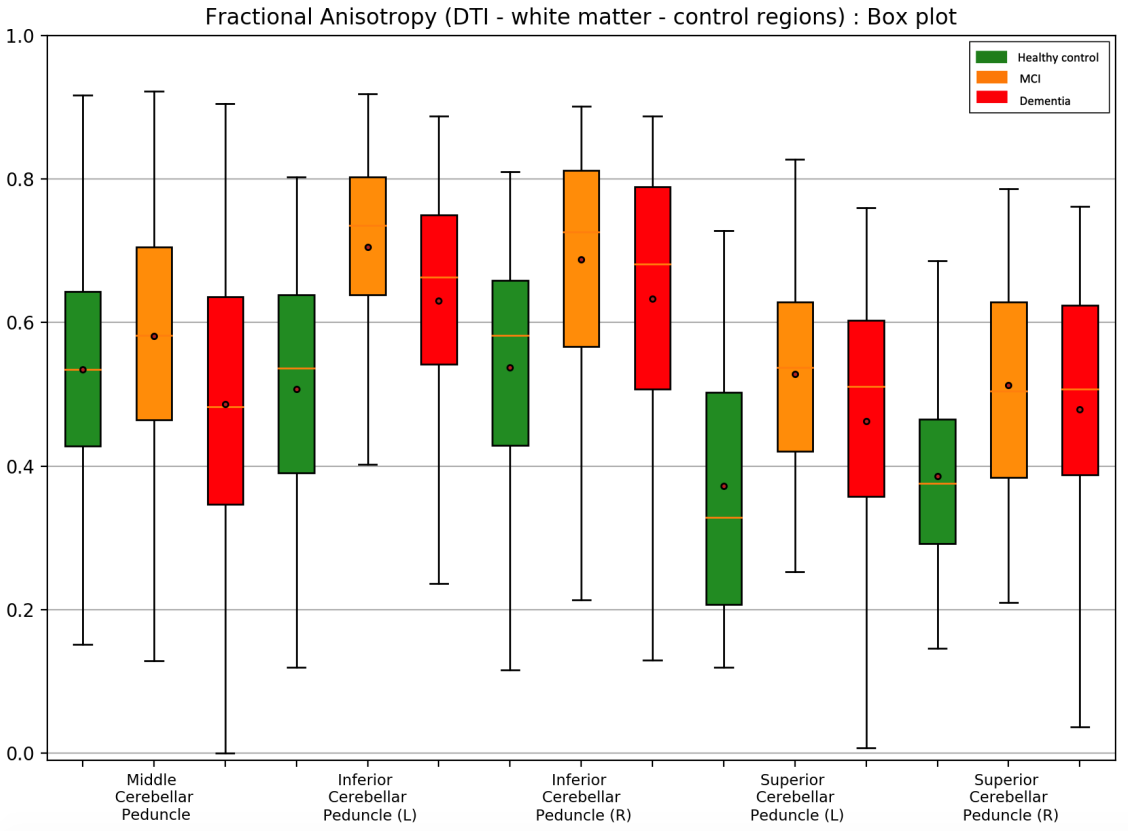


Figure D.1: FA evaluated in regions mildly affected by AD: the middle cerebellar peduncle, the inferior cerebellar peduncle and the superior cerebellar peduncle.

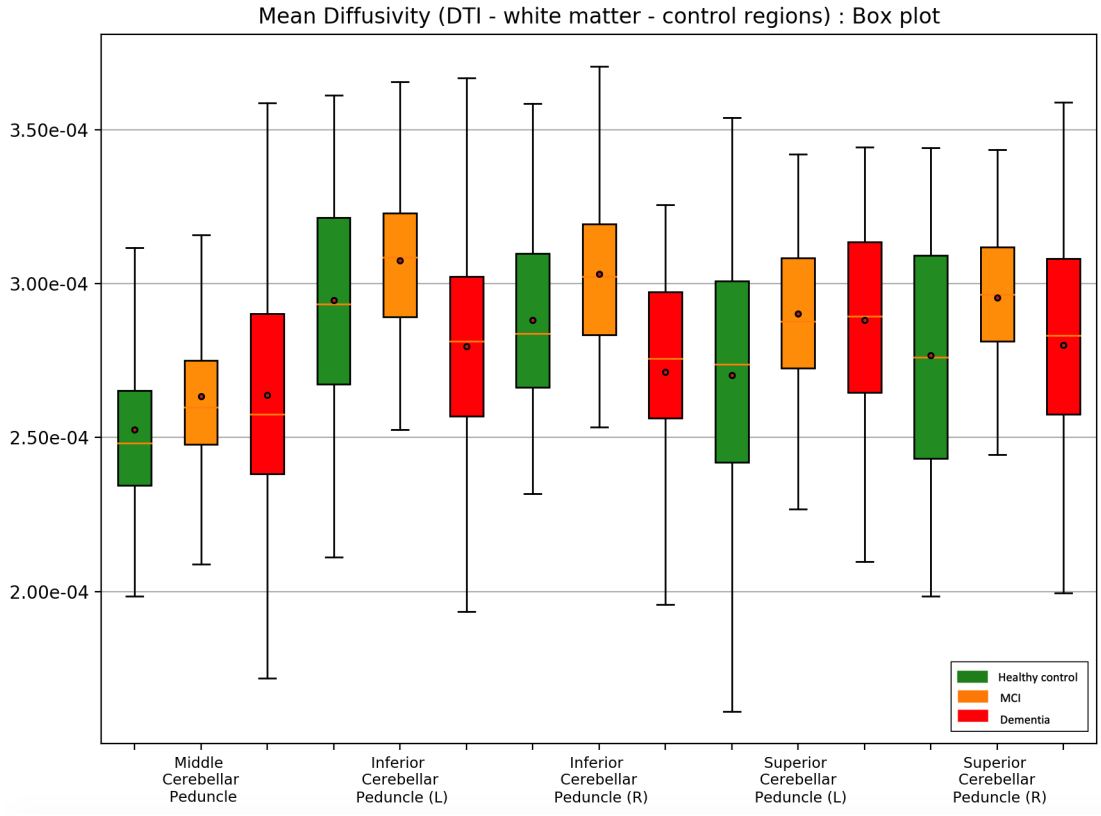


Figure D.2: MD evaluated in regions mildly affected by AD: the middle cerebellar peduncle, the inferior cerebellar peduncle and the superior cerebellar peduncle.

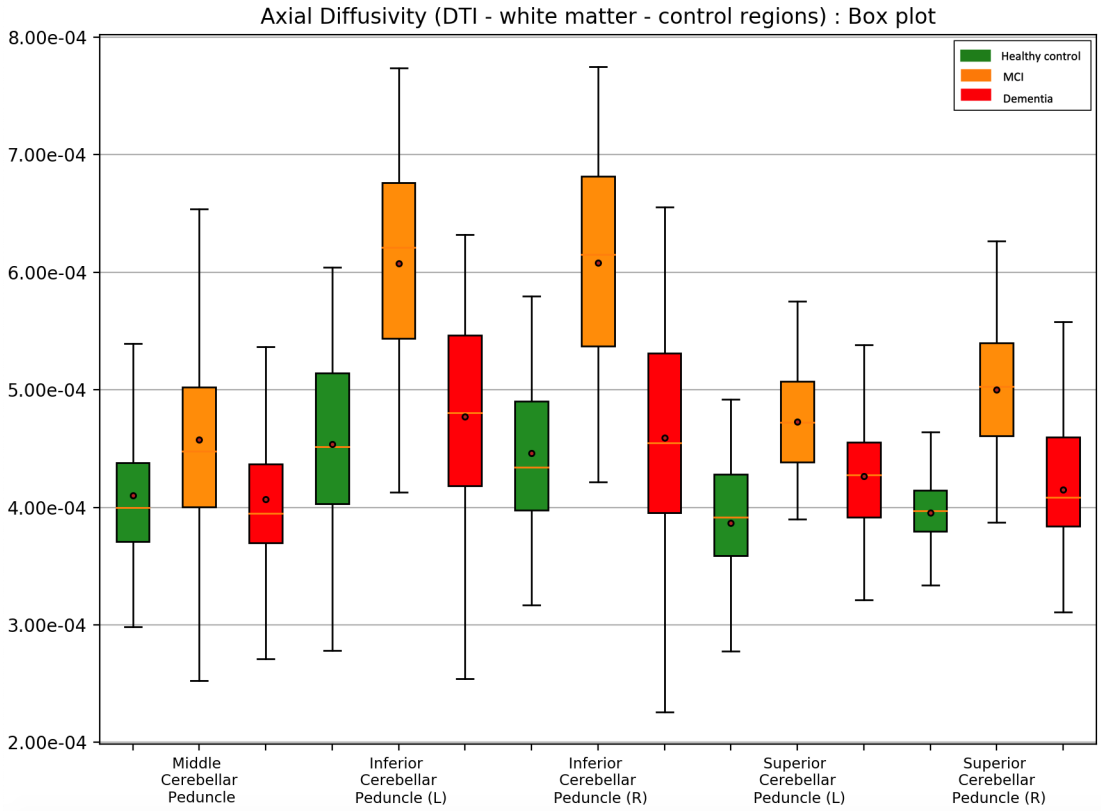


Figure D.3: AxD evaluated in regions mildly affected by AD: the middle cerebellar peduncle, the inferior cerebellar peduncle and the superior cerebellar peduncle.

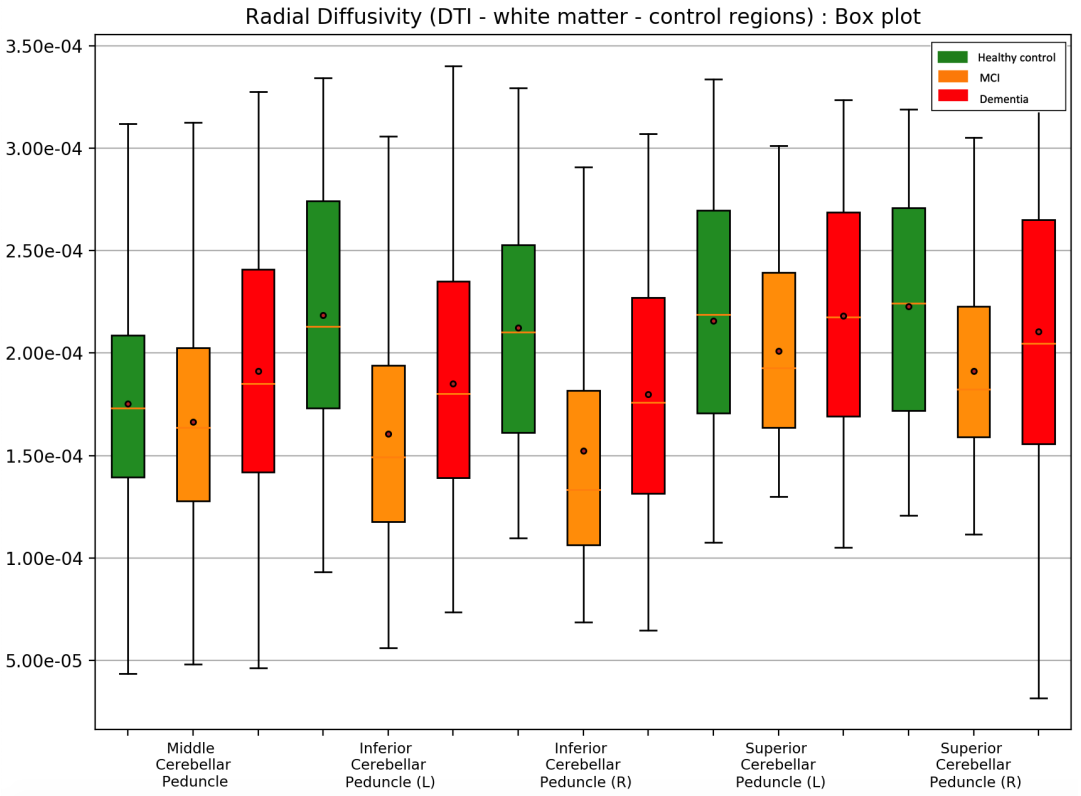


Figure D.4: RD evaluated in regions mildly affected by AD: the middle cerebellar peduncle, the inferior cerebellar peduncle and the superior cerebellar peduncle.

D.1.2 NODDI

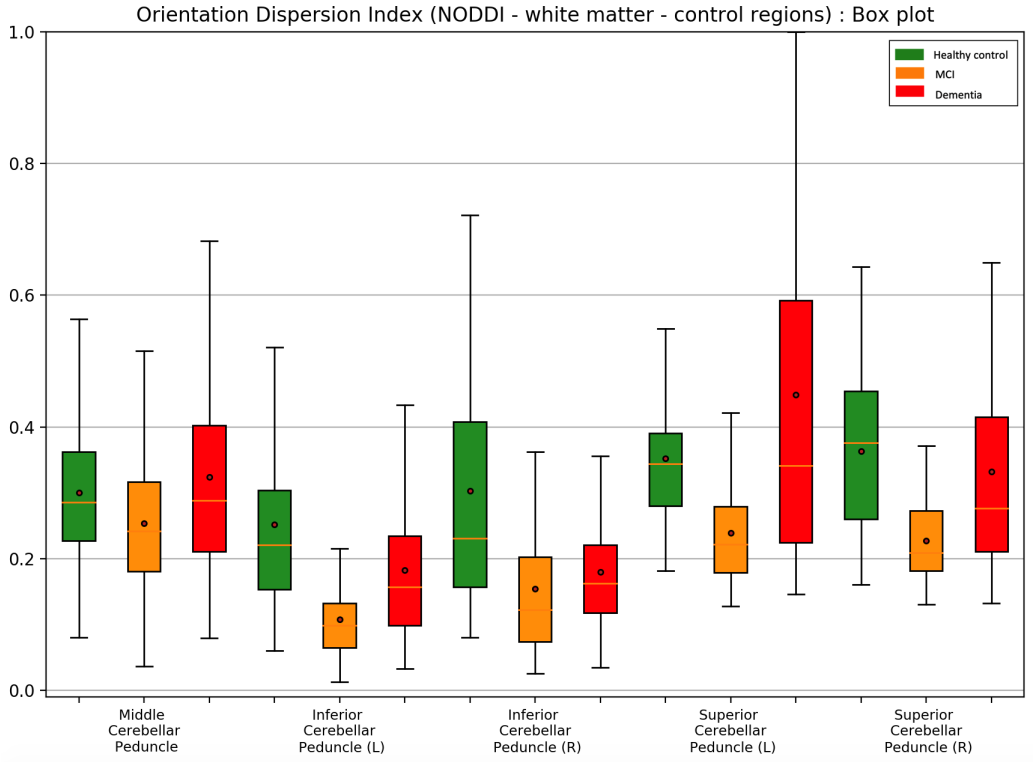


Figure D.5: ODI evaluated in regions mildly affected by AD: the middle cerebellar peduncle, the inferior cerebellar peduncle and the superior cerebellar peduncle.

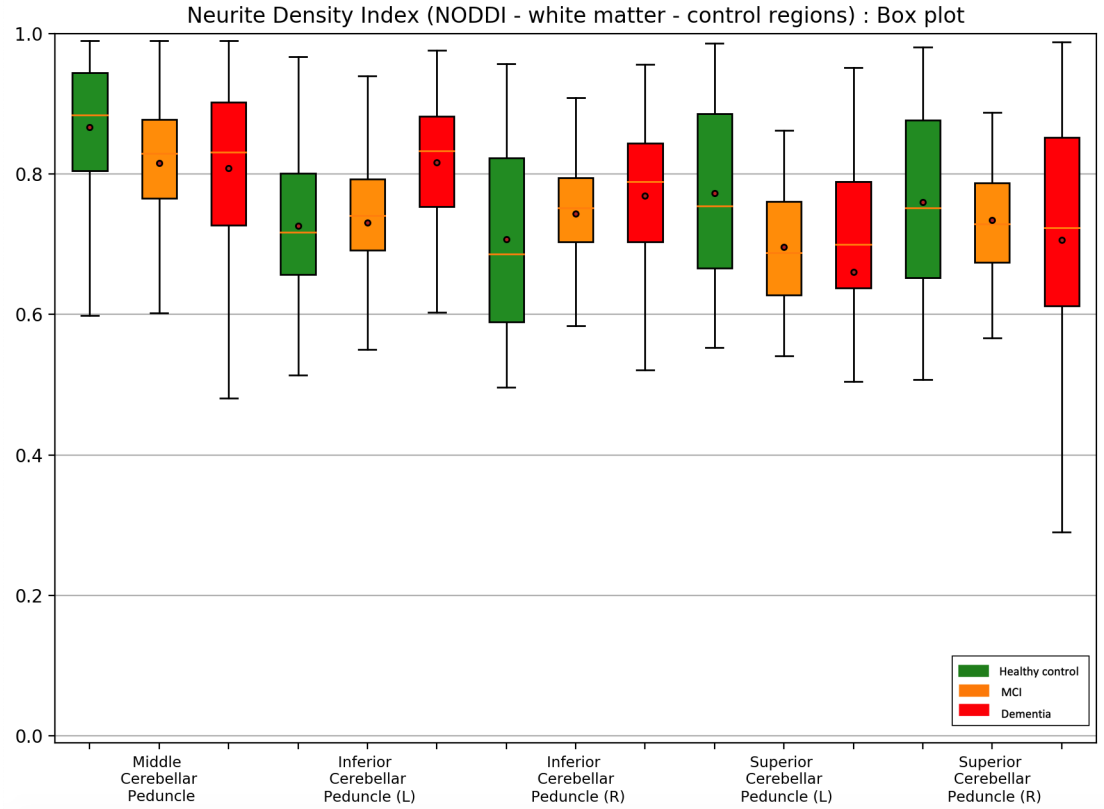


Figure D.6: NDI evaluated in regions mildly affected by AD: the middle cerebellar peduncle, the inferior cerebellar peduncle and the superior cerebellar peduncle.

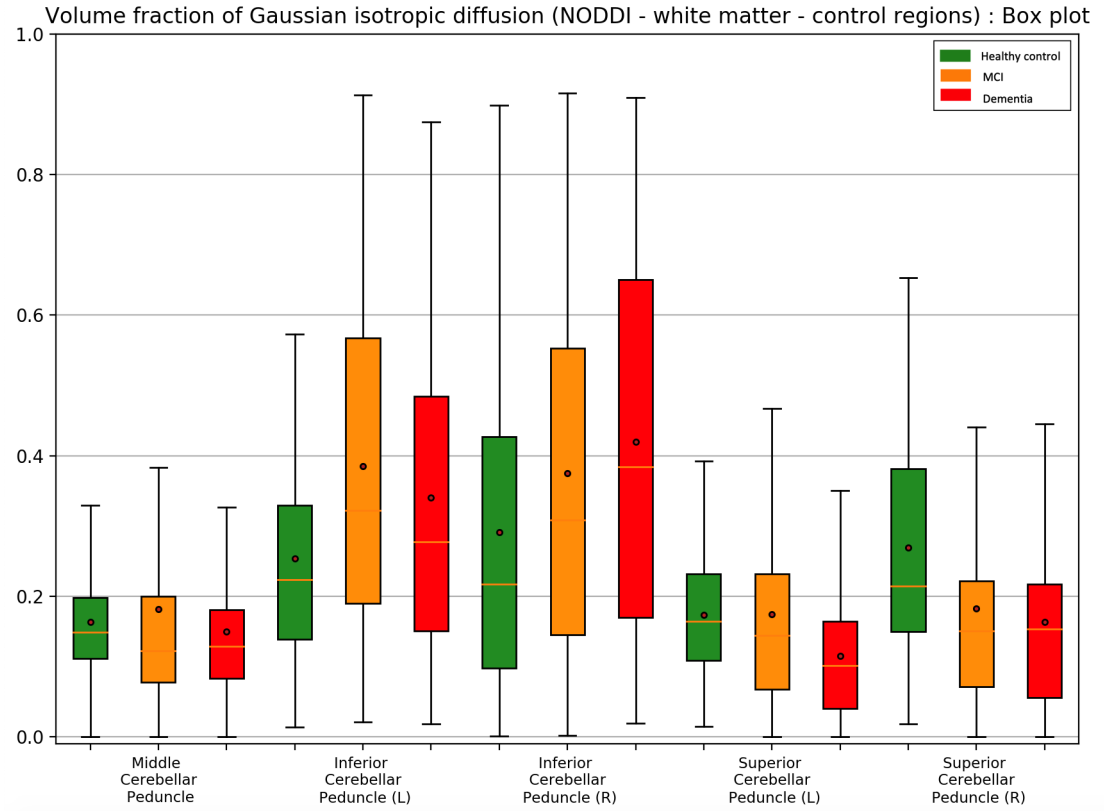


Figure D.7: f_{iso} evaluated in regions mildly affected by AD: the middle cerebellar peduncle, the inferior cerebellar peduncle and the superior cerebellar peduncle.

D.1.3 DIAMOND

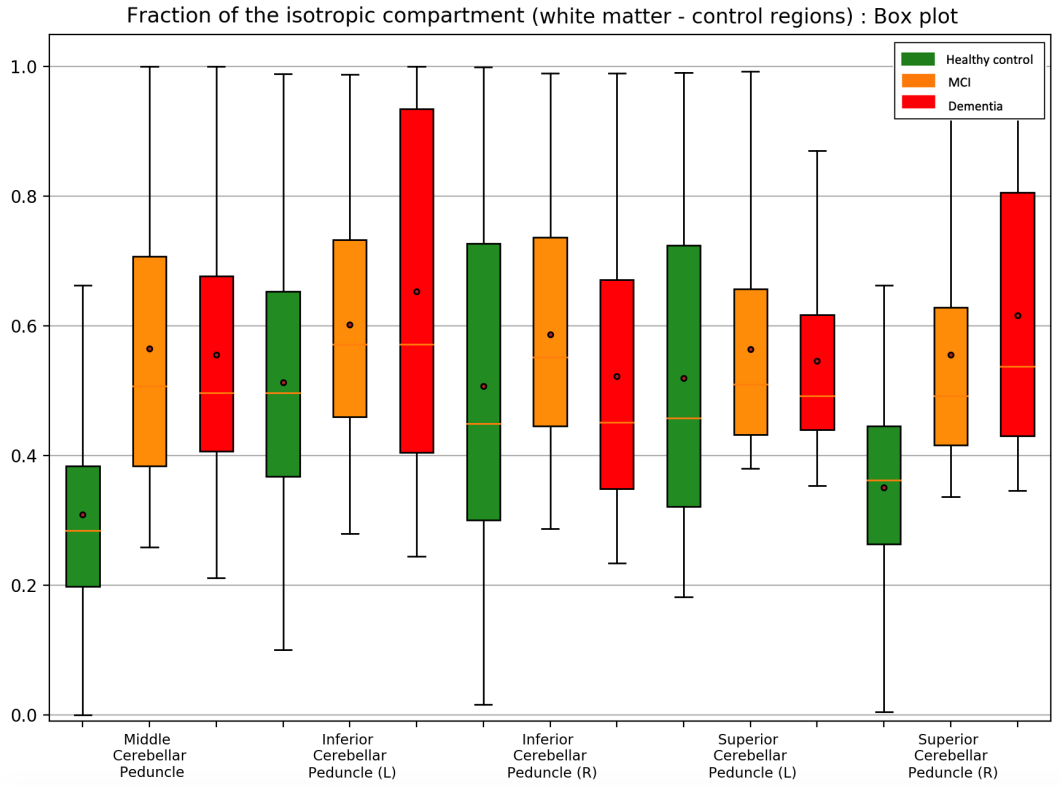


Figure D.8: F_{iso} evaluated in regions mildly affected by AD: the middle cerebellar peduncle, the inferior cerebellar peduncle and the superior cerebellar peduncle.

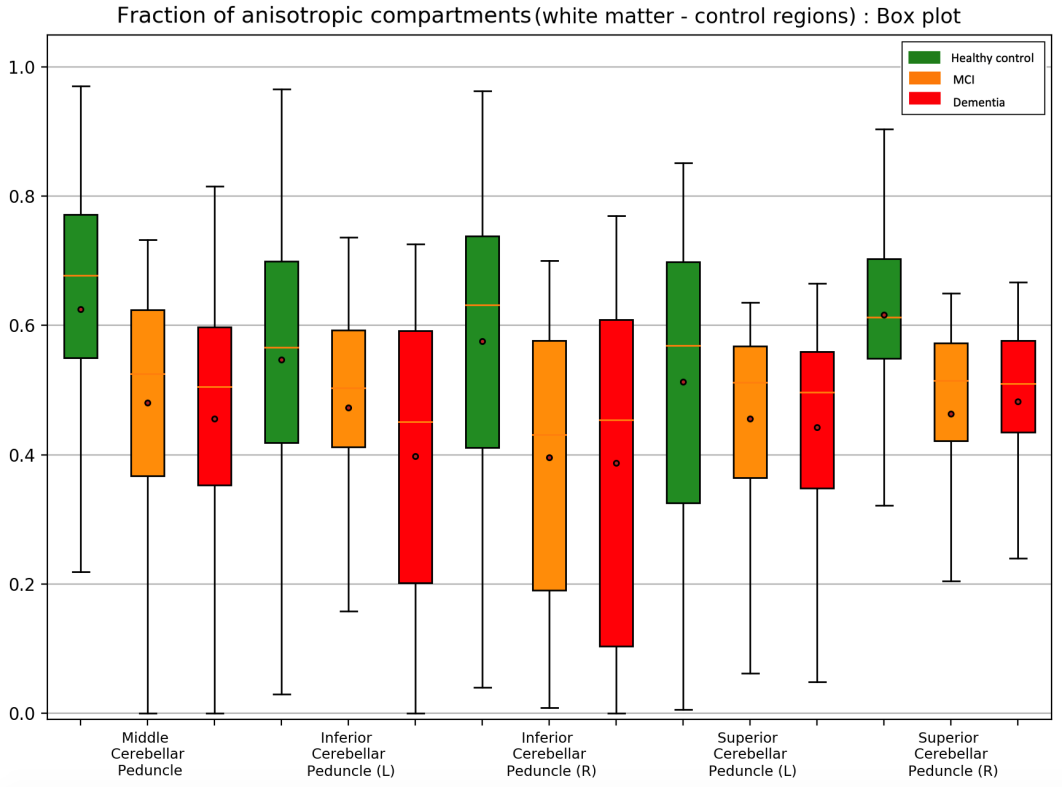


Figure D.9: F_{aniso} evaluated in regions mildly affected by AD: the middle cerebellar peduncle, the inferior cerebellar peduncle and the superior cerebellar peduncle.

D.1.4 Microstructure Fingerprinting

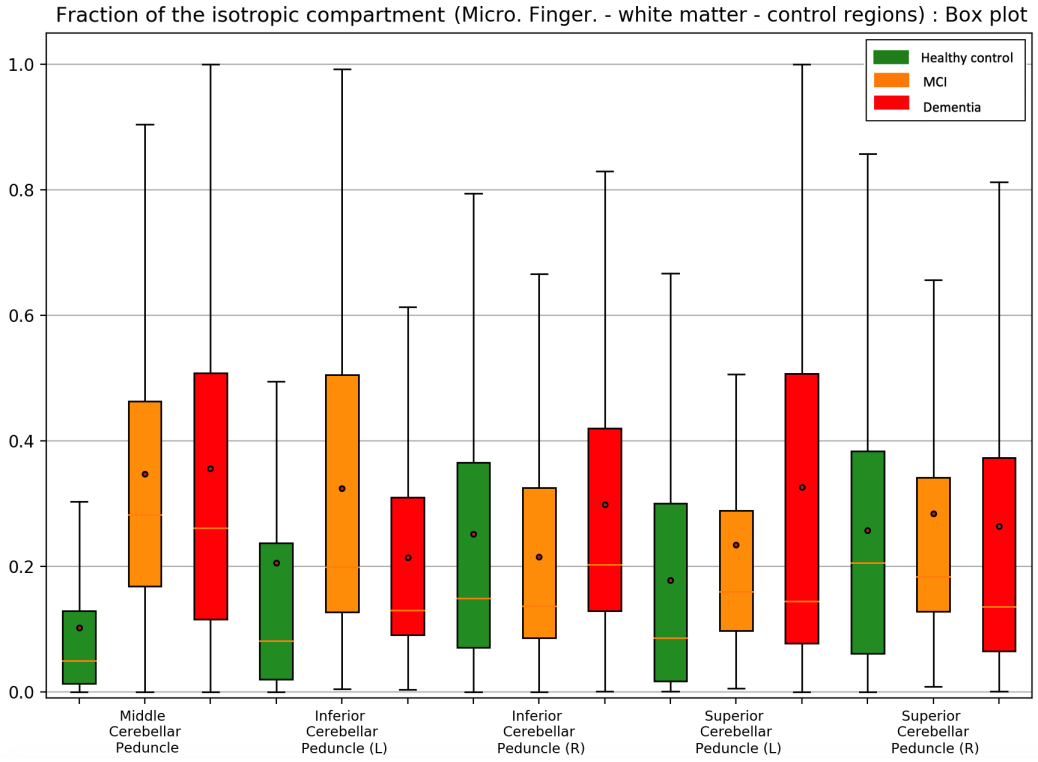


Figure D.10: F_{iso} (MF) evaluated in regions mildly affected by AD: the middle cerebellar peduncle, the inferior cerebellar peduncle and the superior cerebellar peduncle.

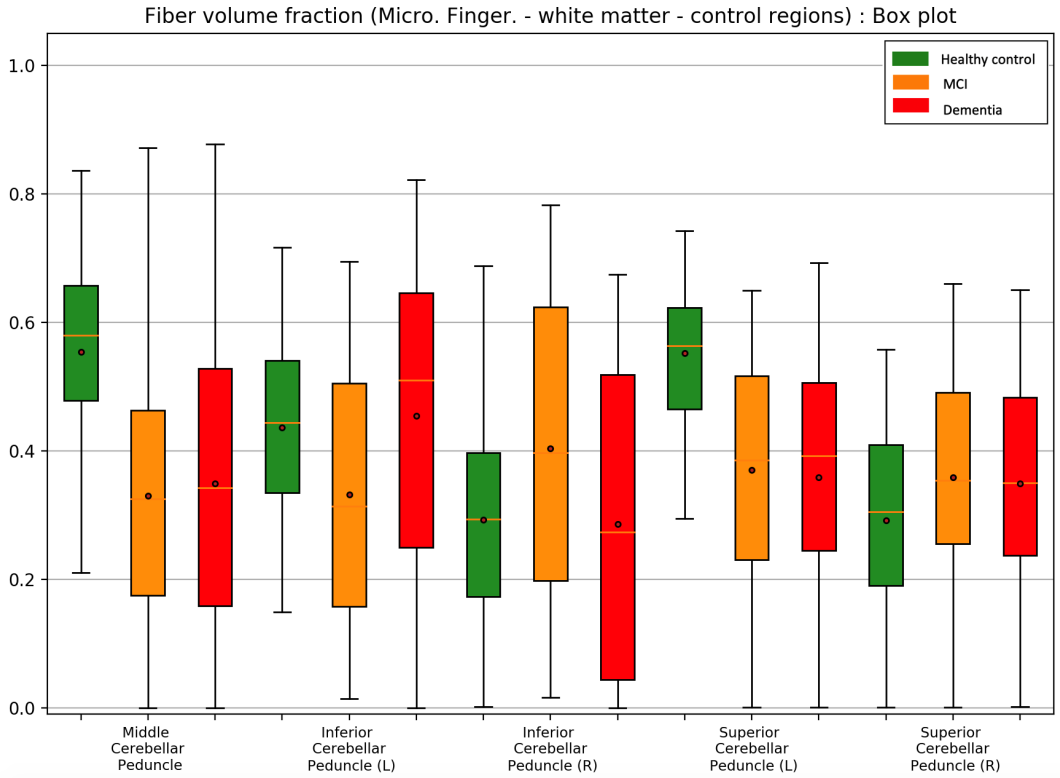


Figure D.11: FVF (MF) evaluated in regions mildly affected by AD: the middle cerebellar peduncle, the inferior cerebellar peduncle and the superior cerebellar peduncle.

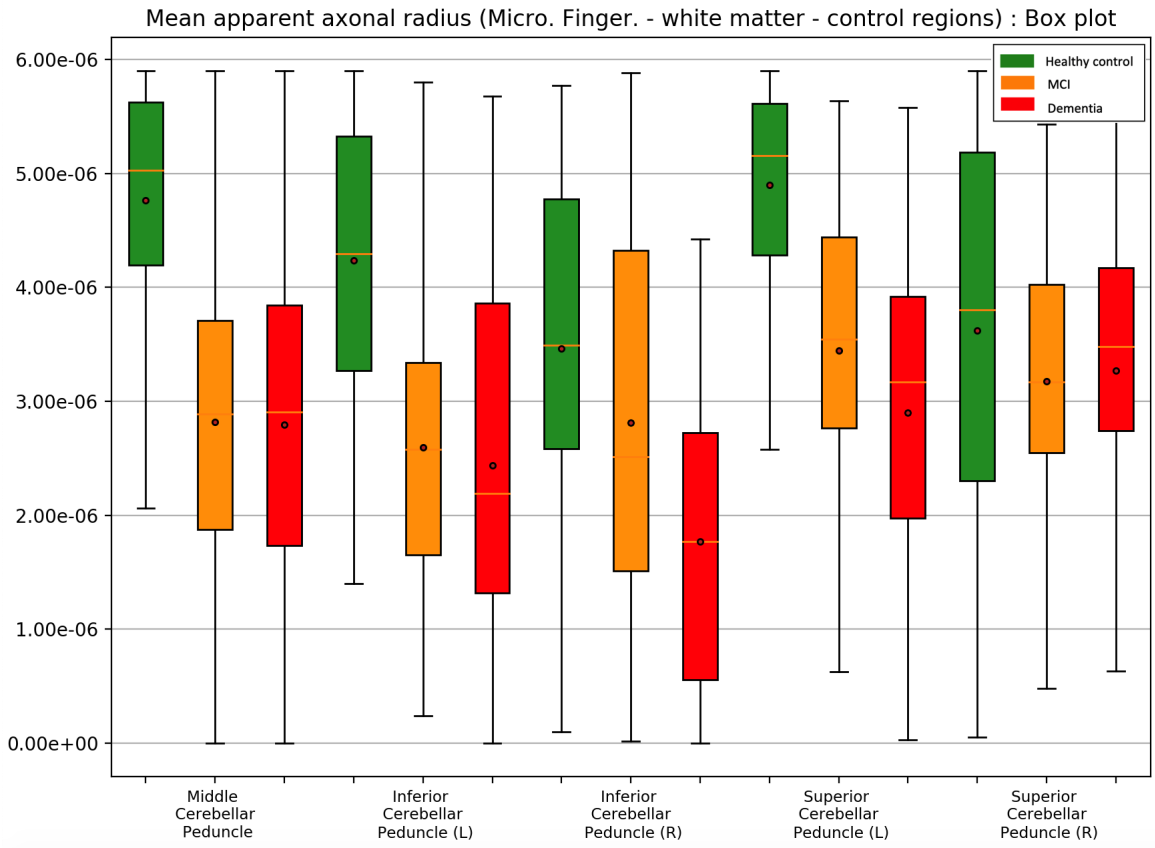


Figure D.12: mRad (MF) evaluated in regions mildly affected by AD: the middle cerebellar peduncle, the inferior cerebellar peduncle and the superior cerebellar peduncle.

D.2 Box plots of cortical and subcortical regions of interest

The cortical and subcortical regions of interest that were mentioned in previous studies as showing abnormal diffusion values are: the cortical and subcortical regions of interest are the hippocampus entorhinal cortex, the inferior temporal cortex (the anterior division, the temporooccipital part and the posterior division), the middle temporal cortex (the temporooccipital part and the posterior division), the fusiform cortex, the precuneous cortex, the frontal pole, the superior frontal gyrus, the parahippocampal gyrus (the anterior division and the posterior division), the posterior cingulate cortex, the hippocampus and the amygdala.

Since DIAMOND and MF are models designed to characterize voxels in white matter, the metrics of those models were not investigated in the cortical ROI. Some studies evaluated DTI metrics in the GM. A study observed an increased MD in the GM that was interpreted as a loss of dendrites [116]. However, the analysis in this Master's thesis suggested a negligible increase in MD (a maximum increase of $5.8 \cdot 10^{-5}$ in a ROI was observed), as represented in Fig.D.13.

The NODDI metrics (ODI, NDI and f_{iso}) were evaluated in the GM. Box plots of the NODDI metrics in the cortical and subcortical regions of interest are represented in Fig.D.14, Fig.D.15 and Fig.D.16. A study [29] conducted on a mouse model of human tauopathy (a rTg4510 transgenic mice) revealed a decreased ODI, an increased NDI and an increased volume fraction of Gaussian isotropic diffusion (f_{iso}) in cortical regions. In that study [29], NDI metrics were correlated with histological measurements of the levels of hyperphosphorylated tau proteins in the cortex [29]. As described in the article, "a lower ODI and higher NDI in the TG animals implies a similar reduction in dendritic complexity, due to atrophy of the cortical layers and accompanied loss of neurite structure [...] ; as such the tissue becomes less dispersed leading to a lower ODI and the reduced volume of cortex with higher density is reflected by higher NDI" [29]. It is also mentioned that atrophies of the GM lead to a higher occupancy of CSF leading to an increased volume fraction of Gaussian isotropic diffusion [29]. In the present study, no difference in ODI and NDI was observed in cortical and subcortical ROI in the AD patients as represented in Fig.D.14, Fig.D.15. However, an increased f_{iso} was observed in all the cortical and subcortical ROI and was therefore hypothesized to reflect the atrophy of the GM [29].

Since the study [29] conducted on a mouse model of human tauopathy observed a correlation between NDI values and the level of hyperphosphorylated tau proteins, further studies could evaluate NODDI metrics in regions where an accumulation of pathological tau proteins is observed with tau-PET images.

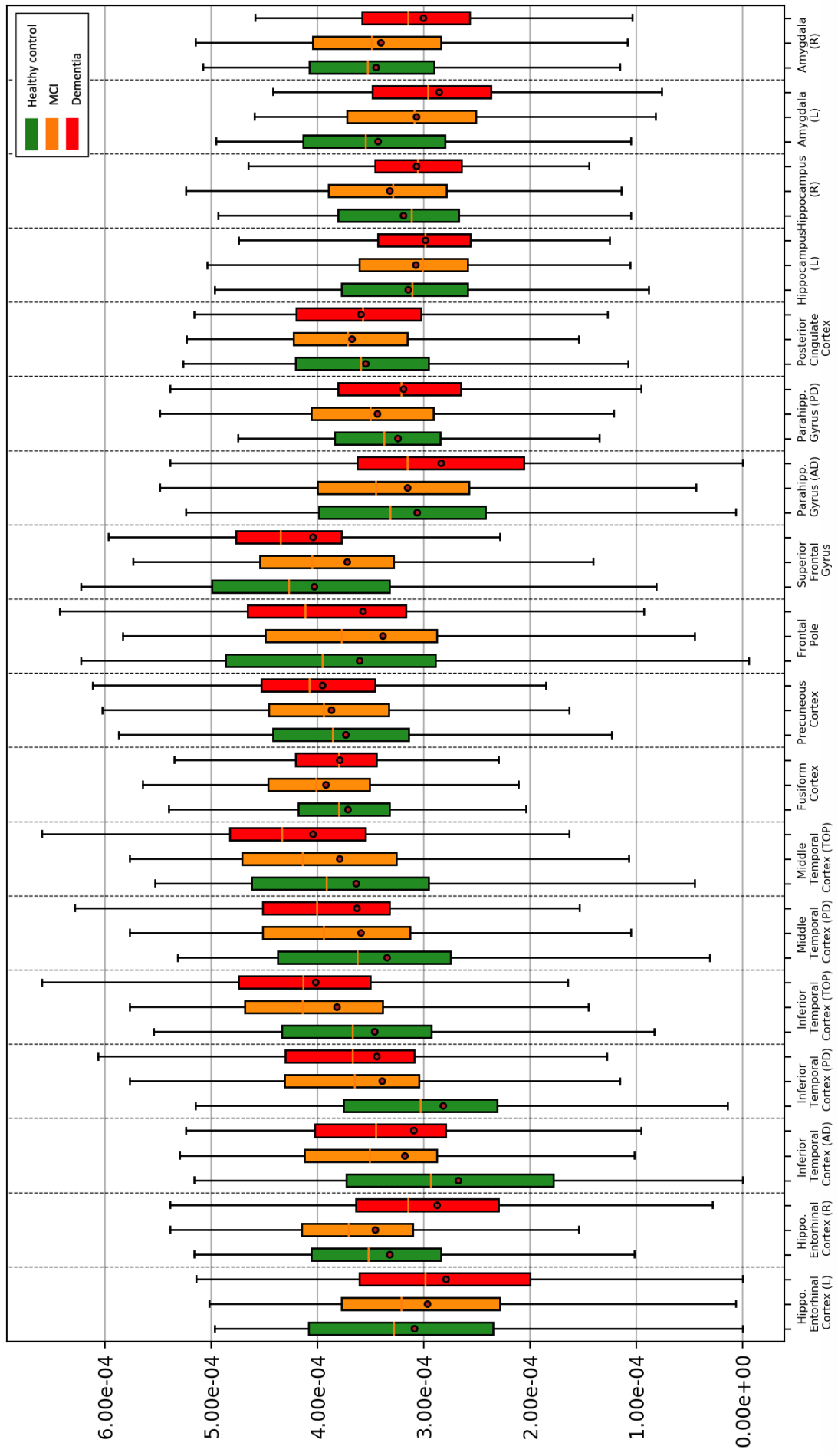


Figure D.13: Box plot of the mean diffusivity in regions of interest for the healthy control (pink), the MCI patient (blue) and the patient with dementia (beige). The horizontal orange line represents the median of the distribution and the black marker represents the mean MD in the region of interest. From left to right, the regions of interest are: the left hippocampus entorhinal cortex, the right hippocampus entorhinal cortex, the anterior division of the inferior temporal cortex, the posterior division of the inferior temporal cortex, the temporooccipital part of the inferior temporal cortex, the posterior division of the middle temporal cortex, the temporooccipital part of the middle temporal cortex, the fusiform cortex, the precuneous cortex, the frontal pole, the superior frontal gyrus, the parahippocampal gyrus (anterior division), the parahippocampal gyrus (posterior division), the posterior cingulate cortex, the left hippocampus, the right hippocampus, the left amygdala and the right amygdala.

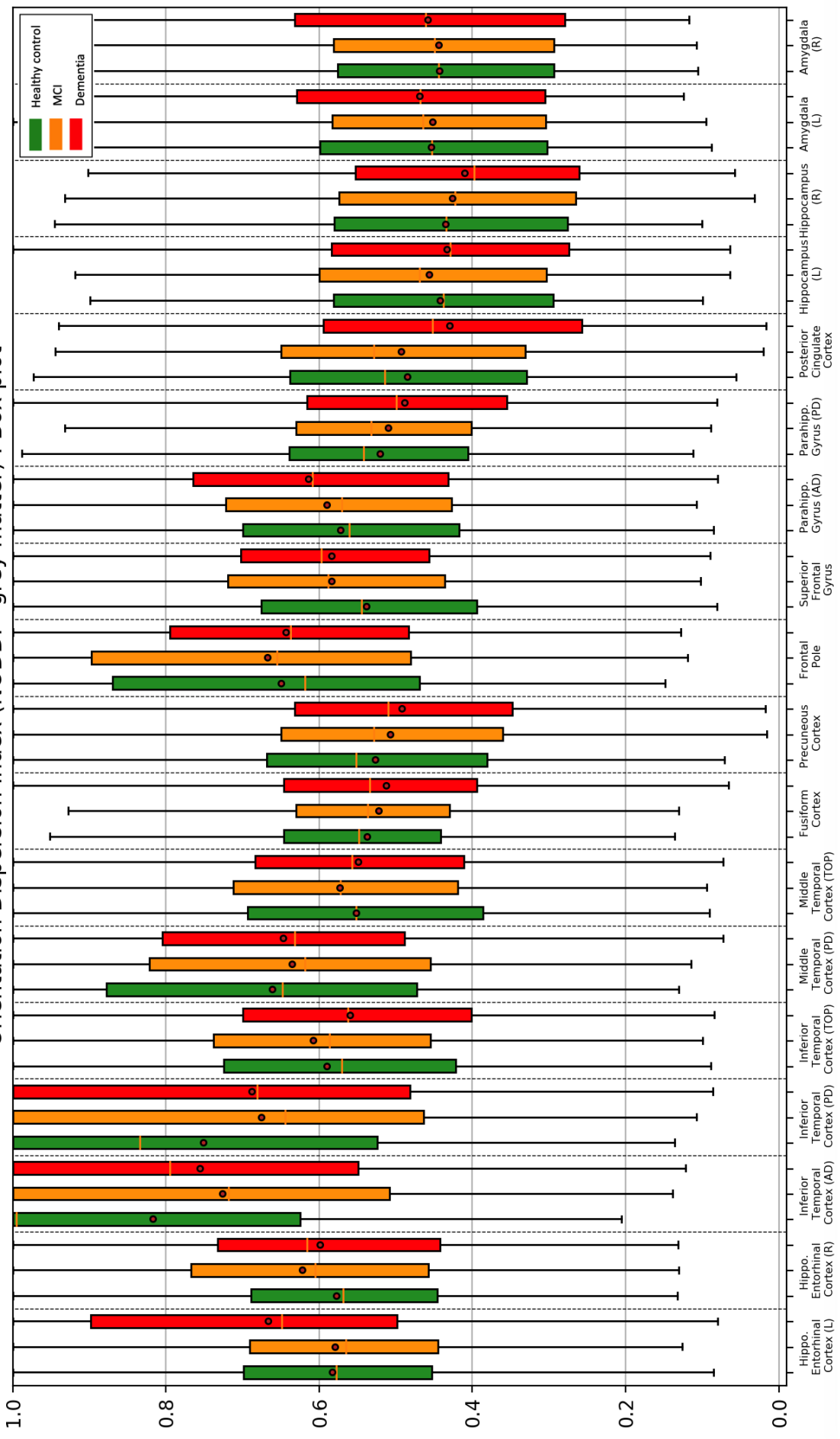


Figure D.14: Box plot of the Orientation Dispersion Index in regions of interest for the healthy control (pink), the MCI patient (blue) and the patient with dementia (beige). The horizontal orange line represents the median of the distribution and the black marker represents the mean ODI in the region of interest. From left to right, the regions of interest are: the left hippocampus entorhinal cortex, the right hippocampus entorhinal cortex, the anterior division of the inferior temporal cortex, the posterior division of the inferior temporal cortex, the temporooccipital part of the inferior temporal cortex, the posterior division of the middle temporal cortex, the temporooccipital part of the middle temporal cortex, the fusiform cortex, the precuneous cortex, the frontal pole, the superior frontal gyrus, the parahippocampal gyrus (anterior division), the parahippocampal gyrus (posterior division), the posterior cingulate cortex, the left hippocampus, the right hippocampus, the left amygdala and the right amygdala.

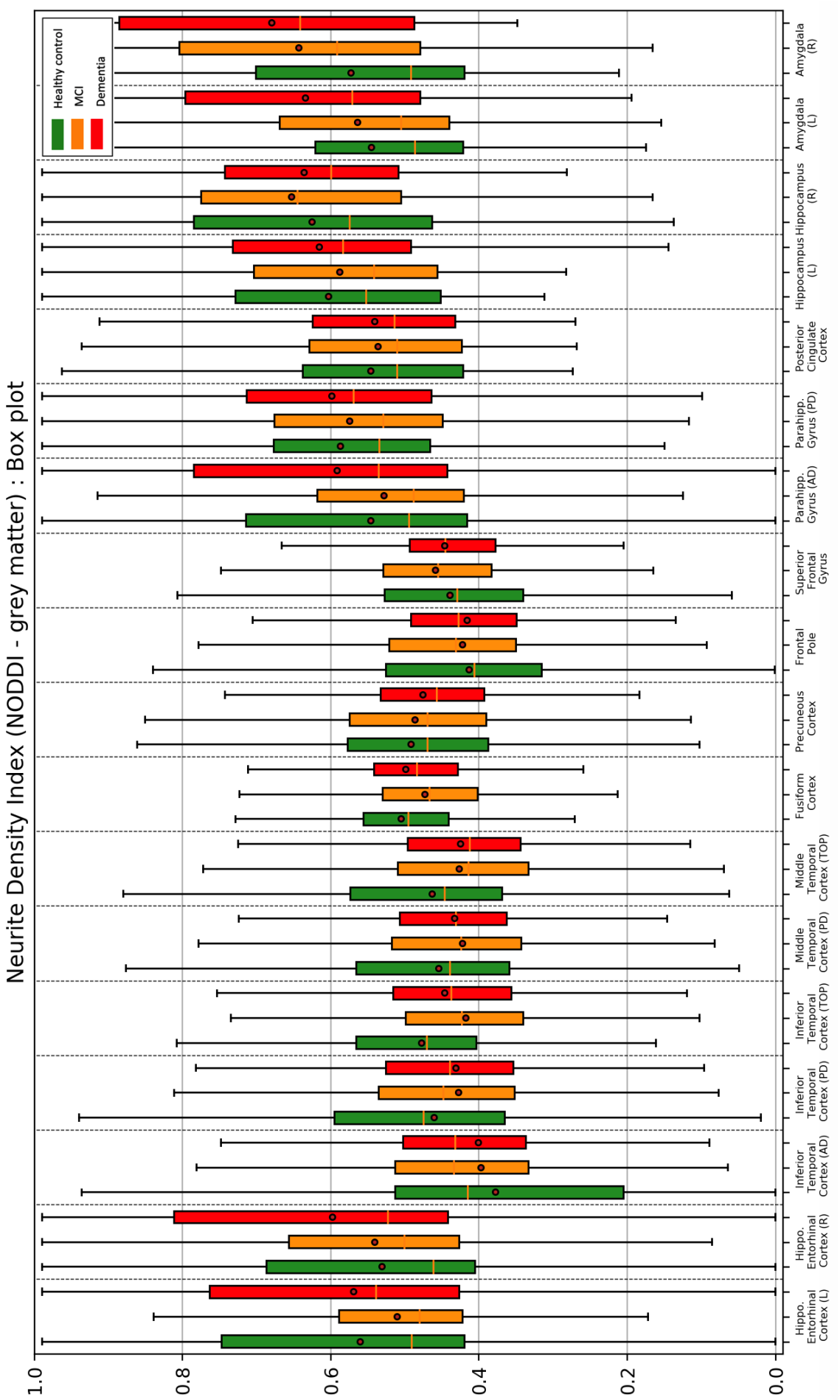


Figure D.15: Box plot of the Neurite Density Index in regions of interest for the healthy control (pink), the MCI patient (blue) and the patient with dementia (beige). The horizontal orange line represents the median of the distribution and the black marker represents the mean NDI in the region of interest. From left to right, the regions of interest are: the left hippocampus entorhinal cortex, the right hippocampus entorhinal cortex, the anterior division of the inferior temporal cortex, the posterior division of the inferior temporal cortex, the temporooccipital part of the inferior temporal cortex, the posterior division of the middle temporal cortex, the temporooccipital part of the middle temporal cortex, the fusiform cortex, the precuneous cortex, the frontal pole, the superior frontal gyrus, the parahippocampal gyrus (anterior division), the parahippocampal gyrus (posterior division), the posterior cingulate cortex, the left hippocampus, the right hippocampus, the left amygdala and the right amygdala.

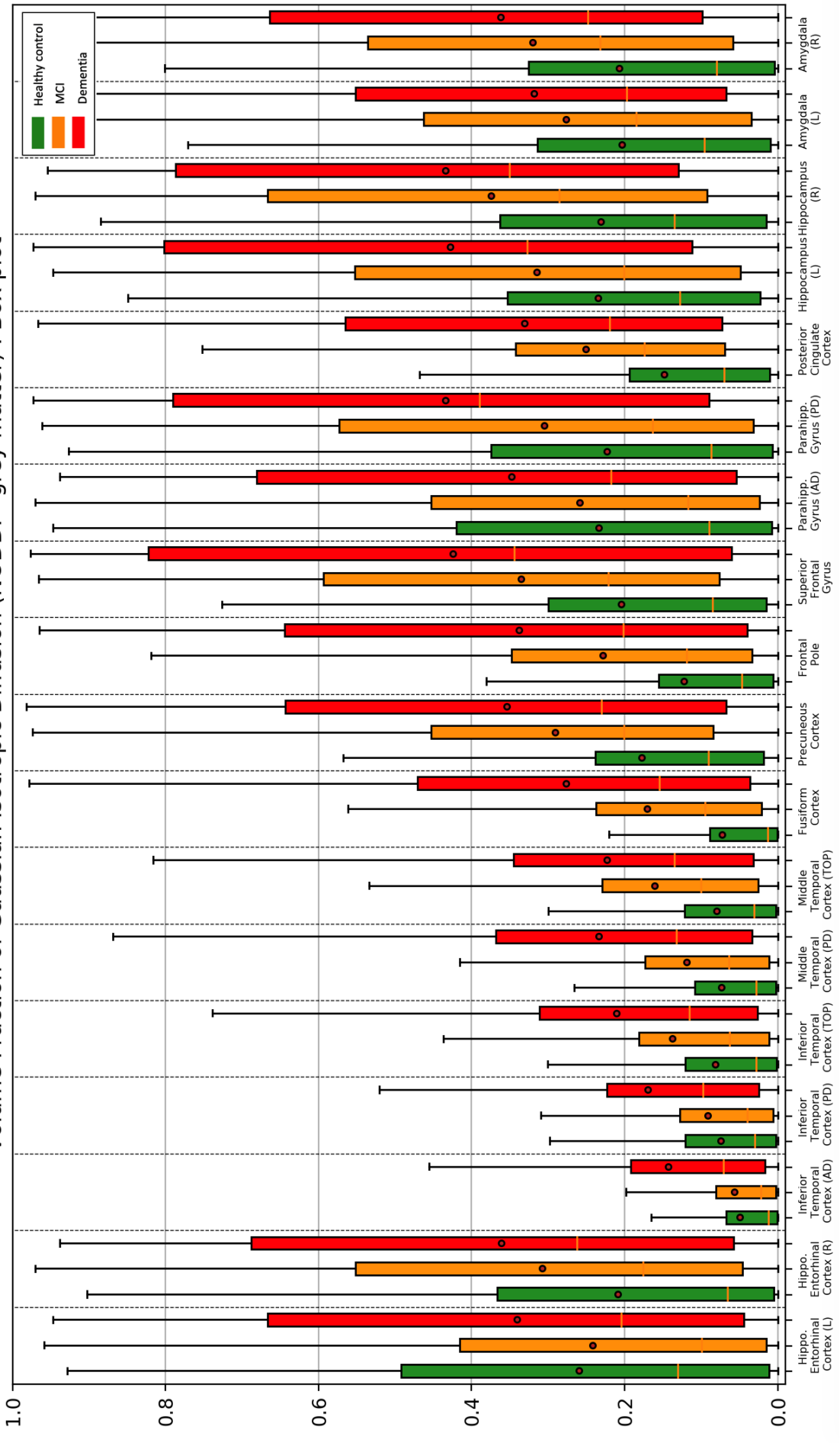


Figure D.16: Box plot of the volume fraction of Gaussian isotropic diffusion (f_{iso}) in regions of interest for the healthy control (pink), the MCI patient (blue) and the patient with dementia (beige). The horizontal orange line represents the median of the distribution and the black marker represents the mean f_{iso} in the region of interest. From left to right, the regions of interest are: the left hippocampus entorhinal cortex, the right hippocampus entorhinal cortex, the anterior division of the inferior temporal cortex, the posterior division of the inferior temporal cortex, the temporooccipital part of the inferior temporal cortex, the posterior division of the middle temporal cortex, the temporooccipital part of the middle temporal cortex, the fusiform cortex, the precuneous cortex, the frontal pole, the superior frontal gyrus, the parahippocampal gyrus (anterior division), the parahippocampal gyrus (posterior division), the posterior cingulate cortex, the left hippocampus, the right hippocampus, the left amygdala and the right amygdala.

D.3 Comprehensive table of metrics

Model	Metric	Structure	μ-HC	σ-HC	μ-AD1	σ-AD1	μ-AD2	σ-AD2
		White matter						
DTI	FA	Fornix	0,55	0,16	0,48	0,14	0,25	0,13
		Genu corpus callosum	0,68	0,15	0,59	0,18	0,38	0,22
		Body corpus callosum	0,63	0,17	0,62	0,18	0,47	0,23
		Splenium corpus callosum	0,66	0,18	0,6	0,25	0,59	0,22
		Left cingulum (parahipp.)	0,28	0,1	0,26	0,1	0,29	0,08
		Right cingulum (parahipp.)	0,32	0,1	0,33	0,12	0,29	0,11
		Left cingulum (c.g.)	0,46	0,17	0,39	0,18	0,5	0,12
		Right cingulum (c.g.)	0,47	0,13	0,43	0,15	0,52	0,13
		Left post. thalamic radiation	0,54	0,11	0,56	0,11	0,47	0,09
		Right post. thalamic radiation	0,58	0,12	0,58	0,11	0,49	0,11
		Left sup. longitudinal fasciculus	0,49	0,12	0,48	0,13	0,46	0,14
		Right sup.longitudinal fasciculus	0,53	0,11	0,54	0,11	0,48	0,12
		Left sup. corona radiata	0,52	0,09	0,51	0,09	0,48	0,12
		Right sup. corona radiata	0,51	0,11	0,53	0,09	0,44	0,12
		Forceps minor	0,33	0,21	0,3	0,18	0,27	0,17
		Left uncinate fasciculus	0,53	0,11	0,54	0,13	0,49	0,11
		Right uncinate fasciculus	0,49	0,11	0,45	0,15	0,45	0,14
		Middle cerebellar peduncle	0,53	0,15	0,58	0,16	0,49	0,19
		Left inf. cerebellar peduncle	0,51	0,17	0,7	0,13	0,63	0,16
		Right inf. cerebellar peduncle	0,54	0,16	0,69	0,15	0,63	0,19
		Left sup. cerebellar peduncle	0,37	0,17	0,53	0,13	0,46	0,2
		Right sup. cerebellar peduncle	0,39	0,13	0,51	0,15	0,48	0,18
	MD	Fornix	2,86E-04	4,25E-05	3,06E-04	4,81E-05	2,80E-04	2,53E-05
		Genu corpus callosum	2,92E-04	4,86E-05	3,00E-04	3,90E-05	3,37E-04	2,95E-05
		Body corpus callosum	3,14E-04	5,56E-05	3,19E-04	4,56E-05	3,17E-04	2,96E-05
		Splenium corpus callosum	2,63E-04	4,35E-05	3,02E-04	4,61E-05	2,92E-04	3,79E-05
		Left cingulum (parahipp.)	3,03E-04	2,54E-05	3,47E-04	3,09E-05	2,98E-04	5,32E-05
		Right cingulum (parahipp.)	3,07E-04	3,06E-05	3,58E-04	4,55E-05	3,39E-04	8,29E-05
		Left cingulum (c.g.)	3,90E-04	7,70E-05	4,01E-04	5,82E-05	3,59E-04	5,14E-05
		Right cingulum (c.g.)	3,50E-04	6,90E-05	3,50E-04	4,39E-05	3,58E-04	6,27E-05
		Left post. thalamic radiation	3,02E-04	3,87E-05	3,15E-04	2,51E-05	3,59E-04	2,99E-05
		Right post. thalamic radiation	2,95E-04	2,37E-05	3,15E-04	2,20E-05	3,65E-04	3,61E-05
		Left sup. longitudinal fasciculus	2,99E-04	4,52E-05	3,16E-04	4,57E-05	3,15E-04	3,74E-05
		Right sup.longitudinal fasciculus	2,95E-04	5,17E-05	2,90E-04	2,83E-05	3,08E-04	3,69E-05
		Left sup. corona radiata	2,77E-04	1,39E-05	2,82E-04	1,64E-05	3,20E-04	2,95E-05
		Right sup. corona radiata	2,84E-04	1,69E-05	2,95E-04	2,14E-05	3,32E-04	3,04E-05
		Forceps minor	3,70E-04	1,16E-04	3,62E-04	1,01E-04	4,04E-04	8,35E-05
		Left uncinate fasciculus	3,10E-04	2,67E-05	3,06E-04	2,43E-05	3,44E-04	2,67E-05
		Right uncinate fasciculus	3,09E-04	2,11E-05	3,49E-04	3,90E-05	3,45E-04	3,25E-05
		Middle cerebellar peduncle	2,52E-04	2,52E-05	2,63E-04	2,37E-05	2,64E-04	3,47E-05
		Left inf. cerebellar peduncle	2,95E-04	3,41E-05	3,08E-04	2,32E-05	2,80E-04	3,61E-05
		Right inf. cerebellar peduncle	2,88E-04	2,95E-05	3,03E-04	2,33E-05	2,71E-04	3,62E-05
		Left sup. cerebellar peduncle	2,70E-04	3,93E-05	2,90E-04	2,41E-05	2,88E-04	3,17E-05
		Right sup. cerebellar peduncle	2,77E-04	3,74E-05	2,96E-04	2,17E-05	2,80E-04	4,42E-05
	AxD	Fornix	4,97E-04	5,99E-05	4,74E-04	8,43E-05	3,30E-04	4,41E-05
		Genu corpus callosum	5,47E-04	5,56E-05	5,20E-04	9,33E-05	5,46E-04	1,02E-04
		Body corpus callosum	5,01E-04	5,50E-05	5,43E-04	8,52E-05	5,47E-04	9,43E-05
		Splenium corpus callosum	4,68E-04	5,07E-05	5,45E-04	8,88E-05	5,09E-04	1,10E-04
		Left cingulum (parahipp.)	4,13E-04	3,54E-05	4,56E-04	4,29E-05	3,99E-04	7,98E-05
		Right cingulum (parahipp.)	4,19E-04	2,75E-05	4,93E-04	5,04E-05	4,43E-04	9,58E-05
		Left cingulum (c.g.)	4,92E-04	4,53E-05	5,08E-04	3,94E-05	5,39E-04	4,43E-05
		Right cingulum (c.g.)	4,62E-04	4,71E-05	4,84E-04	3,81E-05	5,46E-04	4,47E-05
		Left post. thalamic radiation	4,85E-04	4,08E-05	5,31E-04	5,05E-05	5,56E-04	5,13E-05
		Right post. thalamic radiation	5,15E-04	6,11E-05	5,49E-04	5,08E-05	5,77E-04	4,92E-05
		Left sup. longitudinal fasciculus	4,54E-04	5,13E-05	4,76E-04	5,80E-05	4,81E-04	6,48E-05
		Right sup.longitudinal fasciculus	4,49E-04	4,53E-05	4,72E-04	5,70E-05	4,75E-04	5,34E-05
		Left sup. corona radiata	4,49E-04	5,52E-05	4,50E-04	5,26E-05	4,94E-04	4,23E-05
		Right sup. corona radiata	4,52E-04	5,22E-05	4,76E-04	4,83E-05	4,98E-04	5,66E-05
		Forceps minor	4,91E-04	1,13E-04	4,75E-04	1,07E-04	5,12E-04	8,67E-05
		Left uncinate fasciculus	5,33E-04	3,90E-05	4,96E-04	4,23E-05	5,24E-04	6,49E-05
		Right uncinate fasciculus	5,42E-04	2,75E-05	5,50E-04	3,14E-05	5,23E-04	3,31E-05
		Middle cerebellar peduncle	4,10E-04	5,72E-05	4,58E-04	7,57E-05	4,07E-04	5,80E-05
		Left inf. cerebellar peduncle	4,54E-04	6,74E-05	6,07E-04	9,20E-05	4,77E-04	8,66E-05
		Right inf. cerebellar peduncle	4,46E-04	5,80E-05	6,08E-04	9,37E-05	4,59E-04	9,46E-05
		Left sup. cerebellar peduncle	3,87E-04	5,68E-05	4,73E-04	4,38E-05	4,26E-04	4,92E-05
		Right sup. cerebellar peduncle	3,95E-04	3,36E-05	5,00E-04	5,75E-05	4,15E-04	7,94E-05
	RD	Fornix	1,80E-04	5,08E-05	2,22E-04	6,31E-05	2,55E-04	2,21E-05
		Genu corpus callosum	1,63E-04	7,79E-05	1,88E-04	6,58E-05	2,33E-04	6,76E-05
		Body corpus callosum	2,19E-04	8,93E-05	2,04E-04	8,06E-05	2,01E-04	6,01E-05
		Splenium corpus callosum	1,60E-04	7,42E-05	1,78E-04	9,54E-05	1,82E-04	6,87E-05
		Left cingulum (parahipp.)	2,49E-04	3,35E-05	2,94E-04	4,23E-05	2,49E-04	5,75E-05

		Right cingulum (parahipp.)	2,50E-04	4,13E-05	2,91E-04	6,08E-05	2,90E-04	9,74E-05
		Left cingulum (c.g.)	3,37E-04	9,98E-05	3,41E-04	8,56E-05	2,66E-04	7,20E-05
		Right cingulum (c.g.)	2,90E-04	8,71E-05	2,82E-04	6,61E-05	2,63E-04	8,76E-05
		Left post. thalamic radiation	2,11E-04	5,87E-05	2,06E-04	4,25E-05	2,61E-04	4,42E-05
		Right post. thalamic radiation	1,86E-04	4,04E-05	1,98E-04	3,72E-05	2,60E-04	5,01E-05
		Left sup. longitudinal fasciculus	2,23E-04	6,43E-05	2,35E-04	6,39E-05	2,32E-04	5,53E-05
		Right sup.longitudinal fasciculus	2,16E-04	7,35E-05	1,99E-04	4,39E-05	2,25E-04	5,13E-05
		Left sup. corona radiata	1,91E-04	2,72E-05	1,98E-04	2,76E-05	2,33E-04	4,75E-05
		Right sup. corona radiata	2,00E-04	2,85E-05	2,03E-04	3,27E-05	2,49E-04	4,66E-05
		Forceps minor	3,09E-04	1,35E-04	3,05E-04	1,15E-04	3,50E-04	1,02E-04
		Left uncinate fasciculus	2,01E-04	5,21E-05	2,07E-04	4,73E-05	2,55E-04	5,49E-05
		Right uncinate fasciculus	1,97E-04	4,14E-05	2,51E-04	6,42E-05	2,54E-04	5,78E-05
		Middle cerebellar peduncle	1,75E-04	5,00E-05	1,66E-04	5,21E-05	1,91E-04	6,23E-05
		Left inf. cerebellar peduncle	2,18E-04	6,31E-05	1,61E-04	6,05E-05	1,85E-04	6,35E-05
		Right inf. cerebellar peduncle	2,12E-04	5,90E-05	1,52E-04	6,09E-05	1,80E-04	6,38E-05
		Left sup. cerebellar peduncle	2,16E-04	5,74E-05	2,01E-04	4,62E-05	2,18E-04	5,64E-05
		Right sup. cerebellar peduncle	2,23E-04	5,36E-05	1,91E-04	4,69E-05	2,10E-04	6,48E-05
		Right sup. cerebellar peduncle	2,23E-04	5,36E-05	1,91E-04	4,69E-05	2,10E-04	6,48E-05
NODDI	ODI	Fornix	0,18	0,07	0,21	0,1	0,49	0,15
		Genu corpus callosum	0,18	0,09	0,23	0,15	0,26	0,18
		Body corpus callosum	0,25	0,15	0,23	0,14	0,22	0,16
		Splenium corpus callosum	0,22	0,12	0,26	0,19	0,2	0,15
		Left cingulum (parahipp.)	0,37	0,12	0,46	0,18	0,39	0,15
		Right cingulum (parahipp.)	0,38	0,11	0,38	0,12	0,39	0,14
		Left cingulum (c.g.)	0,37	0,15	0,38	0,17	0,23	0,09
		Right cingulum (c.g.)	0,42	0,18	0,48	0,19	0,24	0,08
		Left post. thalamic radiation	0,2	0,07	0,2	0,08	0,18	0,07
		Right post. thalamic radiation	0,22	0,1	0,2	0,08	0,19	0,07
		Left sup. longitudinal fasciculus	0,3	0,13	0,26	0,08	0,28	0,11
		Right sup.longitudinal fasciculus	0,3	0,11	0,31	0,13	0,29	0,11
		Left sup. corona radiata	0,28	0,09	0,26	0,07	0,27	0,08
		Right sup. corona radiata	0,27	0,08	0,27	0,07	0,25	0,07
		Forceps minor	0,46	0,24	0,47	0,22	0,44	0,19
		Left uncinate fasciculus	0,19	0,06	0,22	0,05	0,28	0,12
		Right uncinate fasciculus	0,22	0,06	0,22	0,07	0,26	0,14
		Middle cerebellar peduncle	0,3	0,1	0,25	0,1	0,32	0,16
		Left inf. cerebellar peduncle	0,25	0,13	0,11	0,06	0,18	0,11
		Right inf. cerebellar peduncle	0,3	0,18	0,15	0,11	0,18	0,1
		Left sup. cerebellar peduncle	0,35	0,1	0,24	0,08	0,45	0,28
		Right sup. cerebellar peduncle	0,36	0,12	0,23	0,06	0,33	0,18
	NDI	Fornix	0,78	0,13	0,66	0,14	0,59	0,04
		Genu corpus callosum	0,71	0,13	0,65	0,11	0,53	0,08
		Body corpus callosum	0,67	0,13	0,66	0,13	0,63	0,11
		Splenium corpus callosum	0,77	0,15	0,69	0,16	0,65	0,13
		Left cingulum (parahipp.)	0,56	0,11	0,48	0,07	0,57	0,14
		Right cingulum (parahipp.)	0,6	0,15	0,52	0,09	0,6	0,17
		Left cingulum (c.g.)	0,55	0,14	0,56	0,11	0,55	0,12
		Right cingulum (c.g.)	0,51	0,13	0,45	0,1	0,51	0,12
		Left post. thalamic radiation	0,67	0,08	0,64	0,07	0,47	0,08
		Right post. thalamic radiation	0,65	0,09	0,65	0,07	0,5	0,06
		Left sup. longitudinal fasciculus	0,69	0,13	0,7	0,09	0,62	0,11
		Right sup.longitudinal fasciculus	0,66	0,11	0,64	0,12	0,61	0,1
		Left sup. corona radiata	0,69	0,06	0,69	0,08	0,56	0,09
		Right sup. corona radiata	0,73	0,05	0,73	0,05	0,6	0,09
		Forceps minor	0,51	0,17	0,5	0,14	0,44	0,1
		Left uncinate fasciculus	0,59	0,06	0,55	0,07	0,52	0,07
		Right uncinate fasciculus	0,58	0,08	0,66	0,09	0,51	0,07
		Middle cerebellar peduncle	0,87	0,09	0,82	0,09	0,81	0,12
		Left inf. cerebellar peduncle	0,73	0,11	0,73	0,09	0,82	0,09
		Right inf. cerebellar peduncle	0,71	0,13	0,74	0,07	0,77	0,1
		Left sup. cerebellar peduncle	0,77	0,13	0,7	0,08	0,66	0,21
		Right sup. cerebellar peduncle	0,76	0,13	0,73	0,07	0,71	0,18
	f_{iso}	Fornix	0,39	0,15	0,69	0,12	0,86	0,15
		Genu corpus callosum	0,11	0,08	0,28	0,2	0,45	0,32
		Body corpus callosum	0,15	0,12	0,23	0,13	0,53	0,3
		Splenium corpus callosum	0,19	0,11	0,24	0,16	0,44	0,31
		Left cingulum (parahipp.)	0,11	0,09	0,09	0,12	0,2	0,22
		Right cingulum (parahipp.)	0,12	0,12	0,11	0,1	0,15	0,15
		Body corpus callosum	1,90E-03	5,64E-04	2,30E-03	6,72E-04	2,55E-03	4,72E-04
		Splenium corpus callosum	2,21E-03	6,00E-04	2,43E-03	6,81E-04	2,65E-03	3,81E-04
		Left cingulum (parahipp.)	1,36E-03	4,44E-04	1,99E-03	5,36E-04	2,02E-03	6,66E-04
		Right cingulum (parahipp.)	1,49E-03	4,87E-04	1,94E-03	6,42E-04	2,05E-03	6,36E-04
		Left cingulum (c.g.)	1,44E-03	4,16E-04	1,27E-03	4,81E-04	2,30E-03	6,45E-04
		Right cingulum (c.g.)	1,23E-03	4,18E-04	1,64E-03	6,68E-04	2,01E-03	6,85E-04
		Left post. thalamic radiation	2,02E-03	3,23E-04	2,72E-03	3,83E-04	2,44E-03	4,33E-04
		Right post. thalamic radiation	2,07E-03	4,65E-04	2,74E-03	3,61E-04	2,50E-03	3,74E-04

		Left sup. longitudinal fasciculus	1,75E-03	4,36E-04	2,16E-03	5,94E-04	2,18E-03	5,97E-04
		Right sup.longitudinal fasciculus	1,79E-03	4,23E-04	2,48E-03	5,40E-04	2,11E-03	6,31E-04
		Left sup. corona radiata	1,91E-03	3,19E-04	2,46E-03	4,47E-04	2,25E-03	4,57E-04
		Right sup. corona radiata	1,89E-03	2,75E-04	2,49E-03	4,22E-04	2,41E-03	4,07E-04
		Forceps minor	1,47E-03	5,93E-04	1,71E-03	7,27E-04	1,74E-03	7,01E-04
		Left uncinate fasciculus	1,45E-03	3,21E-04	2,34E-03	5,43E-04	2,23E-03	5,75E-04
		Right uncinate fasciculus	1,66E-03	4,02E-04	2,47E-03	6,22E-04	2,25E-03	5,34E-04
		Middle cerebellar peduncle	2,20E-03	4,69E-04	2,36E-03	7,11E-04	1,94E-03	9,13E-04
		Left inf. cerebellar peduncle	2,16E-03	4,58E-04	2,76E-03	3,35E-04	2,54E-03	5,27E-04
		Right inf. cerebellar peduncle	2,12E-03	5,15E-04	2,77E-03	2,95E-04	2,36E-03	6,71E-04
		Left sup. cerebellar peduncle	1,92E-03	3,61E-04	2,29E-03	6,73E-04	1,76E-03	9,63E-04
		Right sup. cerebellar peduncle	2,08E-03	5,13E-04	2,30E-03	6,72E-04	2,04E-03	9,37E-04
DIAMOND	F_{iso}	Fornix	0,43	0,14	0,88	0,13	0,99	0,05
		Genu corpus callosum	0,21	0,18	0,63	0,2	0,71	0,2
		Body corpus callosum	0,39	0,24	0,59	0,18	0,67	0,18
		Splenium corpus callosum	0,29	0,18	0,58	0,2	0,68	0,24
		Left cingulum (parahipp.)	0,44	0,22	0,73	0,16	0,83	0,19
		Right cingulum (parahipp.)	0,41	0,17	0,73	0,17	0,8	0,2
		Left cingulum (c.g.)	0,54	0,24	0,86	0,17	0,59	0,15
		Right cingulum (c.g.)	0,64	0,28	0,74	0,19	0,62	0,17
		Left post. thalamic radiation	0,3	0,08	0,55	0,1	0,69	0,15
		Right post. thalamic radiation	0,36	0,18	0,53	0,08	0,64	0,12
		Left sup. longitudinal fasciculus	0,4	0,21	0,63	0,14	0,61	0,15
		Right sup.longitudinal fasciculus	0,39	0,17	0,54	0,12	0,62	0,15
		Left sup. corona radiata	0,31	0,1	0,52	0,09	0,64	0,13
		Right sup. corona radiata	0,33	0,07	0,54	0,11	0,6	0,12
		Forceps minor	0,55	0,32	0,76	0,24	0,83	0,21
		Left uncinate fasciculus	0,32	0,09	0,55	0,14	0,63	0,14
		Right uncinate fasciculus	0,21	0,08	0,55	0,14	0,6	0,15
		Middle cerebellar peduncle	0,31	0,17	0,56	0,21	0,56	0,19
		Left inf. cerebellar peduncle	0,51	0,2	0,6	0,19	0,65	0,25
		Right inf. cerebellar peduncle	0,51	0,25	0,59	0,18	0,52	0,21
		Left sup. cerebellar peduncle	0,52	0,22	0,56	0,16	0,55	0,14
		Right sup. cerebellar peduncle	0,35	0,17	0,56	0,18	0,62	0,22
	F_{aniso}	Fornix	0,53	0,19	0,14	0,12	0,15	0,14
		Genu corpus callosum	0,82	0,14	0,42	0,16	0,19	0,17
		Body corpus callosum	0,69	0,17	0,45	0,14	0,21	0,17
		Splenium corpus callosum	0,74	0,19	0,45	0,19	0,37	0,22
		Left cingulum (parahipp.)	0,57	0,2	0,31	0,15	0,28	0,15
		Right cingulum (parahipp.)	0,62	0,15	0,33	0,16	0,26	0,17
		Left cingulum (c.g.)	0,63	0,14	0,4	0,16	0,47	0,12
		Right cingulum (c.g.)	0,67	0,15	0,44	0,13	0,48	0,09
		Left post. thalamic radiation	0,66	0,16	0,39	0,16	0,3	0,15
		Right post. thalamic radiation	0,68	0,12	0,38	0,17	0,38	0,11
		Left sup. longitudinal fasciculus	0,68	0,1	0,45	0,09	0,43	0,11
		Right sup.longitudinal fasciculus	0,67	0,1	0,47	0,09	0,44	0,1
		Left sup. corona radiata	0,7	0,12	0,49	0,08	0,37	0,14
		Right sup. corona radiata	0,68	0,07	0,48	0,08	0,4	0,13
		Forceps minor	0,5	0,29	0,28	0,2	0,27	0,17
		Left uncinate fasciculus	0,65	0,13	0,46	0,13	0,38	0,14
		Right uncinate fasciculus	0,78	0,09	0,37	0,15	0,44	0,09
		Middle cerebellar peduncle	0,63	0,21	0,48	0,18	0,46	0,17
		Left inf. cerebellar peduncle	0,55	0,2	0,47	0,22	0,4	0,16
		Right inf. cerebellar peduncle	0,58	0,24	0,4	0,25	0,39	0,21
		Left sup. cerebellar peduncle	0,51	0,21	0,46	0,16	0,44	0,15
		Right sup. cerebellar peduncle	0,62	0,13	0,46	0,13	0,48	0,15
MF	F_{iso}	Fornix	0,14	0,11	0,66	0,31	0,97	0,13
		Genu corpus callosum	0,1	0,13	0,23	0,27	0,39	0,38
		Body corpus callosum	0,22	0,27	0,24	0,25	0,36	0,35
		Splenium corpus callosum	0,11	0,13	0,24	0,27	0,41	0,39
		Left cingulum (parahipp.)	0,26	0,22	0,65	0,29	0,61	0,33
		Right cingulum (parahipp.)	0,22	0,17	0,46	0,31	0,56	0,31
		Left cingulum (c.g.)	0,32	0,33	0,59	0,33	0,29	0,25
		Right cingulum (c.g.)	0,52	0,35	0,47	0,32	0,34	0,25
		Left post. thalamic radiation	0,07	0,07	0,16	0,17	0,31	0,33
		Right post. thalamic radiation	0,15	0,25	0,13	0,12	0,21	0,24
		Left sup. longitudinal fasciculus	0,19	0,29	0,23	0,25	0,21	0,26
		Right sup.longitudinal fasciculus	0,17	0,26	0,17	0,2	0,25	0,26
		Left sup. corona radiata	0,06	0,11	0,11	0,14	0,2	0,25
		Right sup. corona radiata	0,03	0,04	0,11	0,14	0,15	0,22
		Forceps minor	0,46	0,39	0,57	0,38	0,67	0,38
		Left uncinate fasciculus	0,04	0,05	0,23	0,17	0,26	0,28
		Right uncinate fasciculus	0,17	0,11	0,24	0,25	0,3	0,23
		Middle cerebellar peduncle	0,1	0,15	0,35	0,24	0,36	0,3
		Left inf. cerebellar peduncle	0,21	0,28	0,32	0,28	0,21	0,18
		Right inf. cerebellar peduncle	0,25	0,25	0,22	0,2	0,3	0,24

		Left sup. cerebellar peduncle	0,18	0,2	0,23	0,22	0,33	0,35
		Right sup. cerebellar peduncle	0,26	0,23	0,28	0,25	0,26	0,29
	FVF	Fornix	0.13	0.09	0.06	0.08	0.02	0.01
		Genu corpus callosum	0.59	0.17	0.39	0.19	0.13	0.14
		Body corpus callosum	0.43	0.17	0.37	0.16	0.19	0.17
		Splenium corpus callosum	0.5	0.19	0.38	0.23	0.35	0.24
		Left cingulum (parahipp.)	0.3	0.14	0.11	0.1	0.16	0.16
		Right cingulum (parahipp.)	0.23	0.12	0.29	0.16	0.11	0.13
		Left cingulum (c.g.)	0.36	0.16	0.18	0.14	0.38	0.14
		Right cingulum (c.g.)	0.31	0.22	0.25	0.16	0.37	0.16
		Left post. thalamic radiation	0.39	0.14	0.2	0.12	0.16	0.12
		Right post. thalamic radiation	0.33	0.12	0.26	0.14	0.19	0.13
		Left sup. longitudinal fasciculus	0.52	0.12	0.33	0.12	0.37	0.14
		Right sup.longitudinal fasciculus	0.48	0.14	0.41	0.14	0.31	0.13
		Left sup. corona radiata	0.58	0.15	0.52	0.15	0.27	0.14
		Right sup. corona radiata	0.59	0.13	0.48	0.15	0.32	0.15
		Forceps minor	0.33	0.23	0.22	0.2	0.22	0.17
		Left uncinate fasciculus	0.49	0.11	0.22	0.12	0.36	0.15
		Right uncinate fasciculus	0.25	0.11	0.28	0.15	0.19	0.09
		Middle cerebellar peduncle	0.55	0.14	0.33	0.19	0.35	0.22
		Left inf. cerebellar peduncle	0.44	0.13	0.33	0.21	0.45	0.24
		Right inf. cerebellar peduncle	0.29	0.16	0.4	0.23	0.29	0.23
		Left sup. cerebellar peduncle	0.55	0.1	0.37	0.16	0.36	0.18
		Right sup. cerebellar peduncle	0.29	0.14	0.36	0.16	0.35	0.16
	mRad	Fornix	2,57E-06	9,37E-07	1,14E-06	9,71E-07	9,82E-07	8,47E-07
		Genu corpus callosum	3,84E-01	1,31E-01	2,94E-01	1,37E-01	1,34E-01	1,31E-02
		Body corpus callosum	3,63E-01	1,51E-01	2,88E-01	1,39E-01	1,69E-01	1,54E-01
		Splenium corpus callosum	3,30E-01	1,44E-01	2,35E-02	1,31E-01	2,24E-01	1,47E-01
		Left cingulum (parahipp.)	3,75E-01	1,47E-01	2,35E-01	1,18E-01	2,33E-01	1,53E-02
		Right cingulum (parahipp.)	4,03E-01	1,06E-01	3,03E-01	1,33E-01	2,09E-01	1,51E-01
		Left cingulum (c.g.)	4,68E-01	1,18E-01	3,02E-01	1,17E-01	2,70E-01	1,00E-02
		Right cingulum (c.g.)	4,28E-01	1,30E-02	3,54E-01	1,11E-02	3,27E-01	1,04E-01
		Left post. thalamic radiation	4,64E-01	1,05E-01	3,16E-01	1,28E-01	2,76E-01	1,56E-01
		Right post. thalamic radiation	4,33E-02	9,57E-02	3,29E-01	1,39E-01	3,59E-01	1,28E-02
		Left sup. longitudinal fasciculus	5,34E-01	7,58E-02	4,10E-02	1,04E-01	4,28E-01	1,06E-01
		Right sup.longitudinal fasciculus	5,20E-01	8,46E-02	4,27E-01	1,02E-01	4,04E-01	1,15E-01
		Left sup. corona radiata	5,06E-01	9,55E-02	4,23E-01	1,35E-01	3,49E-01	1,57E-01
		Right sup. corona radiata	5,20E-01	8,55E-02	4,06E-01	1,29E-01	3,32E-01	1,47E-01
		Forceps minor	3,59E-01	2,10E-01	2,47E-01	1,87E-01	2,81E-01	1,88E-01
		Left uncinate fasciculus	5,02E-01	9,07E-02	3,69E-01	1,13E-01	3,96E-01	1,52E-01
		Right uncinate fasciculus	4,42E-01	8,08E-02	2,97E-01	1,49E-01	3,74E-01	1,00E-01
		Middle cerebellar peduncle	4,76E-06	1,04E-06	2,82E-06	1,28E-06	2,79E-06	1,48E-06
		Left inf. cerebellar peduncle	4,24E-01	1,19E-01	2,59E-01	1,22E-02	2,43E-01	1,58E-01
		Right inf. cerebellar peduncle	3,46E-01	1,42E-01	2,81E-01	1,70E-01	1,77E-01	1,28E-01
		Left sup. cerebellar peduncle	4,90E-01	8,71E-02	3,44E-01	1,22E-01	2,90E-01	1,36E-01
		Right sup. cerebellar peduncle	3,62E-01	1,71E-02	3,18E-01	1,18E-01	3,27E-01	1,27E-01
Gray matter								
DTI	MD	Left hipp. entorhinal cortex	3,08E-04	1,19E-04	2,97E-04	1,06E-04	2,79E-04	1,09E-04
		Right hipp. entorhinal cortex	3,33E-04	9,85E-05	3,46E-04	1,01E-04	2,88E-04	1,08E-04
		Inferior temporal cortex (AD)	2,68E-04	1,36E-04	3,18E-04	1,32E-04	3,10E-04	1,31E-04
		Inferior temporal cortex (PD)	2,82E-04	1,27E-04	3,39E-04	1,30E-04	3,45E-04	1,30E-04
		Inferior temporal cortex (TOP)	3,47E-04	1,19E-04	3,82E-04	1,25E-04	4,02E-04	1,04E-04
		Middle temporal cortex (PD)	3,35E-04	1,30E-04	3,59E-04	1,29E-04	3,63E-04	1,35E-04
		Middle temporal cortex (TOP)	3,64E-04	1,27E-04	3,80E-04	1,28E-04	4,04E-04	1,16E-04
		Fusiform cortex	3,72E-04	6,95E-05	3,93E-04	7,93E-05	3,79E-04	6,67E-05
		Precuneous cortex	3,74E-04	9,17E-05	3,87E-04	8,55E-05	3,95E-04	8,48E-05
		Frontal pole	3,61E-04	1,59E-04	3,39E-04	1,45E-04	3,57E-04	1,53E-04
		Superior frontal gyrus	4,03E-04	1,24E-04	3,72E-04	1,19E-04	4,05E-04	1,13E-04
		Parahippocampal gyrus (AD)	3,07E-04	1,20E-04	3,16E-04	1,16E-04	2,84E-04	1,13E-04
		Parahippocampal gyrus (PD)	3,25E-04	7,94E-05	3,44E-04	8,24E-05	3,19E-04	8,59E-05
		Posterior cingulate cortex	3,55E-04	7,72E-05	3,68E-04	6,69E-05	3,59E-04	7,01E-05
		Left hippocampus	3,15E-04	7,56E-05	3,08E-04	7,15E-05	2,99E-04	6,74E-05
		Right hippocampus	3,20E-04	7,33E-05	3,32E-04	7,60E-05	3,07E-04	6,89E-05
		Left amygdala	3,43E-04	8,23E-05	3,07E-04	7,80E-05	2,86E-04	7,65E-05
		Right amygdala	3,45E-04	7,71E-05	3,40E-04	8,18E-05	3,01E-04	7,61E-05
NODDI	ODI	Left hipp. entorhinal cortex	0,58	0,2	0,58	0,2	0,67	0,24
		Right hipp. entorhinal cortex	0,58	0,2	0,62	0,23	0,6	0,22
		Inferior temporal cortex (AD)	0,82	0,23	0,73	0,25	0,76	0,25
		Inferior temporal cortex (PD)	0,75	0,27	0,68	0,26	0,69	0,27
		Inferior temporal cortex (TOP)	0,59	0,23	0,61	0,22	0,56	0,22
		Middle temporal cortex (PD)	0,66	0,24	0,64	0,24	0,65	0,23
		Middle temporal cortex (TOP)	0,55	0,21	0,57	0,21	0,55	0,2
		Fusiform cortex	0,54	0,17	0,52	0,16	0,51	0,18
		Precuneous cortex	0,53	0,19	0,51	0,19	0,49	0,19
		Frontal pole	0,65	0,24	0,67	0,24	0,64	0,22
		Superior frontal gyrus	0,54	0,2	0,58	0,21	0,58	0,19

	Parahippocampal gyrus (AD)	0,57	0,21	0,59	0,23	0,61	0,24
	Parahippocampal gyrus (PD)	0,52	0,17	0,51	0,16	0,49	0,18
	Posterior cingulate cortex	0,48	0,19	0,49	0,2	0,43	0,2
	Left hippocampus	0,44	0,18	0,46	0,18	0,43	0,19
	Right hippocampus	0,43	0,18	0,43	0,19	0,41	0,18
	Left amygdala	0,45	0,18	0,45	0,18	0,47	0,19
	Right amygdala	0,44	0,18	0,44	0,18	0,46	0,2
NDI	Left hipp. entorhinal cortex	0,56	0,24	0,51	0,18	0,57	0,25
	Right hipp. entorhinal cortex	0,53	0,23	0,54	0,21	0,6	0,24
	Inferior temporal cortex (AD)	0,38	0,22	0,4	0,17	0,4	0,18
	Inferior temporal cortex (PD)	0,46	0,23	0,43	0,17	0,43	0,17
	Inferior temporal cortex (TOP)	0,48	0,17	0,42	0,14	0,45	0,15
	Middle temporal cortex (PD)	0,45	0,19	0,42	0,15	0,43	0,15
	Middle temporal cortex (TOP)	0,46	0,17	0,43	0,15	0,43	0,13
	Fusiform cortex	0,51	0,12	0,47	0,12	0,5	0,12
	Precuneous cortex	0,49	0,15	0,49	0,14	0,48	0,13
	Frontal pole	0,41	0,17	0,42	0,17	0,42	0,16
	Superior frontal gyrus	0,44	0,15	0,46	0,14	0,45	0,12
	Parahippocampal gyrus (AD)	0,55	0,24	0,53	0,2	0,59	0,24
	Parahippocampal gyrus (PD)	0,59	0,18	0,57	0,17	0,6	0,18
	Posterior cingulate cortex	0,55	0,16	0,54	0,15	0,54	0,14
	Left hippocampus	0,6	0,18	0,59	0,17	0,62	0,17
	Right hippocampus	0,63	0,19	0,65	0,17	0,64	0,17
	Left amygdala	0,55	0,17	0,56	0,17	0,63	0,19
	Right amygdala	0,57	0,2	0,64	0,2	0,68	0,2
f_{iso}	Left hipp. entorhinal cortex	0,26	0,29	0,24	0,29	0,34	0,32
	Right hipp. entorhinal cortex	0,21	0,27	0,31	0,31	0,36	0,32
	Inferior temporal cortex (AD)	0,05	0,08	0,06	0,08	0,14	0,18
	Inferior temporal cortex (PD)	0,07	0,1	0,09	0,13	0,17	0,2
	Inferior temporal cortex (TOP)	0,08	0,12	0,14	0,19	0,21	0,24
	Middle temporal cortex (PD)	0,07	0,11	0,12	0,15	0,23	0,25
	Middle temporal cortex (TOP)	0,08	0,12	0,16	0,18	0,22	0,24
	Fusiform cortex	0,07	0,13	0,17	0,2	0,28	0,29
	Precuneous cortex	0,18	0,22	0,29	0,26	0,35	0,32
	Frontal pole	0,12	0,17	0,23	0,26	0,34	0,33
	Superior frontal gyrus	0,2	0,26	0,34	0,3	0,42	0,36
	Parahippocampal gyrus (AD)	0,23	0,28	0,26	0,3	0,35	0,32
	Parahippocampal gyrus (PD)	0,22	0,28	0,31	0,32	0,43	0,34
	Posterior cingulate cortex	0,15	0,2	0,25	0,24	0,33	0,3
	Left hippocampus	0,23	0,27	0,31	0,3	0,43	0,34
	Right hippocampus	0,23	0,26	0,37	0,31	0,43	0,33
	Left amygdala	0,2	0,25	0,28	0,28	0,32	0,3
	Right amygdala	0,21	0,27	0,32	0,29	0,36	0,3

Table D.1: Results of the ROI-based analysis of DTI (metrics: FA, MD, AxD, RD), NODDI (metrics: ODI, NDI, f_{iso}), DIAMOND (metrics: F_{iso}, F_{aniso}) and Microstructure Fingerprinting (MF) (metrics: F_{iso}, FVF, mRad). The table shows the mean and standard deviation of the metrics evaluated in the regions of interest (i.e. regions highlighted in the literature and known to be affected by Alzheimer's disease) and control regions mildly affected by Alzheimer's disease (cerebellar peduncles). The ROIs were localized with FSl Atlases: Harvard-Oxford Cortical Structural Atlas, Harvard-Oxford Subcortical Structural Atlas, JHU ICBM-DTI-81 White-Matter Labels and JHU White-Matter Tractography Atlas.

Bibliography

[1] Alzheimer Europe. "Dementia In Europe." In: *The Alzheimer Europe Magazine, Issue 32* (2020).

[2] D.C. Alexander, T.B. Dyrby, M. Nilsson, and H. Zhang. "Imaging brain microstructure with diffusion MRI: practicality and applications". In: *NMR in Biomedicine* (2019). DOI: 10.1002/nbm.3841.

[3] R.R. Weynants and P. Vandenplas. *Physique V - Partie 1 : Mecanique Quantique.* 2006.

[4] F. Peeters. *LGBIO2050 : Medical Imaging, Chapter 4 : Magnetic Resonance Imaging.* UCLouvain, Ecole Polytechnique de Louvain, 2017.

[5] M. Puddephat. *The principles of magnetic resonance imaging.* February 2020. URL: http://www.pixelmeasure.io/pages/84/the-principles-of-magnetic-resonance-imaging.

[6] R. Gruetter. *Fundamentals of Biomedical Imaging : Ultrasounds, X-Rays, PET, MRI Applications, Part 2.* 2019.

[7] L.J. Bond, J.W. Griffin, R.V. Harris, K.N. Denslow, and T.L. Moran. *Evaluation of Non-Nuclear Techniques for Well Logging: Final Report.* 2011.

[8] M. Kleinnijenhuis. *Imaging Fibres in the Brain.* 2014, p. 48. DOI: 10.13140/2.1.4788.7689.

[9] J.P. Ridgway. *Cardiovascular Magnetic Resonance Manual : Relaxation Times, Gradient Echoes and Spin Echoes, Second Edition.* Springer, 2015, pp. 28–33. DOI: 10.1007/978-3-319-20940-1_5.

[10] A. Filler. *Spin Echo Diagram.* February 2020. URL: https://en.wikipedia.org/wiki/File:Spin_Echo_Diagram.jpg.

[11] J. Beaujoin, N.P. Gallagher, F. Boumezbeur, M. Axer, J. Bernard, F. Poupon, D. Schmitz, J.P. Mangin, and C. Poupon. "Post-mortem inference of the human hippocampal connectivity and microstructure using ultra-high field diffusion MRI at 11.7 T." In: *Brain Structure and Function, pp.2157–2179* (2018). DOI: 10.1007/s00429-018-1617-1.

[12] R.C. Van de Ven, B. Hogers, A. Van den Maagdenberg, H.J. de Groot, R.R. Frants, R.E. Poelmann, L. Van der Weerd, and S. Kiihne. "T(1) Relaxation in in Vivo Mouse Brain at Ultra-High Field." In: *Magn Reson Med ; 58(2):390-5* (2007). DOI: 10.1002/mrm.21313.

[13] D. Kurzhunov. *Novel Reconstruction and Quantification Methods for Oxygen-17 Magnetic Resonance Imaging at Clinical Field Strengths.* Freiburg University, July 2017, p. 38. DOI: 10.13140/RG.2.2.22003.02089.

[14] D.W. McRobbie and Elizabeth A. Moore. "Part II - The Specialist Stuff". In: *MRI from Picture to Proton* (2017), pp. 183–364.

[15] T.A.G.M. Huisman. "Diffusion-weighted and diffusion tensor imaging of the brain, made easy". In: *Cancer Imaging* (2010). DOI: 10.1102/1470-7330.2010.9023.

[16] A. Niyigaba Ishimwe. *The influence of spherical pores within the white matter on Diffusion-Weighted MRI signals : a numerical study using Monte-Carlo simulations.* UCLouvain, 2017.

[17] G. Rensonnet, D. Jacobs, B. Macq, and M. Taquet. *A hybrid method for efficient and accurate simulations of diffusion compartment imaging signals.* Conference: 11th International Symposium on Medical Information Processing and Analysis, Cuenca, Ecuador, 2015. DOI: 10.1117/12.2207890.

[18] D. Tromp. *The diffusion tensor, and its relation to FA, MD, AD and RD.* 2020. URL: https://thewinnower.com/papers/3523-the-diffusion-tensor-and-its-relation-to-fa-md-ad-and-rd.

[19] G. Rensonnet. *In vivo diffusion magnetic resonance imaging of the white matter microstructure from dictionaries generated by Monte Carlo simulations : development and validation (PhD Thesis)*. UCLouvain and EPFL, 2019.

[20] Q. Wen et al. "White Matter Alterations in Early-Stage Alzheimer's Disease : A Tract-Specific Study." In: *Alzheimer's and Dementia : Diagnosis, Assessment & Disease Monitoring* (2019). DOI: 10.1016/j.dadm.2019.06.003.

[21] L.J. Lanyon. "Diffusion Tensor Imaging: Structural Connectivity Insights, Limitations and Future Directions". In: *Neuroimaging Methods* (2012), pp. 137–155. DOI: 10.5772/23245.

[22] D.A. Yablonskiy, G.L. Bretthorst, and J.J. Ackerman. "Statistical Model for Diffusion Attenuated MR Signal". In: *Magnetic Resonance in Medicine* (2013), pp. 664–669. DOI: 10.1002/mrm.10578.

[23] B. Scherrer, A. Schwartzman, M. Taquet, M. Sahin, S.P. Prabhu, and S.K. Warfield. "Characterizing Brain Tissue by Assessment of the Distribution of Anisotropic Microstructural Environments in Diffusion-Compartment Imaging (DIAMOND)". In: *Magnetic Resonance in Medicine* (2015). DOI: 10.1002/mrm.25912.

[24] M. Taquet, G. Rensonnet, A. Jankovski, D. Jacobs, A. des Rieux, S.K. Warfield, and B. Scherrer. "Extra-axonal restricted diffusion as an in-vivo marker of reactive microglia." In: *Scientific Reports.* (2019). DOI: 10.1038/s41598-019-50432-5.

[25] H. Zhang, T. Schneider, C. Wheeler-Kingshott, and D. Alexander. "NODDI: Practical in vivo neurite orientation dispersion and density imaging of the human brain". In: *NeuroImage, Volume 61, Issue 4* (2012), pp. 1000–1016. DOI: 10.1016/j.neuroimage.2012.03.072.

[26] M. Tariq and D.C. Alexander. "Bingham-NODDI: Mapping anisotropic orientation dispersion of neurites using diffusion MRI." In: *NeuroImage 133.* (2016). DOI: 10.1016/j.neuroimage.2016.01.046.

[27] G. Kurz, U.D. Hanebeck, and F. Pfaff. "Kullback–Leibler Divergence and Moment Matching for Hyperspherical Probability Distributions". In: *19th International Conference on Information Fusion (FUSION)* (2016), pp. 2087–2094.

[28] I.O. Jelescu, J. Veraart, E. Fieremans, and D. Novikov. "Degeneracy in model parameter estimation for multi-compartmental diffusion in neuronal tissue." In: *NMR Biomed ; 29(1):33-47* (2016). DOI: 10.1002/nbm.3450.

[29] N. Colgan et al. "Application of neurite orientation dispersion and density imaging (NODDI) to a tau pathology model of Alzheimer's disease". In: *NeuroImage* (2015). DOI: 10.1016/j.neuroimage.2015.10.043.

[30] I.O. Jelescu, J. Veraart, V. Adisetiyo, S. Milla, D. Novikov, and E. Fieremans. "One diffusion acquisition and different white matter models: How does microstructure change in human early development based on WMTI and NODDI?" In: *Neuroimage ; 107:242-256* (2017). DOI: 10.1016/j.neuroimage.2014.12.009.

[31] G. Rensonnet, B. Scherrer, S.K. Warfield, B. Macq, and M. Taquet. "Assessing the validity of the approximation of diffusion-weighted-MRI signals from crossing fascicles by sums of signals from single fascicles." In: *Magn Reson Med. ;79(4):2332-2345.* (2018). DOI: 10.1002/mrm.26832.

[32] G. Rensonnet, B. Scherrer, G. Girard, A. Jankovski, S.K. Warfield, B. Macq, J.P. Thiran, and M. Taquet. "Towards microstructure fingerprinting: Estimation of tissue properties from a dictionary of Monte Carlo diffusion MRI simulations." In: *Neuroimage. 1;184:964-980.* (2019). DOI: 10.1016/j.neuroimage.2018.09.076.

[33] Alzheimer's Association. "2019 Alzheimer's Disease Facts and Figures." In: *Alzheimer & Dementia, 15(3):321-387* (2019). DOI: 10.1016/j.jalz.2019.01.010.

[34] G.D. Rabinovici. "Late-onset Alzheimer Disease." In: *Continuum (Minneap Minn) ; 25(1):14-33.* (2019). DOI: 10.1212/CON.0000000000000700.

[35] G. Operto, R. Cacciaglia, O. Grau-Rivera, C. Falcon, and A. Brugulat-Serrat. "White matter microstructure is altered in cognitively normal middle-aged APOE-4 homozygotes." In: *Nature Neuroscience.* (2018). DOI: 10.1186/s13195-018-0375-x.

[36] M.F. Mendez. "Early-onset Alzheimer Disease and Its Variants". In: *Continuum (Minneap Minn)* (2019). DOI: 10.1212/CON.0000000000000687.

[37] U.S. National Library of Medicine. *APP gene - amyloid beta precursor protein.* 2020. URL: https://ghr.nlm.nih.gov/gene/APP.

[38] U.S. National Library of Medicine. *PSEN1 gene - presenilin 1.* 2020. URL: https://ghr.nlm.nih.gov/gene/PSEN1.

[39] U.S. National Library of Medicine. *PSEN2 gene - presenilin 2.* 2020. URL: https://ghr.nlm.nih.gov/gene/PSEN2.

[40] N. Iwamoto, E. Nishiyama, and H. Arai. "Distribution of Amyloid Deposits in the Cerebral White Matter of the Alzheimer's Disease Brain: Relationship to Blood Vessels". In: *Acta Neuropathol ; 93(4):334-40* (1997). DOI: 10.1007/s004010050624.

[41] H.L. Jacobs, T. Hedden, A.P. Schultz, J. Sepulcre, R.D. Perea, R.E. Amariglio, K.V. Papp, and D.M. Rentz. "Structural Tract Alterations Predict Downstream Tau Accumulation in Amyloid-Positive Older Individuals." In: *Neurobiol Aging.* (2018). DOI: 10.1038/s41593-018-0070-z.

[42] D.V. Hansen, J.E. Hanson, and M. Sheng. "Microglia in Alzheimer's disease." In: *Journal Cell Biology 217 (2): 459–472.* (2018). DOI: 10.1083/jcb.201709069.

[43] A.L. Hemonnot, J. Hua, L. Ulmann, and H. Hirbec. "Microglia in Alzheimer Disease: Well-Known Targets and New Opportunities." In: *Front. Aging Neurosci. 11:233.* (2019). DOI: 10.3389/fnagi.2019.00233.

[44] J. Verheijen and K. Sleegers. "Understanding Alzheimer Disease at the Interface between Genetics and Transcriptomics." In: *Trends Genet. 34(6):434-447* (2018). DOI: 10.1016/j.tig.2018.02.007.

[45] E. Spangenberg, R.J. Lee, A.R. Najafi, R.A. Rice, M. Elmore, M. Blurton-Jones, B. Cest, and K. Green. "Eliminating microglia in Alzheimer's mice prevents neuronal loss without modulating amyloid-β pathology." In: *Brain. ; 139(4): 1265–1281.* (2016). DOI: 10.1093/brain/aww016.

[46] E. Spangenberg, P.L. Severson, L.A. Hohsfield, J. Crapser, J. Zhang, E.A. Burton, Y. Zhang, W. Spevak, J. Lin, and N. Phan. "Sustained microglial depletion with CSF1R inhibitor impairs parenchymal plaque development in an Alzheimer's disease model." In: *Nature Communications volume 10, Article number: 3758.* (2019). DOI: 10.1038/s41467-019-11674-z.

[47] G. Kerckhofs. *LGBIO2040 : Biomechanics.* UCLouvain, Ecole Polytechnique de Louvain, 2019.

[48] R. Khoury and E. Ghossoub. "Diagnostic biomarkers of Alzheimer's disease: A state-of-the-art review." In: *Biomarkers in Neuropsychiatry, volume 1.* (2019). DOI: 10.1016/j.bionps.2019.100005.

[49] F. Panza, D. Seripa, M. Lozupone, and B.P. Imbimbo. "Amyloid-β Immunotherapy for Alzheimer's Disease." In: *Annals of Neurology* (2019). DOI: 10.1002/ana.25410.

[50] B.J. Hanseeuw et al. "Association of Amyloid Tau With Cognition in Preclinical Alzheimer Disease. A Longitudinal Study." In: *JAMA Neurol.* (2019). DOI: 10.1001/jamaneurol.2019.1424.

[51] H. Braak and K. Del Tredici. "Evolutional Aspects of Alzheimer's Disease Pathogenesis." In: *Journal of Alzheimer's disease: JAD 33(1)* (2012). DOI: 10.3233/JAD-2012-129029.

[52] P.H. Montenigro, D.T. Corp, D.T. Stein, and R.A. Stern. "Chronic Traumatic Encephalopathy: Historical Origins and Current Perspective." In: *Annual Review of Clinical Psychology 11(1)* (2015). DOI: 10.1146/annurev-clinpsy-032814-112814.

[53] T. Tapiola, I. Alafuzoff, S.K. Herukka, L. Parkkinen, P. Hartikainen, H. Soininen, and T. Pirttila. "Cerebrospinal fluid β-amyloid 42 and tau proteins as biomarkers of Alzheimer-type pathologic changes in the brain." In: *Arch Neurol.; 66(3):382-9* (2009). DOI: 10.1001/archneurol.2008.596.

[54] E. Morris, A. Chalkidou, A. Hammers, J. Peacock, J. Summers, and S. Keevil. "Diagnostic accuracy of ^{18}F amyloid PET tracers for the diagnosis of Alzheimer's disease: a systematic review and meta-analysis." In: *Eur J Nucl Med Mol Imaging. ; 43: 374–385* (2016). DOI: 10.1007/s00259-015-3228-x.

[55] K.A. Johnson, S. Minoshima, N.I. Bohnen, K.J. Donohoe, N.L. Foster, P. Herscovitch, and J.H. Kerlawish. "Appropriate Use Criteria for Amyloid PET - A Report of the Amyloid Imaging Task Force (AIT), the Society of Nuclear Medicine and Molecular Imaging (SNMMI) and the Alzheimer Association (AA)." In: *Alzheimers Dement.; 9(1): e–1-16.* (2013). DOI: 10.1016/j.jalz.2013.01.002.

[56] A. Leuzy, K. Chiotis, L. Lemoine, P.G. Gillberg, O. Almkvist, E. Rodriguez-Vieitez, and A. Nordberg. "Tau PET imaging in neurodegenerative tauopathies—still a challenge." In: *Molecular Psychiatry.* (2019). DOI: 10.1038/s41380-018-0342-8.

[57] T.J. Betthauser, K.A. Cody, M.D. Zammit, D. Murali, A.K. Converse, T.E. Barnhart, C.K. Stone, H.A. Rowley, S.C. Johnson, and B.T. Christian. "In Vivo Characterization and Quantification of Neurofibrillary Tau PET Radioligand ^{18}F-MK-6240 in Humans from Alzheimer Disease Dementia to Young Controls." In: *Journal of Nuclear Medicine.* (2019). DOI: 10.2967/jnumed.118.209650.

[58] C. Aguero, M. Dhaynaut, M.C. Normandin, A.C. Amaral, N.J. Guehl, R. Neelamegam, and M. Marquie. "Autoradiography validation of novel tau PET tracer [F-18]-MK-6240 on human postmortem brain tissue." In: *Acta Neuropathologica Communications: Neuroscience of Disease* (2019). DOI: 10.1186/s40478-019-0686-6.

[59] H.I.L. Jacobs, D.A. Hopkins, H.C. Mayrhofer, E. Bruner, M.W. van Leeuwen, W. Raaijmakers, and J.D. Schmahmann. "The cerebellum in Alzheimer's disease: evaluating its role in cognitive decline". In: *Brain* (2018). DOI: 10.1093/brain/awx194.

[60] M.L. Bayot, V. Reddy, and M.K. Zabel. "Neuroanatomy, Dural Venous Sinuses". In: *StatPearls* (2020). DOI: 29489265.

[61] E. Rodriguez-Vieitez and A. Nordberg. "Imaging Neuroinflammation: Quantification of Astrocytosis in a Multitracer PET Approach." In: *Biomarkers for Alzheimer's Disease Drug Development, Methods in Molecular Biology, vol. 1750, Springer Science and Business Media* (2018). DOI: 10.1007/978-1-4939-7704-8_16.

[62] R.D. Perea, J.S. Rabin, M.G. Fujiyoshi, T.E. Neal, and E.E. Smith. "Connectome-derived diffusion characteristics of the fornix in Alzheimer's disease." In: *NeuroImage: Clinical* (2018). DOI: 10.1016/j.nicl.2018.04.029.

[63] C.D. Mayo, E.L. Mazerolle, L. Ritchie, J.D. Fisk, and J.R. Gawryluk. "Longitudinal Changes in Microstructural White Matter Metrics in Alzheimer's Disease." In: *Neuroimage Clin.* (2016). DOI: 10.1016/j.nicl.2016.12.012.

[64] K. Kantarci, M.E. Murray, C.G. Scwarz, R. Reid, and S.A.Przybelski. "White-matter Integrity on DTI and the Pathologic Staging of Alzheimer's Disease." In: *Neurobiol Aging.* (2017). DOI: 10.1016/j.neurobiolaging.2017.04.024.

[65] S.Y. Yi, B.R. Barnett, M. Torres-Velazquez, Y. Zhang, S. Hurley, P.A. Rowley, D. Hernando, and J.P. Yu. "Detecting Microglial Density With Quantitative Multi-Compartment Diffusion MRI." In: *Front. Neurosci.* (2019). DOI: 10.3389/fnins.2019.00081.

[66] N.T. Doan, A. Engvig, K. Persson, D. Alnaes, T. Kaufmann, J. Rokicki, A. Cordova-Palomera, T. Moberget, A. Braekhus, and M. Lage. "Dissociable Diffusion MRI Patterns of White Matter Microstructure and Connectivity in Alzheimer's Disease Spectrum." In: *Sci Rep 7, 45131.* (2017). DOI: 10.1038/srep45131.

[67] J.S. Rabin, R.D. Perea, R.F. Buckley, K.A. Johnson, R.A. Sperling, and T. Hedden. "Synergism between fornix microstructure and beta amyloid accelerates memory decline in clinically normal older adults." In: *Neurobiology of Aging* (2019). DOI: 10.1016/j.neurobiolaging.2019.05.005.

[68] P.S. Weston, I.J. Simpson, N.S. Ryan, and S. Ourselin. "Diffusion imaging changes in grey matter in Alzheimer's disease: a potential marker of early neurodegeneration." In: *Alzheimers Res Ther.; 7(1):47* (2015). DOI: 10.1186/s13195-015-0132-3.

[69] M.J. Muller, D. Greverus, P.R. Dellani, C. Weibrich, P.R. Wille A. Scheurich, P. Stoeter, and A. Fellgiebel. "Functional Implications of Hippocampal Volume and Diffusivity in Mild Cognitive Impairment." In: *Neuroimage.;28(4):1033-42* (2005). DOI: 10.1016/j.neuroimage.2005.06.029.

[70] S.E. Rose, A.L. Janke, and J.B. Chalk. "Gray and White Matter Changes in Alzheimer's Disease: A Diffusion Tensor Imaging Study." In: *J. Magn. Reson. Imaging;27(1):20-6* (2008). DOI: 10.1002/jmri.21231.

[71] H.I.L. Jacobs, M.P.J. van Boxel, E.H.B.M. Gronenschild, H.B.M. Uylings, J. Jolles, and F.R.J. Verhey. "Decreased gray matter diffusivity: a potential early Alzheimer disease biomarker?" In: *Alzheimers & Dementia;9(1),93-97* (2013). DOI: 10.1016/j.jalz.2011.11.004.

[72] X. Fu, S. Shrestha, M. Sun, Q. Wu, Y. Luo, X. Zhang, J. Yin, and H. Ni. "Microstructural White Matter Alterations in Mild Cognitive Impairment and Alzheimer's Disease." In: *Clin Neuroradiol.* (2019). DOI: 10.1007/s00062-019-00805-0.

[73] C.F. Slattery, J. Zhang, and R.W. Patterson. "ApoE influences regional white-matter axonal density loss in Alzheimer's disease." In: *Neurobiol Aging. ; 57:8-17.* (2017). DOI: 10.1016/j.neurobiolaging.2017.04.021.

[74] T.D. Parker, C.F. Slattery, J. Zhang, J.M. Nicholas, R.W. Paterson, and A.J.M Foulkes. "Cortical microstructure in young onset Alzheimer's disease using neurite orientation dispersion and density imaging." In: *Human Brain Mapping 39(7):3005-3017* (2018). DOI: 10.1002/hbm.24056.

[75] A.P. Merluzzi, D.C. Dean, and N. Adluru. "Age-Dependent Differences in Brain Tissue Microstructure Assessed with Neurite Orientation Dispersion and Density Imaging." In: *Neurobiol Aging. ; 43: 79–88.* (2016). DOI: 10.1016/j.neurobiolaging.2016.03.026.

[76] J. Zhang. *Applications of NODDI for imaging in vivo white matter pathology in neurodegenerative diseases (PhD Thesis).* University College London, 2019.

[77] J. Duque. *LKINE1036 : Compléments de Neurophysiologie : Apprentissage Procédural et Plasticité.* UCLouvain, Faculté des sciences de la motricité, 2019.

[78] J. Pantel, J. Schröder, M. Essig, R. Minakaran, and L.R. Schad. "Corpus Callosum in Alzheimer's disease and vascular dementia : A Quantitative Magnetic Resonance Study." In: *Alzheimer's Disease — From Basic Research to Clinical Applications pp 129-136* (1998). DOI: 10.1007/978-3-7091-7508-8_12.

[79] S. Kozlovskiy, A.V. Vartanov, and E. Nikonova. "Functional role of corpus callosum regions in human memory functioning." In: *International Journal of Psychophysiology 85(3):396-397* (2012). DOI: 10.1016/j.ijpsycho.2012.07.092.

[80] P.C. Mamiya, T.L. Richards, and P.K. Kuhl. "Right Forceps Minor and Anterior Thalamic Radiation Predict Executive Function Skills in Young Bilingual Adults." In: *Front Psychol.; 9: 118.* (2018). DOI: 10.3389/fpsyg.2018.00118.

[81] J. Vega and N.R. Metrus. *The Corona Radiata and Stroke.* 2020. URL: https://www.verywellhealth.com/what-is-the-corona-radiata-3146130.

[82] K. George and J.M. Das. "Neuroanatomy, Thalamocortical Radiations." In: *StatPearls* (2019).

[83] D.O. Okonkwo, M. Collins, R.J. Soose, and A. Kontos. *Brain tracts.* 2020. URL: http://www.team-tbi.com/brain-tracts.

[84] R. Mendoza and W. Schultz. "The role of the striatum in social behavior." In: *Front Neurosci* (2013). DOI: 10.3389/fnins.2013.00233.

[85] K.M. Madhavan, T. McQueeny, S.R. Howe, and P. Shear. "Superior longitudinal fasciculus and language functioning in healthy aging." In: *Brain Research 1562 II-22* (2014). DOI: 10.1016/j.brainres.2014.03.012.

[86] E.A. Stamatakis, M.A. Shafto, G. Williams, P. Tam, and L.K. Tyler. "White Matter Changes and Word Finding Failures with Increasing Age." In: *PLoS One* (2011). DOI: 10.1371/journal.pone.0014496.

[87] J. Holdnack, A. Prifitera, L. Weiss, and D. Saklofske. "Chapter 12 - WISC-V and the Personalized Assessment Approach." In: *Practical Resources for the Mental Health Professional pp. 373-413* (2016). DOI: 10.1016/B978-0-12-404697-9.00012-1.

[88] K. Madhavan, T. McQueeny, S. Howe, and P. Shear. "Working memory, attention, and executive function in Alzheimer's disease and frontotemporal dementia." In: *Brain Res 1562: 11–22.* (2014). DOI: 10.1016/j.brainres.2014.03.012.

[89] M.G. Pop, C. Crivii, and I. Opincariu. "Anatomy and Function of the Hypothalamus." In: *Hypothalamus in Health and Diseases.* (2018). DOI: 10.5772/intechopen.80728.

[90] F.D. Raslau, J.C. Augustinack, A.P. Klein, and V.P. Mathews. "Memory Part 3: The Role of the Fornix and Clinical Cases." In: *American Journal of Neuroradiology 36 (9) 1604-1608.* (2015). DOI: 10.3174/ajnr.A4371.

[91] R. Kassab and F. Alexandre. "Integration of exteroceptive and interoceptive information within the hippocampus: a computational study." In: *Front Syst Neurosci 9:87.* (2015). DOI: 10.3389/fnsys.2015.00087.

[92] S. Ocklenburg and O. Güntürkün. "Chapter 9 - Structural Hemispheric Asymmetries." In: *The Lateralized Brain - The Neuroscience and Evolution of Hemispheric Asymmetries, pp. 239-262.* (2018). DOI: 10.1016/B978-0-12-803452-1.00009-6.

[93] S. Fujie, C. Namiki, and H. Nishi. "The Role of the Uncinate Fasciculus in Memory and Emotional Recognition in Amnestic Mild Cognitive Impairment." In: *Dement Geriatr Cogn Disord 26:432–439.* (2008). DOI: 10.1159/000165381.

[94] E.J. Bubb, C.M. Baddeley, and J.P. Aggleton. "The cingulum bundle: Anatomy, function, and dysfunction." In: *Neuroscience and Biobehavioral Reviews 92 pp. 104-127.* (2018). DOI: 10.1016/j.neubiorev.2018.05.008.

[95] A.E. Cavanna and M.R. Trimble. "The precuneus: a review of its functional anatomy and behavioural correlates." In: *Brain 129 (Pt. 3):564-83* (2006). DOI: 10.1093/brain/awl004.

[96] J. Xu, J. Wang, L. Fan, and W. Zhang. "Tractography-based Parcellation of the Human Middle Temporal Gyrus." In: *Sci Rep. 5:18883* (2015). DOI: 10.1038/srep18883.

[97] J.V. Haxby, E.A. Hoffman, and M.I. Gobbini. "The distributed human neural system for face perception." In: *Trends in Cognitive Sciences - Vol.4, No.6, pp.223-233* (2000). DOI: 10.1016/S1364-6613(00)01482-0.

[98] H. Schultz, T. Sommer, and J. Peters. "The Role of the Human Entorhinal Cortex in a Representational Account of Memory." In: *Front Hum Neurosci. ; 9: 628.* (2015). DOI: 10.3389/fnhum.2015.00628.

[99] K.T. Nishiuchi. "Entorhinal cortex and consolidated memory." In: *Neuroscience Research 84 pp.27–33* (2014). DOI: 10.1016/j.neures.2014.02.012.

[100] K. Bengochea. *Fusiform Gyrus.* 2020. URL: https://www.kenhub.com/en/library/anatomy/fusiform-gyrus.

[101] S.V. Siddiqui, U. Chatterjee, and D. Kumar. "Neuropsychology of prefrontal cortex." In: *Indian J Psychiatry.; 50(3): 202–208.* (2008). DOI: 10.4103/0019-5545.43634.

[102] F. du Boisgueheneuc, R. Levy, E. Volle, M. Seassau, H. Duffau, S. Kinkingnehun, Y. Samson, S. Zhang, and B. Dubois. "Functions of the left superior frontal gyrus in humans: a lesion study." In: *Brain. ;129(Pt 12):3315-28.* (2006). DOI: 10.1093/brain/awl244.

[103] W. Li, W. Qin, H. Liu, and L. Fan. "Subregions of the human superior frontal gyrus and their connections." In: *NeuroImage 78 46–58.* (2013). DOI: 10.1016/j.neuroimage.2013.04.011.

[104] E. Aminoff, K. Kveraga, and M. Bar. "The role of the parahippocampal cortex in cognition." In: *Trends Cogn Sci. ; 17(8): 379–390.* (2013). DOI: 10.1016/j.tics.2013.06.009.

[105] R. Leech and D.J. Sharp. "The role of the posterior cingulate cortex in cognition and disease." In: *Brain. ; 137(1): 12–32.* (2014). DOI: 10.1093/brain/awt162.

[106] K.S. Anand and V. Dhikav. "Hippocampus in health and disease: An overview." In: *Ann Indian Acad Neurol.; 15(4): 239–246.* (2012). DOI: 10.4103/0972-2327.104323.

[107] C. Cristinzio and P. Vuilleumier. "The Role of Amygdala in Emotional and Social Functions: Implications for Temporal Lobe Epilepsy." In: *Epileptologie., Vol.24, p.78-89* (2007). DOI: https://archive-ouverte.unige.ch/unige:44299.

[108] GE Healthcare. "SIGNA Pulse of MR." In: *Tomorrow Today ; volume 21, ISMRM Edition* (2017). URL: http://www3.gehealthcare.nl/~/media/downloads/netherlands/signa%5C%20pulse%5C%20of%5C%20mr_spring%5C%202017.pdf.

[109] J.V. Manjon and P. Coupe. "volBrain : An online MRI brain volumetry system." In: *Frontiers in Neuroinformatics.* (2016). DOI: 10.3389/fninf.2016.00030.

[110] S. Smith et al. "Tract-based spatial statistics: Voxelwise analysis of multi-subject diffusion data". In: *NeuroImage ; volume 31, Issue 4, pp.1487-1505* (2006). DOI: 10.1016/j.neuroimage.2006.02.024.

[111] M. Jenkinson. *TBSS - User Guide.* 2013. URL: https://fsl.fmrib.ox.ac.uk/fsl/fslwiki/TBSS/UserGuide.

[112] P.L. Chiang, H.L. Chen, P.C. Chen, and C.H. Lu. "White matter damage and systemic inflammation in Parkinson's disease." In: *BMC Neuroscience volume 18, Article number: 48* (2017). DOI: 10.1186/s12868-017-0367-y.

[113] S.Y. Yi, N.A. Stowe, B.R. Barnett, K. Dodd, and J.P. Yu. "Microglial density alters measures of axonal integrity and structural connectivity." In: *Biological Psychiatry: Cognitive Neuroscience and Neuroimaging, Elsevier* (2020). DOI: 10.1016/j.bpsc.2020.04.008.

[114] N. Iwamoto, E. Nishiyama, J. Ohwada, and H. Arai. "Distribution of Amyloid Deposits in the Cerebral White Matter of the Alzheimer's Disease Brain: Relationship to Blood Vessels." In: *Acta Neuropathol ; 93(4):334-40* (1997). DOI: 10.1007/s004010050624.

[115] M. Marek, M. Horyniecki, F. Fraczek, and E. Kluczewska. "Leukoaraiosis – new concepts and modern imaging." In: *Pol J Radiol. ; 83: e76–e81.* (2018). DOI: 10.5114/pjr.2018.74344.

[116] S.E. Rose, A.L. Janke, and J.B. Chalk. "Gray and white matter changes in Alzheimer's disease: a diffusion tensor imaging study." In: *J. Magn. Reson. Imaging ;27(1):20-6.* (2007). DOI: 10.1002/jmri.21231.

UNIVERSITÉ CATHOLIQUE DE LOUVAIN
École polytechnique de Louvain
Rue Archimède, 1 bte L6.11.01, 1348 Louvain-la-Neuve, Belgique | **www.uclouvain.be/epl**